Modelling of Turbulent SF_6 Switching Arcs

Thesis submitted in accordance with the requirements of

the University of Liverpool

for the Degree of Doctor in Philosophy

by

Quan Zhang

November, 2014

Department of Electrical Engineering and Electronics

The University of Liverpool

Acknowledgement

First of all, I am greatly indebted to my academic supervisor, Dr. Joseph D Yan, for his guidance, support and encouragement during the period of my postgraduate research.

I am deeply grateful to Prof. Michael T C Fang for his continuous support and all the valuable suggestions throughout every stage of my research work, as well as his encouragement.

I wish to thank my second supervisor, Prof. J W Spencer, for useful discussions. Thanks also to my colleagues, Jian Liu and Yuqing Pei, for all the collaborations, discussions, generation and exchange of ideas, and their friendliness.

I also wish to thank the Department of Electrical Engineering and Electronics for the use of department facilities and the enthusiastic support from all the staff members of this department throughout my study.

My special appreciation is addressed to Shanghai Sieyuan Electric Co. Ltd. for their financial support.

Last, but not least, I would like to express my gratitude to my parents, specially my mother, because without her I would not even be where I am today. Thanks also to my father, for his continuous support and encouragement.

Abstract

There is an overwhelming experimental and theoretical evidence indicating SF_6 arc burning in a supersonic nozzle (known as the switching arc) is turbulent and in local thermodynamic equilibrium (LTE). Such an arcing arrangement is commonly used as the interrupter in gas blast circuit breakers. In order to reduce the development cost of gas blast circuit breakers, it is highly desirable to predict the arc behaviour under the operational conditions encountered in a power system. The major difficulty in achieving full computer aided predictive design of gas blast circuit breakers is the satisfactory prediction of the thermal interruption capability of an arc under turbulent conditions. Mathematical modelling of turbulent SF_6 switching arcs, thus, forms the subject matter of this thesis.

The approach for the modelling of turbulent switching arcs is similar to that for turbulent shear flows due to a direct resemblance between a nozzle arc and a round free jet both of which are dominated by shear flow. The conservation equations for switching arcs are, therefore, derived using Reynolds's approach. The closure of these equations is based on the adoption of Boussinesq assumption to relate Reynolds stress to the time averaged velocity gradients through eddy viscosity. The turbulent heat flux is assumed to be related to Reynolds stress through a constant turbulent Prandtl number.

Additional equations are introduced to determine the turbulence length scale and velocity scale required by eddy viscosity, which are provided by turbulence models. There are numerous turbulence models but none of them are specifically devised for switching arcs. The objective of the present investigation is, therefore, to choose relevant turbulence models to model turbulent SF_6 switching arcs. Our choice of turbulence models is restricted to those which have been applied with success to similar flow conditions as those of a switching arc as well as their suitability for engineering application. We therefore choose the standard k-epsilon model and its two variants (the Chen-Kim model and the RNG model) for the modelling of SF_6 turbulent switching arc. Since the application of the Prandtl mixing length model to

SF_6 switching arcs has met considerable success, this turbulence model is included in our investigation for comparison. In order to demonstrate the effects of turbulence, results based on laminar flow model are presented. Therefore, altogether five flow models have been used to study the nozzle arcs.

Computational results are obtained by the five flow models under a wide range of discharge conditions in terms of different nozzle geometries, the rate of change of current (di/dt) before current zero and the stagnation pressure (P_0). A detailed analysis of the physical mechanisms encompassed in each flow model is given to show the adequacy of a particular model in describing the rapidly varying arc during current zero period. The computed values of the critical rate of rise of recovery voltage (RRRV) are compared with corresponding measurements. It is found that RRRV predicted by laminar flow model is a few orders of magnitude lower than that measured, which indicates that turbulence plays a decisive role in the determination of thermal interruption capability of a nozzle arc. Of the four turbulence models, the Prandtl mixing length model gives the best prediction of RRRV when compared with experimental results. The drawback is that the value of the turbulence parameter of the Prandtl mixing length model needs to be derived from one test result for a given geometry. With our current understanding of the physics of turbulent arcs, the Prandtl mixing length model is the only turbulence model which can be used to predict the thermal interruption capability of a nozzle arc arrangement.

Table of Contents

List of Figures

List of Tables

Chapter 1
Introduction

1.1 Background

High voltage circuit breakers are used in electrical power transmission networks for protection and control of power flow. They can act as either a connection point or an insulating point. During normal operation, they are connection points carrying load current and can be called on to switch off/on a circuit when necessary. In the event of a fault, they are required to switch off a faulty circuit or interrupt a short-circuit current, and thus they become insulating points in the power network.

Among all these duties of high voltage circuit breakers the most arduous one is the interruption of fault current [1.1]. Generally, a high voltage circuit breaker is a device with two metallic contacts located in an interruption chamber and some driving mechanisms, all of which are enclosed in a tank filled with particular insulating materials. During the process of current interruption, the two contacts are separated while carrying a current, and the gap between them is dielectrically broken down after which an electrical arc is generated [1.2]. The arc carries the fault current and the faulty circuit cannot be switched off before the arc is extinguished. One of the main concerns as regards the development of circuit breakers is, therefore, on how to extinguish the arc effectively and with the total breaking time as short as possible to ensure system stability [1.1]. There are generally two requirements for the successful interruption of fault current by a circuit breaker. The first one is to increase the resistance of the arc and its rate of rise especially in the period around a natural current zero to ensure that any possible subsequent current flow is suppressed and finally interrupted after current zero. This phase is known as thermal interruption as it relies upon cooling down the arc to a temperature where thermal ionization cannot be sustained. The other is the dielectric recovery phase after thermal

extinction of the arc. During dielectric recovery, the breaker should be able to withstand full system voltage. To fulfill these requirements and to reduce the manufacturing cost, a circuit breaker should be optimized. Optimization is usually centered around the interrupter size and materials, contact size, geometry and materials, the insulation/arcing gas and the driving mechanism. Application of a good arc interruption medium with high dielectric strength is also essential. The latter reduces the size of a breaker. The development of high voltage circuit breakers has, therefore, been closely related to the search of insulating materials with good arc interruption capability as well as environmentally friendly properties.

1.1.1 Brief History on the Development of High Voltage Circuit Breakers

In the early years, oil circuit breakers [1.1, 1.3, 1.4] and air circuit breakers [1.1, 1.3, 1.4] were used in the power network. The oil circuit breaker is one of the oldest types of circuit breakers, which employs the properties of the arc by using its energy to decompose the oil molecules and, subsequently, the generation of gas, principally hydrogen [1.1]. The high pressure hydrogen gas bubbles created by the arc energy, with properly designed control systems, can be advantageously used to confine, cool and compress the arc which will then increase the rate of deionization of ionized gaseous media and subsequently the extinction of the arc and finally achieving the necessary dielectric strength between the two contacts [1.1, 1.3]. Oil circuit breakers can be classified with reference to the amount of oil used as: the bulk oil circuit breaker (BOCB) [1.1, 1.3, 1.4] which can be used for voltage ranging from 1 kV to 330 kV [1.3], and the minimum oil circuit breaker (MOCB) [1.1, 1.3, 1.4] which are available in voltage levels up to 765 kV using the multi-break technique [1.3, 1.4]. The bulk oil and minimum oil designs have both been proved a very successful circuit breaking technology for which the oil circuit breakers are still in service today in power networks of medium and low voltage levels. There are, however, quite a few disadvantages of using oil as insulating medium including flammability of insulating oil and high maintenance cost of oil circuit breakers [1.3, 1.5]. Disadvantages of oil as insulating medium in high voltage circuit breakers initiated

research on air as a replacement, resulting in the development of air circuit breakers.

Air circuit breakers include the air-break circuit breaker (first developed in 1929 by Slepian at Westinghouse [1.1]) and the air-blast circuit breaker (developed from 1930s [1.1]). The air-break circuit breakers are designed for low voltage levels (up to 15 kV [1.3]). For this type of circuit breakers, arc quenching is achieved by arc elongation as it is forced by the action of magnetic field into the narrow space between insulating plates (known as arc chutes) [1.3, 1.4]. The lengthening of the arc and the cooling of the arc by the surface of the chutes soon lead to a high arc voltage (i.e. high arc resistance), which gives rise to favourable conditions for arc extinction at natural current zero [1.2, 1.3]. The air-blast circuit breakers, on the other hand, are used in high voltage power networks with the voltage levels up to 765 kV [1.3]. These breakers are mostly the double pressure type, in which the arc is cooled and blown in the gap between the contacts by a blast of high pressure compressed air flowing through a nozzle [1.1, 1.4]. A very high pressure level (around 30 to 35 bar) is required to ensure good interruption capability of an air-blast circuit breaker and it is necessary for the condition of the air to be very dry to maintain insulation level and reliability of operation [1.3]. Operation of air-blast circuit breakers, therefore, requires compressors and dryer systems which increase the cost of the breaker [1.4]. Moreover, air does not have very high arc interruption capability and dielectric strength. Thus, for electrical network at extra high voltage level, a large number of interruption units are required which results in large size of the breaker (e.g. for rated voltages above 420 kV, 10 or even 12 interrupters in series are needed per pole [1.4]). These disadvantages result in the use of Sulphur hexafluoride (SF_6) as the replacement of air in high voltage circuit breakers due to its excellent dielectric and arc quenching properties. Air-blast circuit breakers were predominately used in electrical networks at voltages higher than 100 kV before they were gradually replaced by SF_6 gas-blast circuit breakers (hereafter referred to as SF_6 circuit breakers) [1.1, 1.3, 1.4] from late 1950s [1.4]. Modern high voltage circuit breakers are mostly SF_6 gas-blast circuit breakers. A brief review on the development of SF_6 circuit breakers will be given in Section 1.1.2.

Apart from SF_6 circuit breakers which are generally preferred for high voltage levels, in power networks at low and medium voltage levels, vacuum circuit breakers [1.1, 1.3, 1.4] (developed in 1950s and 1960s [1.1, 1.4]) have been extensively used nowadays. A vacuum circuit breaker comprises one or more sealed vacuum interrupter units per pole which basically consists of only a fixed and a movable contacted enclosed in a vacuum bottle [1.4]. When the contacts separate, the arc is supported by ionized metal vapour released from the metallic contacts instead of ionized gas or liquid in other types of circuit breakers [1.4]. At current zero, when the arc is extinguished, the metal vapour is deposited on the condensing shield and the space inside the interrupter, therefore, becomes high vacuum since very few ions are available between two contacts [1.1, 1.4]. The dielectric strength between two contacts thus increases rapidly after arc extinction. The vacuum circuit breakers are advantageous over the other type of circuit breakers in that the vacuum interrupter units are mechanically simple and need no supply of gases or liquids which avoids problems of flammability and emission of hot gas, which may be harmful to environment, etc [1.4]. Besides, vacuum has the fastest dielectric recovery strength after arc interruption at current zero [1.3, 1.4]. Furthermore, the dielectric strength of high vacuum is approximately 8 times that of air and 4 times that of SF_6 (at 1 bar) for a given contact gap, which makes it possible to extinguish an arc with a very small contact gap [1.3]. It is these advantages that make the vacuum circuit breakers become popular in low and medium voltage applications (up to 36 kV [1.3]). However, vacuum circuit breakers do have disadvantages, e.g. higher load losses of vacuum circuit breakers (due to loss of vacuum) as compared with SF_6 breakers and high maintenance cost, which restrict application of vacuum breakers in high voltage applications [1.4].

1.1.2 SF_6 Gas-Blast Circuit Breakers

SF_6 is a very stable, odourless, non-toxic and non-flammable gas. It is one of the heaviest gases known, which is approximately 5 times heavier than air [1.6]. Its dielectric strength is about 4 times higher than air at room temperature and is higher

than that of oil at an absolute pressure above 3 bar [1.1]. The exceptional dielectric and arc quenching properties of SF_6 were discovered in 1950s [1.1, 1.4], which resulted in a new generation of SF_6 gas-blast circuit breakers.

The first generation of SF_6 circuit breakers are of the double pressure type which has the same working principle as the earlier air-blast circuit breakers except using a different insulating and quenching medium [1.4]. The adoption of SF_6 resulted in a considerable increase in voltage and current ratings without resorting to extreme gas pressures and/or using large number of interrupters in series per pole [1.4]. A typical example was the high voltage SF_6 circuit breaker with a high short-circuit current capacity developed in Westinghouse in 1959 [1.4]. This dead tank circuit breaker could interrupt 41.5 kA/138 kV and 37.6 kA/230 kV with only three interrupters per pole, in comparison with requirement of at least four interrupters per pole using an air-blast circuit breaker to achieve similar interruption capability [1.4]. The performance improvement of double pressure SF_6 circuit breakers is, therefore, significant but it requires certain amount of working gas to be compressed and stored permanently in a high-pressure reservoir (typically at 16 bar) [1.2, 1.4]. This can result in liquefaction of SF_6 at low temperature environment and, thus, heating facilities are required to prevent liquefaction which increases the size of the breaker and its cost [1.2, 1.4]. In addition, additional compressor systems are required to maintain high pressure of SF_6 [1.4]. The double pressure SF_6 circuit breakers are, therefore, soon replaced by single pressure puffer type circuit breakers, the development of which dates from late 1960s and 1970s [1.4].

Figure 1.1 shows an example of a puffer type SF_6 circuit breaker (hereafter referred to as puffer circuit breaker). The interrupter is included in an insulating tank which is initially filled with SF_6 gas at a filling pressure of typically 6 bar [1.2, 1.4]. A common characteristic of all puffer circuit breakers is the compression of SF_6 gas during the opening operation inside the compression volume between a cylinder (No.9 in Figure 1.1) and a piston (No.11 in Figure 1.1). In most of the puffer designs, the piston (No.11 in Figure 1.1) is fixed while the cylinder (No.9 in Figure 1.1) moves together with the moving contact. The increase of pressure inside the

compression volume forces the gas to flow through the nozzle (No.5 in Figure 1.1) where it is strongly accelerated, thus forming a favourable environment for arc cooling. The technology for puffer circuit breakers has become the most successful in current interruption, and the excellent properties of SF_6 has greatly increased the interruption capability of this type of breaker: some manufacturers have developed SF_6 puffer type circuit breakers for rated voltage of 550 kV which only requires one interrupter per pole [1.4].

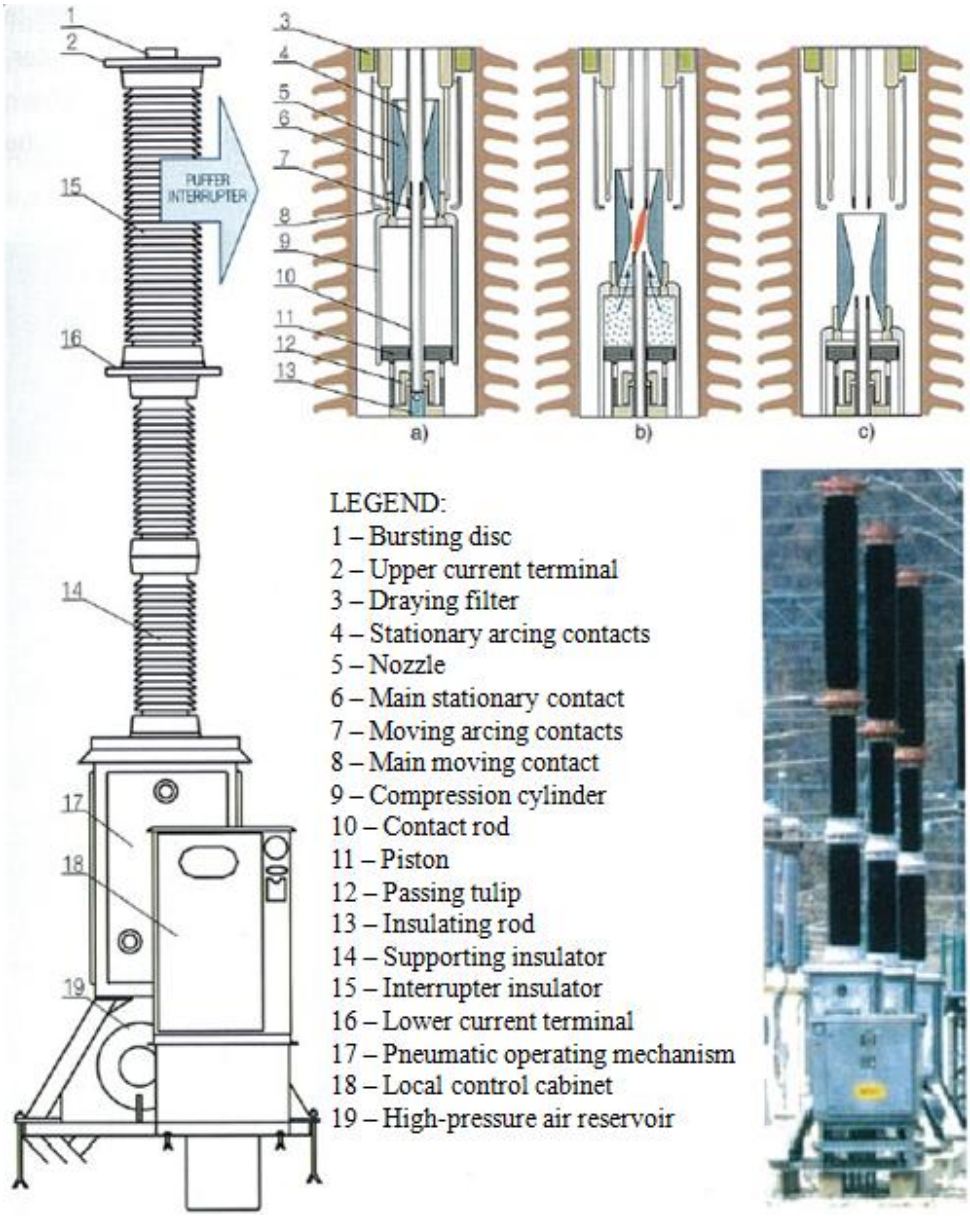

Figure 1.1. A 245 kV SF_6 circuit breaker using a puffer interrupter with insulating nozzle and pneumatic operating mechanism, reproduced from [1.4]: (a) closed position; (b) process of arc-quenching and (c) open position.

However, the main disadvantage of puffer circuit breakers, especially those used for heavy duties (e.g. at current above 40 kA and rated voltage above 245 kV), is the need for relatively long strokes and high operating forces, which can only be provided by using rather complex and powerful operating mechanisms such as pneumatic and hydraulic mechanisms [1.4]. This negatively affects the reliability and the cost of this circuit breaker, which prompts the development of SF_6 circuit breakers with more sophisticated current interruption principle; the self-blast (auto-expansion) circuit breaker (Figure 1.2).

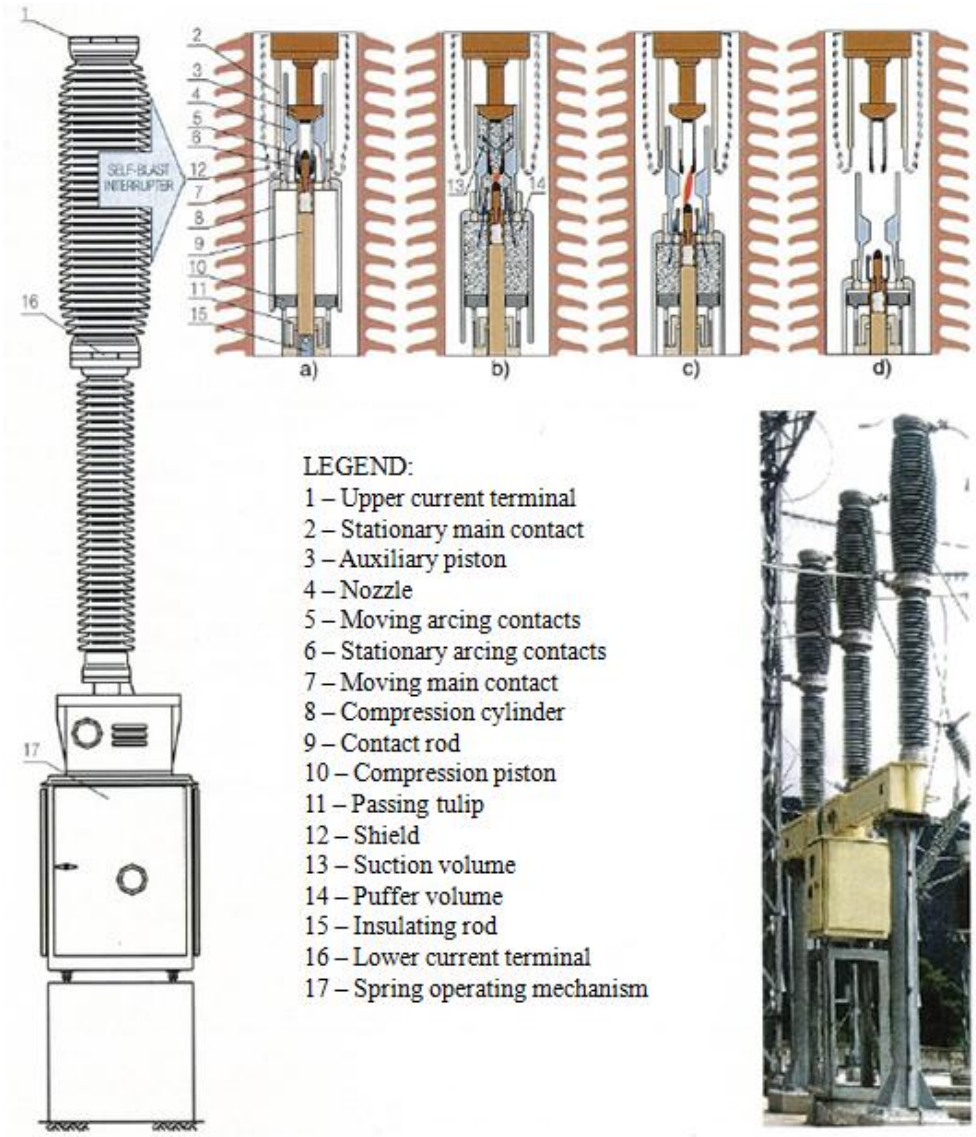

Figure 1.2. A 145 kV SF_6 circuit breaker using combined self-blast and puffer principle of arc quenching with spring operating mechanism, reproduced from [1.4]: (a) closed position, (b) closed-in arc, (c) process of arc quenching and (d) open position.

The self-blast circuit breakers (Figure 1.2) differ from the puffer circuit breakers in that they use mainly the thermal energy of the arc to heat the gas, instead of mechanical energy provided by operating mechanisms, to increase pressure in the expansion volume. This results in significantly reduced operating forces which makes it possible to use low energy spring operating mechanisms, thus reducing the size and cost yet increasing the reliability of the breaker [1.4].

Ideally, it is expected that the arc can somehow provide all the energy required for pressurization with the operating mechanisms providing only energy needed for contact movement, which cannot, however, be achieved. Problems arise when interrupting small currents, in which case the arc energy will not be sufficient to increase pressure to be high enough for efficient gas blast. Design of self-blast circuit breakers, therefore, considers combination of self-blast and classical puffer principle of arc quenching, as shown in Figure 1.3. When interrupting small currents, the self-blast circuit breaker works in a similar way as the puffer circuit breaker, with SF_6 gas compressed in the puffer volume (V1 in Figure 1.3) which is then forced to flow through the expansion volume (V2 in Figure 1.3) and the nozzle (No.2 in Figure 1.3) for arc cooling. When interrupting very high currents, nozzle clogging occurs due to the high temperature and sizeable arc. The thermal energy released from the arc, together with additional mass and energy generated by nozzle ablation, accumulates in the expansion volume (V2 in Figure 1.3) which heats up the gas and increases pressure. Compression of the gas in the puffer volume (V1 in Figure 1.3) also helps to increase pressure. When the gas pressure in the expansion volume (V2 in Figure 1.3) is high enough, the overpressure valve (No.7 in Figure 1.3) will be closed after which all gas required for interruption is trapped with any further increase in gas pressure entirely due to energy from the arc. With the current decay and the shrinking of the arc size (and thus reduction of the pressure in the nozzle interrupter), the pressure difference between the expansion volume (V2 in Figure 1.3) and the contact gap generates a high speed gas flow through the nozzle. It extinguishes the arc at current zero.

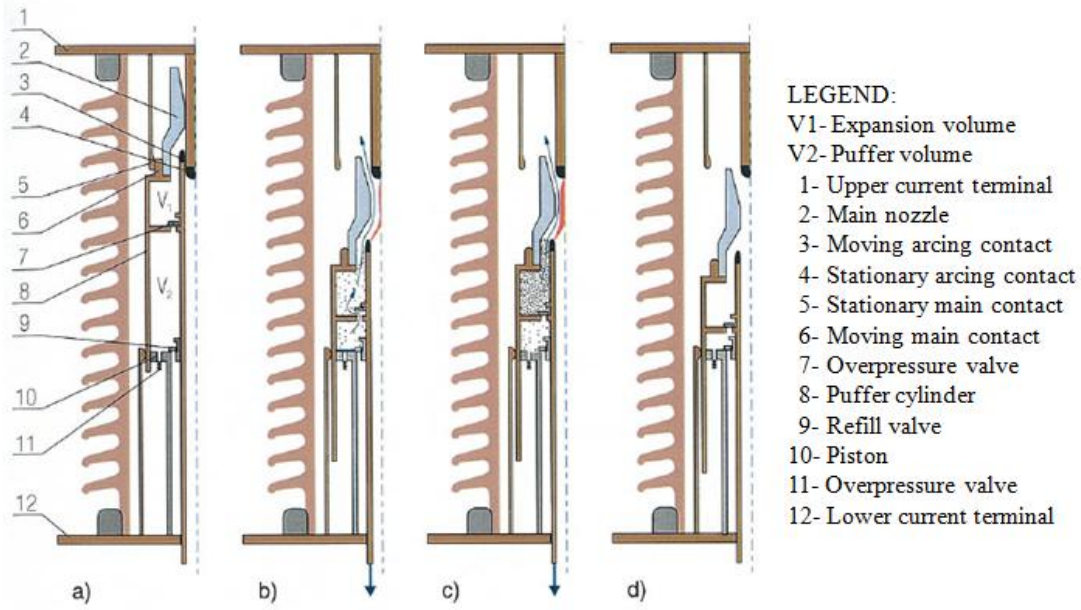

Figure 1.3. SF_6 self-blast double volume interrupter with check valves designed by considering combined self-blast and puffer principle of arc quenching, reproduced from [1.4]: (a) closed position, (b) interrupting small current, (c) interrupting high current and (d) open position.

1.1.3 Development of CAD Tools for Design of Gas-Blast Circuit Breakers

It has readily been shown in Section 1.1.2 that the current interruption process in gas-blast circuit breakers is very complex which involves the interaction of the arc plasma, the gas flow, radiation transport and ablation [1.7]. The high pressure arc formed between two contacts is the key element in all types of gas-blast circuit breakers, which acts as a variable resistor and cannot be avoided during operation of gas blast circuit breakers [1.1, 1.2, 1.6]. It is expected that the arc can be extinguished in a very short time to fulfill the requirements on current interruption and on system stability [1.1, 1.6]. Nevertheless, it is essential to maintain the arc before an attempt is made to extinguish it, which allows enough time for contact separation and subsequently the creation of a contact gap large enough to withstand restriking voltage [1.6]. It should also be noted that arc extinction should occur at current zero in an AC circuit to avoid overvoltage problems [1.1]. The problem with regard to circuit breaker design is, therefore, to control the arc in such a way that the energy of the arc can be effectively removed during current zero period to obtain a rapid rate of rise of arc resistance, while the rate of energy removal from the arc

should not be too fast which results in small currents being chopped before current zero causing overvoltage problems [1.1]. Design of such a complex system is, therefore, very difficult. The development of an SF_6 breaker is up to now still heavily dependent on costly short circuit tests. With the rapid advancement of computing power at ever reducing cost computer aided development tools are now widely used in design offices with the objective to reduce the number of short circuit tests [1.8, 1.9]. The major difficulty in achieving full computer aided predictive design of gas-blast circuit breakers is the satisfactory prediction of the thermal interruption capability of an arc under turbulent conditions, and thus the critical rate of rise of recovery voltage (RRRV) a circuit breaker can withstand. Mathematical modelling of turbulent arc thus forms the subject matter of the present thesis.

In Section 1.2 of this chapter, a brief discussion will be given on the mathematical modelling of switching arcs based on the assumption of local thermodynamic equilibrium (LTE) which will be used for the modelling of turbulent SF_6 arcs. The justification of using this approach for the work in this thesis will be discussed in detail in Chapter 2. The rest of this chapter describes the objective of the present work. Finally, the structure of this thesis will be given.

1.2 Properties of High Pressure Arc in LTE

The thermal interruption capability of a circuit breaker is determined by the arc column between two contacts. The sum of the voltage drop across the cathode and anode sheath regions is much smaller than that of the arc column which is of a few centimetres long [1.10, 1.11]. The gas pressure encountered in circuit breakers is at atmospheric and above. At such pressure, collisions between particles in the arc column are very frequent. For such collision dominated arc and for the discharge conditions normally met in circuit breakers the arc can be regarded as in the state of LTE [1.2, 1.12, 1.13]. The properties of LTE plasmas and the conditions to ensure LTE in the context of circuit breaker plasmas are discussed in Section A.2 of Appendix A.

The arc plasma under LTE state can be treated as a single conductive fluid. The conservation equations for the arc plasma are therefore similar to Navier-Stokes equations (referred to as N-S equations hereafter) [1.14, 1.15] but modified to take into account the effects of radiation transport and the effects of electromagnetic fields. The conservation equations for switching arcs, together with those computing electromagnetic fields, are given in Section A.3 of Appendix A. The effects of radiation transport inside the arc plasma are discussed in Section A.5 of Appendix A.

The solution of conservation equations for switching arcs requires knowledge of the thermodynamic and transport properties, and the equation of state. For an arc plasma in LTE, the thermodynamic and transport properties can usually be related to pressure (p) and temperature (T). The equation of state, on the other hand, relates the gas density (ρ) to p and T. For SF_6, the equation of state, thermodynamic and transport properties are given in tabulated or graphic form in [1.16], all of which are also given in Section A.4 of Appendix A for completeness.

1.3 Objectives of the Present Work

The prediction of thermal interruption capability critically depends on the correct description of the arc behavior during current zero period. There is now consensus that SF_6 arc in nozzle flow is turbulent [1.17]. N-S equations and Maxwell's equations correctly describe arcs in turbulent state. However, direct numerical solution (DNS) [1.18, 1.19] of these equations is not practical as the required grids size and time step are dictated by the smallest eddies [1.19]. Even with the most advanced computers, DNS has only been done for very simple cases, such as an incompressible flow passing a plate [1.20, 1.21] and a flow over a backward-facing step [1.22]. Turbulence models which are mainly based on the statistical treatment of the relevant conservation equations are exclusively adopted for engineering applications [1.23, 1.24]. Turbulence models are usually problem specific and the corresponding turbulence parameters need to be optimized by test results. There are numerous turbulence models in literature [1.23-1.28].

No systematic experimental and theoretical investigation on truculent arc has so far been conducted although the Prandtl mixing length turbulence model has been used to predict RRRV for an SF_6 nozzle arc [1.29]. There have been sporadic investigations on turbulent SF_6 arcs using the standard k-epsilon model and a few of its variations [1.30-1.32], but with conflict claims as regards the success of these turbulence models. No general conclusions on the applicability of these turbulence models to SF_6 switching arcs can be drawn as the verification of these models by test results is very limited.

Turbulence modeling in fluid mechanics and aerodynamics has a very long history and has achieved much success. It is still a major research area as almost all flows of industrial importance are turbulent. There are numerous turbulence models [1.23-1.28] although none has been devised specifically for turbulent switching arcs. The most fruitful approach for turbulent arc modeling is to examine the applicability of those turbulence models, which have a track record of success in fluid mechanics and aerodynamics, to SF_6 turbulent arcs.

The objective of the present investigation is, therefore, to choose relevant turbulence models to model the turbulent SF_6 arc. We choose those turbulence models which are devised for flows having direct similarities with the flow features of a turbulent switching arc. This results in selection of the standard k-epsilon model [1.26] and its two variants (the Chen-Kim model [1.28] and the RNG model [1.27]) for the modelling of SF_6 turbulent switching arc. Since the application of the Prandtl mixing length model to SF_6 switching arcs has met considerable success, this turbulence model is included in our investigation for comparison. Altogether four turbulence models have been chosen to study SF_6 switching arcs. In order to demonstrate the effects of turbulence, results based on laminar flow model are presented. The computed RRRV obtained by the aforementioned turbulence models, together with that obtained by the laminar flow model, will be subjected to verification by experimental results covering a wide range of discharge conditions in terms of different nozzle geometries, rate of change of current before current zero and stagnation pressure. In order to avoid the pressure transients normally

encountered in a circuit breaker, a two-pressure system will be adopted and thus the test results of Benneson et al. [1.33], Frind et al. [1.34] and Frind and Rich [1.35] will be used to judge the relative merits of various turbulence models used for the present investigation.

1.4 Structure of the Thesis

The structure of the thesis is given below:

This chapter gives an introduction of this thesis, which includes the background of the work presented in this thesis and objectives of this work.

Chapter 2 gives a detailed discussion as regards the importance of turbulence on the behaviour of SF_6 switching arcs. The justification of the assumption that a turbulent arc is in LTE is also discussed.

Chapter 3 gives a detailed discussion on the approach for the modelling of turbulent SF_6 switching arcs, which include the application of statistical approach for analysis of turbulent switching arcs and the derivation of time averaged arc conservation equations. The governing equations for the turbulence models chosen for the modelling of turbulent SF_6 switching arc are also given this chapter. These models will be subjected to verification by relevant test results, the details of which are descirbed. Finally, a brief description is given on the implementation of the arc conservation equations and the turbulence models in a general purpose computational fluid dynamics (CFD) software package, PHOENICS, which is used for computer simulations of the present work.

Chapter 4 reports the first part (Part I) of the systematical investigation into the behaviour of a SF_6 nozzle arc, which is concerned with the studies of the flow features in the absence of the arc (cold flow) as well as with a detailed study of the arc behavior under different direct currents for the nozzle used in the experiments of Benenson et al. [1.33]. Computational results are obtained using the laminar flow model and the four turbulence models, i.e. the Prandtl mixing length model, the standard k-epsilon model and its two variants, the Chen-Kim model and the RNG

model. Detailed discussion is given as regards the cold flow features and the behaviour of DC arcs at different currents predicted by different models employed.

Chapter 5 reports the second part (Part II) of the systematical investigation into the behaviour of a SF_6 nozzle arc, which is exclusively concerned with the arc behavior under a current ramp (i.e. a linearly decaying current specified by di/dt) before current zero and a voltage ramp i.e. a linearly increasing recovery voltage specified by dV/dt) after current zero. The four turbulence models, together with the laminar flow model, used in Chapter 4 are again applied in this investigation. A detailed analysis of the physical mechanisms encompassed in each model is given to show the adequacy of a particular model in describing the rapidly varying arc during current zero period. The computed RRRV are compared with the measured RRRV reported in [1.33]. Relative merits of turbulence models employed are discussed.

Chapter 6 reports the third part (Part III) of the systematical investigation into the behaviour of a SF_6 nozzle arc, which studies the effects of the nozzle geometry on the turbulence level during the current zero period that affects the arc characteristics and RRRV. The Prandtl mixing length model and the standard k-epsilon model are used to obtain results. Three nozzles [1.33, 1.34, 1.35] are considered in this investigation. The measured RRRV for these nozzles together with the computational results are used to evaluate the level of turbulence and the influence of the geometrical factors of a nozzle on thermal interruption.

Chapter 7 reports the investigation on the effects of arc-shock interaction on the behaviour of an SF_6 nozzle arc during current zero period. The Prandtl mixing length model is used to simulate the turbulent arc. Detailed discussion is given on the aerodynamic and electrical behaviour of the arc in the presence of the shock and the influence of the shock on SF_6 arc thermal interruption. The computed RRRV are compared with the measured RRRV reported by Frind and Rich [1.35].

In Chapter 8, appropriate conclusions are drawn from the all investigations presented in thesis. Suggestions are also given for the future work.

References

[1.1] Flurscheim C H 1982 *Power Circuit Breaker Theory and Design* Revised edn Peter (London: Peregrinus Ltd.)

[1.2] Yan J D 1997 *Investigation of Electric Arcs in Self-Generated Flow* (PhD thesis: University of Liverpool)

[1.3] Bhel, Bharat Heavy Electricals Limited 2005 *Handbook of switchgears* (New Delhi: Tata McGraw-Hill)

[1.4] Kapetanovic M 2011 *High Voltage Circuit Breakers* (KEMA)

[1.5] Wong T M 2008 *Computer Simulation and Visualisation of Complex Systems: Arcs and Hot Gas Flow in Auto-expansion Circuit Breakers* (PhD thesis: University of Liverpool)

[1.6] Blower R W 1986 *Distribution switchgear* (London: William Collins Sons & Co. Ltd.)

[1.7] Ye X and Dhotre M 2011 CFD simulation of transonic flow in high-voltage circuit breaker *International Journal of Chemical Engineering*. **2012** 609486

[1.8] Yan J D, Fang M T C and Hall W 1999 The development of PC based CAD Tools for auto-expansion circuit breaker design *IEEE Trans. Power Delivery.* **14** 176-81.

[1.9] Yan J D and Fang M T C 1999 Visualization of arcing process in an auto-expansion circuit breaker *IEEE Trans. Plasma Sci*. **27** 40-1

[1.10] Howatson A M 1965 *An Introduction to Gas Discharges* (Oxford: Pergamon Press)

[1.11] Boulos M I, Fauchais P and Pfender E 1994 *Thermal Plasmas Fundamentals and Applications* (New York: Plenum Press)

[1.12] Zhuang Q 1992 *Theoretical Investigation of the Transient Axisymmetric Turbulent Nozzle Arcs* (PhD thesis: University of Liverpool)

[1.13] Kwan S 1996 *Computer Simulation of Arcs in Gas-Blast Circuit Breakers* (PhD thesis: University of Liverpool)

[1.14] Schlichting H 1979 *Boundary Layer Theory* 7th Ed. (New York: McGraw Hill)

[1.15] Anderson D A, Tannehill J C and Pletcher R H 1984 *Computational Fluid Mechanics and Heat Transfer* (New York: Hemisphere Publishing Corporation)

[1.16] Frost L S and Liebermann R W 1971 Composition and transport properties of SF_6 and their use in a simplified enthalpy flow arc model *Proc. IEEE.* **59** 474-85

[1.17] Jones G R and Fang M T C 1980 The physics of how power arcs *Rep. Prog. Phys.* **43** 1415-65

[1.18] Moin P and Mahesh K 1998 Direct numerical simulation: a tool for turbulence research *Annu. Rev. Fluid Mech.* **30** 539-78

[1.19] Bates P D, Lane S N and Ferguson R I 2005 *Computational Fluid Dynamics: Applications in Environmental Hydraulics* (Chichester, West Sussex: John Wiley & Sons Ltd.)

[1.20] Rist U and Fasel H 1995 Direct numerical simulation of controlled transition in a flat-plate boundary layer *J. Fluid Mech.* **298** 211-48

[1.21] Wu X and Moin P 2009 Direct numerical simulation of turbulence in a nominally zero-pressure-gradient flat-plate boundary layer *J. Fluid Mech.* **630** 5-41

[1.22] Le H, Moin P and Kim J 1997 Direct numerical simulation of turbulent flow over a backward-facing step *J. Fluid Mech.* **330** 349-74

[1.23] Wilcox D C 2006 *Turbulence Modeling for CFD* (La Cañada, CA: DCW Industries)

[1.24] Versteeg H K and Malalasekera W 2007 *An Introduction of Computational Fluid Dynamics: The Finite Volume Method* 2nd edn (Harlow: Prentice-Hall)

[1.25] Turbulence models in PHOENICS (London: CHAM). Retrieved 25 Jul. 2014 from: http://www.cham.co.uk/phoenics/d_polis/d_enc/turmod/enc_tu.htm

[1.26] Launder B E and D B Spalding 1974 The numerical computation of turbulent flows *Computer Methods in Applied Mechanics and Engineering*. **3** 269-89

[1.27] Yakhot V, Orszag S A, Thangam S, Gatski T B and Speziale C G 1992 Development of turbulence models for shear flows by a double expansion technique *Phys.Fluids A.* **4** 1510-20

[1.28] Chen Y S and Kim S W Computation of turbulent flows using an extended K-epsilon turbulence closure model, Interim report, NASA, CR-179204

[1.29] Fang M T C, Zhuang Q and Guo X J 1994 Current zero behaviour of an SF_6 gas-blast arc Part II: turbulent flow *J. Phys. D: Appl. Phys.* **27** 74-83

[1.30] Yan J D, Nuttall K I and Fang M T C 1999 A comparative study of turbulence models for SF_6 arcs in a supersonic nozzle *J. Phys. D: Appl. Phys.* **32** 1401-6

[1.31] Song K D, Lee B Y and Park K Y 2004 Calculation of the post-arc current in a supersonic nozzle by using the K-epsilon model *J. Korean Phys. Soc.* **45** 1537–43

[1.32] Bini R, Basse N T and Seeger M 2011 Arc induced turbulent mixing in an SF6 circuit breaker model *J. Phys. D: Appl. Phys*. **44** 025203

[1.33] Benenson D M, Frind G, Kinsinger R E, Nagamatsu H T, Noeske H O and Sheer, Jr R E 1980 Fundamental investigation of arc interruption in gas flows EPRI EL-1455 (Project 246-2)

[1.34] Frind G, Kinsinger R E, Miller R D, Nagamatsu H T and Noeske H O 1977, Fundamental investigation of arc interruption in gas flows EPRI EL-284 (Project 246-1)

[1.35] Frind G and Rich J A 1974 Recovery speed of axial flow gas blast interrupter: dependence on pressure and di/dt for air and SF_6 *IEEE Trans. Power Appar. Syst.* **93** 1675-84

Chapter 2
The Effects of Turbulence on SF_6 Switching Arcs

2.1 Introduction

Almost all circuit breakers at transmission voltage level use SF_6 as an arcing gas. Immediately after the separation of two contacts, an arc is formed inside the interrupter of a breaker. The arc is usually burnt in an axially dominated supersonic flow inside a convergent- divergent nozzle (commonly known as supersonic nozzle). For such an arcing environment (hereafter referred to as the switching arc), there is a wealth of experimental evidence showing that the arc is in turbulent state, especially at the vicinity of current zero [2.1-2.6]. An SF_6 switching arc resembles a thin incompressible shear layer (a high speed rounded free jet), which is in turbulent state when the critical Reynolds number is exceeded. Under the context of a switching arc, in addition to the instability generated by the inertia term of the momentum equation, there are additional driving mechanisms for instability. A detailed discussion will be given to these destabilizing forces. Even in the presence of turbulence, it is not certain if the turbulent eddies generated in the shear layer can penetrate the high temperature arc core, thus affecting the electrical behavior of the arc.

In the context of theoretical investigation of switching arcs, the computed values of RRRV of a switching arc based on LTE and laminar flow for SF_6 switching arc is a few orders of magnitude lower than that measured [2.7]. In addition to the likely influence of turbulence on the electrical behaviour of the arc, there are other processes which can affect arc voltage. These processes are mainly related to the rapid decay of current before a natural current zero and the fast rise of the recovery voltage imposed upon two contacts after current zero. Such rapid variations in discharge conditions make the assumption of arc in LTE doubtful [2.8, 2.9, 2.10].

The causes of departure from LTE (referred to as non-LTE processes for convenience) and their effects on RRRV will be reviewed. The importance of non-LTE processes will be judged by examining whether or not the likely RRRV predicted by an arc model including non-LTE processes is greater or less than that predicted by an LTE arc model with laminar flow (referred to as the laminar RRRV for convenience). Finally, the RRRV reported in the literature for an LTE arc in turbulent flow will be compared with experimentally measured RRRV and with the laminar RRRV. Such a comparison will show the role of turbulence in the determination of the electrical behaviour of an SF_6 switching arc.

2.2 Review of Relevant Experimental Investigation on Arc Turbulence

There is a wealth of experimental evidences showing that the switching arc is turbulent, especially at the vicinity of current zero. The most important experiments related to arc turbulence were conducted in early 1970s by Hermann et al of Brown Boveri Research Centre (hereafter referred to as BBC Group) on a nitrogen arc burning in a supersonic nozzle under well defined experimental conditions [2.1, 2.2]. Experimental study together with the relevant theoretical investigation on the behaviour of a stationary arc (an arc in its steady state) at a constant current of 2 kA (by convention, we refer to constant current as DC and a steady state arc at a given constant current as a DC arc hereafter) has been reported in [2.2], in which the detailed experimental results are given for the measurements of temperature, pressure, arc radius and electrical field. The transient behaviour of this arc is investigated by linearly ramping down the current to zero from 2 kA DC at the rate of current decay, $di/dt = 39A\mu s^{-1}$ [2.1]. High speed streak records of both the 2kA DC arc and the transient arc are shown in Figure 2.1 at a number of different axial positions. At 2 kA DC, the arc section up to the nozzle throat reveals a laminar flow feature, while downstream of the nozzle throat, it can be seen that the edge of the arc becomes turbulent, which is however weak and does not appear to affect the arc core region

(Figure 2.1(a)). The measured electrical field shows that the upstream arc section has higher electrical field than the downstream arc section (Figure 2.2(a)). When the current is ramping down towards zero, in the region downstream of the nozzle throat, turbulence appears to become very strong which is not restricted around the arc edge but is shown to affect the whole arc in the vicinity of current zero (Figure 2.1(b)). The arc section upstream of the nozzle throat, on the other hand, remains more or less laminar even after current zero (Figure 2.1(b)). Furthermore, the downstream arc section which shows turbulent features has been found to have much faster rate of rise of arc resistance (Figure 2.3) as well as higher electrical field (Figure 2.2(b) and 2.2(c)) in comparison with the upstream arc section at the vicinity of current zero. The experimental results of the BBC group indicates that turbulence does affect the electrical behaviour of switching arcs and the turbulent effects appear to be significant at the vicinity of current zero.

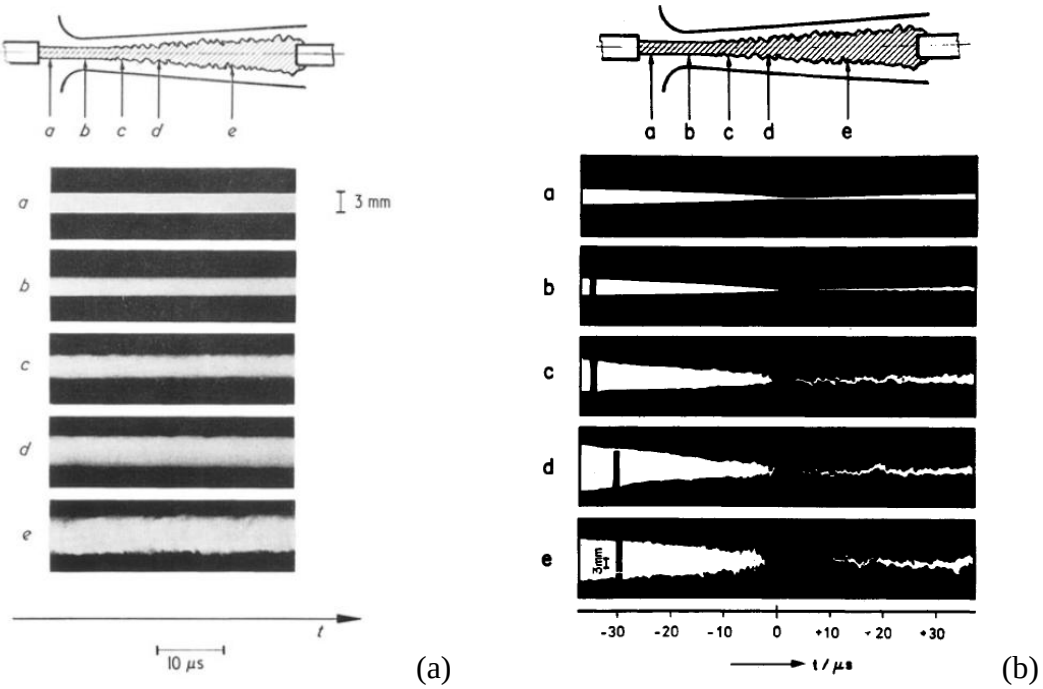

(a) (b)

Figure 2.1. Streak records of the nitrogen nozzle arc investigated by BBC group. (a) Reproduced from [2.2]: self-luminosity streak records of the arc cross section for a 2 kA DC arc at different axial positions. (P_0=23 bar and Time resolution=0.3 µs) and (b) Reproduced from [2.1]: fast streak record of the arc in the vicinity of current zero (P_0=23 bar and di/dt=39Aμs^{-1}).

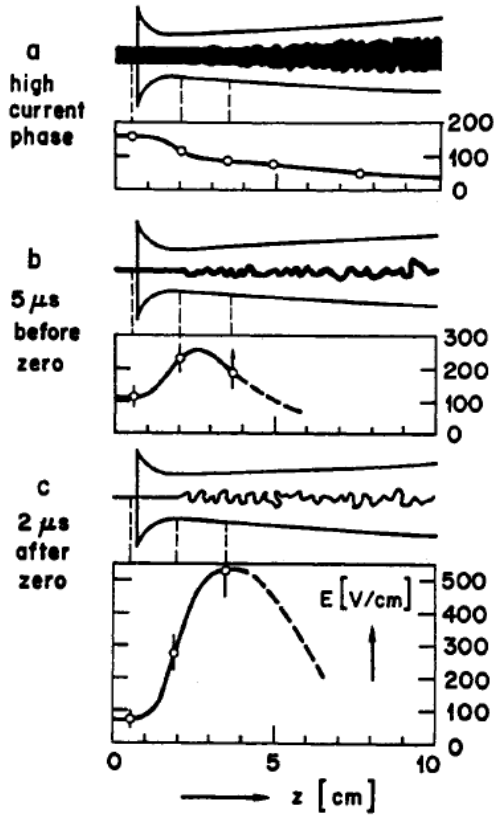

Figure 2.2. Schematic of the arc shape and the measured electrical field at different time instants for the nitrogen arc investigated by BBC group (P_0=23 bar and di/dt=39Aμs^{-1}). Reproduced from [2.1].

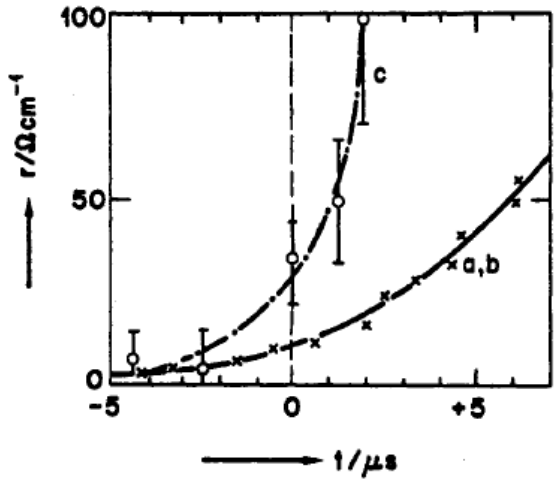

Figure 2.3. Resistance per unit length of different arc sections in the vicinity of current zero. Reproduced from [2.1]. The letters a, b and c correspond to the arc sections as indicated in Figure 2.1.

In addition to the investigation by the BBC group on nitrogen arcs, Leseberg and Pietsch [2.4, 2.5] of Aachen University (hereafter referred to as the Aachen Group) performed experimental study on an SF_6 nozzle arc under both DC and transient conditions. They measured radial temperature profiles at different axial positions of the nozzle for DC arcs at different currents and also a transient arc initially at 1.8 kA DC which is ramped down towards current zero with di/dt=-16 $A\mu s^{-1}$. Their high speed photo of the SF_6 nozzle arc demonstrates that the arc becomes turbulent downstream of the nozzle throat while upstream of the nozzle throat the arc is more or less laminar (Figure 2.4). These qualitative features are almost the same as those of the nitrogen arc investigated by BBC group.

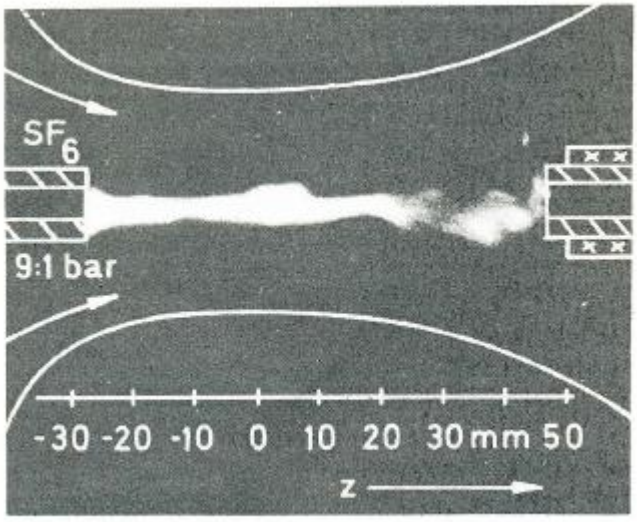

Figure 2.4. A high speed photo of the SF_6 nozzle arc at an instant current of 700A with an exposure of 1 μs. Reproduced from [2.5].

Almost at the same time as the BBC Group, Frind and Rich of GE in the US (hereafter referred to as the GE Group) reported the measurements of the critical rate of rise of recovery voltage (RRRV) for a supersonic nozzle arc with both air and SF_6 as arcing media [2.11]. In two subsequent publications [2.12, 2.13], extensive experimental results are given for nozzle arcs with SF_6, air, nitrogen and their mixtures as the arcing media.

2.3 Mechanisms of Generating Instabilities for Switching Arcs

2.3.1 Similarity between a Switching Arc and a Free Jet

Figure 2.5 shows a typical example of a high speed free jet with a diameter $2b_0$ emerging from an orifice with a uniform velocity U_0 into a standstill environment. The development of such a free jet into a fully developed turbulent jet is depicted in Figure 2.5(b), where a laminar core near the orifice, the development and the merge of the shear layer and the fully developed region are shown. In the fully developed flow region, the flow velocity decreases continuously from the maximum value on the axis to zero at the jet boundary (Figure 2.5(b)). Such a free jet is, therefore, within the category of shear layer flow due to the steep radial gradient of the axial flow velocity at a given axial position which is the typical characteristic of the flow behaviour in a shear layer.

For the switching arc burning in a supersonic nozzle with axially dominant flow Ohmic heating gives rise to very high temperature within the arc core. For moderate currents, the axis temperature of the arc is about two orders of magnitude higher than that of the surrounding gas flow. This results in a very steep radial temperature and velocity gradients especially in the region between the arc core boundary and the thermal boundary where the radiation energy emitted from the arc core is reabsorbed (Figure 2.6). This layer is commonly known as the radiation re-absorption layer. Inside this layer, the velocity drops from its core value to that of the external flow, which is similar to that indicated in Figure 2.5(b). We refer to this region as the velocity shear layer (Figure 2.6). Figures 2.1 and 2.5 show direct resemblance between a round fluid jet and a switching nozzle arc.

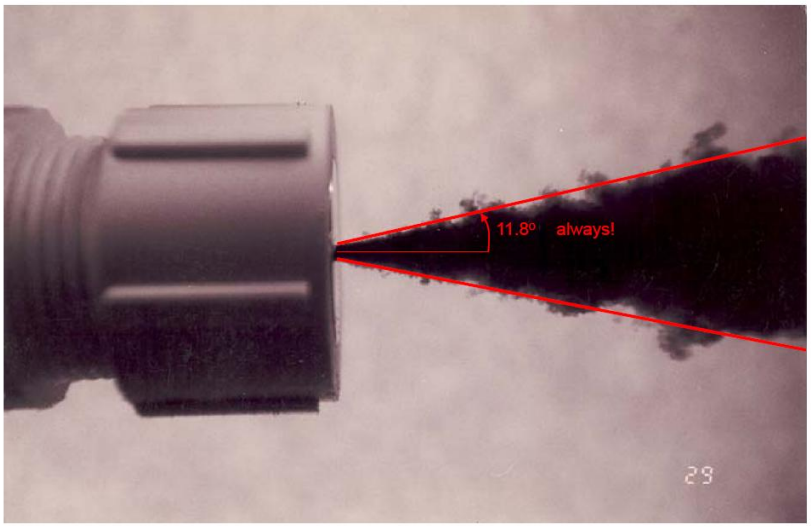

(a)

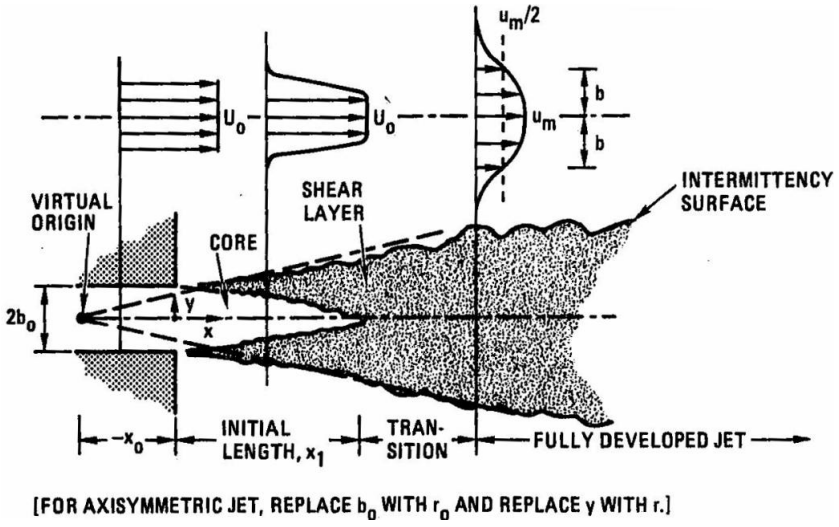

(b)

Figure 2.5. A typical example of a turbulent free jet. (a) Reproduced from [2.14]: a jet emerging from a nozzle orifice which discharges into the standstill environment and (b) Reproduced from [2.15]: schematic diagram showing the development of a free jet into a fully developed turbulent jet.

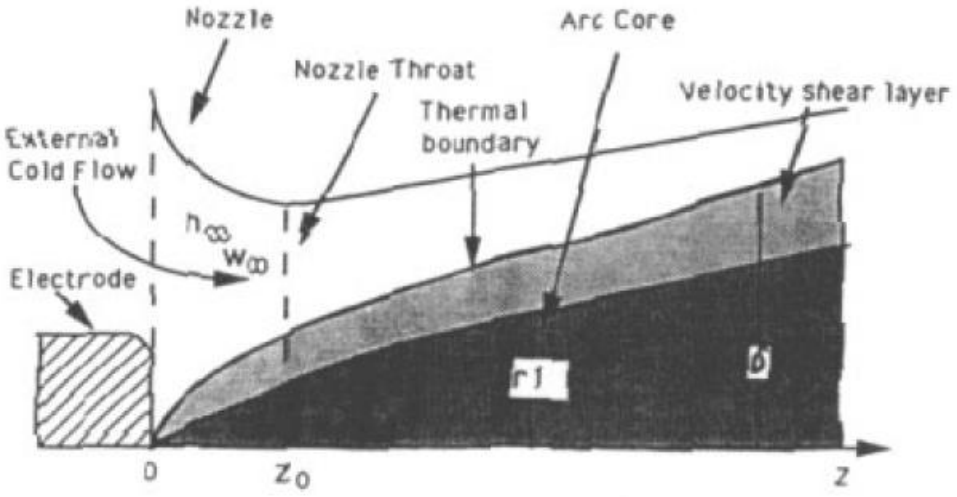

Figure 2.6. Schematic diagram showing the switching arc and its external flow inside a supersonic nozzle. Reproduced from [2.16].

2.3.2 The Mechanisms of Generating Instabilities for Switching Arcs

Although much emphasis has been given to the resemblance between a free incompressible jet and a switching arc, there are differences between the two. The differences are summarized below:

A high velocity free jet is a flow discharging in to standstill surroundings at constant pressure and temperature, and thus there is no force to accelerate the jet. The free jet is also incompressible and has constant material properties (due to constant pressure and temperature).

A switching arc, on the other hand, is far more complex in comparison with a free jet in that it has a temperature range of approximately from 300 K to 25,000 K and a pressure range from 5 bar to 40 bar. In addition, the high temperature is maintained by an electrical power input and the arc is highly transient due to change of arc current. All these aspects result in the following main difference of a switching arc in comparison with a free jet:

(a) For an arc burning in a nozzle, the imposed axial pressure gradient (resulting from large pressure difference inside a nozzle) exerts strong acceleration along the arc which results in high rate of strain.

(b) There is a large density variation caused by pressure differences and temperature gradients, i.e. the arc is highly compressible.

(c) Transport properties, such as electrical conductivity, thermal conductivity etc change by a wide range within the arc for the temperature variation encountered.

(d) At high currents (above 10 kA) Lorentz force also becomes important.

The mechanisms that generate instabilities in the velocity shear layer of the arc are, therefore, different from those generating the shear layer instability in a free jet which is almost entirely due to the inertia term of the momentum equation. For a switching arc, there are a number of other causes which can excite instabilities in addition to hydrodynamic instability. However, there is no systematic experimental investigation on the cause of nozzle arc instability nor are there any quantitative stability analyses. It is not expected in the foreseeable future that the mechanisms for generating instabilities can be proven by linear stability analysis of arc governing equations. This is because the highly non-linear nature of arc conservation equations prevents normal mode analysis as these modes are coupled. There appears, to date, only one quantitative linear stability analysis for a self-similar arc [2.17] which indicates that the steep radial density gradient in the velocity shear layer is the main driving force for instability. Due to lack of rigorous arc stability analysis, we have to look at the mechanisms which generate vortices within the arc. It appears that vorticity generation is often associated with instability. The study of Niemeyer and Ragaller [2.18] shows that the effects due to a combination of radial density gradient and axial pressure gradient and the effects of Lorentz force are responsible for the generation of arc instability, which is now discussed in detail.

For a switching arc, the effects of laminar viscous stress on momentum balance are negligible [2.19], and thus the momentum equation is that for inviscid fluid which is modified to take into account Lorentz force

$$\frac{\partial \mathbf{V}}{\partial t} + (\mathbf{V} \cdot \nabla)\mathbf{V} = \frac{1}{\rho}(-\nabla p + \mathbf{J} \times \mathbf{B}) \tag{2.1}$$

where $\mathbf{V}$ is the velocity vector, p the pressure, $\mathbf{J}$ the current density and $\mathbf{B}$ the magnetic flux density. The second term on the left hand side of Equation (2.1) (the

inertia term) can be rearranged as

$$(\mathbf{V}\cdot\nabla)\mathbf{V} = \frac{1}{2}\nabla(\mathbf{V}\cdot\mathbf{V}) - \mathbf{V}\times(\nabla\times\mathbf{V}) = \frac{1}{2}\nabla(\mathbf{V}\cdot\mathbf{V}) - \mathbf{V}\times\boldsymbol{\omega} \tag{2.2}$$

where $\boldsymbol{\omega}$ stands for vorticity which is given by

$$\boldsymbol{\omega} = \nabla\times\mathbf{V} \tag{2.3}$$

By substituting Equation (2.2) into Equation (2.1) and then taking curl on both two sides, we can derive the vorticity equation for the nozzle arc which is given by

$$\frac{\partial\boldsymbol{\omega}}{\partial t} - \nabla\times(\mathbf{V}\times\boldsymbol{\omega}) = \frac{1}{\rho^2}(\nabla\rho\times\nabla p) + \frac{1}{\rho}\left[(\mathbf{B}\cdot\nabla)\mathbf{J} - (\mathbf{J}\cdot\nabla)\mathbf{B}\right] - \frac{1}{\rho^2}\nabla\rho\times(\mathbf{J}\times\mathbf{B}) \tag{2.4}$$

where use has been made of Equation (2.3), $\nabla\cdot\mathbf{J} = 0$ (charge conservation) and $\nabla\cdot\mathbf{B} = 0$.

For an axisymmetrical switching arc burning in a supersonic nozzle, the radial density gradient is dominant, which is perpendicular to the axial pressure gradient and to the axial component of Lorentz force. For a slender arc, for example, Lorentz force and density gradient are parallel, hence the last term on the right hand side of Equation (2.4) is zero.

Therefore, in addition to the effects of inertia force that causes hydrodynamic instability (mathematically given by the second term on left hand side of Equation (2.4)), there are additional mechanisms for the generation of vortices which may cause instability in the switching arc. These mechanisms are given below:

(a) The effects due to a combination of steep radial density gradient and strong axial pressure gradient (mathematically given by the first term on the right hand side of Equation 2.4);

(b) The effects due to Lorentz force: Lorentz force is not curl free, hence producing vortices. This can be seen by using Ampere's law:

Ampere's law: $\nabla\times\mathbf{B} = \mu\,\mathbf{J}$ (2.5)

Lorentz force: $\mathbf{J}\times\mathbf{B} = \frac{1}{\mu}(\nabla\times\mathbf{B})\times\mathbf{B} = -\nabla\left(\frac{\mathbf{B}^2}{2\mu}\right) + \frac{1}{\mu}(\mathbf{B}\cdot\nabla)\mathbf{B}$ (2.6)

where μ is the Permeability. The component of Lorentz force which is a tensile

stress along the magnetic field line is not a conservative force.

In addition to the instabilities related to the momentum balance, ionization instability, similar to that occurring in MHD plasmas (magnetohydrodynamic generation of electricity), can also take place within the arc core [2.20]. Random movement of arc root especially at low currents at the upstream electrode can also cause instability [2.21]. These instability mechanisms have not so far been investigated for switching arcs.

2.4 Review of Theoretical Modelling of Switching Arcs

2.4.1 Nozzle Arc Theory Based on LTE in Laminar Flow

In the first half of nineteen seventies, algorithms for the solution of arc conservation equations were not sufficiently robust and the computation cost with the then available computer power in terms of storage and speed was very high. Ad hoc assumptions were, therefore, introduced by the BBC group to simplify the governing equations for the analysis of the nitrogen arc shown in Figure 2.1. These assumptions include artificially dividing the arc into two zones radially with top hat temperature distribution in the radial direction for each zone as used in [2.2] or dividing the arc axially with assumed effective lengths, one section being laminar and the other turbulent and assuming three radial zones with a fixed radial temperature profile for each zone for the current zero period as done in [2.1]. Thus, the introduction of turbulence [2.1, 2.2] cannot be fully justified.

The investigation by Zhang et al. [2.19] based on LTE and laminar flow and the solution of the full arc conservation equations with a proper account for radiation transport especially the radiation absorption shows that the calculated electrical field (Figure 2.7), temperature (Figure 2.8), arc radius, velocity and pressure are in excellent agreement with those measured for a nitrogen arc at 2 kA DC. The RRRV of the BBC nitrogen arc predicted by the arc model with laminar flow [2.22] is in agreement with that measured [2.1] within the error expected for the shot to shot variation (Figure 2.9). It appears that, with the limited experimental results,

especially the reproducible RRRV test data, the LTE arc model with laminar flow can describe nitrogen arc behaviour adequately in the high current phases as well as in the current zero period.

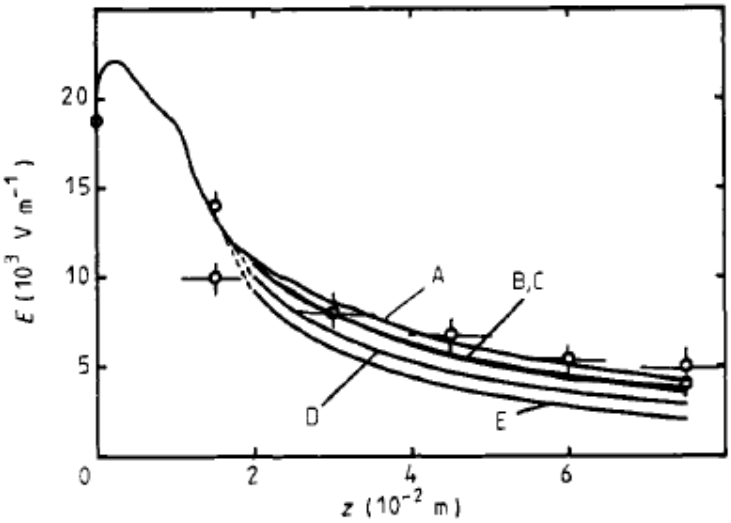

Figure 2.7. Computed [2.19] and measured [2.2] electrical field intensity as a function of axial distance. Curves: A, Computed using measured axial pressure distribution. Thermodynamic and transport properties are dependent on pressure; B, Computed using measured pressure distribution; C, Pressure is iteratively computed assuming isothermal external flow; D, Pressure is iteratively computed assuming adiabatic external flow, E, Pressure is computed from nozzle area. For curves B, C, D and E the thermodynamic (except density) and transport properties at 10atm are used. The open circles are the experimental results after [2.2].

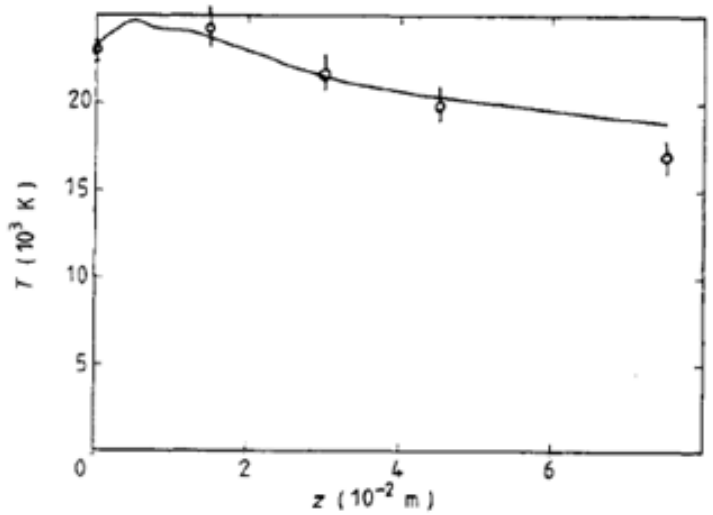

Figure 2.8. The axis temperature as a function of z. The differences between A, B, C, D and E are very small, hence only a single curve is shown. The open circles are the experimental results after [2.2] and the solid curve is computational results from [2.19].

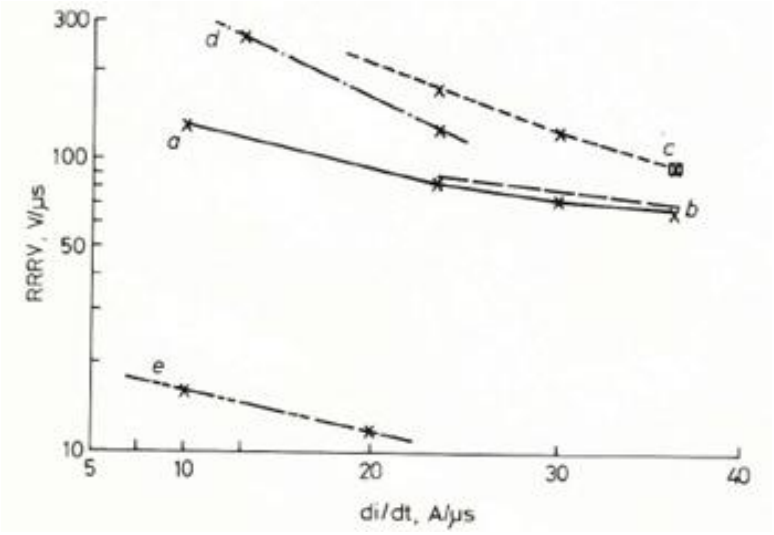

Figure 2.9. Relationship between RRRV and di/dt at P_0 = 23atm. The arc consists of two sections: a self-similar arc section of 1 cm long [2.1] and the nozzle section of 4 cm. Key to the curves: (a) Results of [2.22] with p(z) corresponding to a direct current of 1 kA, (b) p(z) calculated from nozzle geometry [2.22], (c) air [2.1], (d) nitrogen [2.23], (e) Lowke and Lee [2.24]; (x) experimental points [2.1].

When the LTE laminar flow arc model is used to predict the radial temperature profile of an SF_6 nozzle arc, there is a large discrepancy between the predicted and those measured by the Aachen Group (Figure 2.10) [2.7]. As a consequence, the predicted RRRV for SF_6 nozzle arcs in laminar flow is two orders of magnitudes lower than that measured (Figure 2.11) [2.7].

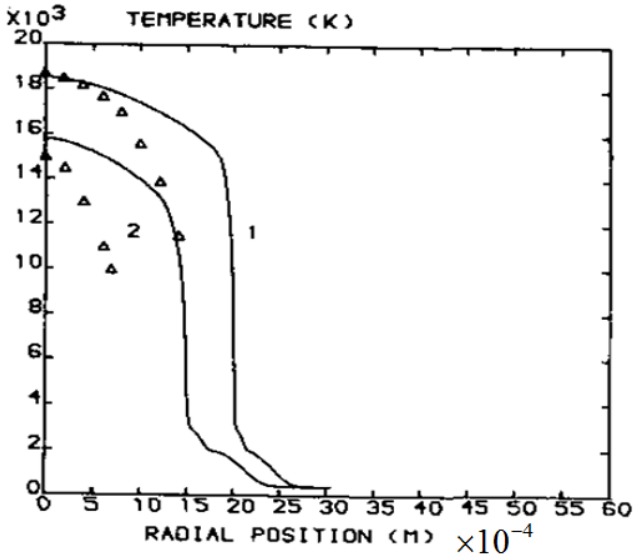

Figure 2.10. Comparison of computed temperature profiles [2.7] (solid lines) and measured results after [2.4, 2.5] (triangles) at Z = 3 cm, P_0 = 9 atm, di/dt = 16 $A\mu s^{-1}$, I_0 = 1000A. Curve 1: I=600A and Curve 2: I=100A.

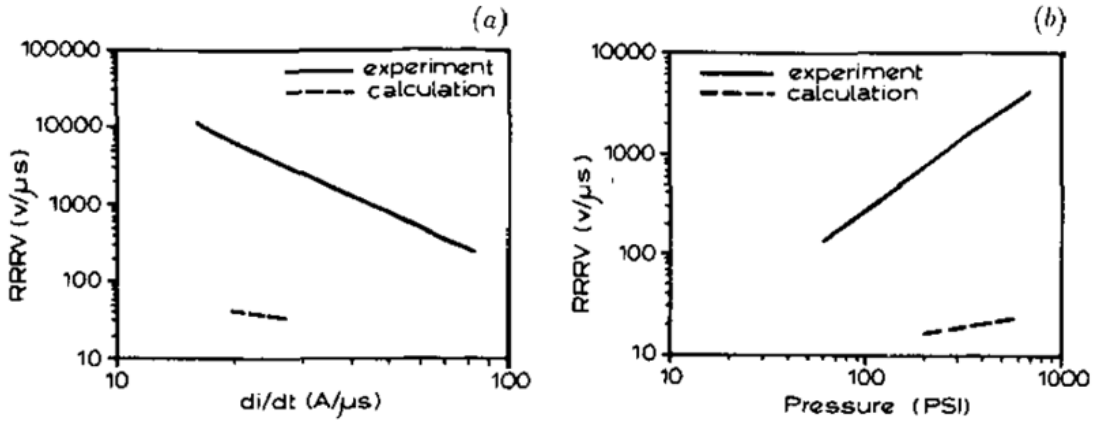

Figure 2.11. (a) Logarithmic relationship between RRRV and di/dt at stagnation pressure 37.5atm. (b) Logarithmic relationship between RRRV and stagnation pressure at a di/dt=27 $A\mu s^{-1}$. Full lines: experiments (after [2.11]) and broken lines: predictions [2.7].

2.4.2 The Effects of Non-LTE on the Switching Arc Behaviour

From the previous discussions, it is apparent that an LTE arc model in laminar flow cannot give a satisfactory account of the experimentally measured RRRV for an SF_6 arc. It is natural to query if the assumption of LTE is correct. It is known that the rapid variation of discharge conditions during current zero period can make an arc depart from LTE [2.8, 2.9, 2.10]. Those processes which are unlikely to attain LTE are summarized below:

(a) The characteristic time of temperature variation during current zero period is about 1 μs. There are many chemical reactions in SF_6 which are not fast enough to reach chemical equilibrium

(b) High electrical field within the arc during current zero period especially after current zero results in higher electron temperature than that of heavy particles, due to inefficient energy transfer between electrons and heavy particles [2.8, 2.10].

(c) Electrical conductivity depends on electrical field because of the departure of electron velocity distribution function from Maxwellian in the direction of electrical field. This becomes appreciable after current zero when recovery voltage is imposed on the breaker.

(d) When current decays towards current zero, the axis temperature can be below 9000 K, and the electron number density is too low to maintain LTE.

Gleizes and his colleagues [2.8, 2.9, 2.10] investigated the combined effects of the aforementioned factors on arc conductance decay during current zero and on RRRV. It has been found that, in the region where electron temperature departs from that of heavy particles, electron temperature is maintained at a higher value due to inefficient exchange of energy with heavy particles for temperature below 8000 K [2.10]. Electrical field usually increases electrical conductivity due to increased ionisation rate and higher electron number density compared with the case where the influence of electric field is not considered [2.8]. These combined effects result in a slower conductance decay (Figure 2.12) and orders of magnitude lower values of RRRV in comparison with those measured and even with those predicted by LTE theory assuming laminar flow [2.10].

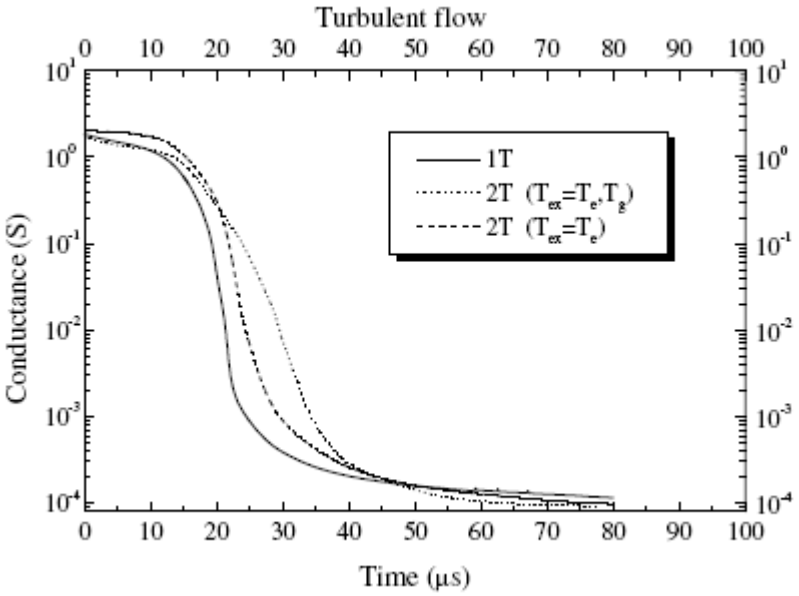

Figure 2.12. Evolution of the conductance during the decay, turbulent case. Reproduced from [2.10].

2.5 Why SF_6 Switching Arc is in LTE and Turbulent?

As previously discussed, the investigation by Gonzalez et al. [2.10] indicates that an arc model based on non-chemical equilibrium, two-temperature and laminar flow cannot account for the RRRV usually achieved by SF_6 circuit breakers. There is overwhelming experimental evidence that SF_6 nozzle arcs are turbulent. In order to achieve agreement with experiments, turbulence enhanced energy transport for electrons and heavy particles are introduced in the respective conservation energy equations for electrons and heavy particles using Prandtl mixing length for a two-temperature chemically non-equilibrium arc model with the same mixing length used for both electrons and heavy particles and an adjustable turbulence parameter which is set to 0.09 [2.10]. Such an approach (i.e. using the same length scales for electrons and heavy particles) is not fully justified. There is little understanding about turbulence in a two-temperature plasma. Also, no consideration has been given to the enhanced diffusion of particle species and chemical reaction rates and, more importantly, the energy exchange between electrons and heavy particles in turbulent flow conditions, all of which are expected to be enhanced by orders of magnitudes as evidenced by turbulent combustion [2.25]. These effects of turbulence make an arc in turbulent state more likely to be in LTE than an arc in laminar flow.

The SF_6 arc model based on LTE and the Prandtl mixing length model for turbulence has achieved good agreement with the measured temperature profile of the Aachen Group (Figure 2.13) and with the measured RRRV of Frind and Rich (Figure 2.14) [2.16]. The direction of future switching arc modeling is to devise an LTE arc model with turbulence which can be applied to a wide range of test conditions commonly met by modern SF_6 circuit breakers.

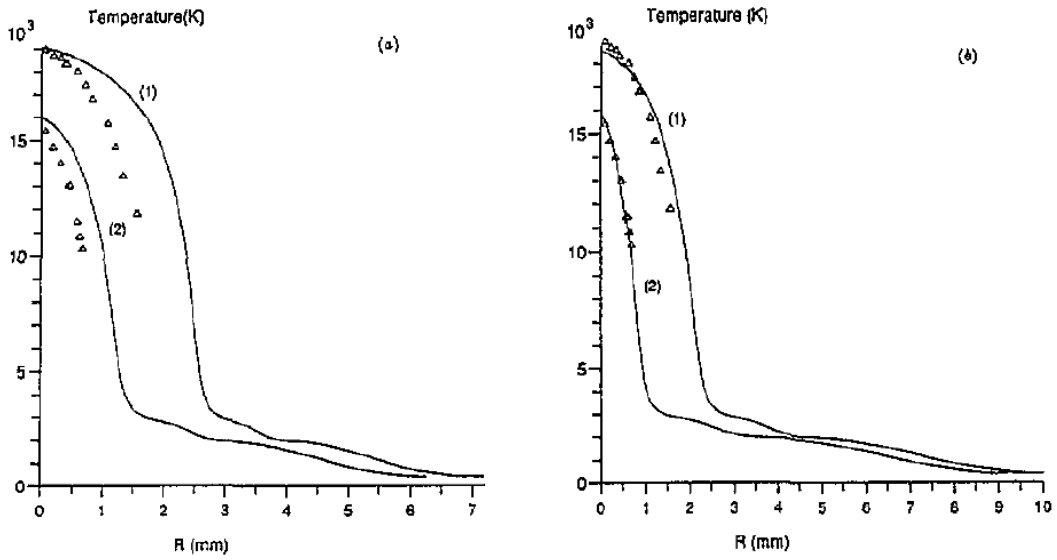

Figure 2.13. Comparison between calculated [2.16] and measured temperature profiles at z=5cm for Aachen nozzle with different values of the turbulence parameter c: (∆) experimental results after [2.4, 2.5]. Stagnation pressure 9 atm, I_0 = 1000A , di/dt = 16 $A\mu s^{-1}$. Instantaneous current: (1) 600A; (2) 100A. (a) c = 0.04, (b) c = 0.075.

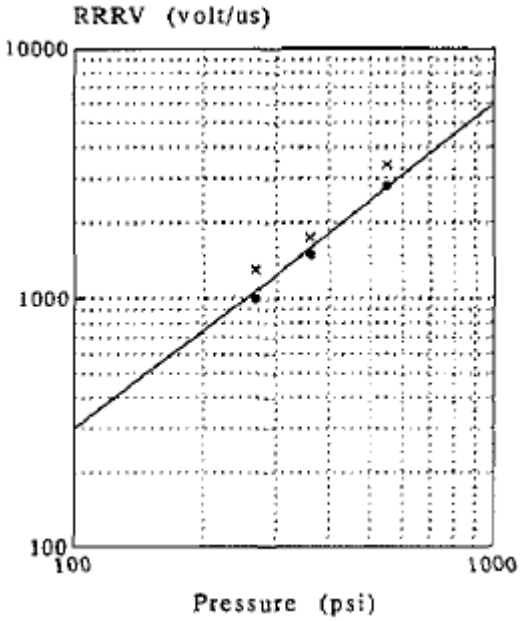

Figure 2.14. Logarithmic relationship between critical rate of rise of recovery voltage and stagnation pressure at di/dt = 27 $A\mu s^{-1}$. Full line is prediction by [2.16] and experimental points are (x) (arc re-ignition) and (●) (arc extinction), after [2.11].

2.6 Concluding Remarks

There is overwhelming experimental evidence showing that the switching arc is turbulent. However, there are no direct experimental measurements on turbulence strength such as the velocity and temperature variance. The importance of turbulence on the behavior of switching arc is indirectly proven by the exclusion of the effects of non-LTE processes and by the good agreement so far achieved between the experimental results and the prediction of turbulence arc model based on the Prandtl mixing length model. Enhanced rates of chemical and ionization reactions and efficient energy exchanges between electrons and heavy particles under turbulent conditions justify the assumption of a turbulent arc in LTE. The focus of the rest of this thesis is the modeling of an LTE turbulent arc.

References

[2.1] Hermann W, Kogelschatz U, Niemyer L, Ragaller K and Schade E 1976 Investigation on the phenomena around current zero in HV gas blast circuit breakers *IEEE Trans. Power Appr. Syst.* **95** 1165-76

[2.2] Hermann W, Kogelschatz U, Niemeyer L, Ragaller K and Schade E 1974 Experimental and theoretical study of a stationary high-current arc in a supersonic nozzle flow *J. Phys. D: Appl. Phys.* **7** 1703-22

[2.3] Howatson A M and Topham D R 1976 The instability of electrical arcs burning axially in accelerated flow *J. Phys. D: Appl. Phys.* **9** 1101-10

[2.4] Leseberg D and Pietsch G 1982 Optical investigation on SF_6 switching arc inside a glass nozzle *Proc. 7th Int. Conf. on Gas Discharges and their applications* (London, UK) (London: Peter Peregrinus) pp 9-12.

[2.5] Leseberg D and Pietsch G 1981 Untersuchung des plasmazustands von schaltlichtbogen in stromendem SF_6 wahrend der unterbrechung von kurzschlusstromen Nr.3019, Westdeutschen Verlag

[2.6] Kobayashi A, Yanabu S, Yamashita S and Ozaki Y 1980 Experimental investigation on arc phenomena ins SF_6 puffer circuit breakers *IEEE Trans. Plasma. Sci.* **PS-8** 339-43

[2.7] Fang M T C and Zhuang Q 1992 Current-zero behaviour of an SF_6 gas-blast arc. Part I: laminar flow *J. Phys. D: Appl. Phys.* **25** 1197-204

[2.8] Gonzaliez J J, Gleizes A and Kerenek P 1994 SF_6 circuit breaker arc modelling: influence of the electric field on the electrical conductivity *J. Phys. D: Appl. Phys.* **27** 985-93

[2.9] Belhaouari J B, Gonzalez J J and Gleizes A 1998 Simulation of a decaying SF_6 arc plasma: Hydrodynamic and kinetic coupling *J. Phys. D: Appl. Phys.* **31** 1219- 32

[2.10] Gonzalez J J, Girard R and Gleizes A 2000 Decay and post-arc phases of a SF_6 arc plasma: a thermal and chemical non-equilibrium model *J. Phys. D: Appl. Phys.* **33** 2759- 68

[2.11] Frind G and Rich J A 1974 Recovery speed of axial flow gas blast interrupter: dependence on pressure and di/dt for air and SF_6 *IEEE Trans. Power Appar. Syst.* **93** 1675-84

[2.12] Frind G, Kinsinger R E, Miller R D, Nagamatsu H T and Noeske H O 1977 Fundamental investigation of arc interruption in gas flows EPRI EL-284 (Project 246-1)

[2.13] Benenson D M, Frind G, Kinsinger R E, Nagamatsu H T, Noeske H O and Sheer, Jr R E 1980 Fundamental investigation of arc interruption in gas flows EPRI EL-1455 (Project 246-2)

[2.14] Benoit Cushman-Roisin Jan. 2012 Turbulent jets, Lecture notes from Thayer School of Engineering, Dartmouth College. Retrieved 25 Aug. 2014 from: https://engineering.dartmouth.edu/~d30345d/courses/engs43/Turbulent-Jet.pdf

[2.15] Blevins R D 1984 *Applied Fluid Dynamics Handbook* (New York: Van Nostrand Reinhold Co.)

[2.16] Fang M T C, Zhuang Q and Guo X J 1994 Current zero behaviour of an SF_6 gas-blast arc Part II: turbulent flow *J. Phys. D: Appl. Phys.* **27** 74-83

[2.17] Blundell R E and Fang M T C 1997 Stability of a dc SF_6 arc in axially accelerating flow *IEEE Trans. on Plasma Sci., Special Issue on High Pressure Arcs and High Frequency Thermal Plasmas*. **25** 852-59

[2.18] Niemeyer L and Ragaller K 1973 Development of turbulence by the interaction of gas flow with plasmas *Z. Naturforsch.* **28a** 1281- 89

[2.19] Zhang J F, Fang M T C and Newland D B 1987 Theoretical investigation of a 2KA DC nitrogen arc in a supersonic nozzle *J. Phys. D: Appl Phys.* **20** 368-79

[2.20] Nelson A H and Haines M G 1969 Analysis of the nature and growth of electrothermal waves *Plasma Phys.* **11** 811-37

[2.21] Mentel J 1977 The influence of vaporization upon the roots of high current arc. I. Different forms of vaporization in the arc roots *Applied Physics.* **14** 269- 76

[2.22] Fang M T C and Lin W Y 1990 Current zero behaviour of a gas blast arc, Part.1: Nitrogen *Proc. IEE Pt. A.* **137** 175-83

[2.23] Hermann W and Ragaller K 1977 Theoretical description of the current interruption in HV gas-blast breaker *IEEE Trans. Power. Appar. Syst.* **96** 1546-55

[2.24] Lowke J J and Lee H 1985 A numerical study of a two-dimensional circuit breaker arc during current interruption *Proc. 8th Int. Conf. Gas discharges and their applications* (Oxford, UK) pp 54-6

[2.25] Poinsot T and Veynante D 2005 *Theoretical and Numerical Combustion* 2nd edn (Philadelphia: Edwards)

Chapter 3
Modelling of Turbulent SF_6 Switching Arcs

3.1 Introduction

It has been shown in Chapter 2 that the RRRV predicted by a laminar flow arc model taking into account non-LTE processes results in the RRRV lower than that predicted by an LTE laminar flow arc model. However, good agreement between the experimentally measured RRRV and that predicted by a turbulent LTE arc model based on the Prandtl mixing length shows that further improvement in arc modeling should be based on a LTE arc in turbulent flow. The drawback of the Prandtl mixing length turbulence model is that the range of applicability of the chosen value of the turbulence parameter is very limited. In the context of a circuit breaker, the value of the turbulence parameter appears to be sensitive to the nozzle geometry, which needs to be readjusted with test results when the nozzle geometry is changed. Further work is, therefore, necessary to improve the modeling of turbulent SF_6 switching arc so that the turbulence parameters have a wide range of applicability.

Turbulence is the non-linear development phase of a linearly unstable flow. In the non-linear regime, the turbulent state is often characterized by the unstable modes with large growth rates as given by linear stability analysis. The usual method for linear stability analysis is not applicable to switching arcs. Due to highly non-linear nature of the conservation equations for arcs in gas flow and the radial and axial gradients of temperature and velocity within an arc, linear stability analysis based on normal modes is not feasible as the modes are coupled. Therefore, in the arc context, linear stability analysis has only been carried out for an arc burning in a flow, the pressure distribution of which ensures that the acceleration of the flow per unit length is constant [3.1]. For such an arc (commonly known as the self-similar arc), its thermodynamic state is axially uniform although velocity increases linearly with

axial distance [3.2]. Using coordinate transformation, Blundell et al. [3.1] have managed to perform a linear stability analysis based on normal modes on an SF_6 self-similar arc assuming that the imposed pressure on the arc is fixed. Disturbances of any frequency within the arc's thermal influence region have been found to be unstable. The unstable waves are amplified when propagating downstream. The most prominent destabilizing mechanisms are due to density gradient and the coupling between the density and velocity fluctuations which are the strongest in the region where the temperature and velocity drop rapidly to those of the external flow (i.e. the velocity shear layer of Figure 2.6 in Chapter 2). Thus, the stability analysis although limited to self-similar arc [3.1] gives additional mechanisms unique to arcs for the generation of shear layer instability. Since a nozzle arc shows a direct resemblance to a round jet (Chapter 2), instability due to inertia force also operates in the velocity shear layer. It is, therefore, of utmost importance that the turbulence in the velocity shear layer needs to be modelled properly.

Turbulence has been an active research area since its discovery by Osborne Reynolds in 1883 in his experiments related to the flow in circular pipe [3.3]. It is commonly accepted that the governing equations for turbulent flow are the same as N-S equations. In principle, these equations can be solved numerically with appropriate initial and boundary conditions. However, as indicated in Chapter 1, such an approach to turbulence (i.e. direct numerical solution to N-S equations (DNS)) has been found not possible even with the present day computer power because of the required spatial and time resolutions for an adequate description of the smallest eddies and the required computation time.

As it is not practical to solve directly N-S equations for turbulent flow, approximate methods for the solution of N-S equations must be devised. Since turbulent flow exhibits randomness, statistical methods have been employed to solve N-S equations. Such an approach reveals the statistical features of the turbulence flow [3.4]. Such an approach also meets the requirements of most engineering applications concerning turbulent flow. For example, a circuit breaker design engineer would only be interested in the time averaged arc voltage but not the small

(in comparison with the mean voltage) high frequency (much higher than 50 Hz) voltage oscillations around the mean.

The equations derived from the statistically treated N-S equations are not closed. Turbulence models are, therefore, used to introduce additional equations to make the number of equations equal to the number of unknowns. These additional equations are usually based on ad hoc assumptions which cannot be justified by a consideration of basic physics. Turbulence models are usually devised for specific applications. There are numerous turbulence models [3.5], but there is no general guidance regarding the choice of turbulence model for the flow problem in hand. It appears that the choice of turbulence model is mainly guided by the experience of the user and the similarities between the problem in hand and those turbulent flow problems already solved successfully.

The modelling of turbulent shear layer flow has the longest history, which was initiated by Prandtl in 1925 [3.6]. Because of its wide range of engineering applications, extensive work has been done on the modeling of turbulent shear layer. Various turbulent shear flow models have been successfully applied to predict the flow behavior. However, the modeling of turbulent arc is still at its infancy. Although the turbulence models for shear layer flow [3.5] are not devised for turbulent switching arc, the resemblance between a round fluid jet (a free shear layer flow) and the switching arc and the importance of shear velocity layer to both round jet and switching arc suggest that we follow, at least as a first attempt for the modelling of turbulent arc, the same approach for the shear layer flow to account for turbulence enhanced momentum and energy transfer. This approach generally utilizes time average (known as the Reynolds's approach) [3.6] to derive the time averaged conservation equations for a turbulent flow assuming constant density and material properties. The additional unknowns, which are known as the Reynolds stresses, are related to the mean motion (i.e. the closure assumption) using Boussinesq assumption and eddy viscosity [3.6]. A brief description of this approach will be given, which includes the derivation of the time averaged conservation equations and the closure of these equations using Boussinesq assumption and eddy viscosity.

The application of Boussinesq assumption and eddy viscosity is not the best way to relate Reynolds stresses to the mean motion due to the introduction of ad hoc assumptions which limit the range of applicability of these turbulence models. An alternative way is to derive the equations describing the Reynolds stresses by taking higher moments of the N-S equations. The resulting Reynolds stress equations are given, which show that the adoption of this approach will not result in a closed set of time averaged equations.

The conservation equations for the turbulent switching arcs, which are derived based on the time averaged conservation equations for turbulent shear flow, are given. These conservation equations are incorporated into the relevant turbulence models for use in subsequent sections to predict the behaviour of SF_6 switching arcs in turbulent state.

The turbulence models employed are subject to verification by the experimental results of [3.7, 3.8, 3.9]. A brief review of these experiments is given, which include the experimental conditions and the experimental results obtained in the form of RRRV.

Finally, a brief description is given with regard to the implementation of the arc conservation equations and turbulence models in a general purpose CFD [3.10, 3.11] software package, PHOENICS [3.12], which are used to obtain results for the work of this thesis.

3.2 Time Averaged Conservation Equations for Turbulent Shear Layer Flow

For a large number of turbulent flows of industrial importance, two experiments performed under identical conditions will yield different results (Figure 3.1). However, when the results are averaged over time, characteristic features of time averaged flow (commonly known as the mean flow) emerge. As stated in Chapter 2, for a number of engineering applications, including circuit breakers, only the mean flow properties are of interests. We therefore derive time averaged equations from the

N-S equations following the same procedure proposed by Reynolds over 150 years ago [3.6, 3.13]. For ease of discussion, the derivation of the time averaged conservation equations is based on the Cartesian coordinate system.

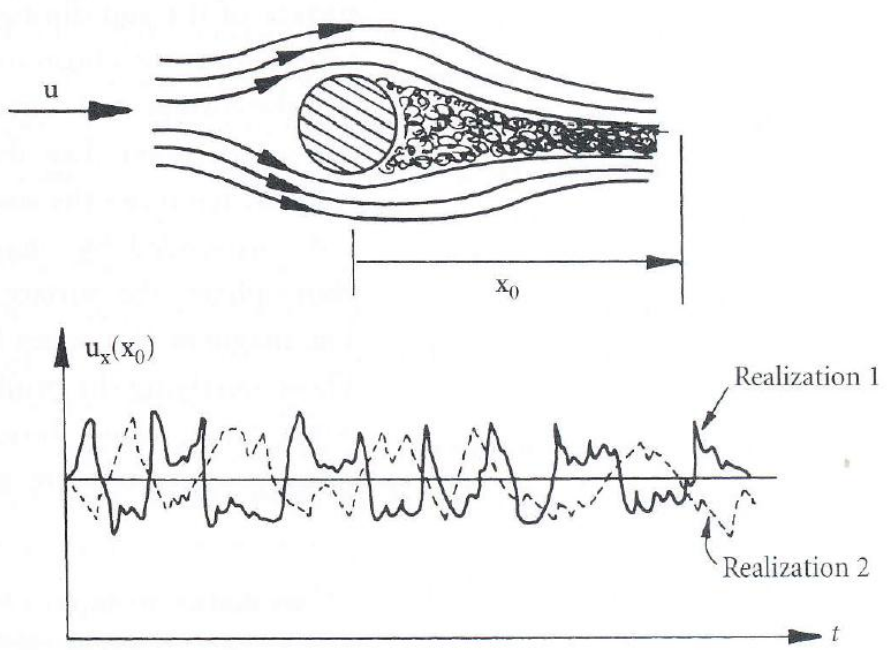

Figure 3.1. Two measurements showing velocity $U_x(x_0)$ as a function of time t obtained with the same experimental conditions. It is shown that two measurements give different variations of $U_x(x_0)$ with t, but with the same time averaged velocity.

With the Reynolds approach, quantities of various properties characterizing the turbulent flow are conventionally decomposed into their time averaged values and the corresponding fluctuations, which is given by

$$\phi = \bar{\phi} + \phi' \tag{3.1}$$

The time averaged flow property is defined as

$$\bar{\phi} = \frac{1}{\Delta t}\int_{t_0}^{t_0+\Delta t} \phi \, dt \tag{3.2}$$

The time averaged properties governs the behaviour of the mean flow. In theory we should take the limit of Equation (3.2) with Δt approaching infinity. However, for practical experiments, Δt must be a finite value, which is therefore required to be larger than the time characterizing the fluctuation but smaller than that characterizing the variation of the mean flow field. The time average of the fluctuation is, by definition, always equal to zero:

$$\bar{\phi}' = \frac{1}{\Delta t}\int_{t_0}^{t_0+\Delta t} \phi'\, dt \equiv 0 \tag{3.3}$$

According to Equation (3.1), the instantaneous velocity component at a given point (for the Cartesian coordinate system) can be written as

$$u_i = \bar{u}_i + u_i' \qquad (i = 1, 2, 3) \tag{3.4}$$

where i = 1, 2, 3 stands for the three components of the position vector, x_1, x_2, x_3.

The other time dependent flow properties can be expressed as

$$\rho = \bar{\rho} + \rho',\ \ p = \bar{p} + p',\ \ T = \bar{T} + T',\ \ h = \bar{h} + h',\ \ \mu = \bar{\mu} + \mu',\ \ k = \bar{k} + k' \tag{3.5}$$

where ρ is the density, p the pressure, T the temperature, h the enthalpy, μ the molecular viscosity and k the thermal conductivity.

Substituting each quantity of the instantaneous N-S equations [3.13] by its mean and fluctuation by Equations (3.4) and (3.5), taking the time average of the resulting equation and with considerable rearrangement, we obtain the time averaged conservation equations for turbulent shear flow:

(a) Time averaged continuity equation

$$\frac{\partial \rho}{\partial t} + \frac{\partial}{\partial x_j}\left(\rho \overline{u_j}\right) = 0 \qquad (j = 1, 2, 3) \tag{3.6}$$

(b) Time averaged momentum equation

$$\frac{\partial}{\partial t}\left(\rho \overline{u_i}\right) + \frac{\partial}{\partial x_j}\left(\rho \overline{u_i}\,\overline{u_j}\right) = -\frac{\partial \overline{p}}{\partial x_i} + \frac{\partial}{\partial x_j}\left(\overline{\boldsymbol{\tau}_{ij}} - \rho \overline{u_i' u_j'}\right) \qquad (i, j = 1, 2, 3) \tag{3.7}$$

(c) Time averaged energy equation

$$\frac{\partial}{\partial t}\left(\rho \bar{h}\right) + \frac{\partial}{\partial x_j}\left(\rho \overline{u_j}\,\bar{h}\right) = \frac{\partial \bar{p}}{\partial t} + \overline{u_j}\frac{\partial \bar{p}}{\partial x_j} + \overline{u_j'\frac{\partial p'}{\partial x_j}} + \frac{\partial}{\partial x_j}\left(\frac{k}{c_p}\frac{\partial \bar{h}}{\partial x_j} - \rho \overline{u_j' h'}\right) + \overline{\Phi} \qquad (j = 1, 2, 3) \tag{3.8}$$

In Equation (3.7), tau is the averaged viscous stress tensor given by

$$\overline{\boldsymbol{\tau}_{ij}} = \mu\left[\left(\frac{\partial \overline{u}_i}{\partial x_j} + \frac{\partial \overline{u}_j}{\partial x_i}\right) - \frac{2}{3}\delta_{ij}\frac{\partial \overline{u}_k}{\partial x_k}\right] \qquad (i, j = 1, 2, 3) \tag{3.9}$$

In Equation (3.8), the time average of the dissipation function is given by

$$\overline{\Phi} = \overline{\boldsymbol{\tau}_{ij}} \frac{\partial \overline{u_i}}{\partial x_j} + \overline{\boldsymbol{\tau}'_{ij} \frac{\partial u'_i}{\partial x_j}} \qquad (i, j = 1, 2, 3) \qquad (3.10)$$

where $\overline{\boldsymbol{\tau}_{ij}}$ is given by Equation (3.9) and $\boldsymbol{\tau}'_{ij}$ is given by

$$\boldsymbol{\tau}'_{ij} = \mu' \left[\left(\frac{\partial u'_i}{\partial x_j} + \frac{\partial u'_j}{\partial x_i} \right) - \frac{2}{3} \delta_{ij} \frac{\partial u'_k}{\partial x_k} \right] \qquad (i, j = 1, 2, 3) \qquad (3.11)$$

It should be noted that, in order to derive Equations (3.6), (3.7) and (3.8), the effects of density fluctuation and fluctuations of material properties on turbulent eddies are assumed to be negligible, which means $\rho'/\rho << 1$, $\mu'/\mu << 1$ and $k'/k << 1$. Turbulence theory for incompressible and constant property fluid is the most mature. Our discussions on turbulence shall assume that this is the case.

The time averaged conservation equations (Equations (3.6), (3.7) and (3.8)) describe the behaviour of the mean flow. The term $-\rho \overline{u'_i u'_j}$ in Equation (3.7) is analogous to viscous stress which is commonly referred to as the Reynolds stress tensor denoted as

$$\boldsymbol{\tau}^R_{ij} = -\rho \overline{u'_i u'_j} \qquad (i, j = 1, 2, 3) \qquad (3.12)$$

Equation (3.12) includes six individual Reynolds stress components all of which are additional unknowns produced from the procedure of time averaging of momentum conservation equation as previously demonstrated. Additional relations are therefore required to relate these unknowns to the mean flow before the time averaged conservation equations can be solved, since the number of unknowns must be equal to the number of equations. The absence of such relations is known as the closure problem of the time averaged conservation equations.

The simplest way of doing this is to relate the Reynolds stress to the mean rate of strain tensor based on Boussinesq hypothesis [3.6, 3.13] which assumes that turbulence is isotropic. The Reynolds stress is therefore given by

$$\boldsymbol{\tau}^R_{ij} = -\rho \overline{u'_i u'_j} = \mu_t \left[\left(\frac{\partial \overline{u}_i}{\partial x_j} + \frac{\partial \overline{u}_j}{\partial x_i} \right) - \frac{2}{3} \delta_{ij} \frac{\partial \overline{u}_k}{\partial x_k} \right] - \frac{2}{3} \delta_{ij} \rho k \qquad (i, j = 1, 2, 3)$$

(3.13)

where μ_t is a scalar quantity and is commonly known as the turbulence viscosity or eddy viscosity. The last term in Equation (3.13) ensures that the sum of the normal stresses is added up to $-\rho\overline{u_i'u_i'}$ in common with pressure tensor for incompressible fluid. δ_{ij} is the Kronecker delta function ($\delta_{ij}=1$ if $i=j$ and $\delta_{ij}=0$ if $i\neq j$). *k* is the average fluctuating kinetic energy per unit mass given by

$$k=\overline{u_i'u_i'}/2 \qquad (i = 1, 2, 3) \qquad (3.14)$$

As the eddies in a turbulent flow move randomly in a manner similar to molecular random motion, in direct analogy to the diffusion coefficient of a gas, eddy viscosity is assumed to be related to a length and a velocity scale characterizing the random motion of the large scale eddies which interact actively with the mean flow

$$\mu_t = C_\mu \rho \lambda_c V_c \qquad (3.15)$$

where C_μ is a constant and λ_c and V_c are, respectively, the length and velocity scale of the turbulent motion. Calculation of the eddy viscosity requires extra equations to determine the length and velocity scales characterizing the turbulent flow, which are provided by turbulence models. In order to close the equations describing turbulent flow, turbulence models inevitably introduce ad hoc assumptions which cannot be justified on physical principles and inevitably introduce unknown constants. These constants need to be determined from experimental results. Turbulence models are numerous and are devised to solve specific problems. Some models based on simple, often dimensional arguments, have proven successful and popular in solving engineering problems. Turbulence models based on eddy viscosity belong to this category. Eddy viscosity turbulence models appear to be the simplest. However, these models commonly assume fluid with constant properties and incompressible.

The eddy motion in a turbulent flow also gives rise to enhanced energy exchange which is expressed by the term $-\rho\overline{u_j'h'}$ in the energy equation. This term is known as the Reynolds heat flux tensor, which is related to the mean flow field through the following expression

$$-\rho\overline{u_j' h'} = \frac{k_t}{c_p}\frac{\partial \bar{h}}{\partial x_j} \qquad (j = 1, 2, 3) \qquad (3.16)$$

Since the turbulence enhanced momentum and energy transport result from the same mechanism, i.e. the convective transport of turbulent eddies, the turbulent Prandtl number is introduced to relate the diffusivity of the turbulence enhanced transport of heat (or any other scale quantities) to the eddy viscosity, which is usually assumed to be a constant:

$$\mathrm{Pr}_t = \frac{\mu_t}{k_t / c_p} = \text{constant} \qquad (3.17)$$

3.3 Reynolds Stress Equation

In principle, one can avoid using Boussinesq assumption to link the Reynolds stresses to the strain tensor of the main flow by taking the first moment of momentum conservation equation, which results in six Reynolds stress equations. The detailed derivation of Reynolds stress equations has been given by George [3.14]. The resulting Reynolds stress equations are given by

$$\begin{aligned}\frac{\partial\left(\overline{u_i' u_k'}\right)}{\partial t} + \bar{u}_j\frac{\partial\left(\overline{u_i' u_k'}\right)}{\partial x_j} = &\overline{\frac{p'}{\rho}\left(\frac{\partial u_i'}{\partial x_k} + \frac{\partial u_k'}{\partial x_i}\right)} \\ &+ \frac{\partial}{\partial x_j}\left[-\frac{1}{\rho}\left(\overline{p' u_i'}\delta_{kj} + \overline{p' u_k'}\delta_{ij}\right) - \overline{u_i' u_k' u_j'} + 2\nu\left(\overline{\mathbf{s}_{ij}' u_k'} + \overline{\mathbf{s}_{kj}' u_i'}\right)\right] \\ &- \left(\overline{u_i' u_j'\frac{\partial u_k'}{\partial x_j}} + \overline{u_k' u_j'\frac{\partial u_i'}{\partial x_j}}\right) - 2\nu\left(\overline{\mathbf{s}_{ij}'\frac{\partial u_k'}{\partial x_j}} + \overline{\mathbf{s}_{kj}'\frac{\partial u_i'}{\partial x_j}}\right)\end{aligned}$$

$$(i, j, k = 1, 2, 3) \qquad (3.18)$$

This equation is known as Reynolds stress equation. The physical meaning of each of the term in this equation is as follows:

(a) Left hand side: the rate of change of Reynolds stress following the mean motion.

(b) Right hand side: the means of different terms are given below:

- First term: the pressure- strain rate term,
- Second Term: the turbulence transport (or divergence) term,
- Third term: the "production" term and,

- Fourth term: the "dissipation" term.

It has been found that the Reynolds stress equation not only involves the mean velocity and Reynolds stresses, but also depends on many more new unknowns which are summarized in Table 3.1.

Table 3.1. Addition terms in Reynolds stress equations.

Additional terms (i, j, k = 1, 2, 3)	Number of unknowns
$\overline{p' \frac{\partial u_i'}{\partial x_j}}$	9
$\overline{p' u_i'}$	3
$\overline{u_i' u_k' u_j'}$	27
$\overline{\mathbf{s}_{ij}' u_k'}$	27
$\overline{s_{ij}' \frac{\partial u_k'}{\partial x_j}}$	9
	Total number of unknowns: 75

It has now been shown that derivation of the equations for Reynolds stresses has not given a single equation relating the Reynolds stress to the mean motion. The resulting Reynolds stress equations are extremely complex and include many more unknowns than the time averaged conservation equations given by Equations (3.6), (3.7) and (3.8). The aim of reducing the number of unknowns has clearly not been met. Such statistical approach can never lead to the closure of time averaged conservations unless some ad hoc assumptions are introduced, and thus it does not show any advantage over the simple method based on Bousssinesq assumption and eddy viscosity as previously discussed. Therefore, the modelling of turbulent SF_6 switching arcs will be based on the derivation of time averaged conservation equations and the adoption of Bousssinesq assumption. The governing equations for turbulent switching arcs and those of turbulence models will be given in Sections 3.4 and 3.5, respectively.

3.4 The Governing Equations for Switching Arcs in Turbulent State

As previously mentioned, the direct resemblance between shear layer flows and switching arcs prompts one to model turbulent switch arcs using the same approach for thin shear layers. Based on the assumption of LTE of the arc state, the turbulent switching arc together with its surrounding cold gas flow can be described by the time averaged conservation equations given by Equations (3.6), (3.7) and (3.8) which are modified to take into account the effects of radiation transfer and electromagnetic field. By assuming axisymmetry of the switching arc, the conservation equations are given below in cylindrical coordinates:

$$\frac{\partial(\rho\phi)}{\partial t}+\frac{1}{r}\frac{\partial}{\partial r}\left[r\rho v\phi-r\Gamma_\phi\frac{\partial\phi}{\partial r}\right]+\frac{\partial}{\partial z}\left[\rho w\phi-\Gamma_\phi\frac{\partial\phi}{\partial z}\right]=S_\phi \tag{3.19}$$

where ϕ is the dependent variable and ρ the gas density. *v* and *w* are respectively the radial and axial velocity components. The source terms (S_ϕ) and the diffusion coefficients (Γ_ϕ) are listed in Table 3.2 for different conservation equations, in which all notations have their conventional meaning. The subscript *l* denotes the laminar part of the transport coefficient and *t* the turbulent part. Viscous stresses are taken into account by the diffusion terms on the left hand side of the two momentum equations in Table 3.2. The part of viscous stresses in the radial momentum equation which cannot be written as part of a diffusion term is included in the source term (Table 3.2). It has been found that molecular viscous effects are negligible in momentum balance for arcs in a supersonic nozzle [3.15]. Viscous heating due to molecular and turbulent stresses is given in the source term for the enthalpy equation (Table 3.2).

Table 3.2. Terms of governing equations.

Equation	ϕ	Γ_ϕ	S_ϕ
Continuity	1	0	0
Z-momentum	w	$\mu_l + \mu_t$	$-\frac{\partial p}{\partial z}$
R-momentum	v	$\mu_l + \mu_t$	$-\frac{\partial p}{\partial r} + \mathbf{J} \times \mathbf{B} - (\mu_l + \mu_t)\frac{v}{r^2}$
Enthalpy	h	$\frac{k_l + k_t}{c_p}$	$\frac{\mathrm{d}p}{\mathrm{d}t} + \sigma E^2 - q + (\mu_l + \mu_t)\left\{2\left[\left(\frac{\partial v}{\partial r}\right)^2 + \frac{v^2}{r^2} + \left(\frac{\partial w}{\partial z}\right)^2\right] + \left(\frac{\partial v}{\partial z} + \frac{\partial w}{\partial r}\right)^2\right\}$

The arcing gas is SF_6. The equation of state and the transport coefficients including electrical conductivity are determined by temperature and pressure. For SF_6, relevant data has been tabulated by Frost and Liebermann [3.16].

For all the investigations presented in this thesis, the arcing current does not exceed 1 kA. There are two reasons why we only use currents up to 1 kA. Firstly, the experimental conditions of [3.7, .3.8, 3.9] are designed to investigate the current zero period of a two-pressure breaker using a current ramp consisting of a current plateau (a constant current, hereafter referred to as DC by convention) and a linearly decaying current (specified by di/dt) before current zero, and a voltage ramp (specified by dV/dt) after current zero. Such an approach assumes that the peak current does not have effects on the arc behaviour during the current zero period, and before current zero period the arc is in quasi-steady state. A more detailed discussion on the justification of using such a current waveform will be given in Section 3.6 of this chapter. Numerical experiments have been conducted to find suitable value of the plateau current for the values of di/dt investigated in [3.7, 3.8, 3.9] such that, at this current, quasi-steady state is still maintained. We have found that 1 kA is suitable. Secondly, for the DC nozzle arcs investigated in Chapter 4, we have found that the features of the DC arcs with a current greater than 1 kA are the same as those of 1 kA

DC. Thus, there is no need to push up the currents. Under this circumstance (current does not exceed 1 kA), the radial component of electrical field is negligible in comparison with the axial component, and the radial variation of axial component is much smaller than its magnitude [3.17, 3.18]. Therefore, the axial electrical field is considered to be constant over the arc cross-section, which can be calculated by the simplified Ohmic law

$$i = E\int_0^\infty \sigma 2\pi r dr \tag{3.20}$$

where i is the instantaneous current and σ the electrical conductivity.

The effects of Lorentz force generated by the interaction of the arc current with its own magnetic field, which is included in the momentum source term, can be neglected for low current arcs (below 2 kA) in a supersonic nozzle [3.15, 3.18].

For an axisymmetric arc with monotonically decreasing radial temperature profile, radiation transport is calculated with the approximate model of Zhang et al. [3.15]. In the high temperature core the boundary of which is defined as the radial position where the temperature reaches 83% of the axis temperature, the net radiation loss, q, in the energy equation is calculated by the net radiation emission coefficient (NEC). The NEC for SF_6 is a function of pressure, temperature and arc radius, the relation of which has been tabulated in [3.19]. The arc radius for the purpose of calculating the NEC is defined as the radial position of 4000 K isotherm. 80% of the radiation flux at the high temperature boundary is assumed to be absorbed in the region from the core boundary to the 4000 K isotherm [3.15]. It has been found necessary that the NEC given in [3.19] to be raised by a factor of 2.5 in order to get agreement between the calculated and measured arc temperature [3.20, 3.21]. Details on the procedure of calculating net radiation loss with this approximate model has been given by [3.15], which are also described in Section A.5 of Appendix A for reference.

The conservation equations of switching arcs (Equation (3.19)) together with the supplementary equations (Equation (3.20) and those of calculating net radiation loss) given in this section, and the governing equations for turbulence models (to be

given in Section 3.5) for calculation of turbulent diffusion coefficients given in Table 3.2, give a complete description of a turbulent switching arc in LTE. All these equations, together with the required data for thermodynamic and transport properties, the equation of state, and NEC for an arc plasma, form the arc model.

3.5 Turbulence Models used for SF_6 Switching Arcs

There are a large number of turbulence models [3.5, 3.14, 3.22-3.27]. However, there is no general theoretical guidance regarding the choice of turbulence models for turbulent arcs in supersonic flows. Our choice of turbulence models is restricted to those which have been applied with success to similar flow conditions as those of an arc burning in a supersonic flow as well as their suitability for engineering application (low computational cost). Thus, we choose those turbulence models which belong to the category of effective eddy viscosity. Reynolds stresses are linearly linked to the mean strain via eddy viscosity by means of Boussinesq hypothesis. Of the turbulence models based on eddy viscosity the Prandtl mixing length model has achieved considerable success in predicting turbulent arc behavior [3.28]. The standard k-epsilon model with the default values of the five turbulence parameters [3.24] and two of its variants (the renormalization group, commonly known as the RNG model [3.25] and Chen-Kim model [3.26]) have been used for the modelling of the turbulent flow in circuit breakers with contradictory claims regarding their successes [3.20, 3.29-3.32]. The test conditions in terms of current, pressure and system geometry covered by the aforementioned investigations are however very limited. Hence, no general conclusions on the relative merits of the turbulence models so far employed can be drawn. The verification of turbulence models suitable for switching applications requires extensive reproducible experimental results covering a wide range of test conditions. Such experimental data is extremely scarce.

We therefore choose the aforementioned four turbulence models for the modelling of turbulent SF_6 switching arcs as they have achieved considerable success

in the prediction of the behavior of turbulent thin shear layers, which have also been used for predicting of switching arc behaviour although there are contradictory claims regarding their successes. As previously mentioned, all these turbulence models are based on eddy viscosity, which compute the turbulence length scale and velocity scale. The eddy viscosity, μ_t, is then obtained by Equation (3.15). Turbulent thermal conductivity, k_t, is related to μ_t through turbulent Prandtl number defined by Equation (3.17), which is assumed to be unity in the present investigation. Details of these four turbulence models are given in Sections 3.5.1 to 3.5.4. In order to demonstrate the effects of turbulence, the laminar flow model is also included, which is obtained by simply setting μ_t and k_t to zero. For simplicity, arc models based on laminar flow and turbulent flow will be referred to collectively as the flow models for future reference. Therefore, altogether five flow models will be used to study the behaviour of SF_6 switching arcs. The computed RRRV will be subjected to verification by experimental results of [3.7, 3.8, 3.9] covering a wide range of discharge conditions in terms of different nozzle geometries, rate of change of current before current zero (di/dt) and stagnation pressure (P_0). Detailed information of these experiments and the measured RRRV will be given in Section 3.6.

3.5.1 The Prandtl Mixing Length Model

This is the simplest and also the oldest turbulence model which relates the turbulence length scale to the width of the jet. For turbulent nozzle arc this length scale marks the boundary of the high velocity core which is measured by the thermal radius of the arc defined by

$$r_\delta = \left(\theta_\delta / \pi\right)^{1/2} \tag{3.21}$$

where θ_δ is the thermal area of the arc given by

$$\theta_\delta = \int_0^\infty \left(1 - \frac{T_\infty}{T}\right) 2\pi r\, dr \tag{3.22}$$

where T_∞ is the temperature near the nozzle wall where the radial temperature gradient is negligible. Turbulence length scale is related to the thermal radius by

$$\lambda_c = cr_\delta \tag{3.23}$$

where *c* is a turbulence parameter the value of which is found by the best fit between model prediction and experimental results. The velocity scale is related to the turbulence length scale and the mean velocity gradient by

$$V_c = \lambda_c\left(\left|\frac{\partial w}{\partial r}\right| + \left|\frac{\partial v}{\partial z}\right|\right) \tag{3.24}$$

Eddy viscosity is given by the following expression according to Equation (3.15):

$$\mu_t = \rho\lambda_c^2\left(\left|\frac{\partial w}{\partial r}\right| + \left|\frac{\partial v}{\partial z}\right|\right) \tag{3.25}$$

3.5.2 The Standard K-Epsilon Model

This model with the recommended default values for the five turbulence parameters [3.24] is the most widely used turbulence model for engineering applications. It gives a general description of the conversion of the energy from the mean flow to chaotic turbulence for the maintenance of turbulent flow, and the dissipation of turbulence energy extracted from the mean flow. The standard k-epsilon model has two transport equations (known as the two-equation model), i.e. one for turbulent kinetic energy per unit mass, *k*, which is defined as

$$k = \frac{1}{2}\left(\overline{u_i' u_i'}\right) = \frac{1}{2}\left[\left(\overline{u_1'}\right)^2 + \left(\overline{u_2'}\right)^2 + \left(\overline{u_3'}\right)^2\right] \qquad (i = 1, 2, 3) \tag{3.26}$$

and the other for the dissipation rate, ε, which is defined as

$$\varepsilon = 2\nu\,\overline{\mathbf{s}_{ij}'\mathbf{s}_{ij}'} \tag{3.27}$$

where

$$\mathbf{s}_{ij}' = \frac{1}{2}\left(\frac{\partial u_i'}{\partial x_j} + \frac{\partial u_j'}{\partial x_i}\right) \tag{3.28}$$

The mechanisms for conversion of the energy from the mean flow to turbulence are described from the equation of *k*. The equation of ε, on the other hand, describes the dissipation of turbulence energy by viscous effects, where e represents the heat at the expense of turbulent kinetic energy which is due to the work done against the

fluctuating viscous stress in order to deform a fluid element. Detailed discussions on how turbulence energy extracted from the mean flow is dissipated by viscous effects are given in [3.22]. This model has been applied to DC nozzle arcs [3.20] and to DC plasma jets [3.30, 3.31].

The governing equations of the standard k-epsilon model are those for k and ε, which are given below:

$$\frac{\partial(\rho k)}{\partial t}+\nabla\cdot\left(\rho\mathbf{V}k-\frac{\rho\nu_t}{\sigma_k}\nabla k\right)=\rho\left(P_k-\varepsilon\right) \tag{3.29}$$

$$\frac{\partial(\rho\varepsilon)}{\partial t}+\nabla\cdot\left(\rho\vec{V}\varepsilon-\frac{\rho\nu_t}{\sigma_\varepsilon}\nabla\varepsilon\right)=\rho\frac{\varepsilon}{k}\left(C_{1e}P_k-C_{2e}\varepsilon\right) \tag{3.30}$$

where P_k represents the generation of turbulence kinetic energy due to the mean velocity gradients, which is given by

$$P_k=\nu_t\left[2\left(\frac{\partial w}{\partial z}\right)^2+2\left(\frac{\partial v}{\partial r}\right)^2+2\left(\frac{v}{r}\right)^2+\left(\frac{\partial w}{\partial r}+\frac{\partial v}{\partial z}\right)^2\right] \tag{3.31}$$

The length and velocity scale of turbulence are respectively defined as

$$\lambda_c\propto\frac{k^{1.5}}{\varepsilon} \tag{3.32}$$

$$V_c\propto\sqrt{k} \tag{3.33}$$

Eddy viscosity is thus given by the following expression according to Equation (3.15):

$$\mu_t=\rho C_\mu\frac{k^2}{\varepsilon} \tag{3.34}$$

There are altogether five model constants in the k-epsilon model equations, the value of which have been adjusted according to test results for a range of fluid flows. The recommended values of these constants are [3.24]: $\sigma_k=1.0$, $\sigma_\varepsilon=1.3$, $C_{1e}=1.44$, $C_{2e}=1.92$ and $C_\mu=0.09$.

3.5.3 The Chen-Kim K-Epsilon Model

It has been recognized that the poor prediction of the spread rate of a turbulent round

free jet by the standard k-epsilon model is due to the inadequacy of the equation for dissipation rate [3.26]. For the standard k-epsilon model a single time scale, *k/ε*, is used which is an over simplification of various time scales associated with energy transfer between eddies of different sizes [3.26]. A second time scale related to production of turbulent kinetic energy is thus introduced to reflect the energy transfer rate from large scale eddies to small scales eddies controlled by the production range time scale to the dissipation range time scale, P_k/ε [3.26]. The additional source term

$$S_\varepsilon = \frac{\rho C_{3e} P_k^2}{k} \tag{3.35}$$

is added to Equation 3.66, which allows the dissipation rate equation to respond to the mean strain rate more efficiently especially in the region where the main strain rate changes rapidly. Such a situation exists inside a supersonic nozzle. Because of the success of the Chen-Kim k-epsilon model in the prediction of the spread rate of a turbulent round jet which has similarities to an arc burning in a supersonic flow, we apply this model to the DC nozzle arc.

The constant, $C_{3e,}$ and the other constants in the standard k-epsilon model are readjusted to achieve best agreement between prediction and experimental results covering a wide range of flow conditions [3.26]. The recommended values for these constants are [3.26]: $\sigma_k = 0.75$, $\sigma_\varepsilon = 1.15$, $C_{1e} = 1.15$, $C_{2e} = 1.90$ $C_{3e} = 0.25$, and $C_\mu = 0.09$.

3.5.4 The RNG K-Epsilon Model

The RNG k-epsilon model is derived from the instantaneous Navier-Stokes equation using a mathematical approach called the renormalization group [3.25]. The effects of the small scale turbulence are represented by means of a random forcing function in the Navier-Stokes equation. The RNG procedure systemically removes the small scale eddies from the governing equations by expressing their effects in terms of

large scale eddies through the modified viscosity (i.e. ν_t in Equations (3.29) and (3.30) is replaced by the effective viscosity $\nu_{eff} = \nu_l + \nu_t$ where ν_l is the molecular viscosity). In addition, the epsilon equation contains a strain-dependent correction term which is given by

$$S_\varepsilon = -\frac{\rho C_\mu \eta^3 (1-\eta/\eta_0)}{1+\beta\eta^3}\frac{\varepsilon^2}{k} \tag{3.36}$$

where $\eta = (k/\varepsilon)\cdot\sqrt{(\rho P_k/\mu_t)}$, $\eta_0 = 4.38$ and $\beta = 0.012$. The other model constants are [3.25]: $\sigma_k = \sigma_\varepsilon = 0.7194$, $C_{1e} = 1.42$, $C_{2e} = 1.68$ and $C_\mu = 0.0845$. In contrast to the standard k-epsilon model only the constant β is adjustable to ensure the best fit with experimental results. The recommended value for β is 0.012. All other constants are explicitly computed as part of RNG process.

The RNG k-epsilon model has been successful in the prediction of plasma jet for arc cutting processes [3.30] and that for a spray system [3.31]. It is also claimed successful in predicting the gas mixing in the expansion volume of a circuit breaker [3.32]. We therefore include this model in our current investigation.

3.6 Experimental Results Used for Verification of Turbulence Models

Of the very limited experimental results available for direct comparison with theoretical predictions, Frind et al. [3.7], Benenson et al. [3.8] and Frind and Rich [3.9] have reported extensive test results in the form of RRRV for a supersonic nozzle interrupter with fixed upstream (meaning stagnation pressure P_0) and downstream (meaning static pressure at the nozzle exit P_e) pressures.

The experimental conditions of [3.7, 3.8, 3.9] are designed to simulate the current zero period of a two-pressure circuit breaker using a current ramp consisting of a current plateau (DC level) and a linearly decaying current (specified by di/dt) before current zero and a voltage ramp (specified by dV/dt) after current zero. In the experiments, nozzle ablation is avoided by using current levels always below an upper limit of the current with which the arc's thermal radius is equal to the nozzle

radius (known as the thermal blocking current) [3.7]. The experiments are based on a two-pressure nozzle-electrode configuration as shown in Figure 3.2. Such a two-pressure system eliminates pressure transients caused by wave reflections within a circuit breaker which inevitably affects the arc in the nozzle interrupter. For such a two-pressure system without nozzle ablation we can divide the whole arcing process into a quasi-steady period and a current zero period. The arc behaviour and its thermal interruption capability are investigated by using a current ramp before current zero and a voltage ramp after current zero. Such an approach assumes that peak current does not have effects on arc behaviour during current zero period. This is to assume that the arc at the start of current zero period does not have memory of its previous arcing history. Before current zero period, the arc is in quasi-steady period. Mathematically, an arc will remember its past if the time dependent terms in conservation equations can no long be neglected. When this happens it is considered that the arc is no longer in quasi-steady state. The choice of the plateau of the current ramp is to ensure that the arc at this current does not have memory.

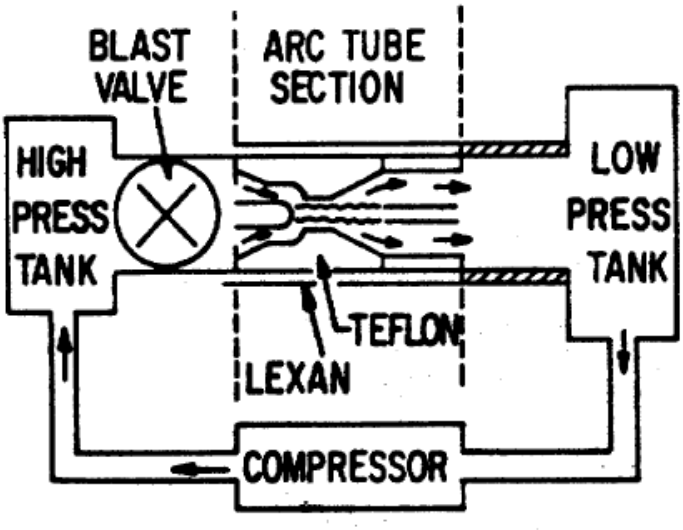

Figure 3.2. Schematic diagram of GE test system used in the experiments of [3.7, 3.8, 3.9]. Stagnation pressure and exit pressures are fixed during arcing.

The assumption of the current zero period being independent of peak arcing current and the absence of pressure transients from other part of a breaker are no longer valid in modern high voltage circuit breakers, e.g. self-blast circuit breakers.

For such breakers, the flow conditions at current zero depend on the whole arcing history. However, the physical processes responsible for arc quenching during current zero period in such breakers are the same as those studied in the experiments of [3.7, 3.8, 3.9]. More importantly, the objective of our investigation is to test the relative merits and applicability of commonly used turbulence models when they are applied to switching arcs. Such tests must be based on the verification of turbulence models by experimental results. It should be noted that all these turbulence models were originally devised for simple flows having a dominant direction of fluid (or gas) motion. Verification on the suitability of turbulence models for switching applications therefore must be based on experimental results obtained under simple flow conditions. To date, the experiments reported in [3.7, 3.8, 3.9] provide the most reliable test data under well defined test conditions. This is the reason why we have chosen to simulate these experimental conditions.

Altogether, arcs in three nozzles, i.e. the nozzle of Frind et al. [3.7], the nozzle of Benneson et al [3.8] and the nozzle of Frind of Rich [3.9], respectively referred to as Nozzle 1, Nozzle 2 and Nozzle 3 hereafter, will be computationally studied in the present investigation. These three nozzles are shown in Figure 3.3, which have different shapes and dimensions as well as electrode configurations. In Figure 3.3, Z=0 indicates the axial position of the nozzle throat. These nozzles have the same expansion half angle (15°) but differ in upstream and throat regions. The throat diameter of Nozzle 2 (12.7 mm) is twice that of Nozzle 1 (6.35 mm). Nozzle 3 is almost the same as Nozzle 2 except that the area variation of Nozzle 3 is continuous.

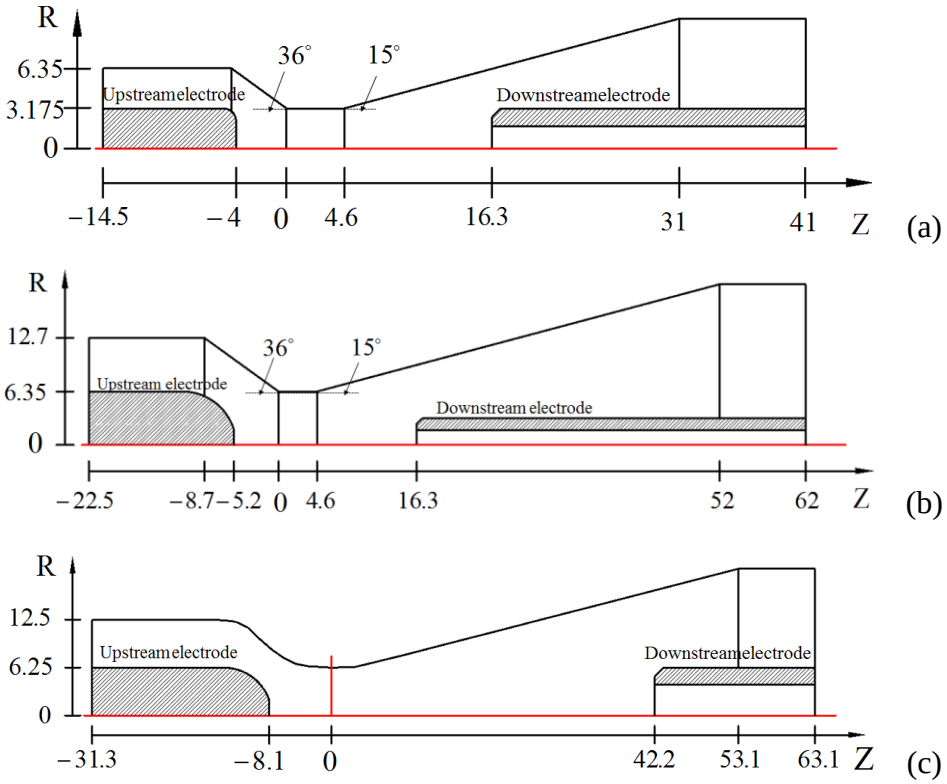

Figure 3.3. Three nozzle geometries used in the experiments of [3.7, 3.8, 3.9]. Unit of dimensions: mm. (a) Nozzle of Frind et al. [3.7] (Nozzle 1), (b) Nozzle of Benenson et al. [3.8] (Nozzle 2) and (c) Nozzle of Frind and Rich [3.9] (Nozzle 3).

The measured RRRV as a function of stagnation pressure (with P_0 ranging from 7.8 atm to 37.5 atm) for the three nozzles are plotted in Figures 3.4(a) and 3.4(b), respectively, for two rates of current decay, di/dt=13 $A\mu s^{-1}$ (13.5 $A\mu s^{-1}$ for Nozzle 3) and 25 $A\mu s^{-1}$ (27 $A\mu s^{-1}$ for Nozzle 3). For Nozzles 1 and 2, the static pressure at the nozzle exit (P_e) is near vacuum in the experiments of [3.7, 3.8] to ensure shock free inside the nozzle. However, for Nozzle 3, P_e is $P_0/4$ in the experiments of [3.9], for which the ratio of the nozzle exit pressure to the nozzle upstream stagnation pressure (P_e/P_0) is consistent with that normally encountered in a real circuit breaker [3.9]. A shock can occur inside the nozzle interrupter with such pressure ratio [3.33], which will be shown later by the computational results in Chapters 6 and 7.

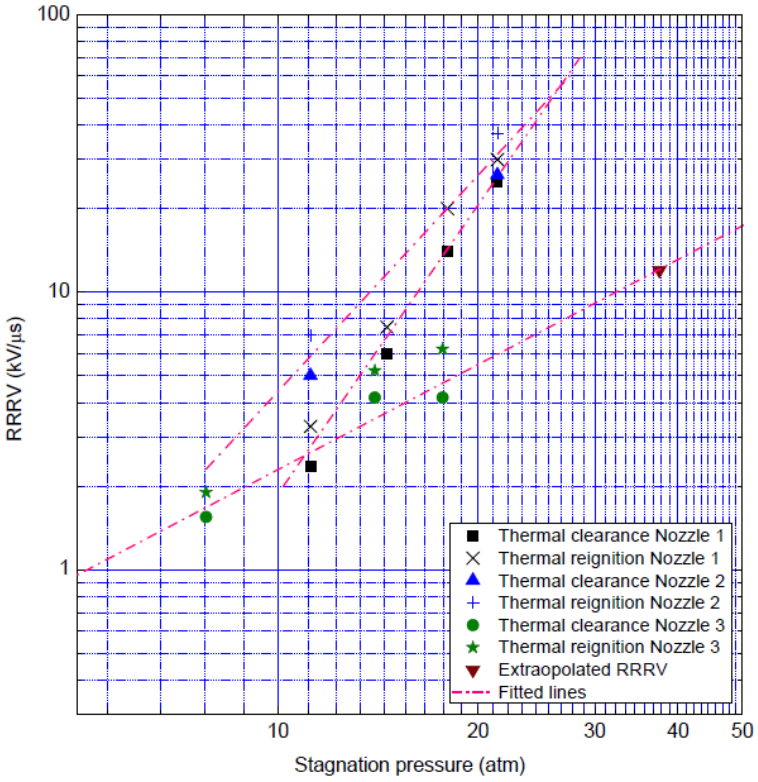

(a)

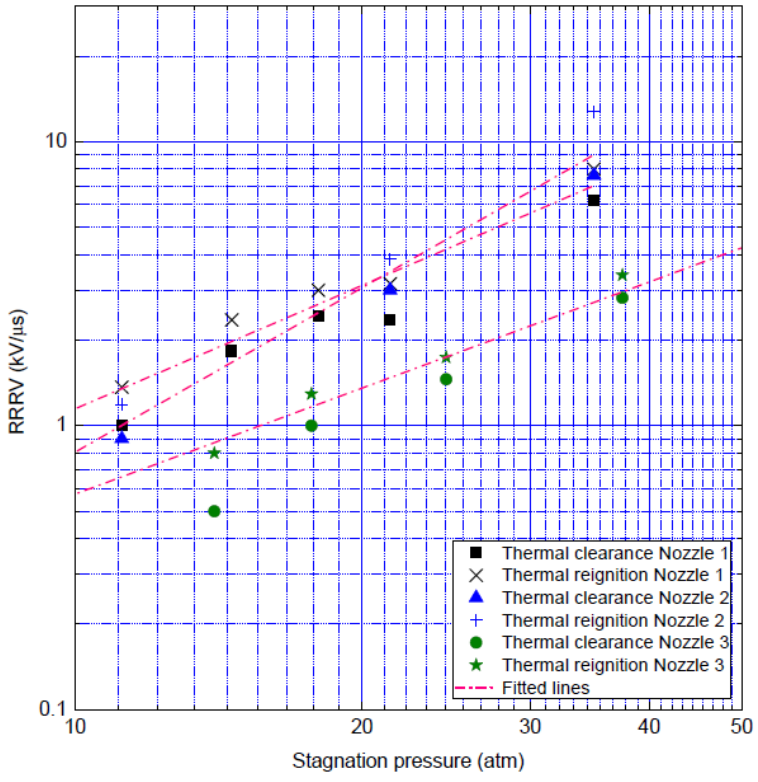

(b)

Figure 3.4. Measured RRRV of an SF_6 switching arc for three nozzles given in Figure 3.3. (a) di/dt=13 Aμs^{-1} for Nozzles 1 and 2, and di/dt=13.5 Aμs^{-1} for Nozzle 3 and (b) di/dt=25 Aμs^{-1} for Nozzles 1 and 2, and di/dt=27 Aμs^{-1} for Nozzle 3.

The scatters of the measurements are not mentioned in [3.7, .3.8, 3.9]. We therefore evaluate the experimental scatter for the measured RRRV (in terms of percentage difference) at a particular set of discharge conditions by using the following relation:

$$\text{Experimental scatter} = \frac{\left|\text{RRRV}_{\text{ignite}} - \text{RRRV}_{\text{clear}}\right|}{\left(\text{RRRV}_{\text{clear}} + \text{RRRV}_{\text{ignite}}\right)/2} \tag{3.37}$$

where $\text{RRRV}_{\text{clear}}$ is the measured RRRV for thermal clearance as shown in Figure 3.4, and $\text{RRRV}_{\text{reignite}}$ is the that for thermal reignition in Figure 3.4. After obtaining the experimental scatters for individual measurements using the above relation, we can then evaluate the average experimental scatter of the measured RRRV for the range of discharge conditions as shown in Figure 3.4, which is found to be around 40%

The computational results in subsequent four chapters, unless otherwise specified, are obtained under discharge conditions identical with the experiments of [3.7, 3.8, 3.9]. The applicability of turbulence models for prediction of switching arc behaviour will be verified by comparing the computed RRRV with corresponding experimental results given in Figure 3.4.

3.7 Implementation of the Arc Model in PHOENICS

This section is concerned with the implementation of the arc model in PHOENICS, a general purpose CFD software package supplied by CHAM [3.12]. In PHOENICS, the flow governing equations are discretized based on finite volume method [3.10, 3.11] which results in a set of algebraic equations, and solved by SIMPLE algorithm, a solution methodology first developed by Patankar and Spalding [3.10]. PHOENICS has been used in Liverpool for nearly 20 years and its capability and accuracy of solution have been rigorously verified [3.34]. Although it is not very user friendly, it does have user interfaces which allow relatively much easier implementation of the arc model as compared with other general purpose CFD packages. We therefore choose PHOENICS Version 3.6.1 (hereafter referred to as PHOENICS for convenience) to implement the arc model.

3.7.1 Structure of PHOENICS

The application of PHOENICS to simulate the behaviour of switching arcs requires the users to implement the arc model through commands and data files and a PHOENICS provided user-interface subroutine written in FORTRAN. Figure 3.5 shows a flow chart describing the procedure of performing computer simulations using PHOENICS. The role of each component as shown in Figure 3.5 and how they interact with each other to execute the simulation have been described in detail in [3.34, 3.35], which are not repeated here. The user-interfaces of PHOENICS are provided mainly through three files, i.e. the Q1 and Ground files and any other user date files (those marked as blue rectangles in Figure 3.5), which allows the user to set up a problem, to insert necessary user defined subroutines and to input other necessary data for a computer simulation task. Implementation of the arc model into PHOENICS is done mainly through these three files, the details of which are given below.

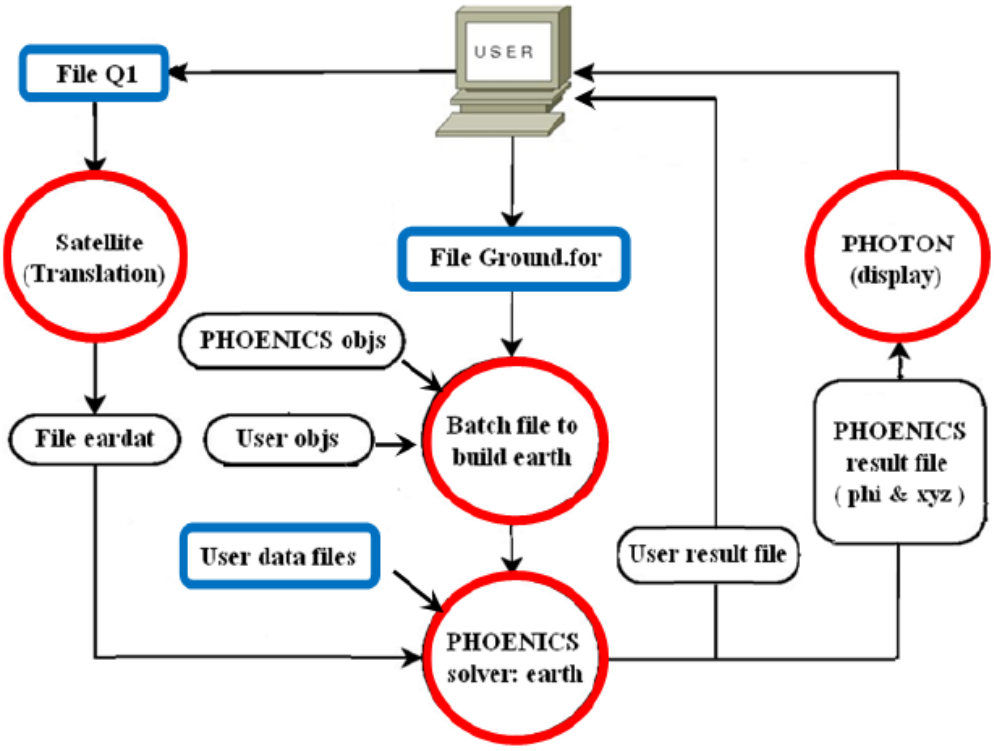

Figure 3.5. Diagram showing information flow in computer simulation of switching arcs based on PHOENICS. Blue rectangles -- files to be prepared by user; Red circles -- Executables to be run during the simulation.

3.7.2 Setting up a Problem in PHOENICS: the Q1 File

The specification of a problem to be computationally investigated using PHOENICS can be written into the Q1 file, which includes all the necessary information required to simulate a flow. The language used to write the Q1 file is known as PHOENICS Input Language (PIL) [3.35] which is similar in some respects to FORTRAN. The information required in the Q1 file to simulate a switching arc is given below:

A Transience and Time Step Specification

In this part, the user needs to define first the nature of the computational problem, i.e. time dependent (transient) or steady state. This is flagged by setting the logical parameter STEADY [3.35]. When performing a transient simulation (STEADY=F), the total time of the simulation and the number of time steps need to be specified which determine the time intervals (time step sizes). This is done by using the PIL command, GRDPWR [3.35]. Otherwise (STEADY=T, meaning a steady state simulation), the time steps need not be specified. In the present investigation, for different stages of the simulation, detailed information on the total computational time and the time step sizes is given in Section 3.7.7.

B The Computational Domain and Grid System

In this part, the user needs to specify

(a) What type of grid system will be used in the simulation, i.e. Cartesian or Cylindrical Polar or Body Fitted Coordinate (BFC) [3.35]? For the present investigation, due to the complexity of the geometry of the computational domain, the grid type of BFC is chosen (by setting BFC = T). BFC is a structured grid system and it is advantageous than the Cartesian and/or Cylindrical Polar grid system in that the curved shape of some components, such as the nozzle and electrodes, can be accurately represented in the grid system.

(b) Definition of the coordinates of important points in the domain and the lines through these coordinates which form the shapes of the computational domain

and the solid parts, and patterns of grid distribution. The coordinates and lines can be specified using the PIL command, GSET, the details of which are given in [3.35].

(c) Definition of frames and how these frames are matched to form the complete grid system in one plane. Frames are also specified using GSET [3.35].

C The Governing Equations to be Solved by PHOENICS Solver

In this part, the user needs to specify the governing equations to be solved by PHOENICS solver, i.e. the EARTH as shown in Figure 3.5. Details are given below:

(a) What governing equations need to be solved by the EARTH? In the present investigation, the equations need to be specified here are the conservation equations for switching arcs given by Equation (3.19). The variables obtained by solving the corresponding governing equations are known as the solved-for variables [3.35] in PHOENICS. The PIL command, SOLVE [3.35], is used to specify equations required. In the present work, the solved-for variables are pressure (P1), radial velocity (V1), axial velocity (W1) and enthalpy (H1). The variables required in a computer simulation task other than the solved-for variables are referred to as stored variables [3.35]. Both the solved-for and stored variables can be stored and written into result files produced by PHOENICS (e.g. a PHI file [3.35]) after one simulation.

(b) What terms will be included in each governing equation to be solved? All the conservation equations given in Section 3.4 are in the form of the Partial Differential Equation (PDE) including the time dependent term, the convection term, the diffusion term and the source term (Equation (3.19)). It should be noted that, in certain cases, not all these terms are necessary. For example, for solution of heat conduction problems, the corresponding governing equation (energy equation) does not have convection term, which can then excluded using the PIL command, TERM [3.35]. For solution of switching arcs involving gas flow fields, on the other hand, convection term is always required which can be included using the same command.

(c) Which solution method will be used for each PDE? There are mainly two solution methods in PHOENICS, i.e. the point-by-point method and the whole field method [3.35]. Appropriate selection of solution methods for a particular governing equation can promote convergence. The solution method can be set up using the PIL command, SOLUTN [3.35].

(d) What method will be used to interpolate the material properties (i.e. diffusion coefficients Γ_ϕ in Table 3.2) at the faces of each grid (i.e. cell face [3.35])? There are mainly two methods provided by PHOENICS, i.e. arithmetic averaging and harmonic averaging [3.35]. In the present investigation, harmonic averaging is always selected to calculate material properties at the solid-gas interfaces due to vast difference in the values of relevant material properties for solids and gas. This can also be done using SOLUTN [3.35].

(e) How are the thermodynamic and transport properties and the equation of state provided to the EARTH? In the present investigation, the tabulated data for all these properties given in [3.16] are provided through user defined subroutines in Ground file, and thus relevant PIL commands are required in the Q1 file (the details are given in Section 3.7.3) which allow access of those subroutines for material properties.

D Implementation of Turbulence Models

For the turbulence models used in the present investigation which belong to the category of effective eddy viscosity, the user needs to give definition on the turbulence length scale (denoted as EL1 [3.35] in PHOENICS) and the kinematic eddy viscosity defined as $\nu_t = \mu_t / \rho$ (denoted as ENUT [3.35] in PHOENICS). These two variables can either be assigned constant values or given expression to calculate. The latter can be done by using the PHOENICS supplied subroutines (refer to the explanation of ENUT in [3.35]). Otherwise, user defined subroutines inserted in Ground file can be used to calculate EL1 and ENUT, by inserting the PIL commands, EL1=GRND and ENUT=GRND, which flag the EARTH to find relevant

subroutines in Ground file.

In the present investigation, for the Prandtl mixing length model, EL1 and ENUT are calculated using our own subroutines the implementation of which is described in Section 3.7.3. For the standard k-epsilon model and its two variants, PHOENICS supplied subroutines are used to calculate EL1 and ENUT, using the following PIL commands:

Standard k-epsilon model: TURMOD(KEMODL) [3.35]

Chen-Kim model: TURMOD(KECHEN) [3.35]

RNG model: TURMOD(KERNG) [3.35]

The above commands activate the PIL command, SOLVE, to solve the relevant governing equations for k-epsilon model (Equations (3.29) and (3.30)). The values of two more solved-for variables, i.e. turbulent kinetic energy (KE) and dissipation rate (EP) [3.35], are obtained and stored. EL1 and ENUT are then calculated by relevant PHOENICS supplied subroutines defining relations given by Equations (3.32) and (3.34).

E Initial Values of Solved-for and Stored Variables

Numerical solution of the PDEs (the arc conservation equations and governing equations for turbulence models in the present investigation) requires the initial conditions. A detailed discussion on the initial conditions, i.e. what they are and what initial conditions are used in the present investigation, is given in Section 3.7.6. In Q1 file, the initial values of a variable can be specified using the PIL command, FIINIT (variable) [3.35], which can give a uniform initial value to a particular variable for the whole computational domain.

However, if different initial values are required for a particular variable in different regions of the computational domain, the user can then initialize the whole domain grid by grid using special data file which are read by relevant subroutines in Ground file. In order to instruct the EARTH to do this, relevant PIL commands are required in Q1 file, with the command, PATCH [3.35], to define the region to be initialized and the command, INIT [3.35], to do initialization using subroutines in

Ground file.

F User Used for Arcing Conditions and Control Parameters

Parameters to be used either by the turbulence model or passed into the Earth for use in the solution procedure are specified in this part. In the present investigation, for SF_6, the parameters required are given in Table 3.3.

Table 3.3. User used for arcing conditions and control parameters for SF_6 gas used in the present investigation.

Parameter	Value
Reference pressure (Pa)	0.0
Specific heat ratio γ	1.085
Gas constant R ($Jkg^{-1}K^{-1}$)	56.0
Specific heat at constant pressure c_p ($Jkg^{-1}K^{-1}$)	575.0
Stagnation pressure P_0 (Pa)	Variable
Exit static pressure P_e (Pa)	Variable
Stagnation temperature T_0 (K)	300
Stagnation density (kgm^{-3})	$P_0/R/T_0$
Stagnation enthalpy (Jkg^{-1})	c_p*T_0
Multiplication factor for NEC	2.50
Percentage of radioactive energy from the arc core to be absorbed in the radiation reabsorption layer [3.15]	0.80
Turbulence parameter for the Prandtl mixing length model c	Variable

G Definition of Solid Objects in the Domain

In the computational domain, the user needs to specify the solid objects, e.g. the nozzle and the electrodes, as well as the area in the domain which allows the gas to flow. This is done by assigning a variable for the material property index, PRPS

[3.35], a value corresponding to particular types of material, i.e. solid conductor, solid insulator or gas. In the present work, the nozzle is made of PTFE material which is non-conductive, while the electrodes are made of copper which is conductive, then relevant material property indices are assigned [3.34, 3.35, 3.36].

H Special Source Terms

In this part, the user needs to specify source terms other than the PHOENICS default source terms for each governing equation. In the present investigation, for switching arcs, these special source terms include Ohmic heating and radiation for the energy equation (Table. 3.2). These user defined source terms are specified by inserting relevant subroutines in Group 13 of the Ground file. In the Q1 file, relevant PIL command, COVAL [3.35], are required to allow the EARTH to access of these subroutines.

I Boundary Conditions

Numerical solution of the descretized governing equations requires boundary conditions. Boundary conditions indicate how a system confined in a computational domain interacts with the environment. In the present investigation, for each of the governing equations to be solved, relevant boundary conditions need to be specified at the nozzle inlet, the nozzle exit, the symmetrical axis and the solid surfaces. A detailed discussion will be given in Section 3.7.5 as regards what boundary conditions are used for the present investigation.

J Parameters for Solution Control

In PHOENICS, the solution algorithm proceeds slab by slab, where a slab means a layer of grids perpendicular to the axial position as shown in Figure 3.6. At each of these slabs, and for each grid, the algebraic equation for each solved for variable which is obtained by the discretization of the corresponding PDE, is iteratively solved until convergence [3.35] is attained. Therefore, the user needs to specify the number of iterations (known as sweep number in PHOENICS the details of which

are given in the explanation of sweeps in [3.35]) which is sufficient to ensure convergence: for steady state simulation, one only needs to specify a sweep number for the simulation, while for transient simulations, each time step of the simulation requires a number of sweeps and the required sweep numbers may be different for different time steps. Details on the sweep numbers used in computer simulations of the present investigation are given in Section 3.7.7.

Convergence control is an important issue in computer simulation to ensure the results are true solutions of the computational problem. One of the mechanisms to avoid divergence of the iterative processes is to specify maximum and minimum values for each solved for variable, using the PIL commands, VARMIN [3.35] and VARMAX [3.35]. They are used to prevent overshooting of variables during the iteration. However, this method does not automatically lead to convergence. In the present investigation, the maximum and minimum values specified for each solved for variable are given below:

VARMIN(P1) =1000.0; VARMAX(P1) =100.0E5

VARMIN(W1) =-2.0E4; VARMAX(W1) =2.0E4

VARMIN(V1) =-2.0E4; VARMAX(V1) =2.0E4

VARMIN(KE) =1.0E-7; VARMAX(KE) =1.0E10

VARMIN(EP) =1.0E-5; VARMAX(EP) =1.0E12

Relaxation is another mechanism to maintain the smoothness of the iterative process and to achieve convergence. It slows down the changes made to the values of the variables during the solution procedure. There are two types of relaxation method. The first method is linear relaxation [3.35], by which the intermediated value of a solved for variable from the value of the previous iteration is determined by a relaxation coefficient, α. Following recommendations from PHOENICS, linear relaxation is used for pressure equation. This variable is solved by whole field solver because a local change will affect the whole field of the variable. Linear relaxation is activated using the PIL command, RELAX [3.35], e.g. for P1 it gives RELAX (P1, LINRLX, α), where LINRLX [3.35] flags the activation of linear relaxation mode.

The other relaxation method is the false-time step relaxation [3.35]. The concept

of false-time-step is based on the fact that during a round of iteration the value of a variable changes from its starting value to its finishing value through a series of intermediate values. The false time step, Δt_f, is implemented by adding to the algebraic equation a source term, which assimilates an imaginary transient case where each time step (known as false-time-step) corresponds to an intermediate value during the iteration process [3.34, 3.35, 3.36]. False-time-step relaxation is activated also using RELAX, e.g. for W1 it gives RELAX (W1, FALSDT, Δt_f), where FALSDT [3.35] flags the activation of false-time-step relaxation mode. For simulation of switching arcs in the present investigation, choices of false-time-step for corresponding governing equations are discussed in Section 3.7.8.

K Restart Options

In some cases, it is necessary to continue the simulation from the states in a previous time step. It can be done by using the PIL command, RESTRT [3.35], which instructs the EARTH to read the results of the specified variables from the PHOENICS solved result file (e.g. PHI file [3.35]) of a previous time step and use them as initial conditions to continue the computer simulation.

3.7.3 The Implementation of User Defined Subroutines: the Ground File

The Ground file provides interfaces for users to insert their own subroutines necessary for their computer simulations using PHOENICS. EARTH will make calls to specific sections in Ground file when corresponding instructions are given in Q1 file. For implementation of the arc model used in the present investigation, a brief description of the subroutines required is given in this section. The description is based on the main structure of the Ground file given below:

Group 1:

(a) Declaration of user defined variables or arrays to be used in Ground file.

(b) Subroutines used to read user data files (described in Section 3.7.4) immediately after the start of the execution of the EARTH programme "earexe.exe". The data

files include that for basic radiation data (NEC) and those providing initial conditions of the solved for variables for both the cold flow simulation and simulation with and arc.

Group 9:

(a) A subroutine used to calculate the gas temperature based on tabulated data of enthalpy-temperature relation given in [3.16]. This subroutine must be inserted in Section 10 of Group 9. It is used when the equation of enthalpy is solved for energy conservation and the PIL command, TMP1=GRND [3.35], is given in Q1 file to instruct the EARTH to look for user defined code for temperature calculation.

(b) When the Prandtl mixing length model is used in the computer simulation, the model is implemented by user defined subroutines which calculate the turbulence length scale and the eddy viscosity. Therefore, two subroutines are required which are given below

- A subroutine used to calculate turbulence length scale, which must be inserted in Section 12 of Group 9. The PIL command, EL1=GRND, is given in Q1 file to instruct Earth to look for this subroutine.
- A subroutine used to calculate eddy viscosity, which must be inserted in Section 12 of Group 9. The PIL command, ENUT=GRND, is given in Q1 file to instruct Earth to look for this subroutine.

(c) A subroutine which gives the equation of state based on the tabulated data in [3.16], which calculates the gas density from gas temperature and pressure. For SF_6, the equation of state for ideal gas is valid for temperature below 1000 K. Therefore, ideal gas law is used to calculate gas density when T <1000 K. The subroutine must be inserted in Section 10 of Group 9. In Q1 file, the PIL command, RHO1=GRND [3.35], is inserted to instruct the EARTH to look for user defined code for density calculation.

(d) Calculation of laminar Prandtl number, PRNDTL [3.35], for equations other than velocity (W1, V1) and mass conservation equation, i.e. Prandtl number for equation of enthalpy (H1). The code must be inserted in Section 7 of Group 9. In

Q1 file, the PIL command, PRNDTL (H1)=GRND [3.35], is inserted to instruct the EARTH to look for user defined code.

(e) A subroutine calculating the molecular kinematic viscosity based in the tabulated data given in [3.16]. The subroutine must be inserted in Section 12 of Group 9.The PIL command, ENUL=GRND [3.35], is given in Q1 file to instruct Earth to look for this subroutine.

Group 11:

This part is for initialization of the field values of PHOENICS solved-for variables. This provides a user interface to set initial values grid by grid which otherwise cannot be done in Q1 file. A subroutine is inserted here which uses data read in Group 1 of Ground file to do grid by grid initialization of solve-for variables. Relevant PIL commands are required in Q1 file to instruct the EARTH to find this subroutine, as previously in Point E of Section 3.7.2.

Group 13:

Subroutines used for implementation of the boundary conditions and special source terms (i.e. Ohmic heating and radiation). The subroutines here will be used when relevant COVAL [3.35] commands are given in the Q1 file to instruct the EARTH to access them for user defined boundary conditions and source terms [3.35].

Group 19:

(a) SECTION 1 ---- Start of time step. This is a user interface to make specific settings before the solution of the next time step is started. For the present investigation, a subroutine, which is used to calculate instantaneous current, is inserted in this section. A user data file is required by this subroutine which gives the current waveform, i.e. the instantaneous current as a function of time (Point c of Section 3.7.4).

(b) SECTION 2 ---- Start of sweep. Iteration of the solution consists of sweeps in the z-direction which is normally the axial direction of gas flow. Users can update certain settings before starting the next sweep. For example,

- The width and corner coordinates of all cells are needed in the simulation and these parameters can only be obtained in this section after the simulation

starts. They cannot be calculated in Section 1 of this group.

- There are other quantities that need to be updated on a sweep basis. For example, the electric conductivity of the arcing gas (σ) needs to be updated based on the temperature and pressure results from the sweep that is just finished, in preparation for the next sweep. The same applies to the value of the molecular diffusion coefficient of enthalpy equation (k_l/c_p) which is used in the enthalpy equation. The reason that both σ and k_l/c_p need to be updated in this section is that the statements in Group 9 only pass the existing values of these two variables to the solver without performing any updating.

(c) SECTION 3 ---- Start of IZ slab. Sometimes a user may wish to update the values of a variable in a single slab before solution on that slab is performed. For example the velocity in a slab may have experienced substantial change during a sweep when iteration is performed from Slab 1 to this slab. To improve the convergence of the iteration, the Mach number of the flow may need to be updated. This can be done here.

(d) SECTION 7 ---- Finish of sweep. This section provides a user with an access point to check or record the results from a sweep by writing to relevant data files. Subroutines for calculation of the energy balance, which are always assessed in Chapters 4 to 7, are also inserted in this section. The energy balance calculations are performed using equations given in Table 4.1 of Chapter 4, Table 5.1 of Chapter 5 and the caption of Figure 7.9 of Chapter 7.

(e) SECTION 8 ---- Finish of time step. In a transient case some parameters, such as the arc voltage, need to be written into a data file at the end of each time step or every N steps. This is normally done in this section.

3.7.4 Other User Data Files

For the present investigation, the user data files which need to be prepared include the following:

(a) A data file providing the data of NEC as a function of temperature and radiation

radius which are given in [3.19]: this is read by the corresponding subroutine in Group 1 of Ground file.

(b) A data file used for gird by grid initialization of solve-for variables for the cold flow simulation (details to be given in Section 3.7.6): this is read by the corresponding subroutine in Group 1 of Ground file, and the initialization is done by the corresponding subroutine in Group 11 of Ground file.

(c) A data file providing the current waveform: this is read by the corresponding subroutine in Section 1 of Group 19 in Ground file.

3.7.5 Boundary Conditions

The governing equations for the arc model need to be supplemented by necessary boundary conditions before they can be solved. In the present investigation, for the nozzles shown in Figure 3.3, the required boundary conditions are given below:

(a) On the nozzle axis, axisymmetric boundary conditions are applied. Thus, all radial derivatives of the dependent variables are set to zero except for the radial velocity which is zero on the axis.

(b) At the nozzle inlet, the axial velocity and density are iteratively computed according to the calculated inlet static pressure by assuming that the gas entering the nozzle undergoes an isentropic process [3.20, 3.37] from a reservoir with stagnation pressure P_0 and stagnation temperature T_0 (300 K).

(c) At the nozzle exit, the static pressure P_e is given. For Nozzles 1 and 2, P_e is set to a very low value to guarantee shock free inside the nozzle in the absence of downstream electrode. This is consistent with the test conditions of [3.7, 3.8]. The axial gradients of enthalpy and velocity are set to zero [3.20]. Diffusion of momentum and energy at the exit is considered to be very small in comparison with convection and is thus neglected [3.20]. Such boundary conditions are suitable when no flow is sucked into the nozzle at the nozzle exit (this is always the case for Nozzles 1 and 2), since the thermodynamic state of the gas flowing out of the nozzle exit is always determined by the gas from inside the nozzle the thermodynamic state of which is obtained during computations. However, if

there is flow sucked into the nozzle from outside of the nozzle exit (e.g. in case of Nozzle 3 with a high P_e applied at the nozzle exit [3.9] which results in a shock inside the nozzle), the thermodynamic state of the gas sucked in is usually not known, which should be correctly specified. A detailed discussion on this will be given in Chapter 7 which reports the investigation of the SF_6 nozzle arc behaviour under shock conditions for Nozzle 3.

(d) At solid surfaces, non-slip boundary condition for velocity is applied through a built-in wall function of PHOENICS [3.37]. These surfaces are assumed to be adiabatic, for which the heat flux is set to zero.

(e) When applying the standard k-epsilon model and its two variants, relevant boundary conditions need to be specified. The turbulent kinetic energy and dissipation rate at the nozzle inlet are given by [10, 11]

$$k_{in} = \frac{3}{2}(w_{in} I)^2 \tag{3.38}$$

$$\varepsilon_{in} = C_\mu^{3/4} \frac{k_{in}^{3/2}}{\ell} \tag{3,39}$$

where w_{in} is the nozzle inlet velocity, I the turbulent intensity set at 5% as recommended by [3.38] and $\ell = 0.07L$. L is the characteristic length of the equipment [3.11, 3.38] given by ($d_{inlet} - d_{electrode}$) where d_{inlet} is the diameter of the nozzle inlet and $d_{electrode}$ the electrode diameter. At the nozzle exit, the axial gradients of k and ε are set to zero.

The arc rooting mechanisms at the upstream and downstream electrodes are not considered. The heat flux into the two electrodes is assumed zero. This ensures that the temperature in front of the upstream electrode is sufficiently high to conduct current. The use of simplified Ohm's law in front of the hollow electrode is equivalent to locating a transparent electrode to collect the current as first suggested by Yan et al. [3.39]. Arc voltage is dominated by arc column and is not sensitive to the boundary conditions assumed at the upstream electrode [3.15].

Detailed descriptions as regards relevant algorisms used by PHOENICS to implement these boundary conditions are given in [3.34, 3.37].

3.7.6 Initial Conditions

For numerical solutions of the governing equations for switching arcs, it is necessary to specify the initial conditions. Initial conditions define the state of the system at the beginning of the process. For a problem which is steady state in nature, the initial conditions are just a first guess of the final solution which should always be independent of the initial guess. However, a good initial guess can accelerate convergence and reduce the computational time, while a bad initial guess may result in divergence of the solutions or converged but physically unrealistic solutions. For a problem which is transient in nature, the initial conditions usually describe the states of the system at the beginning of the process when the time t = 0.

Computational results presented in this thesis include those from computer simulation of the gas flow behviour in the nozzle without an arc (referred to as cold flow hereafter) and that with an arc in the nozzle. The cold flow simulation is steady state in nature. For the purpose of promoting convergence, we aim to find a very good initial condition. It is well known that the one-dimensional isentropic flow theory (referred to as 1D theory hereafter) can accurately predict the behaviour of a gas flow in steady state within a sufficiently gentle supersonic nozzle [3.33]. In the present investigation, for each of the nozzles given in Figure 3.3, the solution of the nozzle flow obtained by 1D theory is used as initial conditions to start cold flow simulations, which results in very quick convergence of the numerical solution. The 1D theory gives variations of pressure (P1) and axial velocity (W1) with axial position inside the nozzle (an example is given in Figure 3.6), while assuming P1 and W1 are uniform in the radial direction at a given axial position. For the other solved-for variables, we let the radial velocity V1 = 0 and the enthalpy H1 = 1.73×10^5 J kg^{-1} (corresponding to the room temperature, 300 K) in the whole computational domain before the simulation.

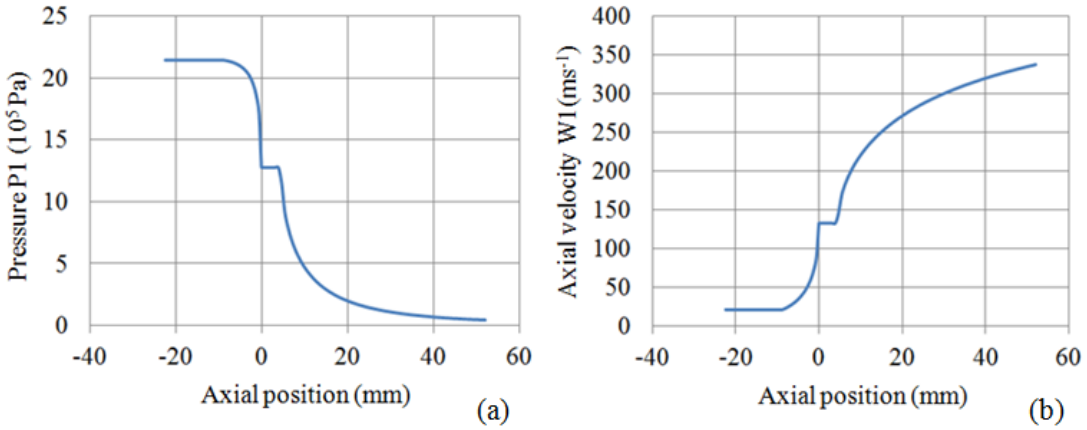

Figure 3.6. Variations of pressure (P1) and axial velocity (W1) with axial position inside Nozzle 2 (Figure 3.3) derived from 1D theory. P_0=21.4 atm. These are used as initial conditions for P1 and W1 in cold flow simulations.

The simulation with an arc in the nozzle generally forms two parts. The first part is for the solution of the nozzle arc at a DC level, e.g. 1 kA DC, which is steady state in nature. For such steady state simulation, we use the numerical solutions from the cold flow simulation as initial conditions for gas pressure (P1) and velocities (V1 and W1) inside the nozzle, and enthalpy (H1) for regions outside the arc. To initiate an arc between two electrodes, we arbitrarily define an initial high temperature arc column between two contacts (Figure 3.7). The arc column is assumed to have the same arc radius (2 mm) and a uniform radial enthalpy (H1) distribution (Figure 3.7(b)) along the axial direction between two contacts.

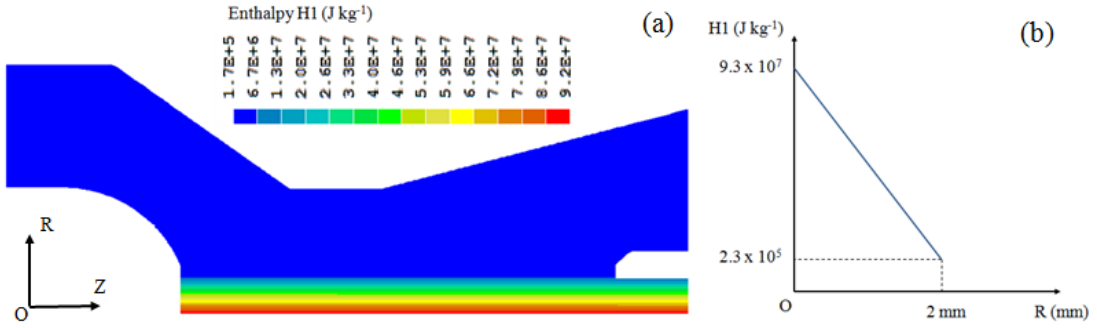

Figure 3.7. Diagram showing the initial arc column between two contacts. (a) Enthalpy (H1) contour inside Nozzle 2 showing the initial arc column which are used as initial conditions for H1 in simulations with DC arcs, and (b) radial enthalpy distribution for the initial arc column, where H1=9.3×10^7 and $\times2.310^5$ J kg^{-1} correspond to temperatures of 20000 K and 400 K, respectively.

The second part of the arc simulation, on the other hand, is for the solution of the nozzle arc under linearly decaying current conditions, which is transient in nature. In the computations of all discharge conditions, the current is ramped down from 1 kA DC plateau which is consistent with relevant experimental conditions, and thus we use the numerical solutions obtained by simulation of the 1 kA DC arc as initial conditions for this part of simulation. This requires a restart of computer simulation from an existing PHI file for the 1 kA DC arc (Point K of Section 3.7.2).

3.7.7 Simulation Procedures

In the present investigation, the computer simulation is initiated by letting the gas flow into the nozzle towards the nozzle exit with specified boundary conditions. Immediately after the flow reaches steady state, the flow is exposed to an arc at 1 kA DC. The current is then ramped down towards zero with a specified di/dt after the DC arc reaches steady state. After current zero, a linearly rising recovery voltage with a specified dV/dt is imposed to find RRRV. Thus, the procedure of computer simulation for the arcing process includes four stages given below:

A Computation of the Cold Flow

With specified P_0 and P_e, the simulation is run without considering an arc until the solution reaches steady state. Although the simulation is steady state in nature, we still include the time-dependent term for Equation (3.19). Such method of solving steady state problems is known as the time marching method. The principle of time marching is to start with a guessed flow distribution (initial conditions) and integrate the time dependent equations of motion and energy forward with time until a steady state solution is obtained [3.40]. We have chosen this method, since it has been widely used for simulating high speed compressible flows (e.g. flow in a supersonic nozzle, similar to flow conditions for switching arcs), due to its advantages over directly solving the steady flow governing equations for such flow conditions as discussed in [3.11, 3.40].

In order to accelerate convergence of the solution and save time, we have used

the gas pressure and axial velocity derived from 1D theory as initial conditions (Figure 3.6). It should be noted that, for different nozzle geometries and discharge conditions (e.g. different values of P_0 and P_e and current level), and the application of different flow models, the time period required for the numerical solution to reach steady state can be different. It is found that, for the flow inside Nozzles 1 or 2 which is shock free, with adoptions of different discharge conditions and different models, the maximum time period required for the cold flow solution to reach steady state is approximately 2 ms. After 2 ms, solutions of flow behaviour inside the nozzle are almost not changing with time. For Nozzle 3, on the other hand, there is always a shock inside the nozzle, resulting in flow separation and generation of vortices in the shock region. Due to stagnant nature of the vortices, a longer time period (approximately 4 ms) is required for the solutions to reach steady state. To ensure the solutions to reach steady state effectively, for the investigations in this thesis, the total computational time for the cold flow simulations is specified to be 2 ms for Nozzles 1 and 2, and 4 ms for Nozzle 3, despite the discharge conditions and the flow models applied.

For the cold flow simulations, the size of the time step is 5 μs. The number of sweeps for each time step is 500 to ensure solution convergence in each time step. The linear relaxation factor, α, for P1 equation is 0.2. The false-time-steps, Δt_f, for V1, W1, H1, KE and EP equations are all set to 1 μs.

B Computation of the DC Nozzle Arcs

As soon as the cold flow solutions reach steady state, we initiate the simulation with an arc at 1 kA DC. For the investigation of Chapter 4, the currents used range from 50 A DC to 1 kA DC. The time marching approach is again used to obtain steady state solutions for these DC arcs. For the investigations of this thesis, from the initial conditions for DC arc simulations given in Section 3.7.6, for Nozzles 1 and 2, the total computational time for DC arc simulations is specified to be 1.5 ms to ensure the solutions of the DC arcs inside the nozzle reach steady state. For Nozzle 3,

this total computational time is specified to be 4 ms.

For all the computations of DC nozzle arcs, the size of each time step is 1 μs and the number of sweeps for each time is 500. The linear relaxation factor, α, for P1 equation is 0.1. The false-time-steps, Δt_f, for V1, W1, H1, KE and EP equations are all set to 0.05 μs.

C Computation of the Transient Nozzle Arc before Current Zero

As soon as the solutions of the 1 kA DC arc reach steady state, we restart the simulation from the results of 1 kA DC arc and, in the mean time, ramp down the current with a specified di/dt until the current reaches its zero point. The total computational time required for this state of simulation is uniquely determined by the value of di/dt, e.g. for di/dt=25 $A\mu s^{-1}$, the total time = 1000 A/25 $A\mu s^{-1}$ = 40 μs.

It should be noted that, for turbulent SF_6 switching arcs, the states of arc (e.g. temperature and arc radius) and, subsequently, the arc resistance, change very rapidly shortly before final current zero. Therefore, a very small time step size should be used to catch these features and to ensure the accuracy of the computation. We, therefore, use 0.05 μs as the size of the time step from the instant when the current is below 300 A to that of the current zero. For instants when the current is above 300 A, a relative larger time step size (0.1 μs) is used to save computational time. The number of sweeps for each time step is 500. The linear relaxation factor, α, for P1 equation is 0.1. The false-time-steps, Δt_f, for V1, W1, H1, KE and EP equations are all set to 0.005 μs. A sensitivity study for time step sizes was performed and the results showed that, by further reducing time step size, the difference of the results was less than 5%. This means the selection of time step size here is reasonable.

D Computation of the Nozzle Arc after Current Zero

As soon as the computation before current zero is completed, we restart the simulation from the results at current zero and, in the mean time, apply a linearly increasing recovery voltage with a specified dV/dt. This stage is simulation aims to

find the RRRV of the nozzle arc. It is known that, for gas blast circuit breakers, the characteristic time for thermal extinction and/or reiginition is always within 10 μs [3.28, 3.41]. Thus, for the present investigation, the total computational time for this stage is specified as 10 μs. Due to rapid variation of arc characteristics during current zero period as previously indicated, the size of each time step is set to 0.01 μs. The number of sweeps for each time step is 300. The linear relaxation factor, α, for P1 equation is 0.1. The false-time-steps, Δt_f, for V1, W1, H1, KE and EP equations are all set to 0.01 μs.

3.8 Concluding Remarks

This chapter gives a detailed discussion on the approach for the modelling of turbulent SF_6 switching arcs, which have similarities to that for turbulent shear layer flows due to the resemblance between a switching arc and shear layer flows.

A brief description is given to the approach for the modelling of turbulent shear layer flows. This includes the derivation of time averaged conservation equations for turbulent flows using Reynolds's approach and the closure of the time averaged conservation equations using Boussinesq assumption and eddy viscosity to link the unknown Reynolds stresses to the stain tensor of the main flow. One can avoid using such a closure method by taking the first moment of momentum conservation equation to derive the Reynolds stress equations. However, this approach introduces far more unknowns than the time averaged momentum equation. For engineering problems, it is more beneficial to devise ways to close the time averaged conservation equations. This is the method which will be adopted in the modeling of turbulent SF_6 switching arcs.

The turbulence models chosen for turbulent SF_6 switching arcs, in addition to the Prandtl mixing length model which has achieved considerable success in predicting turbulent arc behavior, are basically the two-equation models (i.e. the standard k-epsilon model) and their variants (i.e. the Chen-Kim model and the RNG model) which are relevant in the nozzle arc context. These models will be subjected

to verification by relevant test results, the details of which are described in this chapter.

The conservation equations for SF_6 switching arcs and the governing equations for turbulence models, which form the arc model, will be solved by using a general purpose CFD software package, PHOENICS. A brief description has been given as regards the implementation of the arc model in PHOENICS.

References

[3.1] Blundell R E and Fang M T C 1997 Stability of a dc SF_6 arc in axially accelerating flow *IEEE Trans. on Plasma Sci., Special Issue on High Pressure Arcs and High Frequency Thermal Plasmas*. **25** 852-59

[3.2] Zhang J F and Fang M T C 1989 Dynamic behavior of high-pressure arcs near the flow stagnation point *IEEE Trans. Plasma Sci.* **17** 524-33

[3.3] Drazin P G and Reid W H 2004 *Hydrodynamic Stability* 2nd edn (Cambridge: Cambridge University Press)

[3.4] Tennekes H and Lumley J L 1972 *A First Course in Turbulence* (Massachusetts: MIT Press)

[3.5] Wilcox D C 2006 *Turbulence Modeling for CFD* (La Cañada, CA: DCW Industries)

[3.6] Schlichting H 1979 *Boundary Layer Theory* 7th edn (New York: McGraw Hill)

[3.7] Frind G, Kinsinger R E, Miller R D, Nagamatsu H T and Noeske H O 1977 Fundamental investigation of arc interruption in gas flows EPRI EL-284 (Project 246-1)

[3.8] Benenson D M, Frind G, Kinsinger R E, Nagamatsu H T, Noeske H O and Sheer, Jr R E 1980 Fundamental investigation of arc interruption in gas flows EPRI EL-1455 (Project 246-2)

[3.9] Frind G and Rich J A 1974 Recovery speed of axial flow gas blast interrupter: dependence on pressure and di/dt for air and SF_6 *IEEE Trans. Power Appar. Syst.* **93** 1675-84

[3.10] Patankar S V 1980 Numerical Heat Transfer in Fluid Flow, (New York: Hemisphere Publishing Corporation)

[3.11] Versteeg H K and Malalasekera W 2007 *An Introduction to Computational Fluid Mechanics-the Finite Volume Method* 2nd edn (Harlow, UK: Prentice-Hall)

[3.12] PHOENICS is the name of a commercial CFD package supplied by CHAM which is based at Bakery House, 40 High Street, Wimbledon Village, London, SW19 5AU, UK.

[3.13] Anderson D A, Tannehill J C and Pletcher R H 1984 *Computational Fluid Mechanics and Heat Transfer* (New York: Hemisphere Publishing Corporation)

[3.14] George W K Jan. 2013 Lectures in Turbulence for the 21st Century. Retrieved 1 Sept. 2014 from: http://www.turbulence-online.com/Publications/Lecture_Notes/Turbulence_Lille/TB_16January2013.pdf

[3.15] Zhang J F, Fang M T C and Newland D B 1987 Theoretical investigation of a 2KA DC nitrogen arc in a supersonic nozzle *J. Phys. D: Appl Phys.* **20** 368-79

[3.16] Frost L S and Liebermann R W 1971 Composition and transport properties of SF_6 and their use in a simplified enthalpy flow arc model *Proc. IEEE.* **59** 474–85

[3.17] Cowley M D 1974 Integral methods of analysing electric arcs: I. Formulation *J. Phys. D: Appl. Phys.* **7** 2218-22

[3.18] Yan J D, Fang M T C and Jones C 1997 Electrical and aerodynamic behaviour of arcs under shock conditions *IEEE Trans. Plasma Sci.* **25** 840–5

[3.19] Liebermann R W and Lowke J J 1976 Radiation emission coefficients for sulfur hexafluoride arc plasmas *J. Quant. Spectrosc. Radiat. Transfer.* **17** 253–64

[3.20] Yan J D, Nuttall K I and Fang M T C 1999 A comparative study of turbulence models for SF_6 arcs in a supersonic nozzle *J. Phys. D: Appl. Phys.* **32** 1401–6

[3.21] Dixon C M, Yan J D, and Fang M T C 2004 A comparison of three radiation models for the calculation of nozzle arcs *J. Phys. D: Appl. Phys.* **37** 3309–18

[3.22] Davidson P A 2004 *Turbulence: An Introduction for Scientists and Engineers* (Oxford: Oxford University Press)

[3.23] Cebeci T 2004 *Turbulence Models and Their Applications: Efficient Numerical Method* (Long Beach, CA: Horizons Publishing Inc.)

[3.24] Launder B E and D B Spalding 1974 The numerical computation of turbulent flows *Comput. Methods Appl. Mech. Eng.* **3** 269–89

[3.25] Yakhot V, Orszag S A, Thangam S, Gatski T B and Speziale C G 1992 Development of turbulence models for shear flows by a double expansion technique *Phys. Fluids* A **4** 1510–20

[3.26] Chen Y S and Kim S W Computation of turbulent flows using an extended K-epsilon turbulence closure model *Interim Report* NASA CR-179204

[3.27] Turbulence models in PHOENICS (London: CHAM). Retrieved 25 Jul. 2014 from: http://www.cham.co.uk/phoenics/d_polis/d_enc/turmod/enc_tu.htm

[3.28] Fang M T C, Zhuang Q and Guo X J 1994 Current zero behaviour of an SF_6 gas-blast arc: II. Turbulent flow *J. Phys. D: Appl. Phys.* **27** 74–83

[3.29] Song K D, Lee B Y and Park K Y 2004 Calculation of the post-arc current in a supersonic nozzle by using the K-epsilon model *J. Korean Phys. Soc.* **45** 1537–43

[3.30] Zhou Q, Li H, Xu X, Liu F, Guo S, Chang X, Guo W and Xu P 2009 Comparative study of turbulence models on highly constricted plasma cutting arc *J. Phys. D: Appl. Phys.* **42** 015210

[3.31] El-Hadj A A and Ait-Messaoudene 2005 Comparison between two models and analysis of the effect of the substrate movement on the flow field of a plasma jet *Plasma Chem. Plasma Process.* **25** 699–722

[3.32] Bini R, Basse N T and Seeger M 2011 Arc induced turbulent mixing in an SF6 circuit breaker model *J. Phys. D: Appl. Phys*. **44** 025203

[3.33] Anderson J D 2003 *Modern compressible flow* 3rd edn (New York: McGraw-Hill)

[3.34] Kwan S 1996 *Computer Simulation of Arcs in Gas-Blast Circuit Breakers* (PhD thesis: University of Liverpool)

[3.35] PHOENICS Encyclopedia (London: CHAM). Retrieved 3 Spet. 2014 from: http://www.cham.co.uk/phoenics/d_polis/d_enc/enc_pil.htm

[3.36] Wong T M 2008 *Computer Simulation and Visualisation of Complex Systems: Arcs and Hot Gas Flow in Auto-expansion Circuit Breakers* (PhD thesis: University of Liverpool)

[3.37] Boundary conditions in PHOENICS (London: CHAM). Retrieved 5 Sept. 2014 from: http://www.cham.co.uk/phoenics/d_polis/d_lecs/general/bcond.htm

[3.38] Guidelines for Specification of Turbulence at Inflow Boundaries. Retrieved 5 Spet. 2014 from: http://www.esi-cfd.com/esi-users/turb_parameters/

[3.39] Yan J D, Fang M T C and Hall W 1999 The development of PC based CAD tools for auto-expansion circuit breaker design IEEE Transactions on Power Delivery, **14** 176-181

[3.40] Ng K C, Yusoff, M Z, Munisamy K, Hasini H and Shuaib N H 2008 Time-marching method for computations of high-speed compressible flow on structured and unstructured grid *Am. J. Engg. & Applied Sci.* **1 (2)** 89-94, 2008

[3.41] Yan J D, Fang M T C and Hall W 1999 The development of PC based CAD Tools for auto-expansion circuit breaker design *IEEE Trans. Power Delivery.* **14** 176-81.

Chapter 4
The Modelling of a Turbulent SF_6 Arc in a Supersonic Nozzle: I. Cold Flow Features and DC Arc Characteristics

4.1 Introduction

In this chapter and the subsequent two chapters (Chapters 5 and 6), a systematic investigation is carried out, which studies the behaviour of an SF_6 switching arc burning in a supersonic nozzle by using the five flow models given in Chapter 3. The suitability of these models for switching applications is verified by comparison between computed RRRV and the corresponding measurements of [4.1, 4.2, 4.3].

Preliminary investigation [4.4] of an SF_6 nozzle arc indicates that the differences in arc voltages predicted by the aforementioned four turbulence models at the plateau of a current ramp, 1 kA DC, are less than 15% of each other, which is well within the experimental scatter normally encountered during the tests of circuit breakers. This result seems to indicate that turbulence at high currents is not a decisive factor for the determination of arc voltage. This appears to be in agreement with a DC nitrogen nozzle arc at 2 kA for which laminar theory can give a satisfactory account of the arc behaviour [4.5]. This prompts the present investigation into the role of turbulence in DC SF_6 nozzle arcs and its implications towards the prediction of arc's current zero behaviour (this chapter).

The investigation presented in this chapter forms the first part of the systematic investigation into the behaviour of an SF_6 nozzle arc (hereafter referred to as Part I). Part I is concerned with the studies of the cold flow features as well as with a detailed study of the arc behavior under different DC currents for Nozzle 2 (Figure 3.3) used in the experiments of Benenson et al. [4.1]. The second part (hereafter

referred to as Part II, which will be presented in Chapter 5) is exclusively concerned with the arc behavior under a current ramp before current zero and a voltage ramp after current zero. The computed RRRV for Nozzle 2 will be compared with corresponding measurements reported in [4.1]. Relative merits of turbulence models employed will be discussed in detail in Part II. It is well known that nozzle geometry determines the flow conditions, hence the turbulence level inside a nozzle during the current zero period, which affects the arc characteristics and, subsequently, RRRV characterizing the thermal interruption capability of a nozzle. Therefore, the effects of the nozzle geometry on SF_6 arc thermal interruption will also be investigated by applying different turbulence models, which forms the third part (hereafter referred to as Part III, to be presented in Chapter 6) of the systematic investigation. The computational results together with the measured RRRV for three nozzles [4.1, 4.2, 4.3] will be used to evaluate the influence of the geometrical factors of a nozzle on the arc characteristics and on thermal interruption.

No experimentally measured DC arc voltages for Nozzle 2 are available for direct comparison with the computational results reported in Part I. However, the importance of the cold flow on the voltage withstanding capability of a nozzle interrupter, especially in the presence of upstream and downstream electrodes and the influence of the arc behaviour under different direct currents (corresponding to the plateau of the current ramp) on the current zero period of a breaker, warrants a detailed report of the relevant computational results at two stagnation pressures (11.2 atm and 21.4 atm) investigated by Benenson et al. [4.1].

This chapter is organized as follows. Section 4.2 gives details of the computational domain and grid distribution. The cold flow features and the effects of upstream and downstream electrodes on the flow are discussed in Section 4.3. This is followed by a discussion of DC arc-flow interaction, the arc features and the DC arc voltage-current (V-I) characteristics as predicted by the four turbulence models and the laminar flow model. Finally, appropriate conclusions are drawn.

4.2 Computational Domain and Grid Distribution

Computation has been performed on Nozzle 2 used in experiments of Benenson et al. [4.1]. The detailed dimensions of the nozzle and the grid system are shown in Figure 4.1. The distance between two electrodes is 21.5mm. The diameter of the nozzle inlet is 25.4 mm and that of the outlet is 38.1 mm. The flat nozzle throat is 4.6 mm long with a diameter of 12.7 mm. The upstream electrode has a round tip and the outer diameter is identical with the nozzle throat diameter. The downstream electrode is hollow, which has an outer diameter of 6.35 mm and an inner diameter of 3.6 mm.

The grid system adopted in the computation is BFC (Point B in Section 3.7.2 of Chapter 3). The grid distribution is indicated in Figure 4.1, with fine radial grids being employed in the arc region, i.e. the region with R from 0 to 2.5 mm (Figure 4.1), where the average radial grid density is approximately 0.03 mm. In the outer regions, i.e. R > 2.5 mm, the total radial grid number is 80 (Figure 4.1). The average axial grid density between two electrodes is approximately 0.1 mm. Altogether 162×408 grids are used to obtain results.

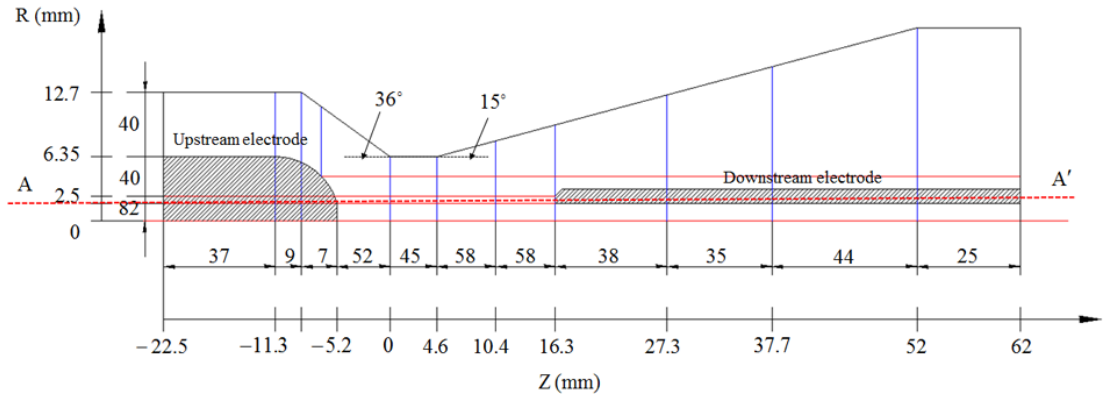

Figure 4.1. Nozzle geometry and grid system. The computation domain is divided into eleven intervals in the axial direction and four in radial direction, respectively. The axial and radial coordinates defining the intervals and the number of grids in each interval are indicated above. Z=0 indicates the axial position of the inlet of flat nozzle throat.

4.3 Results and Discussion

Computations have been carried out for two stagnation pressures (P_0 = 11.2 atm and 21.4 atm) and for DC currents ranging from 50 A to 1 kA for the nozzle of Figure 4.1. Results are given for the cold flow features and the behviour of DC nozzle arcs predicted using the five flow models given in Chapter 3. As there are no DC arc voltage measurements available for the optimization of the turbulence parameter, *c*, of the Prandtl mixing length model, *c* is adjusted to give the closest agreement with the measured RRRV in [4.1] for P_0 = 21.4 atm and di/dt= 25 $A\mu s^{-1}$. The value of *c* is 0.048 for the nozzle of Figure 4.1. Based on the computational results obtained, we can predict the behaviour of the cold flow and DC nozzle arcs inside the nozzle. Detailed interpretations of these results are given below.

4.3.1 Features of the Cold Flow and the Influence of Upstream and Downstream Electrodes

4.3.1.1 General Features of the Cold Flow

Computations of the cold flow have been performed using the flow models previously mentioned. The Prandtl mixing length model is not used for the computation of cold flow as the internal nozzle flow is not of thin shear layer type, thus the turbulence length scale is difficult to define. It has been found that the computational results obtained by all flow models are almost identical except in the region close to the upstream electrode tip and to the shock region due to the presence of downstream electrode in the supersonic flow region. The qualitative trends of pressure and velocity variations in these two regions are similar although their magnitudes differ greatly depending on the flow models. The results obtained by the standard k-epsilon model are, therefore, used to illustrate the features of the cold flow.

Figure 4.2 shows the pressure distribution together with isobars and the Mach number distribution inside the whole nozzle. In the region adjacent to the inlet of the

flat nozzle throat, the pressure variation in the radial direction is very large. The discontinuous nozzle area variation at Points B and C acts as an expansion corner [4.6] where isobars are bunched. Through the expansion wave zone at Point B, the flow direction is gradually turned to align with the surface of the flat nozzle throat region, and, at Point C, to the surface of divergent nozzle section. The presence of a hollow electrode in the supersonic region of the nozzle (the downstream electrode) generates a shock in front of it as shown in Figure 4.2, which propagates towards the nozzle wall and the nozzle axis. The presence of the upstream solid electrode causes flow to separate, thus creating a wake of almost constant pressure within which the flow circulates [4.7].

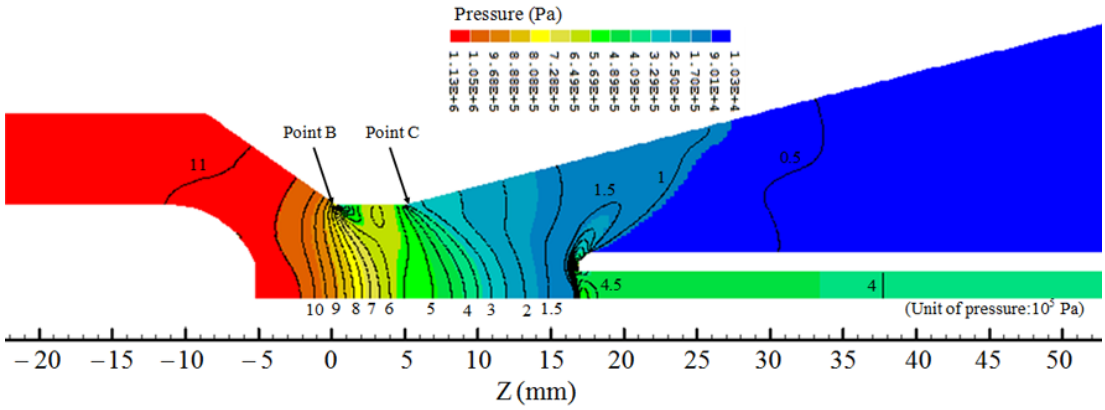

(a)

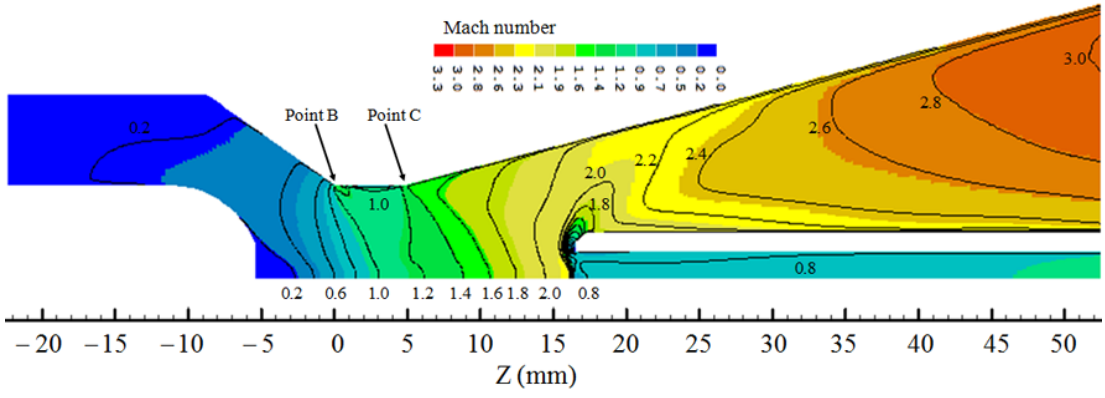

(b)

Figure 4.2. Pressure and Mach number distributions for the cold flow at P_0=11.2 atm. (a) Pressure distribution together with isobars and (b) Mach number distribution together with isobars.

4.3.1.2 Effects of the Downstream Electrode

The pressure distribution and the isobars near the downstream electrode are shown in Figure 4.3(a) and the Mach number together with the streamlines in Figure 4.3(b). The isobars in front of the flat Surface 2-3 (Figure 4.3(a)) of the downstream electrode are very dense showing the existence of the shock. The variations of pressure and Mach number along the horizontal line passing the centre of Surface 2-3 (Line AA' in Figures 4.3 and 4.5) exhibit the features of a normal shock (Figure 4.4) [4.6]. A bow shock can, therefore, be identified in front of the hollow electrode tip, the compression region of which extends to the nozzle axis (Figures 4.3 and 4.5). The flow behind the bow shock but adjacent to Line AA' is similar to that near a stagnation point. Pressure decreases in the radial direction from the centre of Surface 2-3, thus ensuring the turning of the flow from that parallel to the axis to that nearly vertical along Surface 2-3. Pressure between the bow shock and Surface 3-4-5 increases in the direction normal to the bow shock but decreases along the bow shock surface to ensure the direction of the flow as required by the nozzle wall and Surface 4-5 (Figure 4.3(b)).

Pressure and Mach number along Line AA' (Figure 4.4) and on the axis (Figure 4.5) before the shock are almost identical for all flow models. However, the detailed shock structure in front of the downstream electrode tip (such as the isobar distribution shown in Figure 4.3(a)) and the flow behind the shock within the hollow region of the downstream electrode are dependent on the flow model (Figure 4.5). The results for laminar flow and those computed by the Chen-Kim model and RNG model are almost the same. This indicates that the effects of turbulence on the cold flow are negligible in the region not affected by the shock. The shock structure and the flow immediately behind the shock are known to be dependent on the turbulence models [4.8]. As no experimental results are reported in [4.1] for the cold nozzle flow, no conclusions regarding the accuracy of the flow models employed can be drawn. However, since the results of all turbulent models in the region away from the shock are almost identical with those of laminar flow, the shock structure predicted by the

laminar flow model is perhaps closer to the reality.

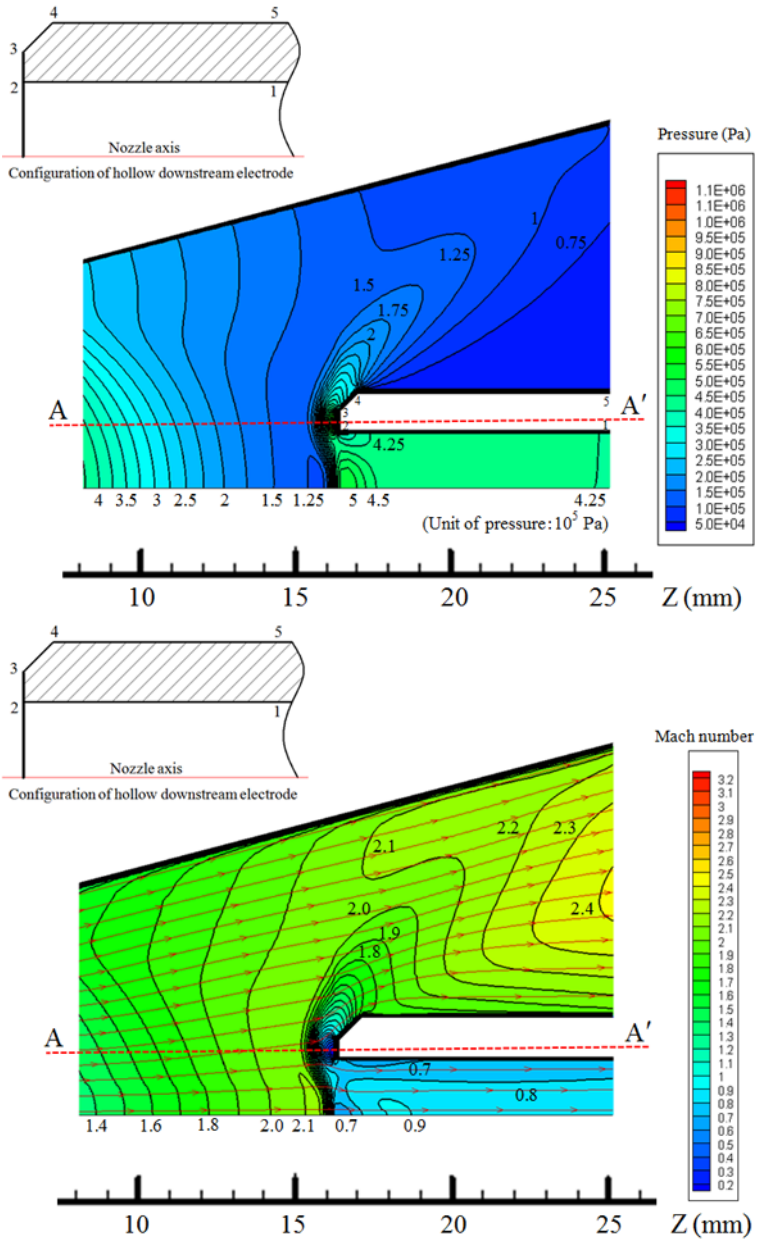

Figure 4.3. Flow pattern near the downstream electrode computed at P_0=11.2 atm. (a) Pressure distribution together with isobars and (b) Mach number distribution with constant Mach contours and flow streamlines.

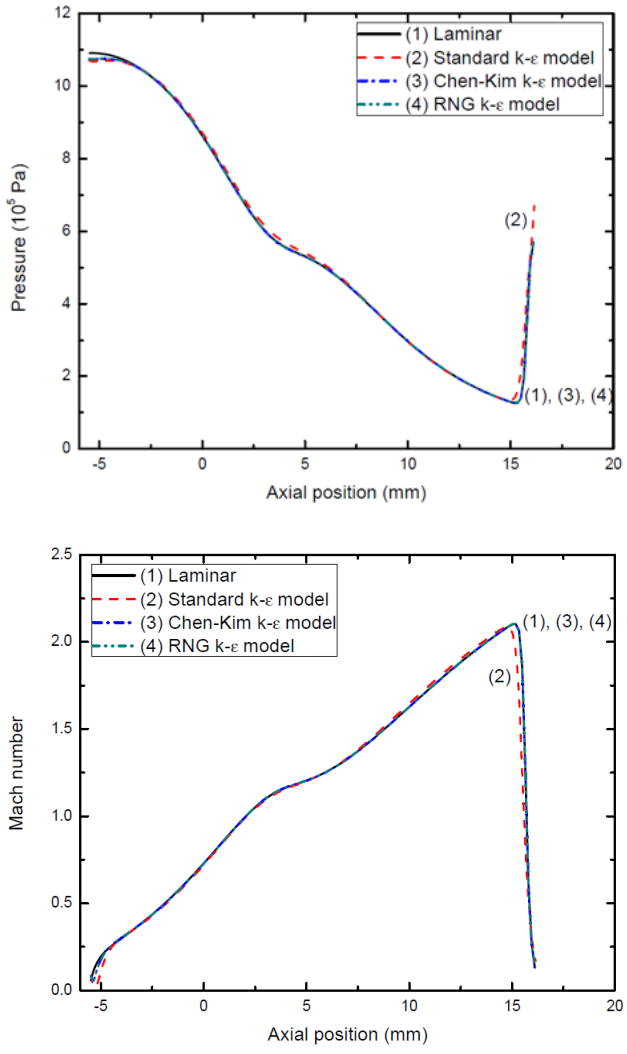

Figure 4.4. Variations of pressure and Mach number along Line AA' for the cold flow computed by four flow models. P_0=11.2 atm. (a) Pressure distribution and (b) Mach number distribution.

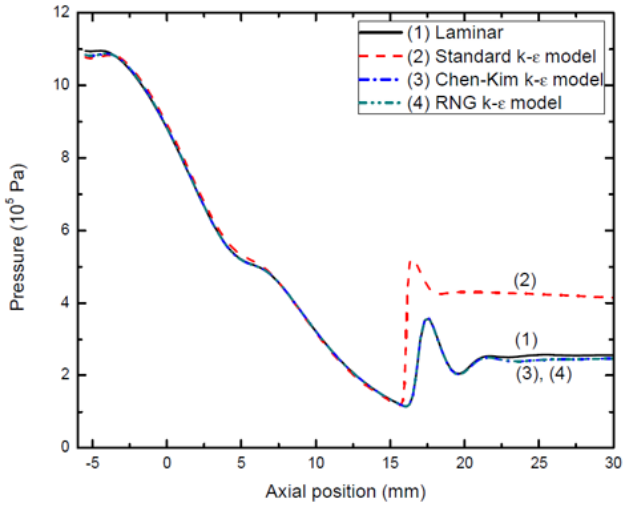

(a)

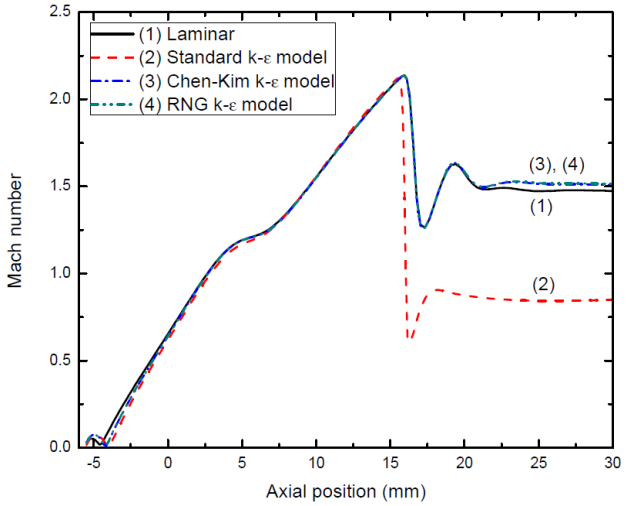

(b)

Figure 4.5. Variations of pressure and Mach number along the nozzle axis for the cold flow computed by four flow models. P_0=11.2 atm. (a) Pressure distribution and (b) Mach number distribution.

4.3.1.3 Effects of the Upstream Electrode

Figure 4.6 shows the pressure distribution and streamlines near the upstream electrode and those in the transonic region of the nozzle. Close to Point D on the electrode surface the flow starts to separate, thus creating a wake region of approximately constant pressure (Figure 4.7(a)) [4.7]. The flow circulates in the wake region. The flow separation point and the velocity and pressure inside the wake are known to be dependent on the flow model (Figure 4.7). However, the pressure

differences in the wake predicted by different models are less than 2% of the absolute pressure within the wake (Figure 4.7(a)). No experimental results are available at present to judge the relative merits of the flow models used. For the reason mentioned above, results of the laminar flow model are expected to be closer to reality.

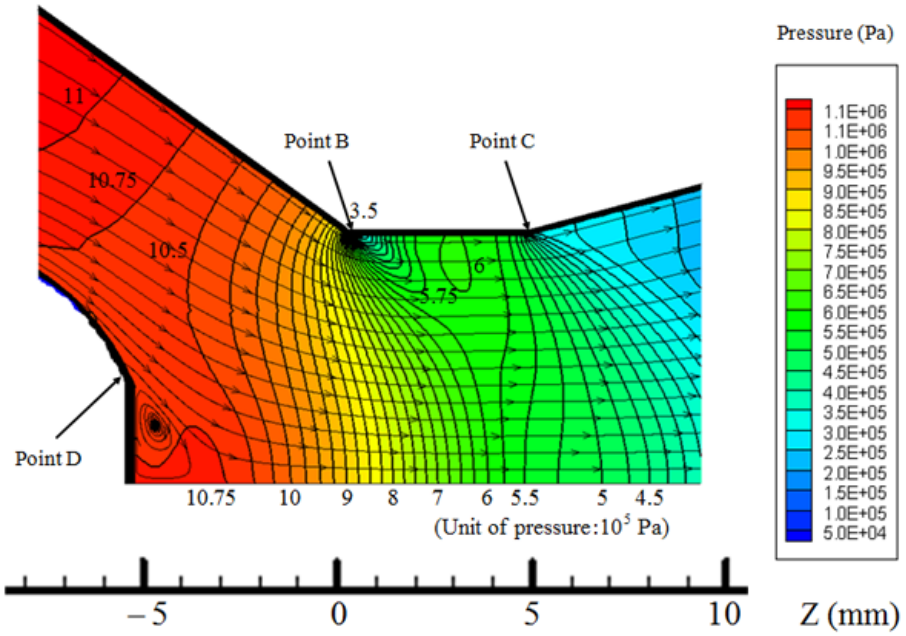

Figure 4.6. Pressure isobars and streamlines near the upstream electrode computed by the standard k-epsilon model at P_0=11.2 atm.

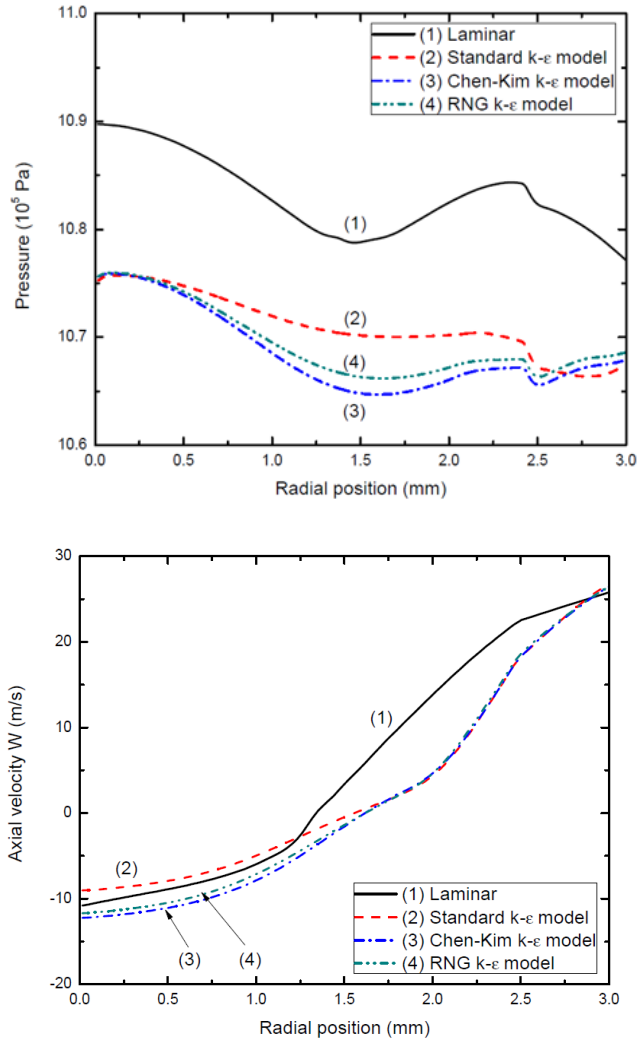

Figure 4.7. Radial distributions of pressure and axial velocity near the upstream electrode for the cold flow computed by four flow models. P_0=11.2 atm. (a) Pressure distribution and (b) Distribution of axial velocity.

The wake near the upstream electrode and the shock region close to the downstream electrode are not expected to influence the thermal interruption capability of the nozzle interrupter (Figure 4.1) as the voltage drop in these two regions is expected to be much smaller than that of the arc column. However, these two regions can affect the dielectric strength of a breaker, the details of which will be given in Section 4.3.1.5.

4.3.1.4 The Influence of Stagnation Pressure

For SF_6, the equation of state for ideal gas is valid for temperature up to 1000 K. The density of SF_6 is, therefore, proportional to pressure for a given temperature. Cold flow results indicate that the flow is mainly driven by pressure gradient and viscous stresses are negligible in comparison with pressure gradient. For turbulent flow, Reynolds stress is proportional to density. Under these conditions, it can easily be shown that the solutions of the conservation equations for laminar or turbulent flow are uniquely determined by normalized pressure P/P_0. Thus, velocity and Mach number are independent of stagnation pressure, and the computed pressure expressed in normalized pressure is the same for any stagnation pressure. Computation results for stagnation pressures of 11.2 atm and 21.4 atm given in Figure 4.8 are in agreement with the above conclusions.

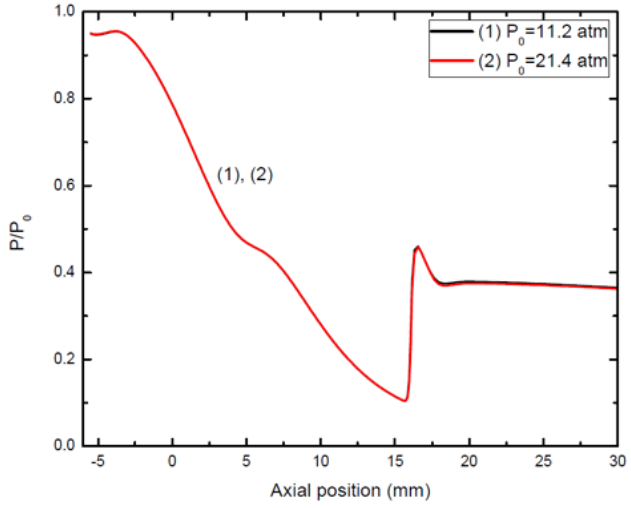

(a) of Figure 4.8

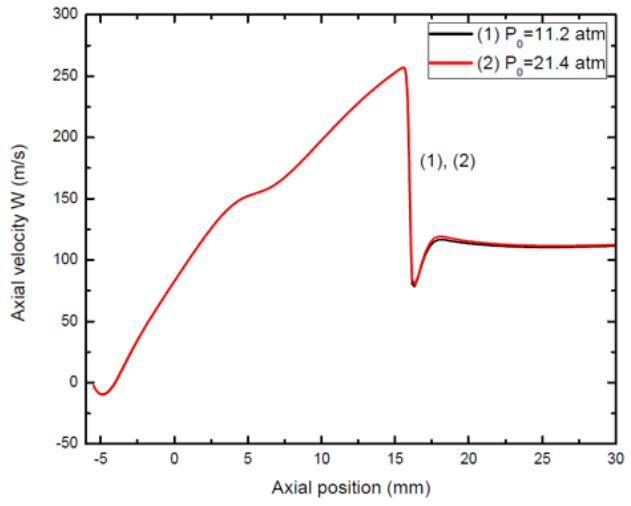

(b) of Figure 4.8

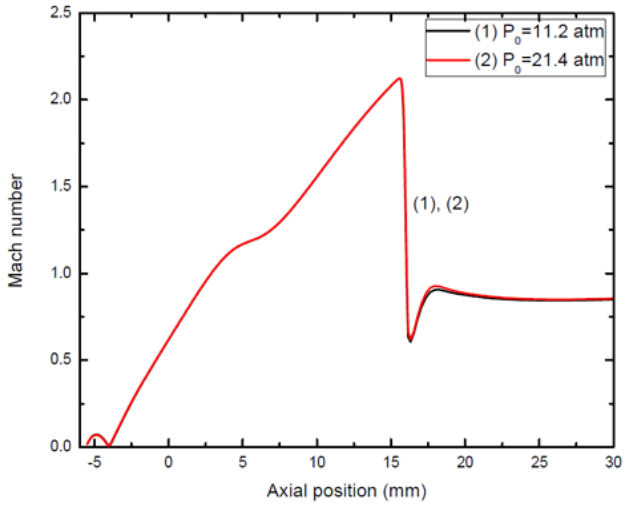

(c) of Figure 4.8

Figure 4.8. Comparison of (a) normalized pressure, (b) axial velocity and (c) Mach number along the nozzle axis for the cold flow at two stagnation pressures (P_0=11.2 and 21.4 atm). Standard k-epsilon model is used to obtain these results.

4.3.1.5 Electrode effects on the dielectric strength

The dielectric strength of a nozzle interrupter immediately after the thermal extinction of the arc depends on the distribution of E/P between the two electrodes. The presence of the bow shock makes E/P highly non-uniform near the downstream electrode. The gas temperature of the circulating flow in the wake region near the upstream electrode immediately after arc interruption can be around 2000 K to 3000 K [4.9]. In such a hot gas, there are still a large number of residue charged particles. The dielectric strength is, therefore, greatly reduced. It is important, therefore, to optimize the electrode configuration from cold flow point of view to ensure a smaller flow circulation region.

4.3.2 Characteristics of DC nozzle arcs

4.3.2.1 General features

Ohmic heating inside the arc creates a high temperature and low gas density region within the nozzle. The presence of the arc reduces the effective area for the flow, thus modifying the pressure distribution within the nozzle, which in turn affects the arc

[4.10]. The interaction between the arc and its surrounding cold flow determines the arc characteristics.

The present investigation covers a current range from 50 A to 1 kA. At 1 kA DC, computational results show that the arc cross section defined as the boundary of the 4000 K isotherm (hereafter referred to as the electrical boundary) at the stagnation pressure of 11.2 atm does not exceed 8% of the nozzle area (Figure 4.9). The disturbance to the cold flow due to the presence of the arc is quite small, which results in the pressure distribution within the nozzle to be nearly the same as that of cold flow except in the regions close to the two electrodes. The qualitative features of the nozzle arc predicted by various flow models are similar. Unless otherwise specified, the results given in this section are those obtained by the standard k-epsilon model.

On the arc axis, Ohmic input is balanced by net radiation loss (emission minus absorption). This is a common feature for axially flow dominated high pressure arcs when current is 1 kA and above. The axis temperature for the arc in Figure 4.9 reaches 22,000K at which such a balance occurs. It is well known that arc axis temperature does not exceed 27,000K even for current up to 80 kA [4.11]. Such small range of variation of axis temperature with currents is due to that arc voltage only slightly increases with current (hence small increase in electrical field). This results in a small increase in Ohmic input. Thus, when current is increased, net radiation loss should be increased to balance the Ohmic input by raising the axis temperature. However, the required increase in temperature is small because the net radiation loss increases rapidly with temperature [4.12].

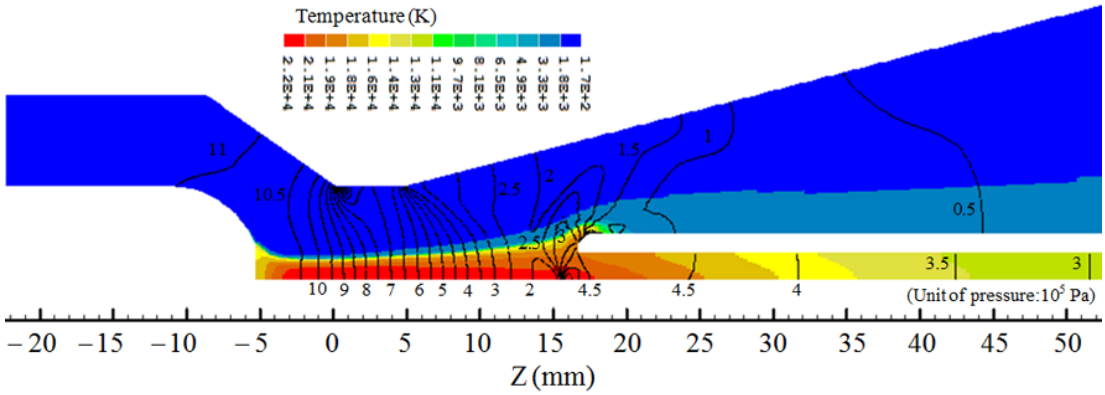

Figure 4.9. Temperature contour together with pressure isobars in the nozzle at 1 kA DC and at P_0=11.2 atm.

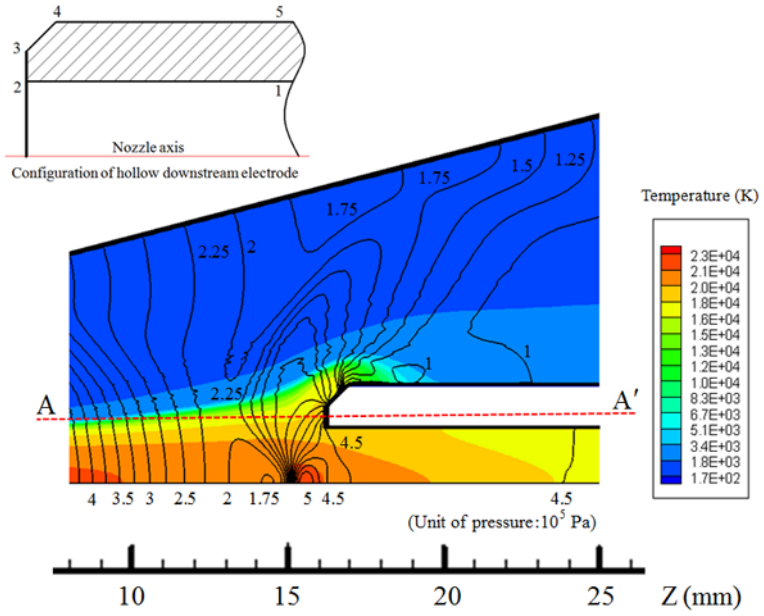

Figure 4.10. Temperature contour together with pressure isobars near the upstream electrode at 1 kA DC showing the formation of a compression region close to the tip of the downstream electrode. P_0=11.2 atm.

The 1 kA DC arc greatly disturbs the flow near the downstream electrode tip (Figure 4.10). In contrast with the cold flow, the hot gas covers the downstream electrode tip, which renders the local flow subsonic for the Prandtl mixing length model and the standard k-epsilon model and slightly above sonic for the laminar flow model, the Chen-Kim model and the RNG model (Figures 4.10 and 4.11(a)). Since the flow needs to be decelerated towards the surface of the electrode in order to satisfy non-slip boundary condition for velocity, this creates a compression zone (Figures 4.10 and 4.11(b)) in front of the electrode tip. It should, however, be noted

that the pressure distribution near the flat tip shows a compression wave rather than a shock (Figures 4.10 and 4.11(b)), since the local flow field is generally subsonic (Figure 4.11(a)). The pressure waves emanating from Surface 2-3-4 are bunched on the arc axis, thus creating a pressure distribution similar to a shock (Figures 4.10 and 4.12). The bunching of the pressure waves is a direct consequence of the wave travelling towards the axis encountering a rising temperature, thus a region of increasing sound speed. The qualitative features of the shapes of the pressure isobars near the axis but originated from Surface 2-3-4 agree with the Snell's law of sound wave refraction [4.13].

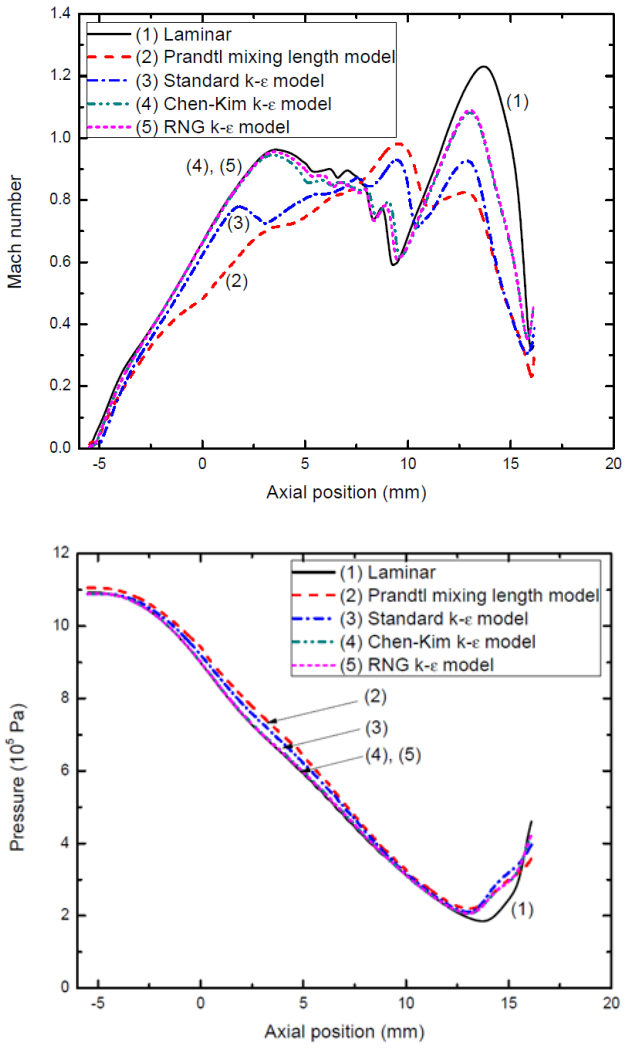

Figure 4.11. Variations of Mach number and pressure along Line AA' computed by five flow models at 1 kA DC. P_0=11.2 atm. (a) Mach number distribution and (b) pressure distribution.

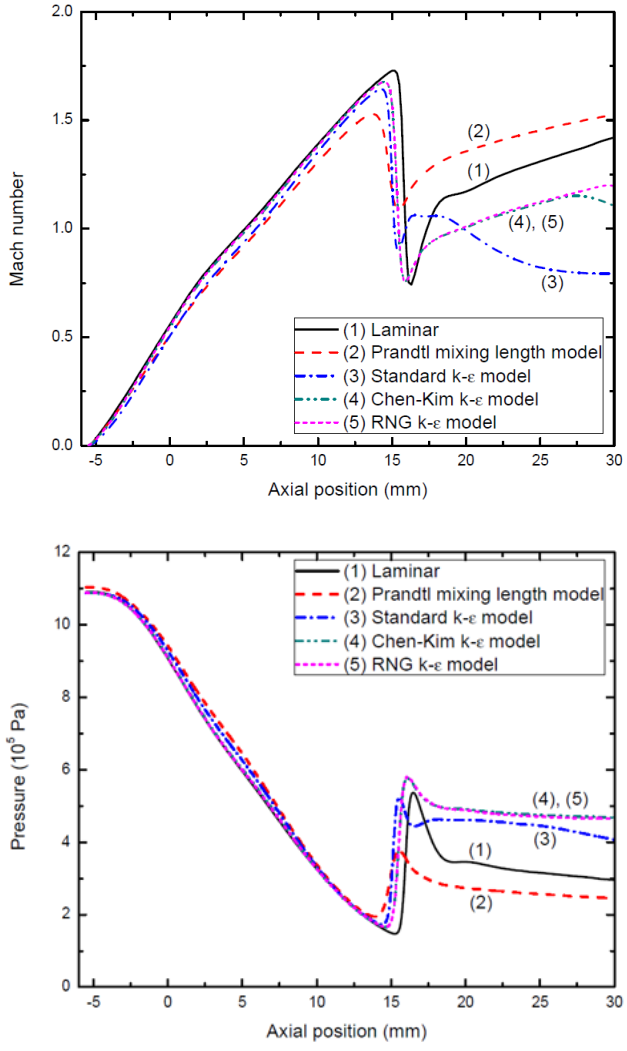

Figure 4.12. Variations of Mach number and pressure along the nozzle axis computed by five flow models at 1 kA DC. P_0=11.2 atm. (a) Mach number distribution and (b) pressure distribution.

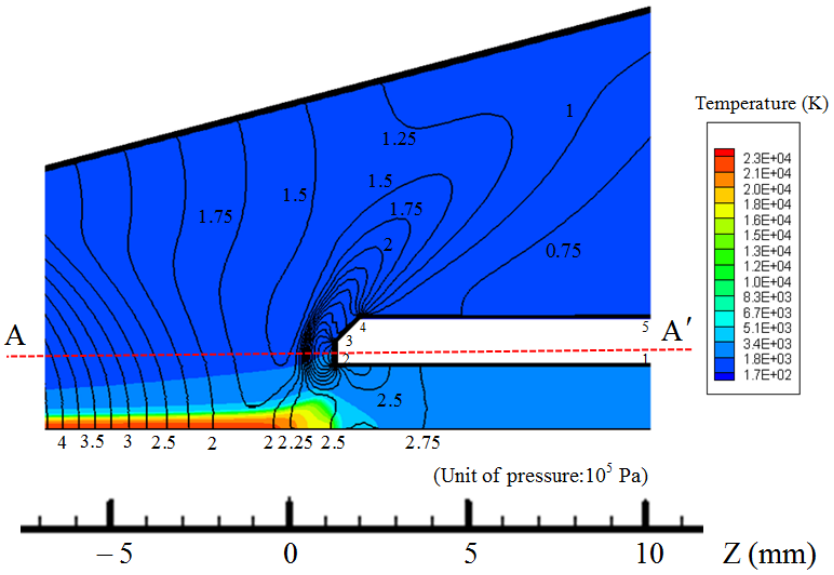

Figure 4.13. Temperature contour together with pressure isobars near the upstream electrode at 50 A DC showing the reappearance of the bow shock. P_0=11.2 atm.

When current is decreased, the thermal influence region of the arc is reduced. At a current below 100 A, the bow shock as observed in the cold flow reappears (Figures 4.13 and 4.14), which extends to the nozzle axis (figures 4.13 and 4.15). This will be the likely case when the current is reduced to zero during the interruption of a fault current by a circuit breaker. The pressure distributions predicted by the five flow models along the line AA' and on the axis (Figs 4.14(a) and 4.15(a)) are close to each other before the shock. However, the turbulence levels associated with the standard k-epsilon model and the Prandtl mixing length model are much higher than those predicted by Chen-Kim and RNG models, which results in lower axis velocities (Figure 4.16). Within the arc, the flow is entirely subsonic for the standard k-epsilon model and the Prandtl mixing length model (Figure 4.15(b)). Although all five flow models predict the shock in front of the hollow electrode, this shock needs to penetrate into the arc. It is well known that the shock is broadened and the strength reduced by viscous and thermal conduction effects. The concentration of isobars becomes less dense (Figures 4.13, 4.17(a) and 4.18(a)) when the shock propagates into the region with increased eddy viscosity and turbulent thermal conductivity. Since the oncoming flow is subsonic for the standard k-epsilon model and the Prandtl mixing length model, this pressure rise region near the arc axis can no longer be regarded as a part of the bow shock originated from the tip of the downstream

electrode. Upon entering the pressure rise region, the flow decelerates by the adverse pressure gradient and the greatly enhanced viscosity due to turbulence. For the standard k-epsilon model and the Prandtl mixing length model, the flow on the axis is arrested, thus creating a reverse flow region (Figures 4.16 and 4.17(b)) between two flow stagnation points. A vertex is also clearly formed, which increases the arc size (Figure 4.17(b)). For the Chen-Kim and the RNG k-epsilon models, computational results indicate that the supersonic flow in front of the downstream electrode decelerates into the shock but its direction has not been reversed (Figures 4.16 and 4.18(b)) due to weaker turbulence level. The arc size is, however, still broadened due to deceleration of the gas flow (Figure 4.18(b)).

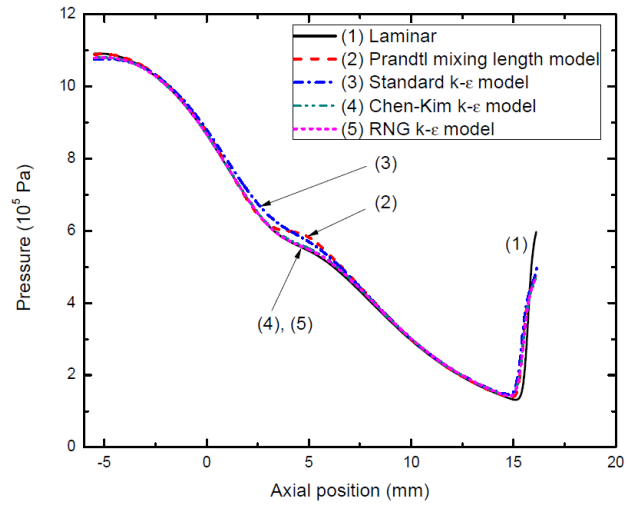

(a)

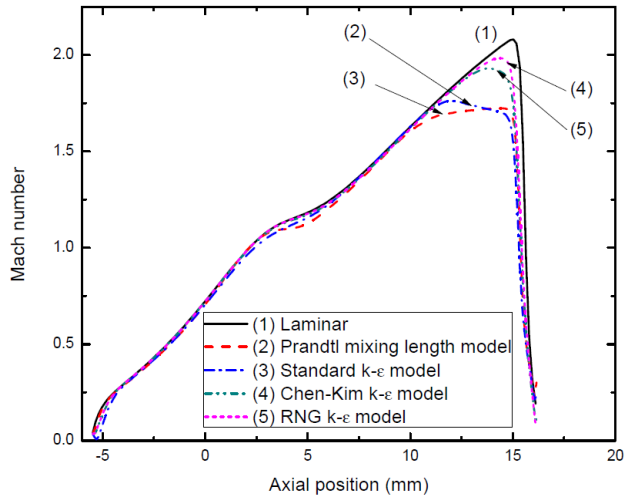

(b)

Figure 4.14. Variations of Mach number and pressure along Line AA' computed by five flow models at 50 A DC. P_0=11.2 atm. (a) Mach number distribution and (b) pressure distribution.

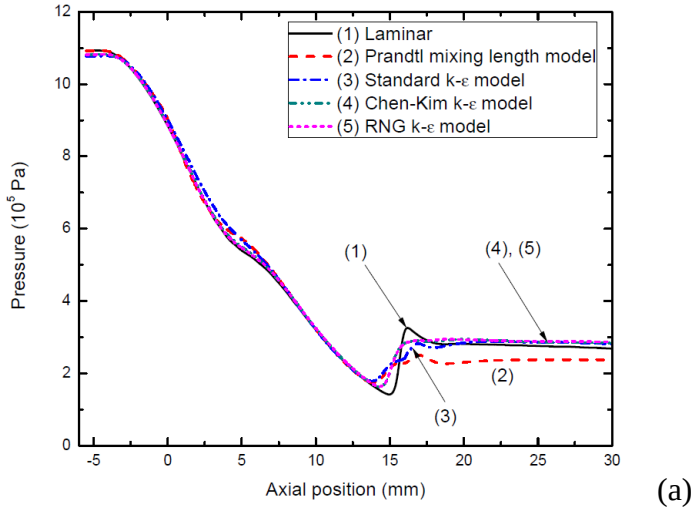

(a)

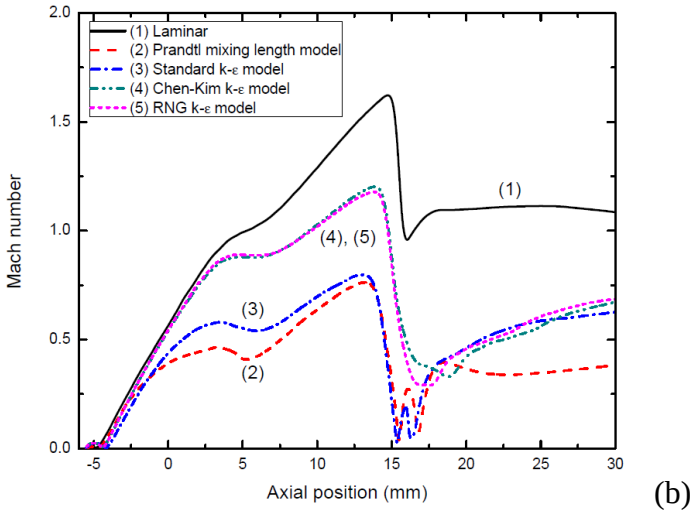

(b)

Figure 4.15. Variations of Mach number and pressure along the nozzle axis computed by five flow models at 50 A DC. P_0=11.2 atm. (a) Mach number distribution and (b) pressure distribution.

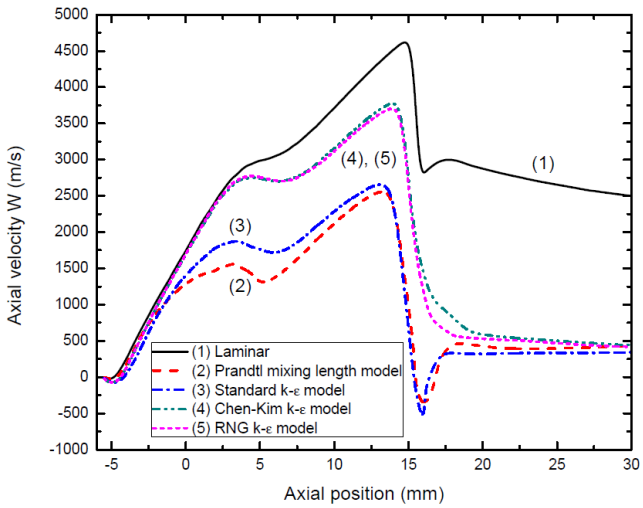

Figure 4.16. Axial velocity distributions along the nozzle axis computed by various turbulence models at 50 A DC and P_0=11.2 atm.

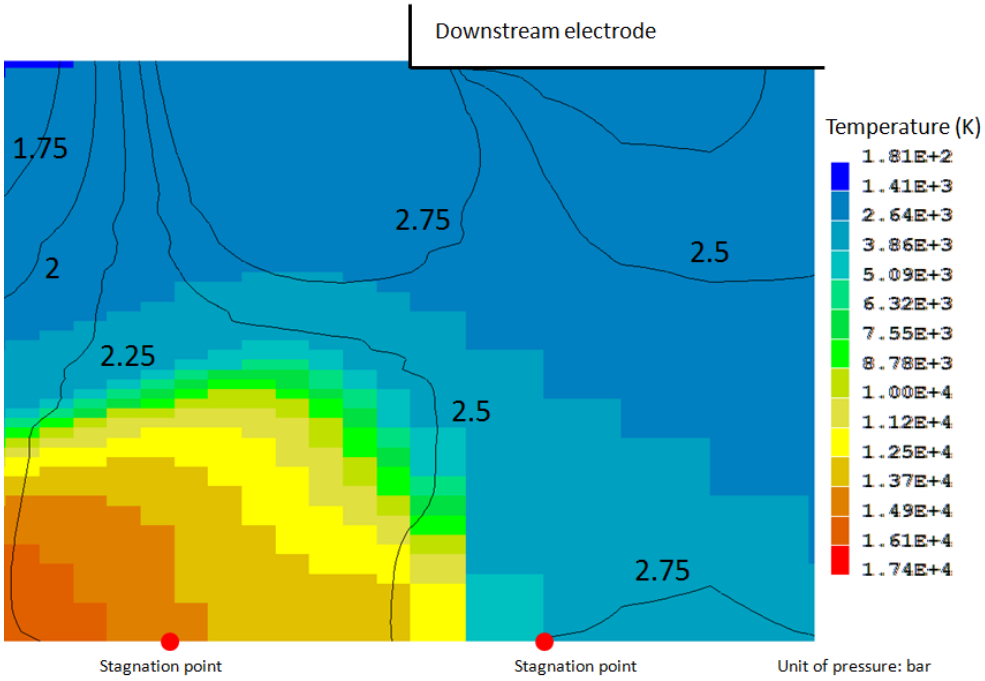

(a)

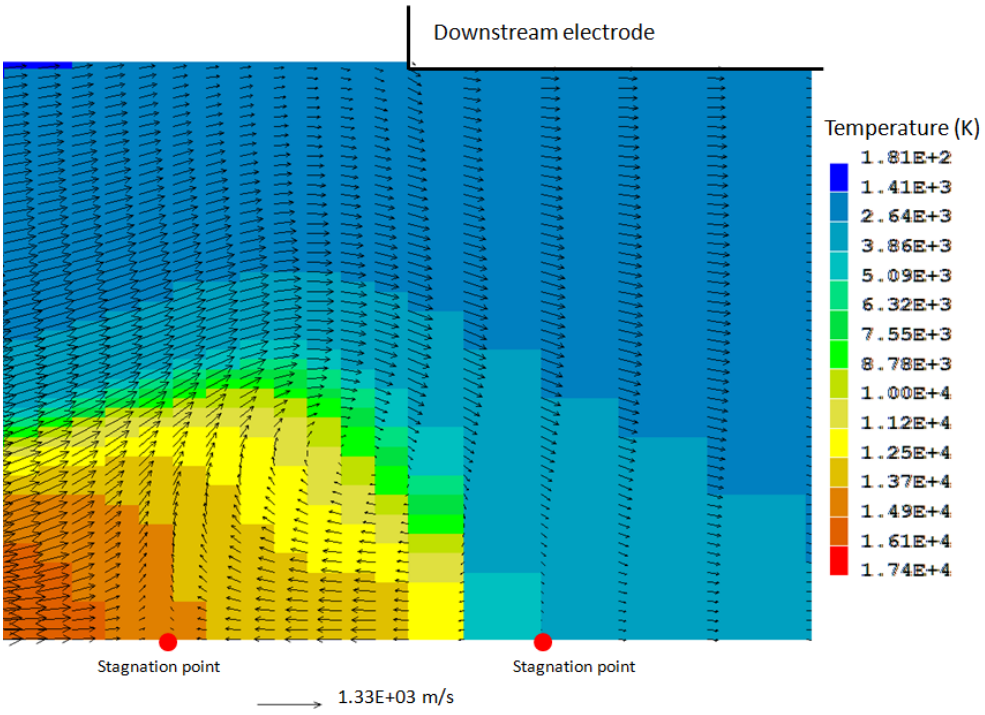

(b)

Figure 4.17. Flow field near the downstream electrode obtained by the standard k-epsilon model at 50 A DC. P_0=11.2 atm. (a) Temperature contour together with pressure isobars and (b) plot of velocity vector.

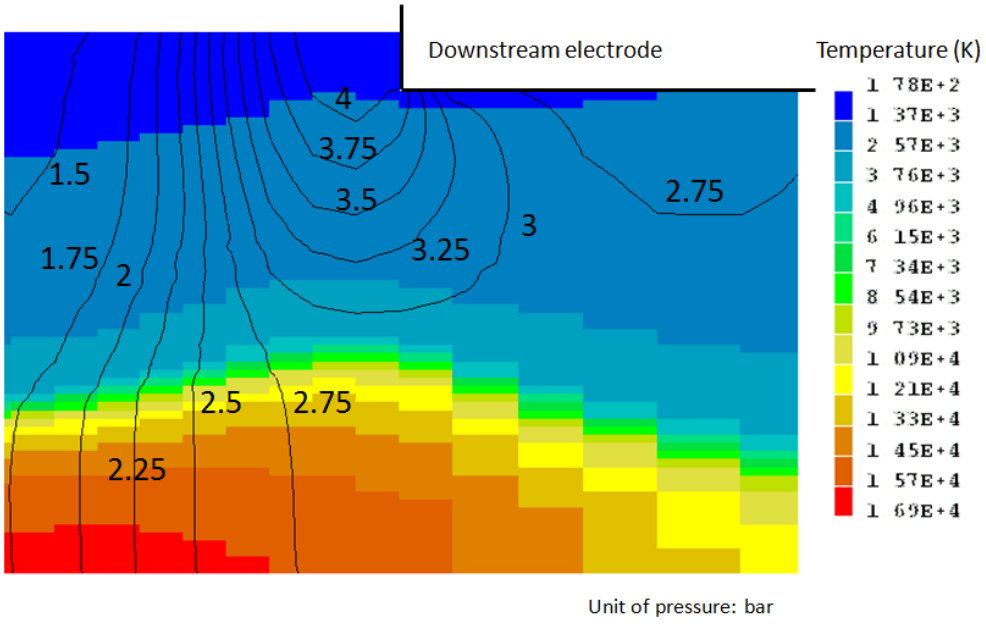

(a)

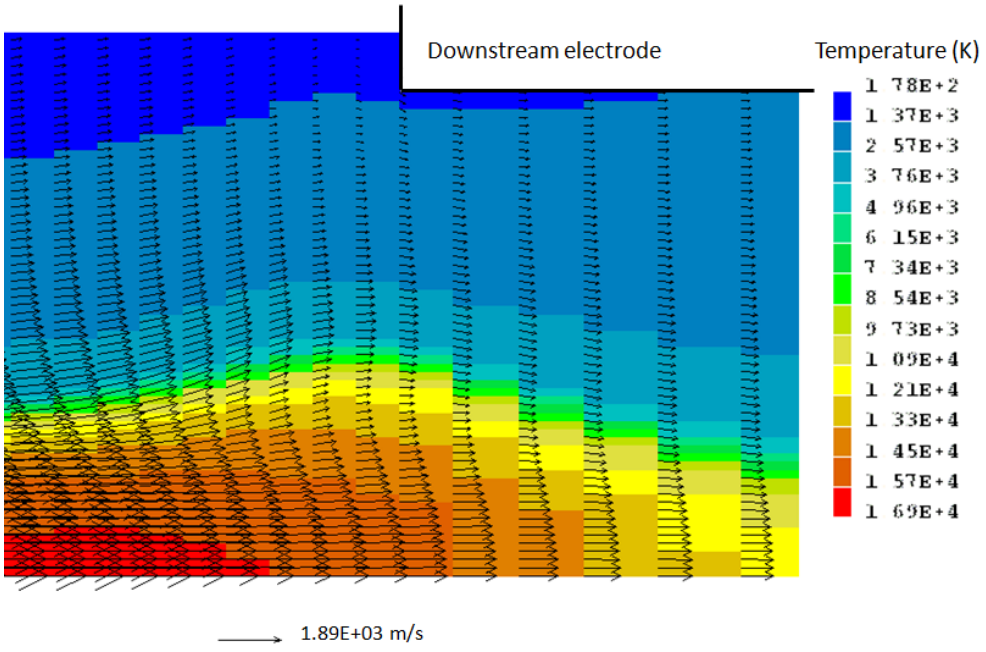

(b)

Figure 4.18. Flow field near the downstream electrode obtained by the Chen-Kim k-epsilon model at 50 A DC. P_0=11.2 atm. (a) Temperature contour together with pressure isobars and (b) plot of velocity vector.

The presence of the arc also affects the wake region near the upstream electrode tip. At 1 kA DC, the wake no longer exists due to the presence of the arc. When the current is reduced, the wake and flow circulating regions reappear as shown in Figure 4.19. Caution should be exercised regarding the accuracy of the prediction by

various flow models used in the present investigation. As previously indicated, the flow in the regions close to the electrodes is dependent on the flow models. In the absence of experimental results for the verification of the flow models our discussion can only be regarded as qualitative in nature. However, the influence of the two electrode regions on the arc and the flow in the rest of the nozzle is small. They hardly affect the arc voltage as the voltage taken up by these two regions is negligible in comparison with the total arc voltage.

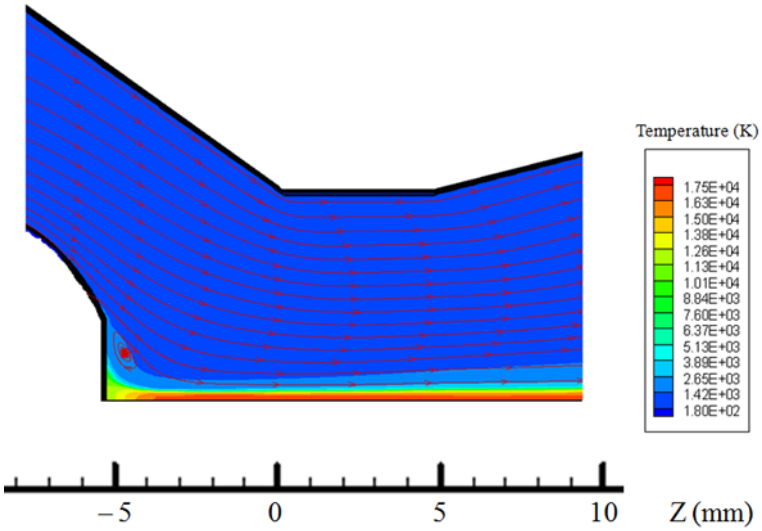

Figure 4.19. Temperature distribution together with the streamlines near the upstream electrode at 50 A DC and at P_0=11.2 atm.

4.3.2.2 DC Arc V-I Characteristics

The DC voltage-current (V-I) characteristics of the nozzle arc computed by various flow models (Figure 4.20) are typical of high pressure arcs. When the current is large (600 A and above), the arc voltage is almost independent of current (the flat part of V-I characteristics). For small currents, it exhibits negative V-I characteristics. The spread in arc voltages of the flat part of the V-I characteristics predicted by all five flow models differ by less than 15% of the mean voltage. The mean voltage at a given current is the average of the voltages computed by the five flow models. This implies that turbulence does not play a dominant role in the determination of the arc voltage. At low currents, the arc voltage strongly depends on the flow models and the

aforementioned spread increases to 35% of the mean at 50 A (Figure 4.20). The physical processes responsible for these features of the V-I characteristics and the voltage spread by various flow models are discussed in the following two subsections.

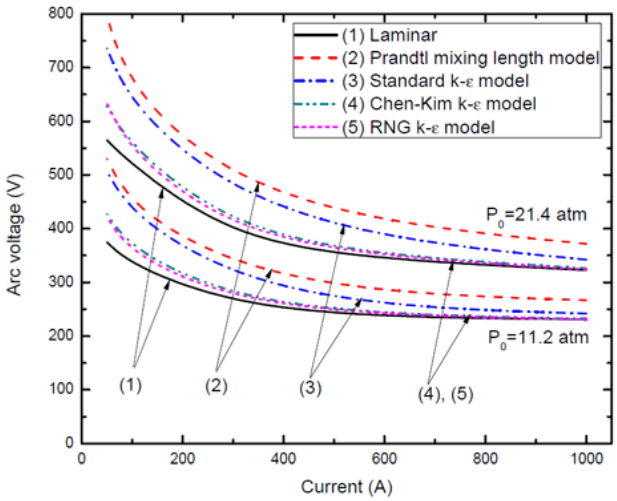

Figure 4.20. The voltage-current (V-I) characteristics for the DC arcs computed by the five flow models at two stagnation pressures.

4.3.2.3 Characteristics of the Nozzle Arc with Radiation Dominated High Temperature Core

Examination of the computational results for the flat part of the V-I characteristics given by various flow models shows that the axis temperature for currents 600 A and above is not sensitive to current. Typical axial variation of axis temperature for this current range is shown in Figure 4.21(a) although the results are for 1 kA. Excluding the regions close to the two electrodes, the axis temperature difference calculated by the different flow models is less than 5% of the mean temperature. The arc radius as defined by the radial position of the 4000 K isotherm is found to be proportional to the square root of the current (Figure 4.21(b)) for a given stagnation pressure.

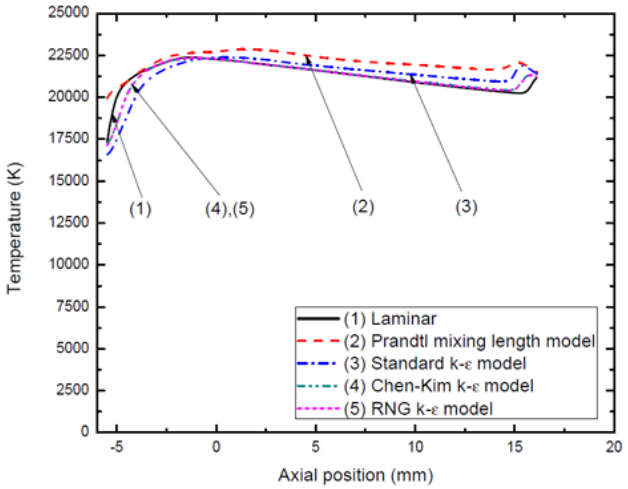

(a)

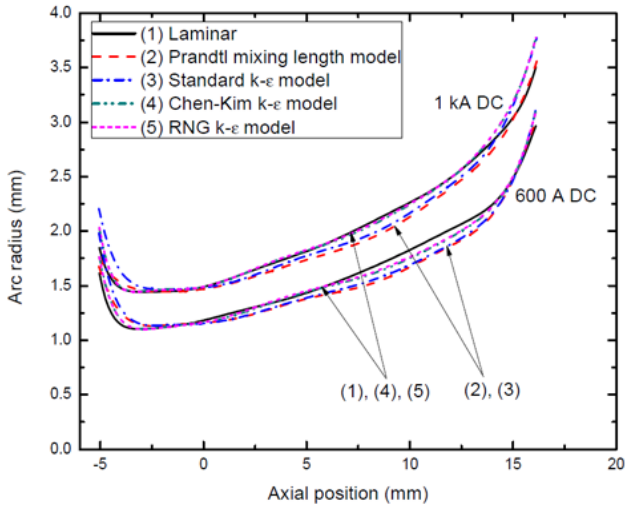

(b)

Figure 4.21. Variations of axis temperature and arc radius computed by five flow models for currents 600 A and above at P_0=11.2 atm. (a) Axis temperature at 1 k A DC and (b) arc radius at 1 kA DC and 600 A DC.

The electrical field at an axial position not only depends on the axis temperature and arc radius but also on the radial temperature profile. Typical radial temperature profiles are given in Figure 4.22 which shows the temperature profiles at 1 kA DC for two typical axial positions corresponding to the nozzle throat region (Z=2.3 mm) and the region downstream of the nozzle throat (Z=7.9 mm). The temperature profile inside the arc core is rather flat. The boundary of the arc core is defined as the radial position corresponding to a temperature of 83.3% of the axis temperature [4.5] (henceforth known as the core boundary). Such flat temperature profile indicates that, within the core, radiation transport is dominant. On the axis, Ohmic input is balanced by net radiation loss, which determines the axis temperature for known Ohmic input.

The energy balance at the core boundary for the whole arc is given in Table 4.1 for all flow models used.

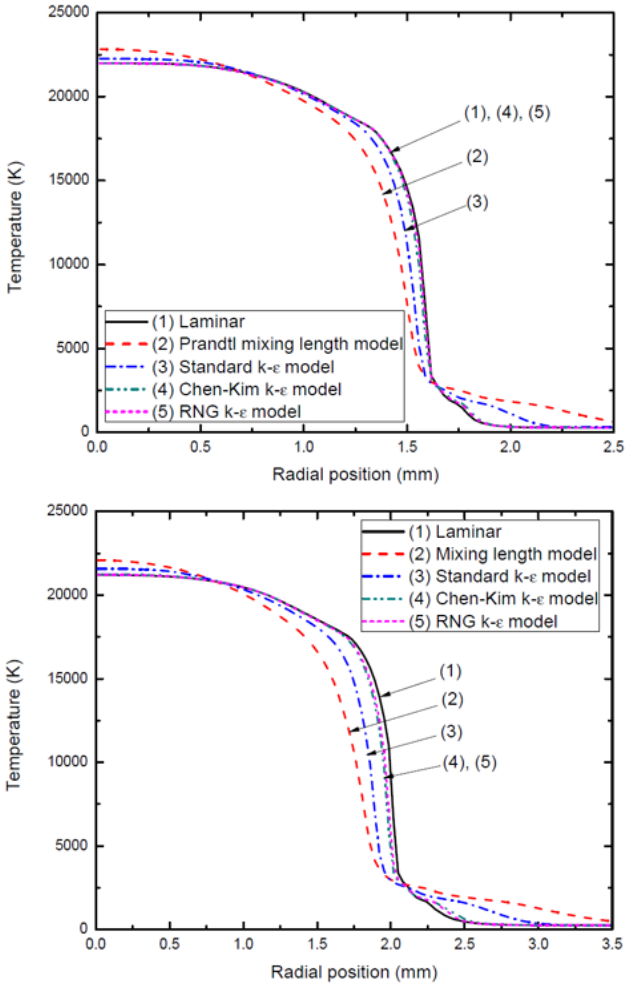

Figure 4.22. Radial temperature profiles at two axial positions computed by five flow models at 1 kA DC and at P_0=11.2 atm. (a) Z=2.3 mm and (b) Z= 7.9mm.

Table 4.1 shows that for all flow models the dominant energy loss process is due to radiation. For the Prandtl mixing length model and the standard k-epsilon model, radial thermal conduction (nearly all due to turbulent heat conduction) accounts respectively for 24.3% and 13.8% of Ohmic input. Thus, the radial temperature gradients of the profiles predicted by these two models are greater than those predicted by other flow models as shown in Figure 4.22. The results of Chen-Kim model and those of RNG model are almost identical which are in turn very close to the results given by the laminar flow model. Although there is a large difference between the relative importances of various energy loss processes predicted by the

five flow models (Table 4.1), the differences in electrical power input predicted by different flow models are very small. This is due to the very small differences in axis temperatures and in the core sizes (Figure 4.22) computed by various flow models. This results in nearly equal arc conductance. Since 80% of the current is carried by this core, the arc voltages predicted by various flow models are, therefore, very close to each other.

Table 4.1. Percentage of electrical power input associated with various energy transport processes for the whole arc length at the core boundary calculated by five flow models at 1 kA DC and P_0=11.2 atm. The power associated with the pressure work is not shown as it only accounts for 5 to 7% of the power input. This applies to all tables. Positive means power input and negative power loss.

Model	Power input (10^5 W)	Radial thermal conduction	Radiation loss	Axial enthalpy convection	Radial enthalpy convection
(1)	1.89	-4.1%	-67.7%	-19.1%	-1.7%
(2)	1.88	-24.3%	-62.8%	-4.5%	-4.3%
(3)	1.90	-13.8%	-66.8%	-10.9%	-4.0%
(4)	1.87	-4.8%	-70.1%	-15.3%	-4.8%
(5)	1.87	-4.6%	-70.1%	-15.1%	-5.0%

Method of calculation: $\text{Power input} = \int_{Z1}^{Z2}\left[\int_0^R \sigma E^2 2\pi r dr\right]dz$,

$$\text{Radiation loss} = -\int_{Z1}^{Z2}\left[\int_0^R q 2\pi r dr\right]dz \Big/ \text{Power input},$$

$$\text{Radial thermal conduction} = \int_{Z1}^{Z2}\left[\int_0^R \frac{1}{r}\frac{\partial}{\partial r}\left(r\frac{k}{c_p}\frac{\partial h}{\partial r}\right)2\pi r dr\right]dz \Big/ \text{Power input}$$

$$\text{Axial enthalpy convection} = -\int_{Z1}^{Z2}\left[\int_0^R \rho w\frac{\partial h}{\partial z}2\pi r dr\right]dz \Big/ \text{Power input}$$

$$\text{Radial enthalpy convection} = -\int_{Z1}^{Z2}\left[\int_0^R \rho v\frac{\partial h}{\partial r}2\pi r dr\right]dz \Big/ \text{Power input}$$

where *R* refers to the radial position of the core boundary or electrical boundary (table 4.2) and (Z2-Z1) the arc length.

Key to the models: (1) Laminar flow model, (2) Prandtl mixing length model, (3) Standard k-epsilon model, (4) Chen-Kim k-epsilon model and (5) RNG k-epsilon model.

To assess the influence of turbulence, we need to know the arc energy balance at the electrical boundary. This is because between the arc core boundary and the electrical boundary, nearly 80% of the radiation flux coming out of the arc core is absorbed in this region, thus altering the energy balance. Table 4.2 shows how electrical power input into the electrically conducting core is balanced by various energy transport processes.

Table 4.2. Percentage of electrical power input associated with various energy transport processes for the whole arc length at the electrical boundary calculated by five flow models at 1 kA DC and P_0=11.2 atm. Mathematical expressions for power input and power loss and the key to the models are the same as those in Table 4.1.

Model	Power input (10^5 W)	Radial thermal conduction	Radiation loss	Axial enthalpy convection	Radial enthalpy convection
(1)	2.29	-1.2%	-25.1%	-91.9%	24.7%
(2)	2.65	-50.6%	-12.2%	-48.7%	17.9%
(3)	2.41	-30.6%	-18.3%	-66.4%	23.2%
(4)	2.30	-8.8%	-23.5%	-82.6%	22.8%
(5)	2.29	-8.2%	-23.6%	-83.1%	22.4%

Due to the radiation absorption, the energy balance at the electrical boundary has been greatly altered in comparison with that at the core boundary. For laminar flow, Chen-Kim and RNG models, electrical power input is balanced by radiation and axial and radial convections while thermal conduction has the least influence on energy balance. For the Prandtl mixing length model and the standard k-epsilon model, radial thermal conduction and axial convection are the most important energy loss processes although the turbulence effect as predicted by the Prandtl mixing length model is much stronger than that of the standard k-epsilon model.

The modifications to the dissipation rate equation of the standard k-epsilon model by Chen-Kim and RNG models are intended to increase the dissipation rate, thus reducing the turbulence. The complex non-linear interactions between average turbulent kinetic energy, the mean flow, and the dissipation rate result in a much reduced average kinetic energy (Figure 4.23) and dissipation rate (Figure 4.24) for

Chen-Kim and RNG models as compared with those of the standard k-epsilon model. It should be noted that turbulence intensity increases towards the downstream electrode due to the axial development of turbulence (Figure 4.23(b)).

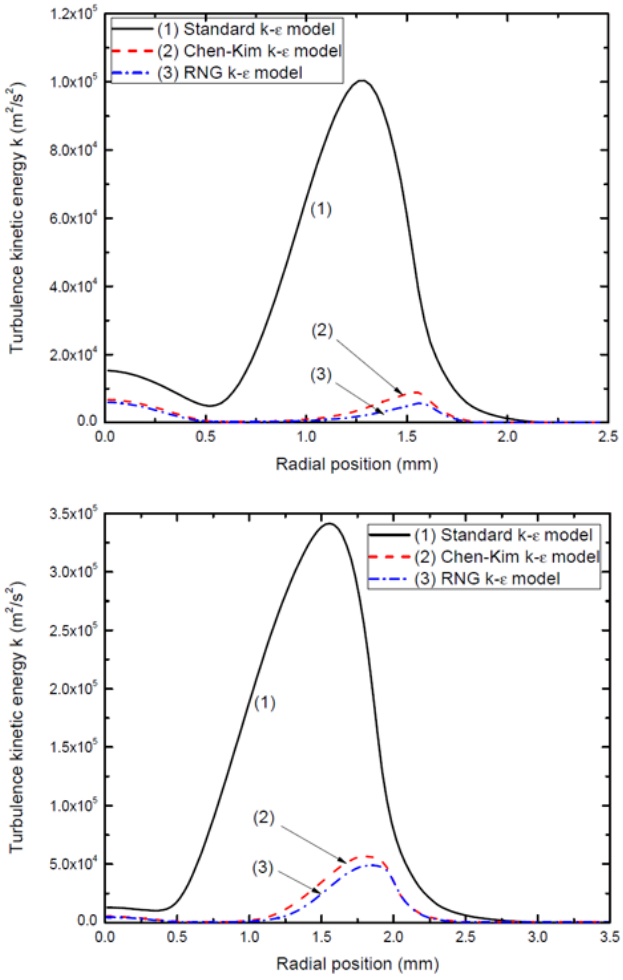

Figure 4.23. Radial profiles of turbulence kinetic energy at two axial positions computed by three flow models at 1 kA DC and at P_0=11.2 atm. (a) Z=2.3 mm and (b) Z= 7.9mm.

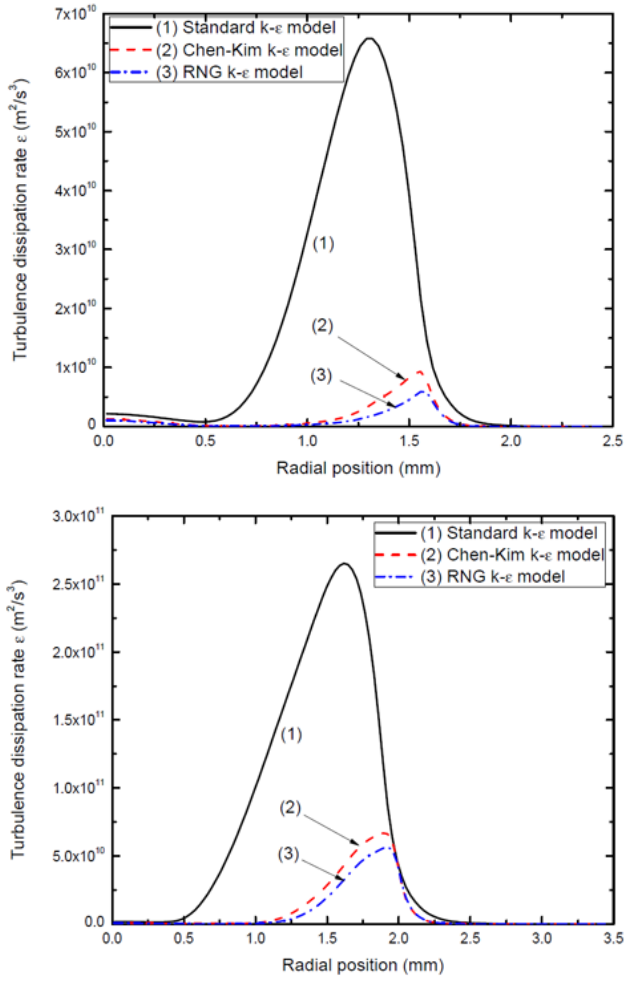

Figure 4.24. Radial profiles of turbulence dissipation rate at two axial positions computed by three flow models at 1 kA DC and at P_0=11.2 atm. (a) Z=2.3 mm and (b) Z= 7.9mm.

The radial distributions of the average turbulent kinetic energy and the dissipation rate have two peaks, one of which is on the nozzle axis and the other in the region where velocity reduces rapidly (Figure 4.25). Careful examination of the results show that the first peak on the nozzle axis is attributed to the axial gradient of axial velocity (dw/dz) and the other peak is due to the large radial gradient of axial velocity (Figure 4.25). Both velocity gradients affect the distributions of the average turbulent kinetic energy and the dissipation rate through the rate of generation of turbulent kinetic energy given by Equation (3.31).

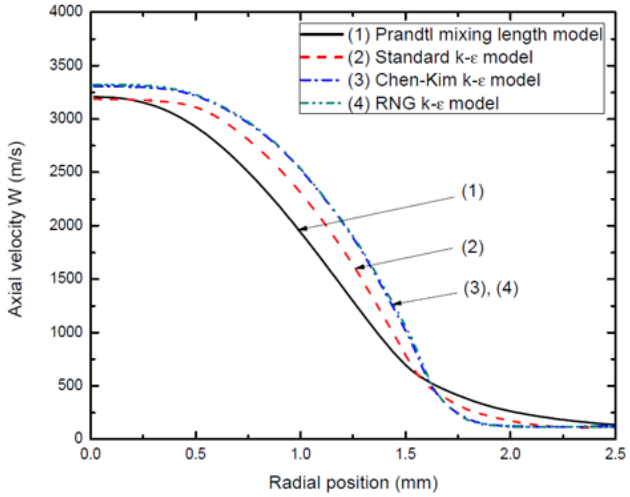

Figure 4.25. Radial profiles of axial velocity at two axial positions computed by four flow models at 1 kA DC and at P_0=11.2 atm. (a) Mid nozzle throat (Z=2.3 mm) and (b) Z= 7.9mm.

Turbulence enhanced momentum and energy transports are determined respectively by eddy viscosity μ_t and k_t / c_p in momentum and energy conservation equations. Since k_t / c_p is directly related to μ_t through turbulent Prandtl number, it is sufficient to examine μ_t (Figure 4.26) in order to see why the four turbulences models give widely different turbulence levels. Chen-Kim and RNG models give the smallest values of μ_t,, hence the lowest level of turbulence. The Prandtl mixing length model has the largest μ_t because of the adoption of the thermal radius of the arc as the turbulence length scale, which is larger than the length scales computed by the other three turbulence models (Figure 4.27). μ_t inside the arc core computed by the four turbulence models are all very low. This means that the large eddies

generated in the region where radial velocity gradient is high cannot easily penetrate the arc core region, thus rendering radiation transport being dominant.

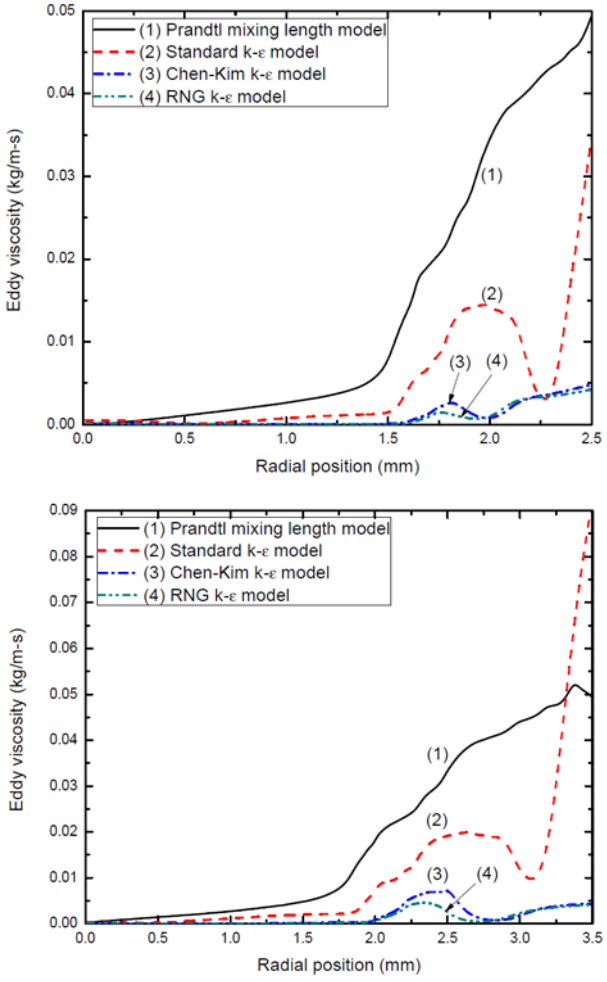

Figure 4.26. Radial profiles of the eddy viscosity (μ_t) at two axial positions computed by four flow models at 1 kA DC and at P_0=11.2 atm. (a) Z=2.3 mm and (b) Z= 7.9mm.

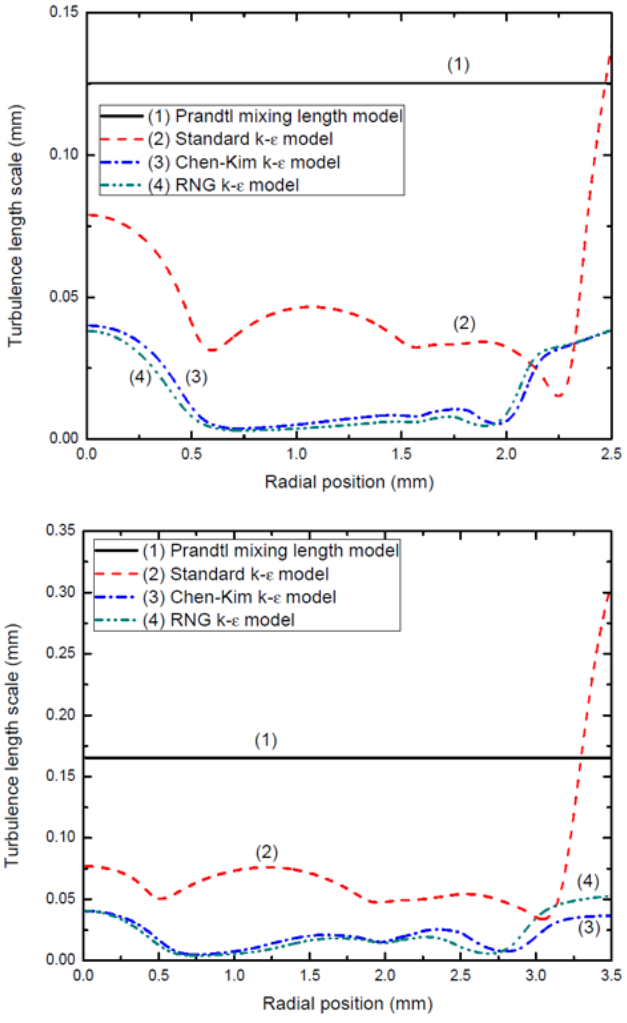

Figure 4.27. Radial profiles of turbulence length scale at two axial positions computed by four flow models at 1 kA DC and at P_0=11.2 atm. (a) Z=2.3 mm and (b) Z= 7.9mm.

Arcs in the current range corresponding to the flat part of V-I characteristics exhibit similar features to those of the 1 kA DC arc. For the flat part of the V-I characteristic, Ohmic input on the axis is entirely balanced by radiation. When current is reduced, the required adjustment in axis temperature in order for the net radiation loss to balance the reduced Ohmic input is very small. This is because for a small change in temperature, net radiation loss of SF_6 changes by a large amount for temperatures above 20000 K [4.12]. This explains why the axis temperature of a 600 A arc is almost the same as that of 1 kA. Since the arc cross section is proportional to the current and the arc temperature within the core is not sensitive to the current, the arc voltage is, therefore, almost independent of the current.

4.3.2.4 Characteristics of the Nozzle Arc with Radiation and Thermal Conduction Dominated High Temperature Core

The arc voltage increases with decreasing current for currents below 600 A. The axis temperature at 300 A is reduced to 17000 K (Figure 4.28) due to reduced Ohmic input. When the arc size is reduced, radial thermal conduction in the high temperature core is expected to become more important for two reasons: firstly, the relative importance of thermal conduction (energy taken out from a surface) to radiation loss (energy loss related to the volumetric effect) is inversely proportional to the arc radius, and, secondly, net radiation loss decreases rapidly with temperature for temperature below 18000 K [4.12]. In the core region, thermal conduction is appreciable (Table 4.3). The radial temperature profile in the high temperature core is no longer flat especially near the core boundary (Figure 4.29). There is considerable radial temperature gradient inside the arc core (figure 4.29). It has also been found that the dependence of arc cross section on current is stronger than the linear relationship found for the flat part of the V-I characteristics. Thus, the rate of reduction in arc conductance due to decreases in arc temperature and in arc radius is faster than the rate of current reduction. Therefore, arc voltage increases with decreasing current giving rise to negative V-I characteristics.

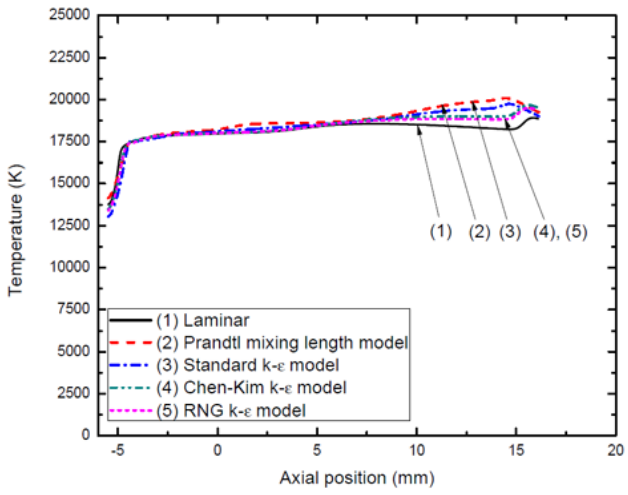

Figure 4.28. Variations of axis temperature at 300 A DC and P_0=11.2 atm.

Table 4.3. Percentage of electrical power input associated with various energy transport processes for the whole arc length at the core boundary calculated by five flow models at 50 A DC and P_0=11.2 atm. Mathematical expressions for power input and power loss and the key to the models are the same as those in Table 4.1.

Model	Power input (10^4 W)	Radial thermal conduction	Radiation loss	Axial enthalpy convection	Radial enthalpy convection
(1)	1.72	-24.9%	-66.7%	-3.5%	-0.82%
(2)	2.08	-54.9%	-46.0%	2.5%	1.1%
(3)	2.13	-47.1%	-51.4%	-0.7%	1.3%
(4)	1.91	-34.0%	-61.8%	-1.2%	0.05%
(5)	1.89	-34.7%	-61.3%	-1.0%	0.15%

Detailed energy balance calculations at the high temperature core boundary by various flow models (Table 4.3) at 50 A DC confirm the dominance of thermal conduction and radiation. For the laminar flow model and turbulent flow models other than the Prandtl mixing length model, radiation at the core boundary is still the most important energy loss mechanism. Energy balance at the electrical boundary (Table 4.4) reveals that for the Prandtl mixing length model and the standard k-epsilion model, turbulent thermal conduction is the dominant energy loss process, while for laminar flow and the Chen-Kim and RNG models, radiation loss is the most important. The reason for such a difference in dominant energy loss mechanisms between different flow models is the intensity of turbulence. Turbulence intensity is determined by the eddy viscosity. Radial profiles of eddy viscosity at two axial positions are given in Figure 4.30 with μ_t predicted by the Prandtl mixing length model the largest. It should also be noted that at the electrical boundary axial convection is nearly balanced by radial convection (Table 4.4).

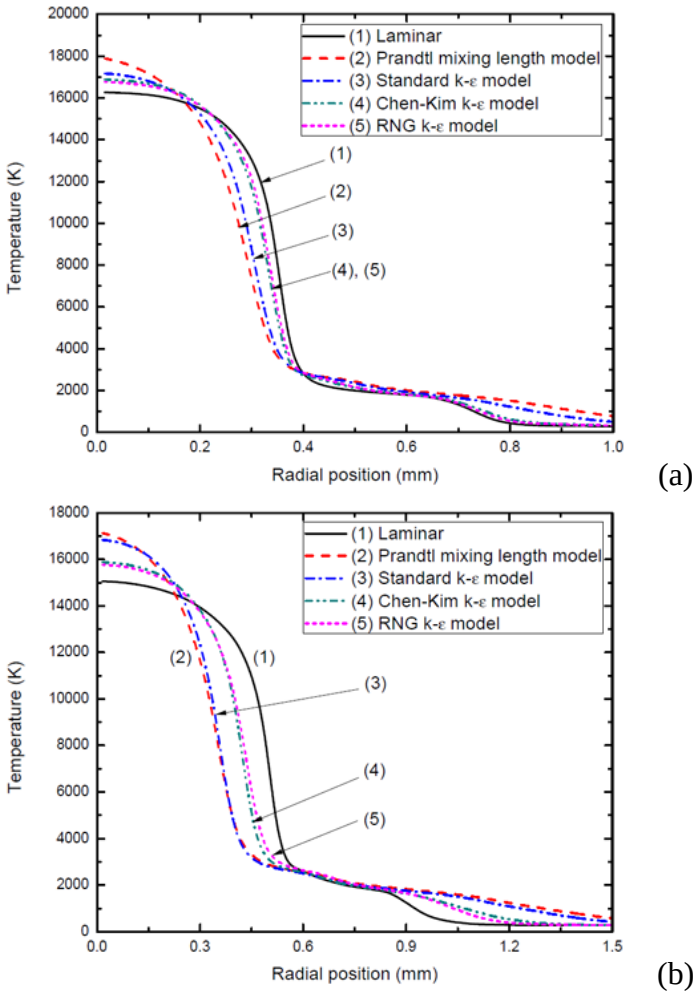

Figure 4.29. Radial temperature profiles computed by the four turbulence models at two axial positions at 50 A DC. P_0=11.2 atm. (a) Z=2.3 mm and (b) Z=7.9mm.

Table 4.4. Percentage of electrical power input associated with various energy transport processes for the whole arc length at the electrical boundary calculated by five flow models at 50 A DC and P_0=11.2 atm. Mathematical expressions for power input and power loss and the key to the models are the same as those in Table 4.1.

Model	Power input (10^5 W)	Radial thermal conduction	Radiation loss	Axial enthalpy convection	Radial enthalpy convection
(1)	1.87	-4.3%	-56.6%	-67.7%	32.7%
(2)	2.62	-62.6%	-31.1%	-17.2%	13.6%
(3)	2.51	-55.8%	-38.7%	-15.9%	14.2%
(4)	2.13	-33.8%	-50.0%	-31.0%	18.8%
(5)	2.12	-35.5%	-48.9%	-30.0%	18.3%

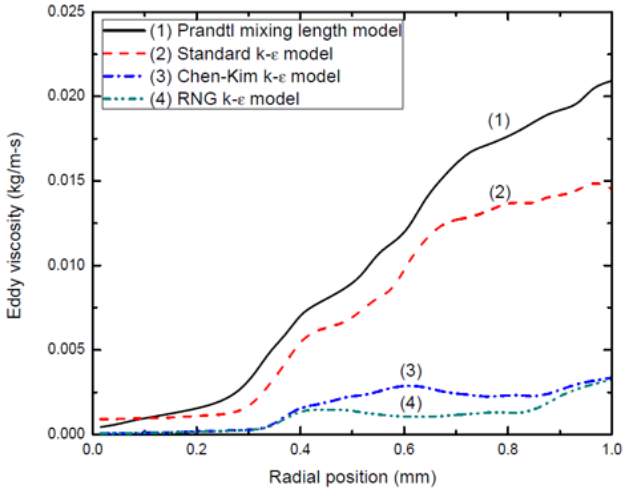

(a)

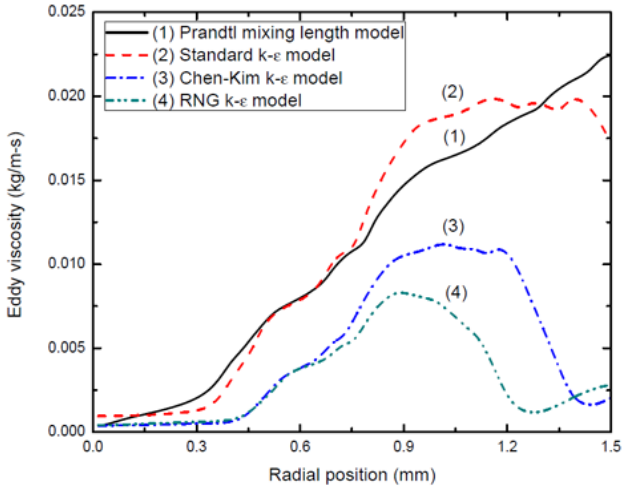

(b)

Figure 4.30. Radial profiles of the eddy viscosity at two axial positions computed by five flow models at 50 A DC and at P_0=11.2 atm. (a) Z=2.3 mm and (b) Z= 7.9mm.

4.3.2.5 The Effects of the Stagnation Pressure

For higher stagnation pressures (e.g. P_0=21.4 atm), the qualitative features of the arc and its surrounding flow are similar to those of 11.2 atm for all flow models used. Within the range of current investigated (50 A to 1 kA), the arc voltage is found to be approximately proportional to the square root of the stagnation pressure irrespective of the flow models (figure 4.21). This is in agreement with the voltage-stagnation pressure scaling law derived from the arc integral analysis [4.10]. The axis temperature does not appear to be sensitive to the stagnation pressure for a given current, while the arc radius is found to be inversely proportional to $(P_0)^{0.25}$.

Relative importance of various energy transport processes at the core boundary and at the electrical boundary remain the same as those given in Tables 4.1 to 4.4 although the percentage of electrical power taken out by radiation loss is slightly increased due to increased radiation with pressure and reduction in arc size.

4.4 Concluding Remarks

The cold flow and the arc under direct currents burning in Nozzle 2 with fixed stagnation pressure have been investigated computationally using five flow models given in Chapter 3.

For the cold flow, the computational results for different flow models are nearly the same except in the region close to the two electrodes. There is a bow shock in front of the downstream hollow electrode and a wake near the tip of the upstream electrode. However, the size of the wake and the strength and the structure of the shock differ widely between flow models. The implications of the wake and shock on dielectric breakdown have been discussed.

The V-I characteristic of the nozzle arc consists of a flat part (current not less than 600A) where the arc voltage is independent of current and a part with negative V-I characteristic where the arc voltage rises when current is reduced. The reasons for the shape of the V-I characteristic are explained for the first time. On the flat part of the V-I characteristic, radiation is the dominant energy transport process within the arc core where 80% of the current is conducted. Turbulence has little influence on the arc voltage. Thus, arc voltage at high current is not an effective means for the verification of flow models. When current is reduced below 600A, thermal conduction and radiation inside the arc core are dominant energy transport mechanisms. Arc voltage depends on the flow model and there is a large difference between the voltage predicted by the Prandtl mixing length model and that by laminar flow model. A detailed examination is conducted to find the causes why the turbulence intensities predicted by different turbulence models vary a great deal.

References

[4.1] Benenson D M, Frind G, Kinsinger R E, Nagamatsu H T, Noeske H O and Sheer, Jr R E 1980 Fundamental investigation of arc interruption in gas flows EPRI EL-1455 (Project 246-2)

[4.2] Frind G, Kinsinger R E, Miller R D, Nagamatsu H T and Noeske H O 1977 Fundamental investigation of arc interruption in gas flows EPRI EL-284 (Project 246-1)

[4.3] Frind G and Rich J A 1974 Recovery speed of axial flow gas blast interrupter: dependence on pressure and di/dt for air and SF_6 *IEEE Trans. Power Appar. Syst.* **93** 1675-84

[4.4] Zhang Q, Yan J D and M T C Fang 2012 Modelling of turbulent arc burning in a supersonic nozzle *Proc. Int. Conf. on 19th Gas Discharges and Their Applications (Beijing, China (2-7 Sept 2012)) (High Voltage Engineeing: Special Issue on Gas Discharges and Their Applications* vol 38*)* ed Z C Guan (Wuhan: High Voltage Engineering) pp 202-5

[4.5] Zhang J F, Fang M T C and Newland D B 1987 Theoretical investigation of a 2kA arc in a supersonic nozzle *J. Phys. D: Appl. Phys.* **20** 368-79

[4.6] Anderson J D 2003 *Modern compressible flow* 3rd edn (New York: McGraw-Hill)

[4.7] Shayler P J and Fang M T C 1980 Flow near the upstream electrode of gas-blast circuit breakers *IEE Proc. Generat., Transmiss. Distrib.* **127** 26–32

[4.8] Balabel A, Hegab A M, Nasr M and Samy M El-Behery 2011 Assessment of turbulence modeling for gas flow in two-dimensional convergent-divergent rocket nozzle *Applied Mathematical Modelling*. **35** 3408-22

[4.9] Yan J D, Fang M T C and Liu Q S 1997 Dielectric breakdown of a residue SF_6 plasma at 3000 K under diatomic equilibrium *IEEE Trans. Dielectrics and Electrical Insulation*. **4** 114-9

[4.10] Fang M T C, Ramakrishnan S and Messerle H K 1980 Scaling laws for gas-blast circuit-breaker arcs during the high current phase *IEEE Trans. Plasma Sci*. **PS-8** 357-62

[4.11] Zhang J L, Yan J D, Murphy A B, Hall W and Fang M T C 2002 Computational investigation of arc behaviur in an auto-expansion circuit breaker contaminated by ablated nozzle vapor *IEEE Trans. Plasma Sci*. **30 (2)** 706-19

[4.12] Liebermann R W and Lowke J J 1976 Radiation emission coefficients for sulfur hexafluoride arc plasmas *J. Quant. Spectrosc. Radiat. Transf.* **17** 253-64

[4.13] Stephens R W B and Bate A E 1966 *Acoustics and Vibrational Physics* (New York, NY: St. Martin's Press)

Chapter 5
The Modelling of a Turbulent SF_6 arc in a Supersonic Nozzle: Part II. Current Zero Behaviour of the Nozzle Arc

5.1 Introduction

The investigation presented in this chapter forms the second part of a systematic investigation into the behaviour of SF_6 nozzle arc (hereafter referred to as Part II). Part II is exclusively concerned with the arc behaviour during current zero period under a current ramp specified by a rate of current decay (di/dt) before current zero and a voltage ramp (dV/dt) after current zero.

The features of the cold flow (in the absence of the arc) and the DC voltage-current characteristics of the SF_6 arc burning in Nozzle 2 used in the experiments of Benenson et al. [5.1] are the subject matter in Part I of the investigation (Chapter 4). Altogether five flow models, which are the laminar flow model, the Prandtl mixing length model, the standard k-epsilon model and its two variants, the Chen-Kim model and the RNG model, have been used in Part I. It has been shown in Part I that for current higher than 600 A, radiation transport is the dominant energy transport mechanism. Arc voltages predicted by different flow models differ within 15% of the mean arc voltage, which is well within the experimental scatter. For currents below 600 A, turbulence enhanced thermal conduction within the electrically conducting core gradually becomes the dominant energy transport process. Arc voltages predicted by different flow models are found to be strongly dependent on the flow models.

The five flow models will again be used in Part II to study the arc behaviour during current zero period and to compute the thermal interruption capability of

Nozzle 2 in terms of the RRRV. The experimental conditions of [5.1] which are studied in this chapter, and the measured RRRV, are reviewed in Section 3.6 of Chapter 3. Comparison between the computed and measured RRRV at three stagnation pressures (P_0=11.2 atm, 21.4 atm and 35 atm) and two rates of current decay (di/dt=13 $A\mu s^{-1}$ and $25A\mu s^{-1}$) will be used to judge the relative merits of the flow models.

This chapter is organized as follows. Discussions of the computational results are given in Section 5.2, where an analysis of the physical mechanisms encompassed in each turbulence model is also given to show the adequacy of a particular turbulence model in describing the rapidly varying arc during current zero period. Section 5.3 presents the comparison between the computed and measured RRRV. Relative merits of turbulence models used are discussed in Section 5.4. Finally, appropriate conclusions are drawn.

5.2 Results and Discussion

Computation has been performed on Nozzle 2 used by Benenson et al. [5.1], the geometry and the grid system of which have been given in Figure 4.1. At the nozzle inlet three stagnation pressures, P_0=11.2 atm, 21.4 atm and 35 atm, have been applied. At the nozzle exit, the static pressure P_e is set to a very low value to guarantee shock free inside the nozzle in the absence of the downstream electrode. The current is ramped down to zero with a fixed rate of decay, di/dt, from a DC plateau (I_0) of 1 kA. Two rates of current decay, di/dt=13 $A\mu s^{-1}$ and 25 $A\mu s^{-1}$, have been investigated. After current zero, a linearly increasing voltage ramp, dV/dt, is applied to investigate the thermal interruption capability of the nozzle arc. Before the current is reduced, the arc is assumed to be in a steady state. With the choice of 1 kA as the current plateau (I_0), the arc is still in quasi-steady state immediately after the current is ramped down. Therefore, the choice of 1 kA ensures that the arc at current zero is independent of I_0.

For the Prandtl mixing length model, the turbulence length scale (λ_c) is related

to the thermal radius of the arc (r_δ) through an adjustable parameter *c* (Section 3.5.1 of Chapter 3). The value of *c* is adjusted to give the closest agreement with the measured RRRV for P_0 = 21.4 atm and di/dt= 25 $A\mu s^{-1}$. This value of *c* was 0.048 as mentioned in Chapter 4. At this point, it is necessary to introduce a modification made to the calculation of arc's thermal radius which determines the turbulence length scale and the choice of *c*, and, the reason for such a modification. Previously, to determine the value of T_∞ in Equation (3.22) (given in Section 3.6.1 of Chapter 3) and the boundary for integration ("∞" the upper boundary for integration of Equation (3.22)), we search in the positive *r*-direction from the arc axis to the nozzle wall for the radial position where the minimum temperature is located. The value of T_∞ is then this minimum temperature and "∞" standards for the radial position corresponding to this minimum temperature which is normally near the nozzle wall. However, it has been found that the computed temperature distribution close to the nozzle wall is not very reasonable due to application of large grid size in this region. Such computational problem can be solved using very fine grid size near the nozzle wall, which is however not necessary for two reasons: firstly, for currents not exceeding 1 kA (always the case in all the investigations for this thesis), the predicted arc characteristics is not sensitive to the solution near the nozzle wall due to the fact that the area of the arc cross section is very small in comparison with the area of the nozzle cross section as mentioned in Section 4.3.2.1 of Chapter 4 (thus the arc boundary is far away from the nozzle wall), and, secondly, it is computationally expensive to use fine grid size.

Nevertheless, since the values of temperature near the nozzle wall, which are to be assigned to T_∞, are not very reasonable, we believe this can affect the calculation of the arc's thermal radius. In addition, when calculating the thermal area of the arc (θ_δ, given by Equation (3.22)), we only need to do integration until the arc's thermal boundary, outside which the radial temperature gradient is negligible, i.e. T_∞/T (*T* is the local temperature at a given radial position) becomes effectively unity. A modification is, therefore, made to the current approach of calculating the thermal area, which changes the definition of T_∞ and the upper boundary for integration "∞"

for Equation (3.22). In the modified approach, we find the value of T_∞ by searching in the positive r-direction from the arc axis until the following relation is satisfied.

$$\left|\frac{T_j - T_{j-1}}{T_j}\right| \leq 0.01 \qquad (j=1, 2, 3\ldots n) \qquad (5.1)$$

where T_{j-1} is the temperature at radial position of r_{j-1} (the radial grid j-1) and Tj the temperature at radial position of r_j (the radial grid j). This means that the relative difference for the temperature of the adjacent two radial grids should not exceed 1%, i.e. the radial temperature gradient is negligible. The value of T_∞ is then the value of T_j and "∞" the radial position of r_j, which is actually the thermal boundary of the arc. When calculating the thermal area of the arc, the integration is done from the nozzle axis to the thermal boundary of the arc, which is reasonable. However, it should be noted that, for arcs at high currents, the radial temperature profile has a very flat high temperature arc core. This means that the criterion given by Equation (5.1) may be satisfied well within the arc core, which is not expected. We, therefore, arbitrarily start searching when the temperature is below 500 K, since the temperature at the thermal boundary of the arc (typically around 300 K) is always below this value.

By using this modified approach, the turbulence parameter c is readjusted to 0.057 for the nozzle of Figure 4.1 to achieve agreement with relevant experimental results for P_0 = 21.4 atm and di/dt= 25 Aμs^{-1}. The same value of c will be used for all the other discharge conditions (with different values of P_0 and di/dt).

Turbulence parameters for the standard k-epsilon model, the Chen-Kim model and the RNG model are kept as their default values (given in Section 3.5 of Chapter 3).

Based on the computational results obtained, we can predict the behaviour of the nozzle arc before current zero and, subsequently, the thermal interruption capability of the nozzle arc. A detailed analysis of the physical mechanisms encompassed in each model is given below to show the adequacy of a particular model in describing the rapidly varying arc during current zero period.

5.2.1 Arc Behaviour before Current Zero

Immediately after the current is ramped down from the 1 kA plateau, the arc and its surrounding flow maintains quasi-steady state. When the current is further ramped down towards current zero, the effects of thermal and momentum inertia become significant. Temperature and velocity fields cannot adjust quickly to those corresponding to the DC arc at the same current. The arc is, therefore, no longer in quasi-steady state. The period from the instant when the arc deviates from quasi-steady state is commonly known as the start of the current zero period (hereafter referred to as the current zero period). From this instant onwards, the arc depends on the rate of current decay and the state of the arc at current zero is determined by the accumulated effects of arcing from the start of current zero period to current zero. A comparative study of different flow models will be conducted and the physical mechanisms responsible for the differences in the predicted results between various flow models will be given. The qualitative features of the arc behaviour during current zero predicted by the five flow models are similar for different P_0 and di/dt. The predicted results at P_0=21.4 atm and di/dt=13Aμs^{-1} will, therefore, be used to illustrate the typical arc behaviour and the differences between flow models.

5.2.1.1 Overall Features

For the transient arc with the current ramped down from the 1 kA plateau towards zero, the general features of the arc and the surrounding gas flow inside the nozzle and the variation of these features with current is very similar to those of the DC arcs investigated in Chapter 4, e.g. the flow features in front of the upstream electrode and those in front of the downstream electrode. In front of the upstream electrode, the wake does not exist at high currents, which reappears shortly before current zero (similar to that shown in Figure 4.19). Near the downstream electrode, the variation of the flow feature with the current ramp is consistent with that discussed in Section 4.3.2.1 of Chapter 4, i.e. at currents above 600 A, the pressure distribution shows a

compression wave rather than a shock (similar to that shown in Figure 4.10), while for currents below 100 A, the bow shock reappears in front of the downstream electrode (similar to that shown in Figure 4.13).

The variations of axis temperature, arc radius defined as the 4000 K isotherm and electrical field with axial position at different current levels on the ramp before current zero are respectively given in Figures 5.1, 5.2 and 5.3 for those obtained by the standard k-epsilon model and the Chen-Kim model. Results obtained by the Prandtl mixing length model, the RNG model and the laminar flow model are not given, since the qualitative features of the results obtained by the Prandtl mixing length model are the same as those for the standard k-epsilon model, and the results for the RNG model and the laminar flow model are similar to those for the Chen-Kim model.

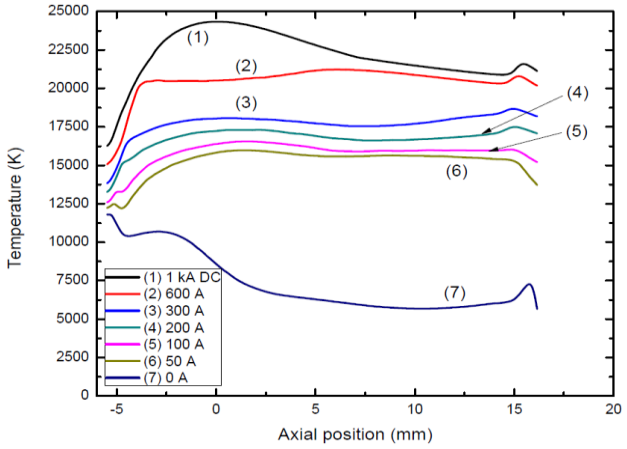

(a)

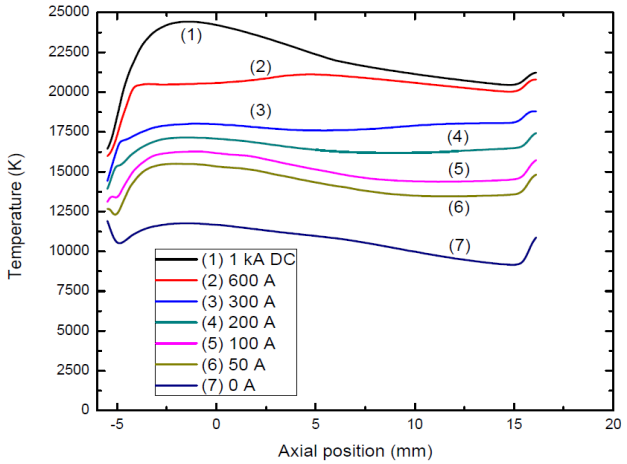

(b)

Figure 5.1. Variation of axis temperature with axial position at different current levels on the ramp computed by two flow models. P_0=21.4 atm and di/dt=13 Aμs^{-1}. (a) Standard k-epsilon model and (b) Chen-Kim k-epsilon model.

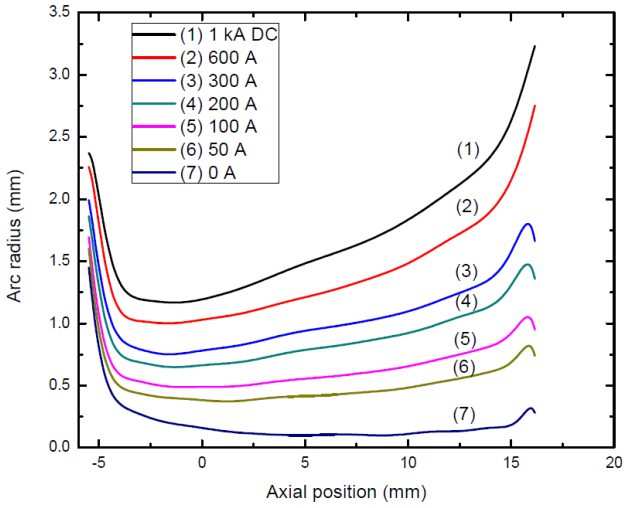

(a)

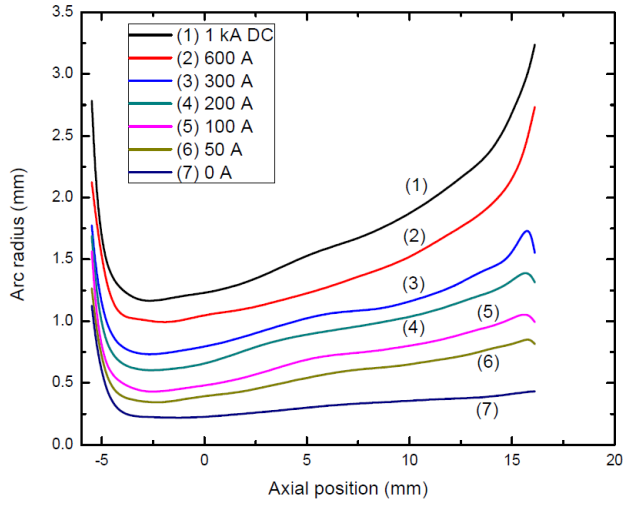

(b)

Figure 5.2. Variation of arc radius with axial position at different current levels on the ramp computed by two flow models. P_0=21.4 atm and di/dt=13 Aμs^{-1}. (a) Standard k-epsilon model and (b) Chen-Kim k-epsilon model.

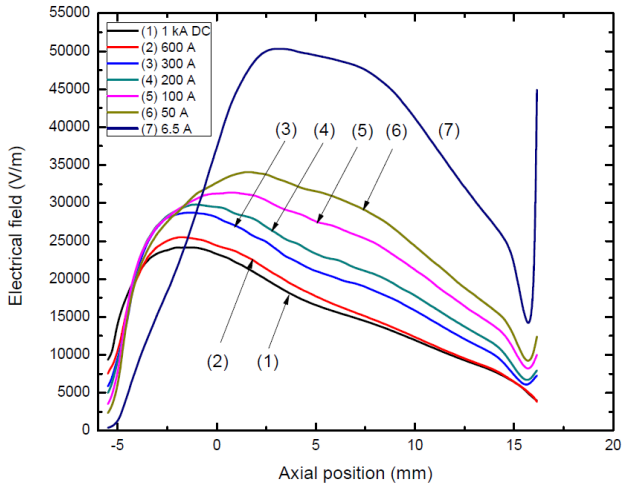

Figure 5.3. Variation of electrical field with axial position at differemt current levels on the ramp computed by two flow models. P_0=21.4 atm and di/dt=13 Aμs^{-1}. (a) Standard k-epsilon model and (b) Chen-Kim k-epsilon model.

When the current is large (600 A and above), the axis temperature (Figure 5.1) and arc radius (Figure 5.2) computed by the five flow models show little differences between each other, and thus the electrical field distributions computed by different flow models are similar (Figure 5.3). The spread in arc voltages computed by the five flow models are, therefore, less than 15% of the mean voltage of those predicted by the five flow models (Figure 5.4). In addition, for all the flow models, the axis temperature is not sensitive to the current (Figure 5.1), and the arc radius is roughly proportional to the square root of current (Figure 5.2). The arc voltage is, thus,

almost independent of the current (Figure 5.4). All these features are similar to those of DC arc V-I characteristics reported in Chapter 4.

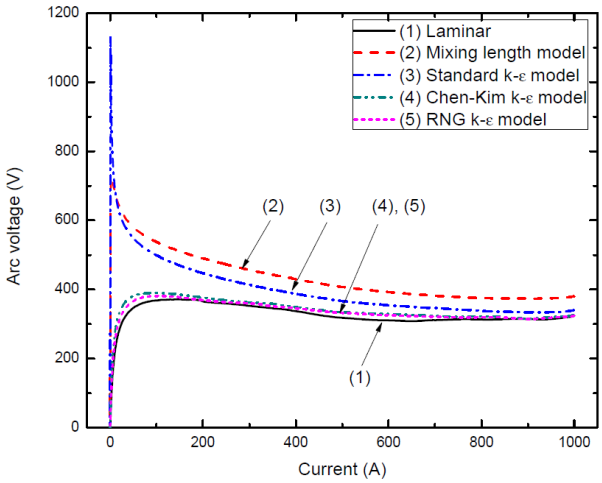

Figure 5.4. The voltage-current (V-I) characteristics for the nozzle arcs computed by five flow models corresponding to the current ramp. P_0=21.4 atm and di/dt=13 Aμs^{-1}.

When the current is further ramped down towards current zero (below 600 A), the axis temperature is reduced with current decay due to reduced Ohmic input (Figure 5.1). The dependence of the arc radius on current is found to be stronger than that for currents above 600 A (Figure 5.2). The arc voltage, therefore, starts to rise with decreasing current (Figure 5.4). Furthermore, the overall features of the transient arc predicted by different flow models become quite different for currents below 600 A, which results in the arc voltage to be strongly dependent on the flow models before current zero (Figure 5.4). It has been found that the axis temperature and arc radius predicted by the standard k-epsilon model and/or the Prandtl mixing length model decrease rapidly shortly before current zero when the current is below 50 A (i.e. in the last 4 μs before current zero), especially in the region downstream of the nozzle throat (Figures 5.1(a) and 5.2(a)). This is responsible for a rapid increase of electrical field (Figure 5.3(a)), and thus a high voltage extinction peak shortly before current zero (Figure 5.4). For the Chen-Kim model, the RNG model and the laminar flow model, the axis temperature and the arc radius show a monotonic decrease when the current is ramped down towards zero (Figures 5.1(b) and 5.2(b)), and the rates of decrease of the axis temperature and arc radius are much lower than

those predicted by the Prandtl mixing length model and the standard k-epsilon model. The electrical field distribution predicted by these three models decreases rapidly at the last 4 μs before current zero (Figure 5.3(b)). As a result, the arc voltages predicted by the Chen-Kim model, the RNG model and the laminar flow model show no extinction peak before current zero (Figure 5.4).

The axis temperature (Figure 5.1) and arc radius (Figure 5.2) shortly before current zero computed by different flow models all indicate that there is a local high temperature region in front of the hollow downstream electrode with broadened arc size. This is due to the presence of the bow shock which results in the stagnant nature of the local flow field. However, when applying the Prandtl mixing length model and the standard k-epsilon model, it is found that the axis temperature and arc radius are both reduced immediately in front of the downstream electrode (Figure 5.1(a) and 5.2(a)), which results in a sudden increase of electrical field in this region as shown in Figure 5.3(a). Careful examination of the results shows that the deceleration of the flow into the shock and the resulting flow reversal predicted by these two models (axial velocity similar to that shown in Figure 4.16, and, flow pattern similar to that shown in Figure 4.17, in Section 4.3.2.1 of Chapter 4) gives rise to large values of the local velocity gradients (i.e. dw/dz and dw/dr) right in front of the downstream electrode, which has the effects of increasing the eddy viscosity (μ_t) and thus the turbulence level. The resulting strong turbulence cooling effect is responsible for the low temperature and small arc radius in front of the downstream electrode. For the Chen-Kim model and the RNG model as well as the laminar flow model, the results indicate that the flow in front of the downstream electrode decelerates into the shock but its direction is not reversed (axial velocity similar to that shown in Figure 4.16, and, flow pattern similar to that shown in Figure 4.18, in Section 4.3.2.1 of Chapter 4). The temperature rise in front of the downstream electrode is due to deceleration of the gas flow. Reduction of axis temperature and arc radius right in front of the downstream electrode does not happen when applying these three models (Figures 5.1(b) and 5.2(b)). No experimental results are available to judge the accuracy of different flow models in predicting the flow behaviour near the two electrodes.

Nevertheless, as previously discussed in Chapter 4, the influence of the two electrode regions on the electrical behaviour of the arc, and thus the thermal interruption capability of the nozzle interrupter, is negligible. Since the present investigation concerns the thermal interruption of the nozzle arc, we only consider the accuracy of the five flow models in predicting the behaviour of the arc and the flow in the nozzle excluding the two electrode regions.

The large differences in the overall features of the transient arc predicted by different flow model, and the resulting differences in the V-I characteristics, indicate that the energy transport processes predicted by these models are very different. The physical processes responsible for these features and the differences in predicted arc voltages between various flow models are discussed in the following subsections.

5.2.1.2 The Behaviour of the Arc in Quasi-Steady State

The features of the computational results for the flat part of the V-I characteristics given by various flow models (Figure 5.4) are very similar to those of the corresponding DC arcs with radiation dominated high temperature core reported in Section 4.3.2.3 of Chapter 4. These features are, therefore, not repeated.

For all flow models applied, the energy balance calculation is conducted for the whole arc length and at both the arc core boundary (defined as the radial position corresponding to a temperature of 83.3% of the axis temperature) and the electrical boundary (defined by the radial position corresponding to a temperature of 4000 K) of the arc at 600 A (Tables 5.1 and 5.2). Results show that at high currents radiation is the dominant energy transport mechanism within the arc core (Table 5.1), which results in a rather flat radial temperature profile inside the core (Figure 5.5). Radial thermal conduction (nearly all due to turbulent heat conduction when a turbulence model is applied) is found to be significant at the electrical boundary (Table 5.2) which results in the radial temperature profile between the arc core boundary and the electrical boundary to be sensitive to flow models (Figure 5.5). Nevertheless, turbulence has little influence on the arc voltage since more than 80% of the current is conducted within the arc core where radiation is dominant.

Table 5.1. Electrical power input together with various energy transport processes for the whole arc length at the core boundary calculated by five turbulence models at 600 A instant. P_0=21.4 atm and di/dt=13 $A\mu s^{-1}$. The power associated with the pressure work is not shown as it only accounts for 5 to 7% of the power input. This applies to all tables. Positive means power input and negative power loss.

Model	Power input (W)	Radiation loss (W)	Radial thermal conduction (W)	Axial enthalpy convection (W)	Radial enthalpy convection (W)	Rate of change of energy storage (W)
(1)	1.49×10^5	-1.04×10^5	-6.62×10^3	-2.39×10^4	-1.13×10^4	-9.06×10^3
(2)	1.60×10^5	-9.07×10^4	-6.00×10^4	-9.33×10^2	-6.79×10^3	-6.85×10^3
(3)	1.61×10^5	-9.98×10^4	-4.13×10^4	-1.04×10^4	-8.23×10^3	-8.12×10^3
(4)	1.59×10^5	-1.08×10^5	-1.21×10^4	-2.65×10^4	-9.69×10^3	-8.63×10^3
(5)	1.57×10^5	-1.07×10^5	-1.04×10^4	-2.69×10^4	-9.66×10^3	-8.65×10^3

Method of calculation: $\text{Power input} = \int_{Z1}^{Z2}\left[\int_0^R \sigma E^2 2\pi r dr\right]dz$,

$$\text{Radiation loss} = -\int_{Z1}^{Z2}\left[\int_0^R q 2\pi r dr\right]dz,$$

$$\text{Radial thermal conduction} = \int_{Z1}^{Z2}\left[\int_0^R \frac{1}{r}\frac{\partial}{\partial r}\left(r\frac{k}{c_p}\frac{\partial h}{\partial r}\right)2\pi r dr\right]dz$$

$$\text{Axial enthalpy convection} = -\int_{Z1}^{Z2}\left[\int_0^R \rho w\frac{\partial h}{\partial z}2\pi r dr\right]dz$$

$$\text{Radial enthalpy convection} = -\int_{Z1}^{Z2}\left[\int_0^R \rho v\frac{\partial h}{\partial r}2\pi r dr\right]dz$$

$$\text{Energy storage} = \int_{Z1}^{Z2}\left[\int_0^R \rho\frac{\partial h}{\partial t}2\pi r dr\right]dz$$

where *R* refers to the radial position of the core boundary or electrical boundary and (Z2-Z1) the arc length.

Key to the models: (1) Laminar flow model, (2) Prandtl mixing length model, (3) Standard k-epsilon model, (4) Chen-Kim k-epsilon model and (5) RNG k-epsilon model.

Table 5.2. Percentage of electrical power input associated with various energy transport processes for the whole arc length at the electrical boundary calculated by five turbulence models at 600 A instant. P_0=21.4 atm and di/dt=13 Aμs^{-1}. Mathematical expressions for power input and power loss and the key to the models are the same as those in Table 5.1.

Model	Power input (10^5 W)	Radiation loss (W)	Radial thermal conduction (W)	Axial enthalpy conduction (W)	Radial enthalpy convection (W)	Rate of change of energy storage (W)
(1)	1.84×10^5	-5.82×10^4	-1.85×10^3	-1.80×10^5	4.46×10^4	-2.75×10^4
(2)	2.34×10^5	-3.50×10^4	-1.51×10^5	-8.33×10^4	2.47×10^4	-2.46×10^4
(3)	2.11×10^5	-4.89×10^4	-9.71×10^4	-1.11×10^5	3.24×10^4	-2.77×10^4
(4)	1.96×10^5	-6.11×10^4	-2.87×10^4	-1.51×10^5	3.24×10^4	-2.78×10^4
(5)	1.94×10^5	-6.07×10^4	-2.49×10^4	-1.55×10^5	3.38×10^4	-2.86×10^4

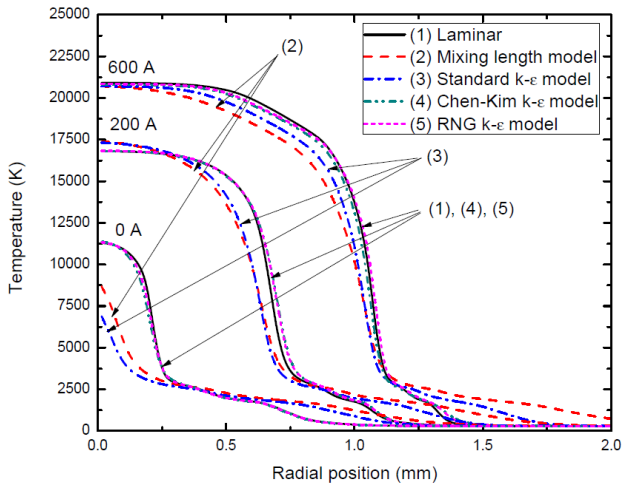

(a)

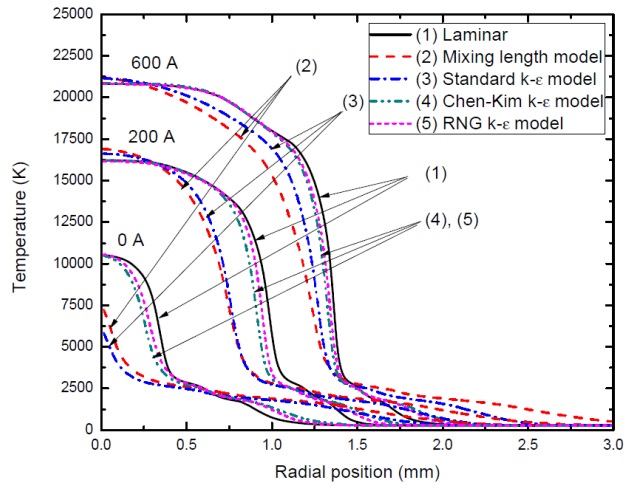

(b)

Figure 5.5. Radial temperature profiles at two axial positions computed by five flow models at at three instants before current zero (600 A, 200 A and current zero). P_0=21.4 atm and di/dt=13 Aμs^{-1}. (a) Z=2.3 mm and (b) Z= 7.9mm.

It is found that, for all the flow models applied, at the core boundary, the rate of change of energy storage accounts for less than 7% of the Ohmic input (Table 5.1). Since the high temperature core is mainly responsible in conducting the current, the arc at the current of 600 A and above can be considered in quasi-steady state although, at the electrical boundary, the rate of energy storage accounts for more than 10% of the Ohmic input (Table 5.2).

5.2.1.3 The Behaviour of the Arc in Current Zero Period

When the current is below 600 A, the arc voltage start to rise with the current decay and gradually becomes strongly dependent on the flow models (Figure 5.4). The energy balance calculation at the arc core boundary and electrical boundary at 200 A (Tables 5.3 and 5.4) indicates that the rate of change of energy storage cannot be neglected in comparison with the Ohmic input and the other energy transport mechanisms, which means the arc deviates from quasi-steady state. Thus, from the instant of 200 A, the arc starts to deviate from quasi-steady state, after which the arc is commonly known to be in current zero period. During current zero period, the arc depends on the rate of current decay, and the state of arc at current zero is determined by the accumulated effects of arcing from the start of current zero period to current zero. It should be noted that the definition of current zero period is not precise.

Table 5.3. Electrical power input together with various energy transport processes for the whole arc length at the core boundary calculated by five flow models at 200 A instant. P_0=21.4 atm and di/dt=13 $A\mu s^{-1}$. Mathematical expressions for power input and power loss and the key to the models are the same as those in Table 5.1.

Model	Power input (W)	Radiation loss (W)	Radial thermal conduction (W)	Axial enthalpy convection	Radial enthalpy convection	Rate of change of energy storage (W)
(1)	6.47×10^4	-4.81×10^4	-6.00×10^3	-1.00×10^4	-2.05×10^3	-7.21×10^3
(2)	7.31×10^4	-4.38×10^4	-2.88×10^4	-1.04×10^3	-9.39×10^2	-4.22×10^3
(3)	7.27×10^4	-4.58×10^4	-2.53×10^4	-2.54×10^3	-1.21×10^3	-5.48×10^3
(4)	6.71×10^4	-4.86×10^4	-9.16×10^3	-8.88×10^3	-2.49×10^3	-6.87×10^3
(5)	6.59×10^4	-4.78×10^4	-8.19×10^3	-9.31×10^3	-2.61×10^3	-7.09×10^3

Table 5.4. Electrical power input together with various energy transport processes for the whole arc length at the electrical boundary calculated by five flow models at 200 A instant. P_0=21.4 atm and di/dt=13 $A\mu s^{-1}$. Mathematical expressions for power input and power loss and the key to the models are the same as those in Table 5.1.

Model	Power input (W)	Radiation loss (W)	Radial thermal conduction (W)	Axial enthalpy convection	Radial enthalpy convection	Energy storage (W)
(1)	7.30×10^4	-3.85×10^4	-9.21×10^2	-6.35×10^4	1.33×10^4	-2.44×10^4
(2)	9.82×10^4	-2.64×10^4	-6.85×10^4	-1.82×10^4	2.98×10^3	-1.77×10^4
(3)	8.97×10^4	-3.16×10^4	-5.37×10^4	-2.08×10^4	1.11×10^3	-2.09×10^4
(4)	7.54×10^4	-3.90×10^4	-1.49×10^4	-3.92×10^4	2.33×10^3	-2.20×10^4
(5)	7.38×10^4	-3.85×10^4	-1.25×10^4	-4.12×10^4	3.05×10^3	-2.22×10^4

For the arc in current zero period, turbulence enhanced thermal conduction gradually becomes the most dominant energy loss mechanism. This has been confirmed by detailed energy balance calculations. Energy balance at the arc core boundary at 200 A (Table 5.3) indicates that for the Prandtl mixing length model and the standard k-epsilon model the predicted radial thermal conduction becomes appreciable although radiation loss is still the most important energy loss mechanism. The radial temperature profiles computed by these two models are, therefore, no longer flat in the arc core, which have considerable radial temperature gradient (Figure 5.5). For the Chen-Kim model and the RNG model as well as the laminar

flow model, radiation loss is till the dominant energy loss mechanism while radial thermal conduction has little influence (Table 5.3), for which the corresponding radial temperature profiles still have a flat arc core (Figure 5.5). Energy balance at the electrical boundary at 200 A (Table 5.4) reveals that for the Prandtl mixing length model and the standard k-epsilon model radial thermal conduction is the dominant energy loss mechanism, while for the laminar flow model, the Chen-Kim and the RNG models radiation loss is still the most important.

The reason for such a difference in dominant energy loss mechanisms between different flow models is due to the intensity of turbulence, which is determined by the eddy viscosity (μ_t). Radial profiles of μ_t at two axial positions (Z=2.3 mm, the middle of the nozzle throat, and, Z=7.9 mm downstream of the nozzle throat in the diverging section of the nozzle) are given in Figure 5.6 which indicates that μ_t predicted by the Prandtl mixing length model and the standard k-epsilon model being significantly higher than that predicted by the Chen-Kim model and the RNG model. It is also noted that μ_t computed by the standard k-epsilon model is nearly comparable to that obtained by the Prandtl mixing length model at 200 A inside the electrical boundary. This is different from the case at high currents (600 A and above) when the Prandtl mixing length model predicts the largest value of μ_t in comparison with all the other models (Figure 5.7), which means the rate of rise of μ_t computed by the standard k-epsilon model is larger than that computed by the Prandtl mixing model. The arc voltage predicted by the standard k-epsilon model, therefore, becomes the highest shortly before current zero in comparison with the other flow models, although it is lower than that predicted by the Prandtl mixing length model at early instants when the current is high (Figure 5.4).

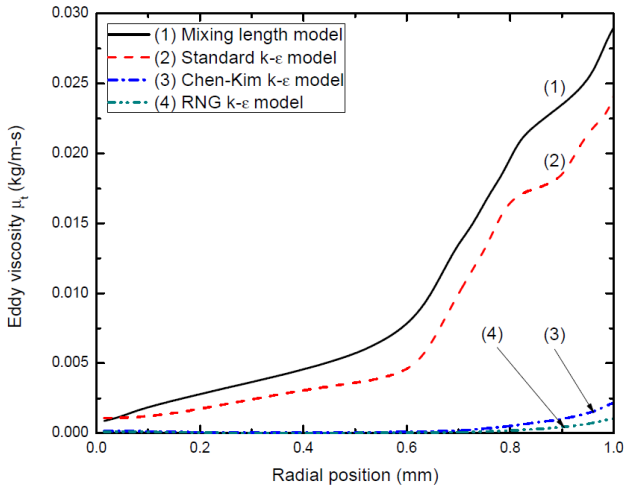

(a)

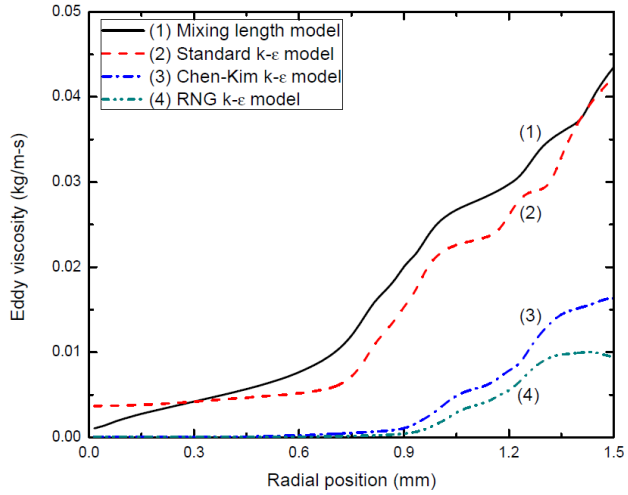

(b)

Figure 5.6. Radial profiles of the eddy viscosity at two axial positions computed by four flow models at 200 A instant. P_0=21.4 atm and di/dt=13 $A\mu s^{-1}$. (a) Z=2.3 mm and (b) Z= 7.9mm.

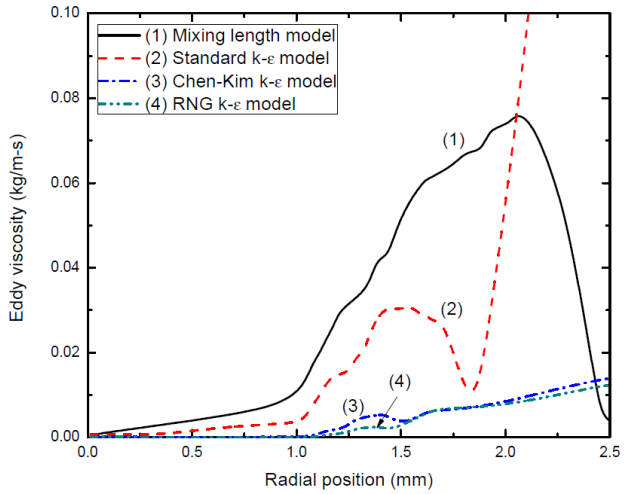

(a)

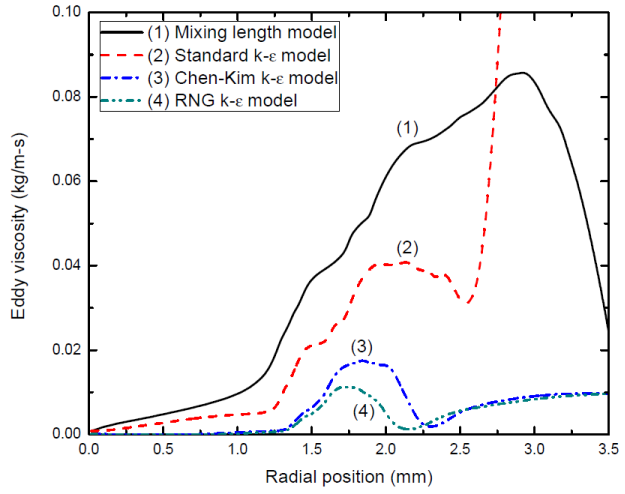

(b)

Figure 5.7. Radial profiles of the eddy viscosity at two axial positions computed by four flow models at 600 A instant. P_0=21.4 atm and di/dt=13 Aμs^{-1}. (a) Z=2.3 mm and (b) Z= 7.9mm.

The reason for a fast rate of rise of eddy viscosity predicted by the standard k-epsilon model than that computed by the Prandtl mixing length model is attributed to the differences in definitions of the length scale (λ_c) and velocity scale (V_c) of turbulence for these two models. This results in different trends in the variations of both λ_c and V_c with the current decay predicted by the Prandtl mixing length model and the standard k-epsilon model, which is discussed in Section 5.2.1.4.

5.2.1.4 Comparative Studies of Different Flow Models

A. The Prandtl Mixing Length Model

For the Prandtl mixing length model, the turbulence length scale (λ_c) is defined with the adoption of the thermal radius of the arc (Equation (3.21)), which is a constant for a given axial position. As the arc size shrinks with the current decay, λ_c is also reduced (Figure 5.8). The turbulence velocity scale (V_c), on the other hand, is related to the local velocity gradients as well as the turbulence length scale (Equation (3.24)). Due to reduction of λ_c, V_c inside the arc core does not appear to increase rapidly when the current is ramped down (Figure 5.9), although the radial gradient of axial velocity ($\partial w/\partial r$) may increasing with current decay due to contraction of the arc size. When the current is below 100 A, the velocity scale also starts to reduce with decreasing current (Figure 5.9). The maximum turbulence velocity scale for a given current corresponds to the inflexion point of the radial velocity profile. The results (Figures 5.8 and 5.9) also indicate that the turbulence level is increased towards the downstream electrode.

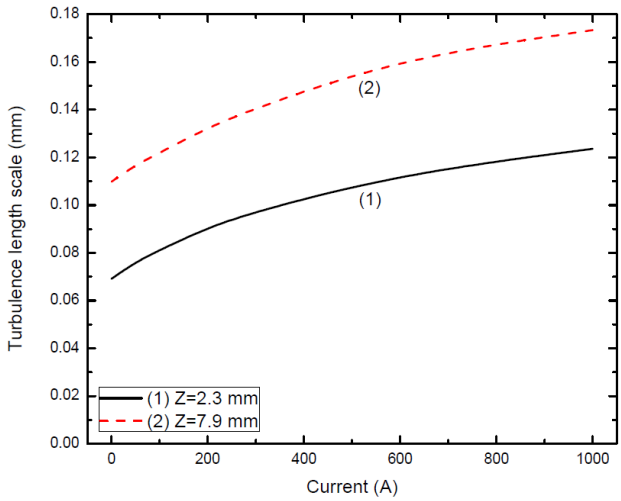

Figure 5.8. Variation of turbulence length scale with current decay computed by the Prandtl mixing length model for two axial positions. P_0=21.4 atm and di/dt=13 $A\mu s^{-1}$.

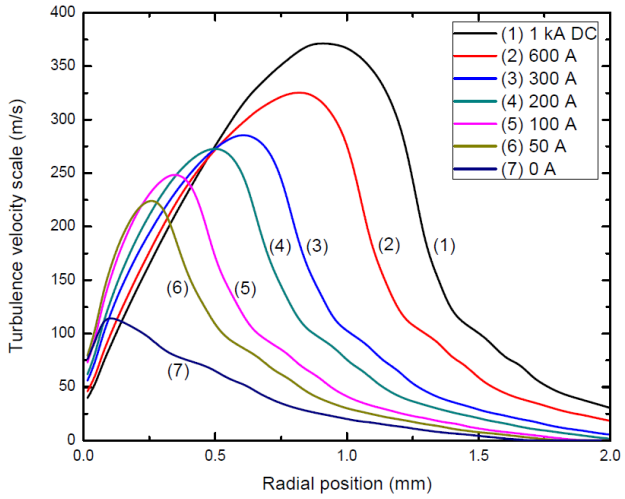

Figure 5.9. Variation of turbulence velocity scale with radial position at different current levels on the ramp computed by the Prandtl mixing length model for two axial positions. P_0=21.4 atm and di/dt=13 Aμs^{-1}. (a) Z=2.3mm and (b) Z=7.9mm.

B. The Standard K-Epsilon Model

For the standard k-epsilon model, the turbulence length scale (λ_c) is related to the turbulence kinetic energy (k) and dissipation rate (ε) through the relation given by Equation (3.32). The variations of k and ε with the change of current are shown in Figures 5.10 and 5.11 for the axial positions of Z=2.3 mm and 7.9 mm, respectively. It is found that when the current is above 100 A, the values of k and ε in the arc core increase due to the transport of turbulent energy and dissipation rate (mainly by the diffusion process and/or radial inflow of the gas) from large value region towards the arc core. The relation between λ_c and the current (Figure 5.12) are more complicated as compared with that predicted by the Prandtl mixing length model (Figure 5.8).

The values of λ_c are, however, smaller than those computed by the Prandtl mixing length model (comparing results given by Figures 5.12 and 5.8). Nevertheless, turbulence velocity scale (V_c), which is defined as the square root of k by Equation (3.33), is significantly increased inside the arc core when the current is ramped down (Figure 5.13) as the values of k inside the arc core increases with decreasing current (Figure 5.10). V_c, therefore, becomes larger than that predicted by the Prandtl mixing length model for currents below 300 A, while at high currents (600 A and above), the values of V_c predicted by both models are comparable to each other. This explains a faster rate of rise of μ_t computed by the standard k-epsilon model when the current is ramped down (Figure 5.14), for which μ_t becomes comparable to that computed by the Prandtl mixing length model at 200 A instant (Figure 5.6) although it is smaller than μ_t computed by the Prandtl mixing length model at 600 A instant and above (Figure 5.7). The turbulence level predicted by the standard k-epsilon model is thus increased rapidly, which will result in a reduction of the local velocity gradients, and subsequently the rate of generation of turbulence kinetic energy P_k (Equation (3.31)) shortly before current zero. The values of both k and ε, therefore, start to decrease when the current is below 100 A (Figures 5.10 and 5.11). However, this does not result in a reduction of λ_c shortly before current zero (Figure 5.12), while λ_c predicted by the Prandtl mixing length model is always reducing with current (Figure 5.8). In addition, V_c is still much higher than that computed by the Prandtl mixing length model although k is decreased. Therefore, μ_t computed by the standard k-epsilon model becomes higher than that computed by the Prandtl mixing length model shortly before current zero and at current zero (Figures 5.14 and 5.15). Energy balance calculation at current zero reveals that turbulence enhanced radial thermal conduction computed by the standard k-epsilon model becomes stronger than that computed by the Prandl mixing length model at the arc core boundary (Table 5.5). At the electrical boundary, the values of radial thermal conduction computed by these two models are nearly the same (Table 5.6). At higher instantaneous currents the radial thermal conduction computed by the standard k-epsilon model is weaker than that computed by the Prandtl mixing length model at both the arc core boundary

(Tables 5.1 and 5.3) and the electrical boundary (Tables 5.2 and 5.4). The higher turbulence level predicted by the standard k-epsilon model shortly before current zero gives rise to the lowest axis temperature and the smallest arc radius at current zero in comparison with those obtained by all the other flow models (Figure 5.16).

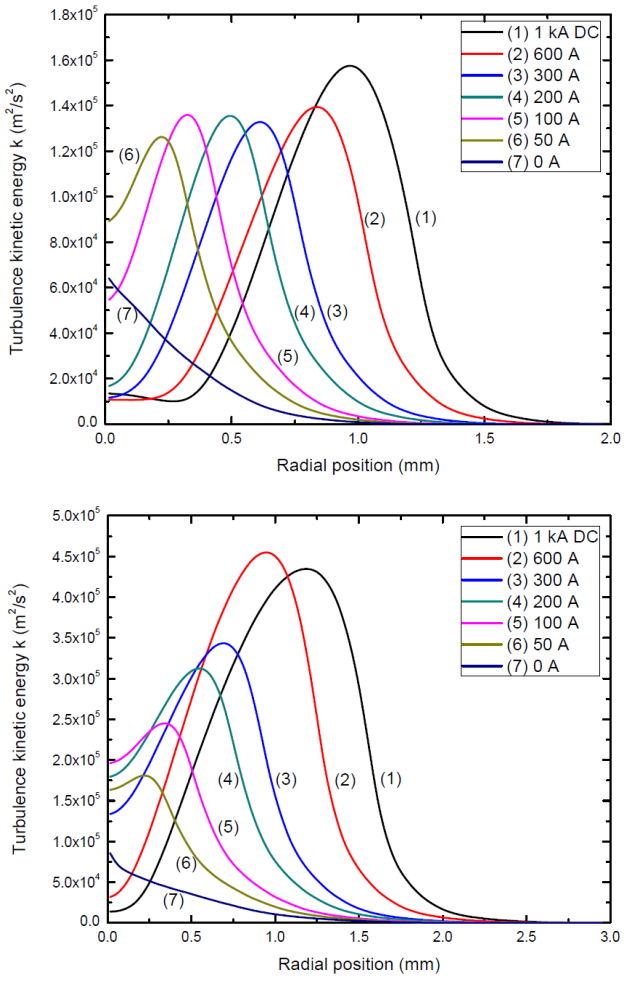

Figure 5.10. Variation of turbulence kinetic energy (*k*) with radial positions at different current levels on the ramp computed by the standard k-epsilon model for two axial positions. P_0=21.4 atm and di/dt=13 $A\mu s^{-1}$. (a) Z=2.3 mm and (b) Z=7.9 mm.

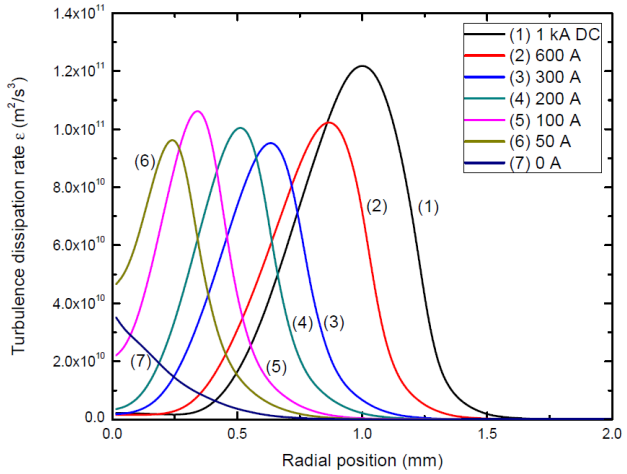

(a)

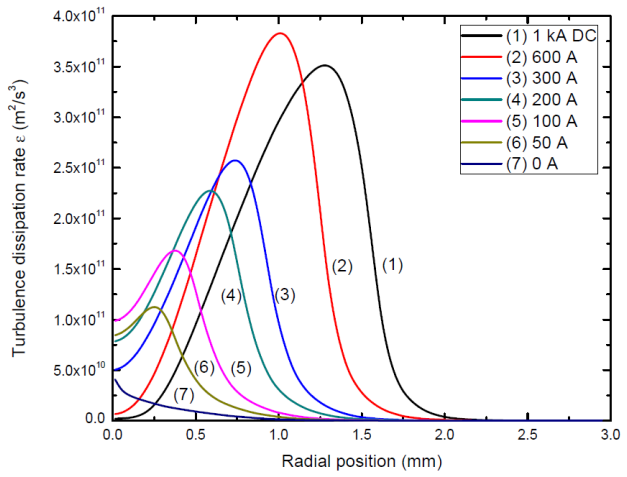

(b)

Figure 5.11. Variation of turbulence dissipation rate (ε) with radial positions at different current levels on the ramp computed by the standard k-epsilon model for two axial positions. P_0=21.4 atm and di/dt=13 Aμs^{-1}. (a) Z=2.3 mm and (b) Z=7.9 mm.

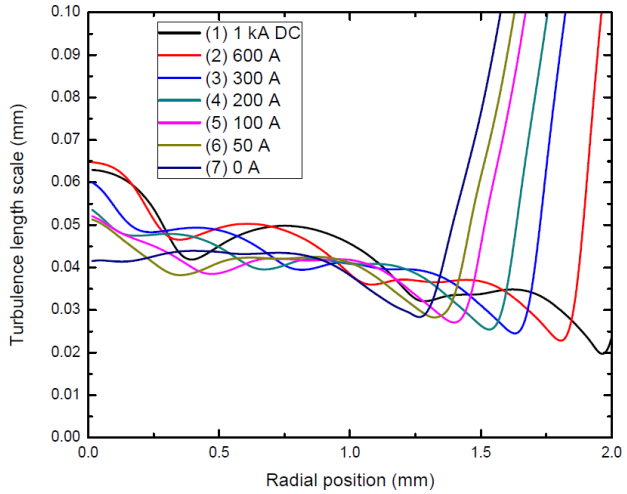

(a)

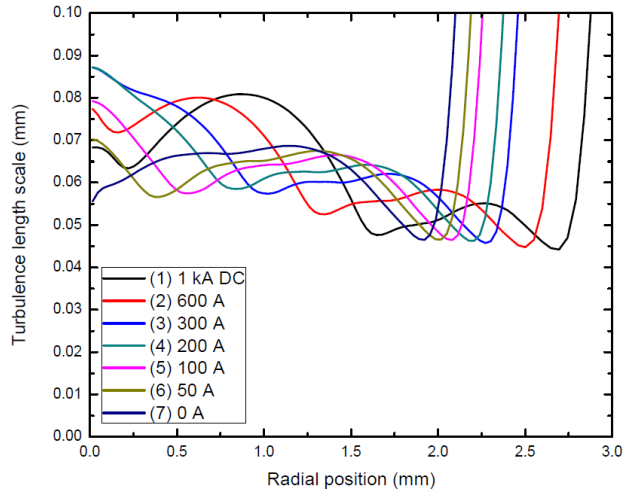

(b)

Figure 5.12. Variation of turbulence length scale with current decay computed by the standard k-epsilon model. P_0=21.4 atm and di/dt=13 Aμs^{-1}. (a) Z=2.3 mm and (b) Z=7.9 mm.

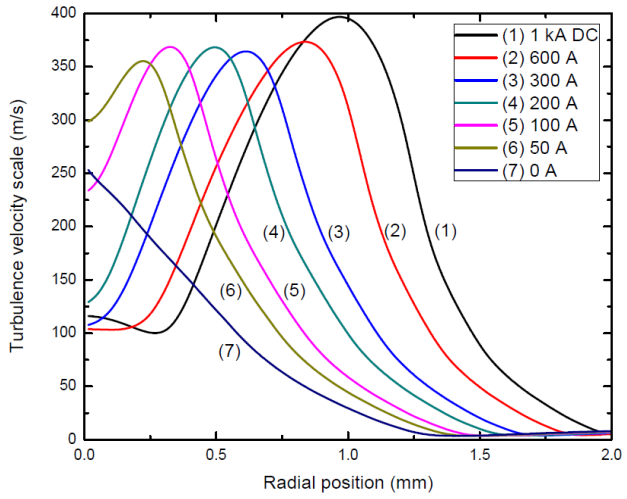

(a)

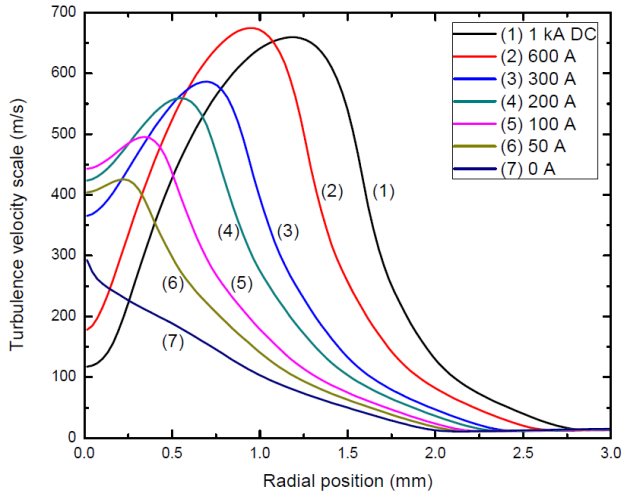

(b)

Figure 5.13. Variation of turbulence velocity scale with radial positions at different current levels on the ramp computed by the standard k-epsilon model for two axial positions. P_0=21.4 atm and di/dt=13 Aμs^{-1}. (a) Z=2.3 mm and (b) Z=7.9 mm.

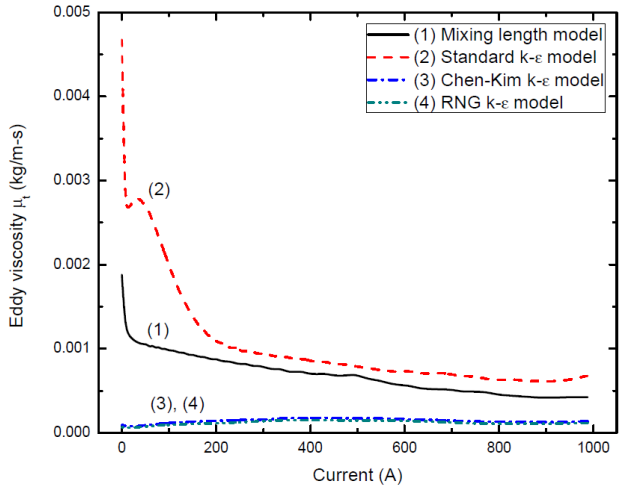

(a)

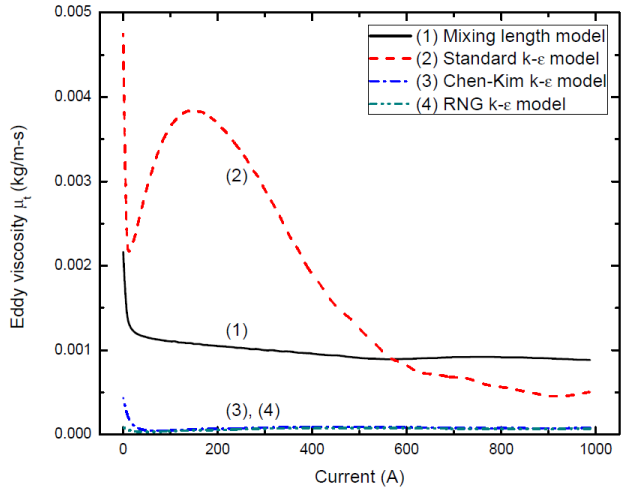

(b)

Figure 5.14. Variation of eddy viscosity on the nozzle axis computed by different turbulence models when current decays to zero for two axial positions. P_0=21.4 atm and di/dt=13 Aμs^{-1}. (a) Z=2.3 mm and (b) Z= 7.9mm. For Prandtl mixing model the value of eddy viscosity one grid off axis (r=0.015 mm) is taken as the axis value.

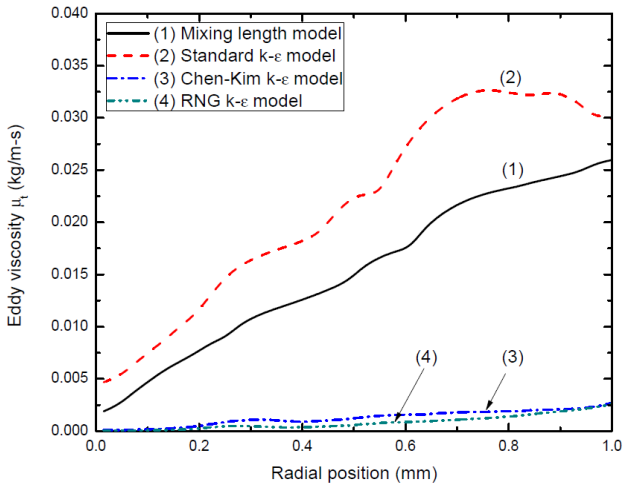

Figure 5.15. Radial profiles of the eddy viscosity at two axial positions computed by four flow models at current zero. P_0=21.4 atm and di/dt=13 Aμs^{-1}. (a) Z=2.3 mm and (b) Z= 7.9mm.

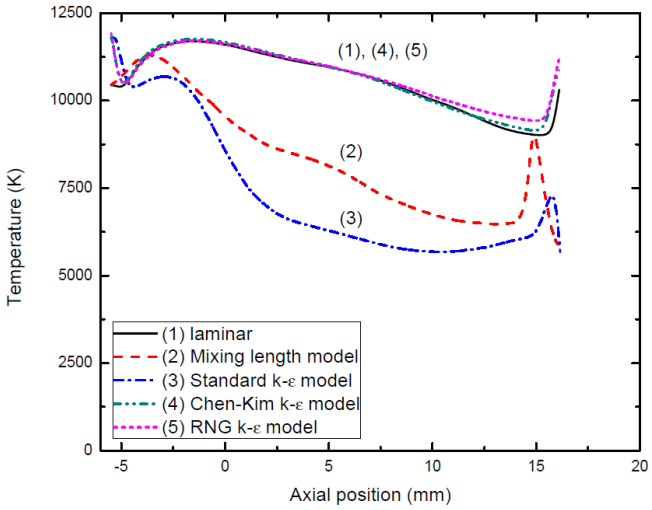

(a)

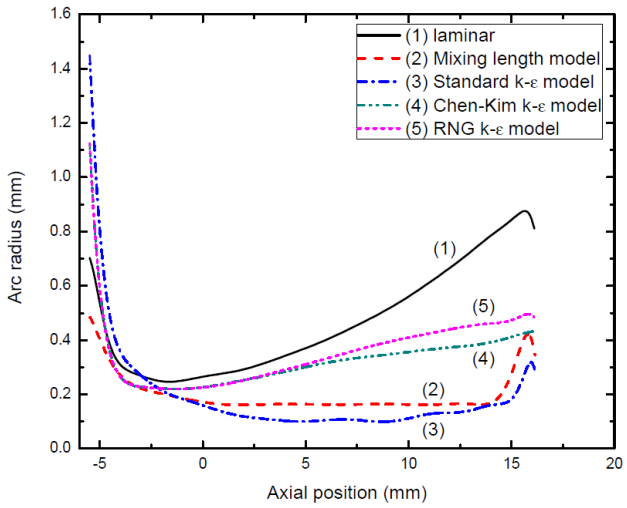

(b)

Figure 5.16. Variations of axis temperature and arc radius with axial position computed by five flow models at current zero. P_0=21.4 atm and di/dt=13Aμs^{-1}. (a) Axis temperature and (b) arc radius.

Table 5.5. Electrical power input together with various energy transport processes for the whole arc length at the core boundary calculated by five flow models at current zero. P_0=21.4 atm and di/dt=13 Aμs^{-1}. Mathematical expressions for power input and power loss and the key to the models are the same as those in Table 5.1.

Model	Power input (W)	Radiation loss (W)	Radial thermal conduction (W)	Axial enthalpy convection (W)	Radial enthalpy convection (W)	Rate of change of Energy storage (W)
(1)	0.0	-1.08×10^{3}	-1.09×10^{3}	-9.49×10^{2}	-8.66×10^{2}	-4.76×10^{3}
(2)	0.0	-1.96×10^{2}	-2.44×10^{3}	-1.13×10^{2}	-5.90×10^{2}	-3.41×10^{3}
(3)	0.0	-4.22×10^{2}	-3.30×10^{3}	-2.10×10^{2}	-1.04×10^{3}	-5.19×10^{3}
(4)	0.0	-9.43×10^{2}	-2.05×10^{3}	-5.54×10^{1}	-8.99×10^{2}	-4.33×10^{3}
(5)	0.0	-1.03×10^{3}	-1.76×10^{3}	-1.93×10^{2}	-8.91×10^{2}	-4.35×10^{3}

Table 5.6. Electrical power input together with various energy transport processes for the whole arc length at the electrical boundary calculated by five flow models at current zero. P_0=21.4 atm and di/dt=13 Aμs^{-1}. Mathematical expressions for power input and power loss and the key to the models are the same as those in Table 5.1.

Model	Power input (W)	Radiation loss (W)	Radial thermal conduction (W)	Axial enthalpy convection (W)	Radial enthalpy convection (W)	Rate of change of energy storage (W)
(1)	0.0	-1.03×10^3	-3.65×10^2	-7.71×10^3	-5.39×10^3	-1.57×10^4
(2)	0.0	-1.79×10^2	-5.66×10^3	-6.23×10^2	-4.11×10^3	-1.08×10^4
(3)	0.0	-3.52×10^2	-5.43×10^3	-4.30×10^2	-4.99×10^3	-1.16×10^4
(4)	0.0	-8.71×10^2	-3.47×10^3	-3.16×10^3	-6.24×10^3	-1.44×10^4
(5)	0.0	-9.51×10^2	-2.94×10^3	-3.87×10^3	-6.11×10^3	-1.47×10^4

C. The Chen-Kim Model and the RNG Model

Variations of length scale (λ_c) and velocity scale (V_c) of turbulence with the change of current predicted by the Chen-Kim model and the RNG model are similar to those defined by the standard k-epsilon model. However, modifications to the dissipation rate equation of the standard k-epsilon model by these two models are intended to reduce turbulence (as indicated in Chapter 4), which results in reduced turbulence kinetic energy (k) and dissipation rate (ε) in comparison with those of the standard k-epsilon model. The predicted λ_c and V_c, and thus the eddy viscosity (μ_t), have the lowest values (Figures 5.6, 5.7, 5.14 and 5.15). The turbulence level, and thus the turbulence enhanced radial thermal conduction, predicted by the Chen-Kim model and the RNG model, are, therefore, the lowest (Tables 5.1 to 5.6), which results in the higher axis temperature and the larger arc radius at current zero (Figure 5.16) obtained by these two models as compared with those computed by the other two turbulence models. The arc voltage predicted by these two models is, therefore, lower, which does not appear to have extinction peak, neither (Figure 5.4).

5.2.1.5 The Dominant Energy Loss Mechanisms and the Characteristic Time for Arc Conductance Variation

A. The Dominant Energy Transport Mechanism

When the current is ramped down towards zero from the plateau of 1kA DC, the arc passes through the quasi-steady phase (current not less than 600A) during which Ohmic input is mainly taken out by radiation transport and the arc voltage predicted by the five flow models is within 15% of the average voltage of those voltages computed by the five flow models. As the axis temperature is much higher than 12,000K below which radiation transport is negligible, a radiation transport dominated core can be identified (Table 5.1 and Figure 5.5). Since more than 80% of the current (hence arc voltage is determined by the core) is carried by this core, it can be ascertained that radiation is the most important energy loss mechanism during quasi-steady phase for all flow models employed in current investigation.

When current is further reduced towards zero, the arc cannot maintain its quasi-steady state although the axis temperature is much higher than 12,000K (e.g. at 200A, Figure 5.5). For the Prandtl mixing length model and the standard k-epsilon model at the core boundary radiation and turbulence enhanced thermal conduction are the dominant energy removal processes while for the other three models radiation is still the dominant energy transport process (Table 5.3). Much radiation is absorbed in the region between the core boundary and the electrical conducting boundary, thus reducing the amount of energy taken out by radiation. For the laminar flow model, the Chen-Kim model and the RNG model, at the electrical boundary radiation, axial and radial convection are all important while for the Prandtl mixing length model and the standard k-epsilon model energy inside the electrical conducting core is mainly taken out by radiation and turbulence enhanced thermal conduction (Table 5.4).

The axis temperature of all the five flow models decreases at a very rapid rate a few microseconds before current zero. At current zero (Figure 5.16(a)), the very low axis temperature renders radiation loss negligible. The electrical behavior of the arc is determined by the energy balance at the electrical conducting boundary (Table 5.6)

which indicates that turbulence enhanced thermal conduction and radial convection cooling associated with the radial mass inflow are the dominant cooling mechanisms for the Prandtl mixing length model and the standard k-epsilon model. For the other three flow models, turbulence enhanced thermal conduction, radial and axial convection cooling control the thermal state of the arc.

B. Characteristic Time for Arc Conductance Variation just before Current Zero

The interruption of a fault current by a circuit breaker in an electrical network may affect the network operation due to the rapid rise of arc resistance a few microseconds around a current zero. In addition, electrical engineers often use a black box arc model (e.g. Cassie's model [5.2] and Mayr's model [5.3]) to describe the dynamic behaviour of arc conductance for power network simulation of switching phenomena. Such black box of arc model requires information on the characteristic time of arc conductance variation. The characteristic time for arc conductance variation (τ_G) is computed for the five flow models using $G/|dG/dt|$ at the instants 2.0 μs, 1.5 μs, 1.0 μs, 0.5 μs and 0.05 μs before current zero. These results are tabulated below for the five models (Table 5.7). The computational results show that the characteristic time changes with time. Thus, the assumption of constant characteristic (e.g. assuming τ_G to be a constant) of the black box arc models is questionable. The finding that the characteristic time for arc conductance varies with time, as indicated by computational results presented in this section, needs to be further verified by experiments.

Table 5.7. The arc conductance (G) and characteristic time for arc conductance variation (τ_G) shortly before current zero computed by the five flow models. P_0=21.4 atm and di/dt=13 Aμs^{-1}.

Time instant before current zero (μs)	Flow model	Arc conductance before current zero G (10^{-2} S)	characteristic time τ_G (μs)
2.0	(1)	8.50	2.70
	(2)	4.19	1.88
	(3)	4.34	1.79
	(4)	7.43	2.45
	(5)	7.87	2.60
1.5	(1)	6.93	2.19
	(2)	3.04	1.36
	(3)	3.12	1.28
	(4)	5.89	1.92
	(5)	6.30	1,98
1.0	(1)	5.33	1.69
	(2)	1.95	0.90
	(3)	1.95	0.86
	(4)	4.38	1.42
	(5)	4.76	1.53
0.5	(1)	3.78	1.31
	(2)	0.92	0.46
	(3)	0.87	0.42
	(4)	2.88	0.98
	(5)	3.24	1.11
0.05	(1)	2.51	0.97
	(2)	0.11	0.066
	(3)	0.058	0.042
	(4)	1.59	0.60
	(5)	1.97	0.78

Key to the models: (1) Laminar flow model, (2) Prandtl mixing length model, (3) Standard k-epsilon model, (4) Chen-Kim k-epsilon model and (5) RNG k-epsilon model.

5.2.2 Arc Behaviour after Current Zero and RRRV

A linearly increasing voltage at a given rate of rise (dV/dt) is used after current zero to investigate the thermal interruption capability of the nozzle configuration. The value of the rate of rise of recovery voltage (dV/dt), at which the arc will just be extinguished, is commonly known as the critical rate of rise of recovery voltage (RRRV). This will be found computationally using the five flow models. The qualitative features of the arc behaviour after current zero are similar when for different values of P_0 and di/dt. Unless otherwise specified, results are for P_0=21.4 atm and di/dt=13 Aμs^{-1}.

Figure 5.17 shows typical results of post-arc current computed by the Prandtl mixing length model and the standard k-epsilon model at different values of dV/dt. Results obtained by the Chen-Kim model, the RNG model and the laminar flow model are given in Figure 5.18. The axis temperature and electrical field distributions at different instants after current zero are given in Figures 5.19, 5.20, 5.21 and 5.22 respectively for the Prandtl mixing length model, the standard k-epsilon model, the Chen-Kim model and the laminar flow model. Results obtained by the RNG model are qualitatively very similar to those for the Chen-Kim model which are, therefore, not given here.

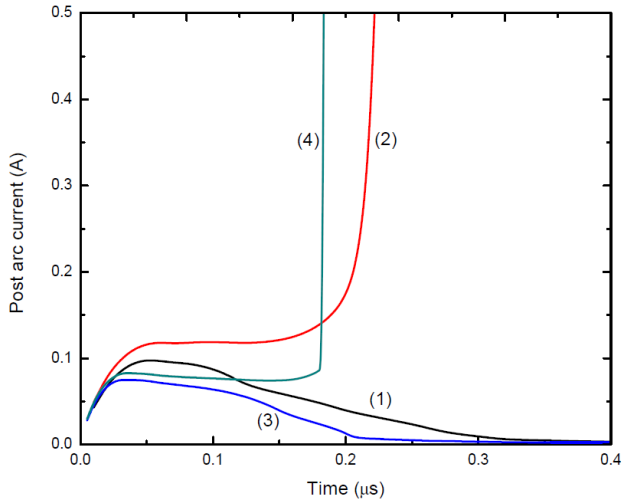

Figure 5.17. Post-arc current computed by two flow models. P_0=21.4 and di/dt=13 Aμs^{-1}. Key of the curves are:
Prandtl mixing length model: (1) dV/dt=18 kV$\mu s^{-1}$and (2) dV/dt=19 kVμs^{-1};
Standard k-epsilon model: (3) dV/dt=80 kVμs^{-1} and (4) dV/dt=85 kVμs^{-1}.

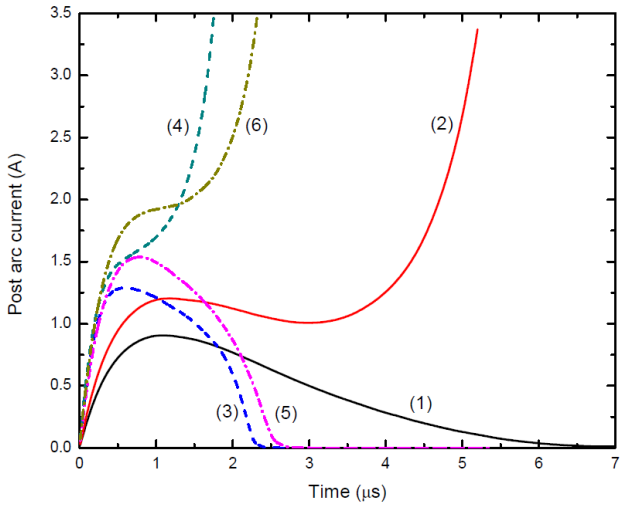

Figure 5.18. Post-arc current computed by three flow models. P_0=21.4 and di/dt=13 Aμs^{-1}. Key of the curves are:
Laminar flow model: (1) dV/dt=0.1 kVμs^{-1} and (2) dV/dt=0.13 kVμs^{-1};
Chen-Kim k-epsilon model: (3) dV/dt=0.45 kVμs^{-1} and dV/dt=0.5 kVμs^{-1};
RNG k-epsilon model: (5) dV/dt=0.3 kVμs^{-1} and dV/dt=0.35 kVμs^{-1}.

For the Prandtl mixing length model, when the arc is thermally extinguished, the arc temperature decays rapidly in 0.5 μs after current zero in the region of approximately 9 mm long downstream of the exit of the flat nozzle throat, i.e. from Z=5 mm to Z=14 mm (Figure 5.19(a)). It is this critical section of the arc that takes up most of the recovery voltage, where turbulent thermal conduction is mainly responsible for the rapid cooling of the arc. The electrical field of this critical section also increases rapidly with the temperature decay (Figure 5.19(b)). The standard k-epsilon model predicts a longer critical section than that predicted by the Prandtl mixing length model, which is from Z=2.5 mm to Z=14 mm (Figures 5.20(a) and 5.20(b)). The axis temperature of this critical section also decays more rapidly, which falls below 4000 K within only 0.25 μs (Figure 5.20(a)). This is due to a higher level of turbulence predicted by the standard k-epsilon model shortly before current zero in comparison with that computed by the Prandtl mixing length model as previously discussed. The RRRV computed by the standard k-epsilon model (82.5 kVμs^{-1}) is therefore significantly higher than that obtained by the Prandtl mixing length model (18.5 kVμs^{-1}).

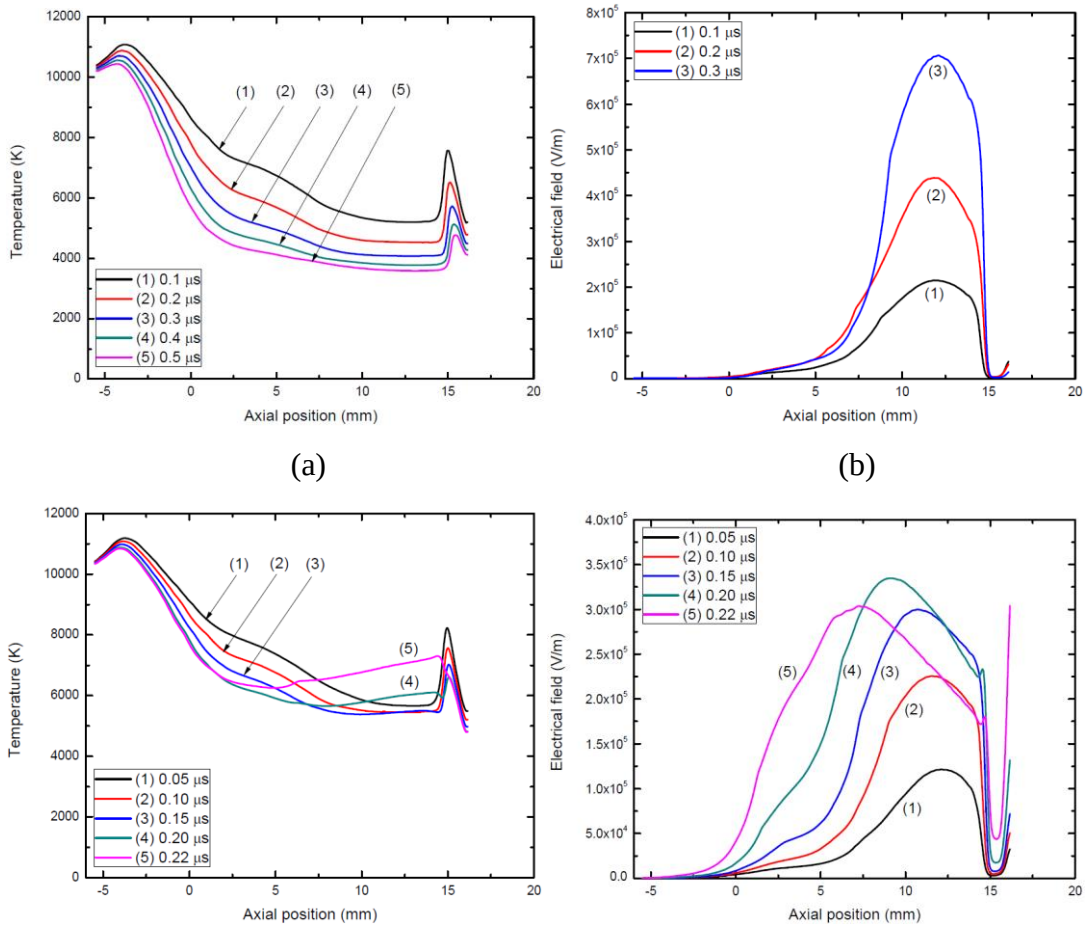

Figure 5.19. Variations of axis temperature and electrical field with axial position at various instants after current zero obtained by the Prandtl mixng length model. (a) Axis temperature distribution and (b) electrical field distribution for dV/dt = 18 $kV\mu s^{-1}$ (thermal clearance); (c) Axis temperature distribution and (d) electrical field distribution for dV/dt = 19 $kV\mu s^{-1}$ (thermal reignition).

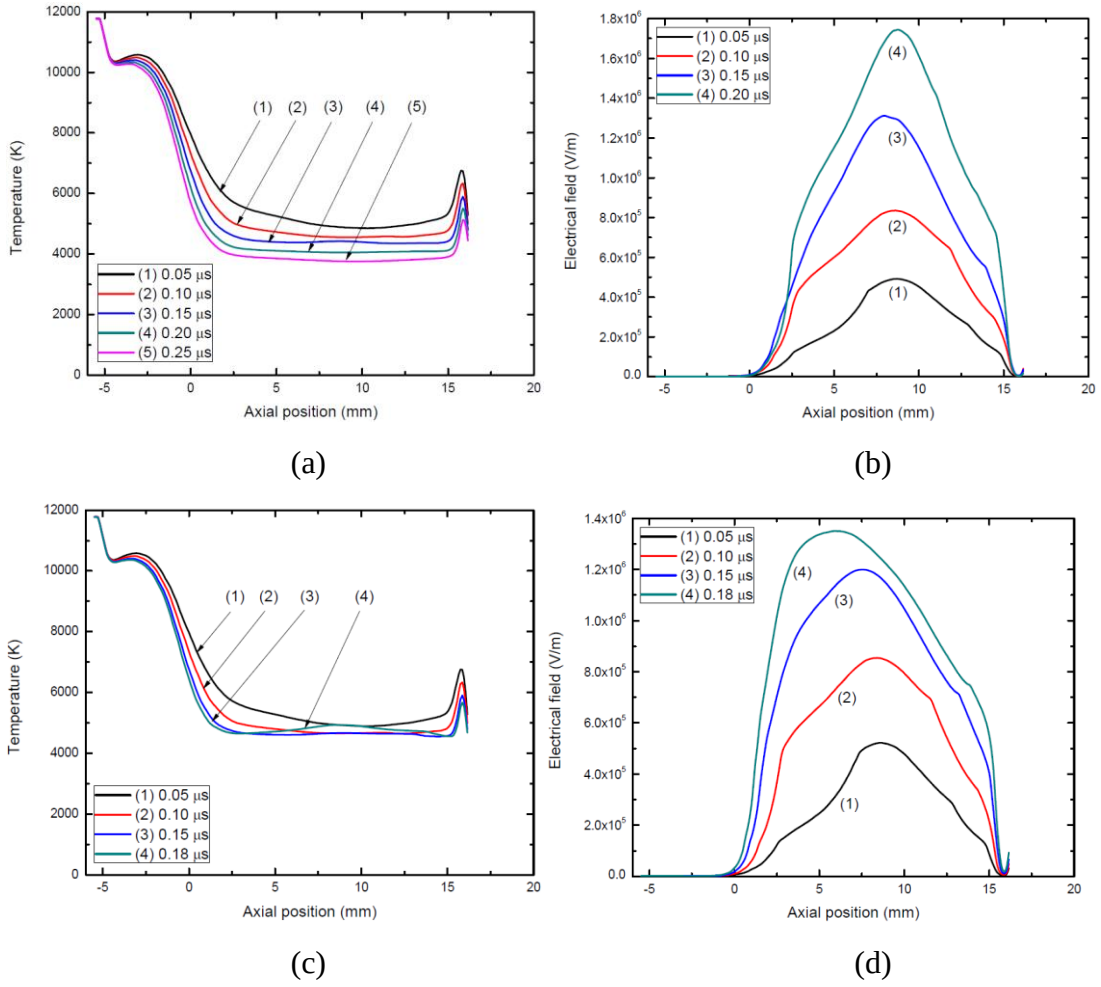

Figure 5.20. Variations of axis temperature and electrical field with axial position at various instants after current zero obtained by the standard k-epsilon model. (a) Axis temperature distribution and (b) electrical field distribution for dV/dt = 80 $kV\mu s^{-1}$ (thermal clearance); (c) Axis temperature distribution and (d) electrical field distribution for dV/dt = 85 $kV\mu s^{-1}$ (thermal reignition).

If dV/dt exceeds RRRV, temperature in the critical region still reduces immediately after current zero but this temperature decay is soon arrested as Ohmic input is pumped into a very thin core of the critical section, after which the axis temperature starts to increase. The rapid increase in axis temperature (Figures 5.19(c) and 5.20(c)) does not result in collapse of the voltage taken up by this section (as indicated by Figures 5.19(d) and 5.20(d) that electrical field is still going up) as the temperature away from the axis is still decreasing (thus arc radius is still reducing) due to thermal inertia. When the decay of temperature away from the axis has been arrested, the rate of rise of current is extremely rapid for a given dV/dt above RRRV

(Figure 5.17). Thus, the critical section is also responsible for thermal reignition when dV/dt is above RRRV. The duration before arc reignition is approximately 0.2 μs for the Prandtl mixing length model (Figure 5.17). It is even shorter for the standard k-epsilon model (Figure 5.17).

Chen-Kim and RNG models give similar results. The critical section of the arc is from Z= 8 mm to Z=14mm (Figures 5.21(a) and 5.21(b)), which is shorter than that predicted by the Prandtl mixing length model and the standard k-epsilon model. When the arc is thermally extinguished, the rate of temperature decay predicted by these two models appears to be quite slow (Figure 5.21(a)), for which the duration of thermal recovery and/or reignition is more than 5 times that predicted by the Prandtl mixing length model and 10 times that by the standard k-epsilon model. This is due to much weaker turbulence level predicted by the Chen-Kim and the RNG model as compared with the other two models. The values of computed RRRV obtained the Chen-Kim model (0.48 $kV\mu s^{-1}$) and the RNG model (0.33 $kV\mu s^{-1}$) are, therefore, of two orders of magnitude lower than those computed by the Prandtl mixing length model and the standard k-epsilon model.

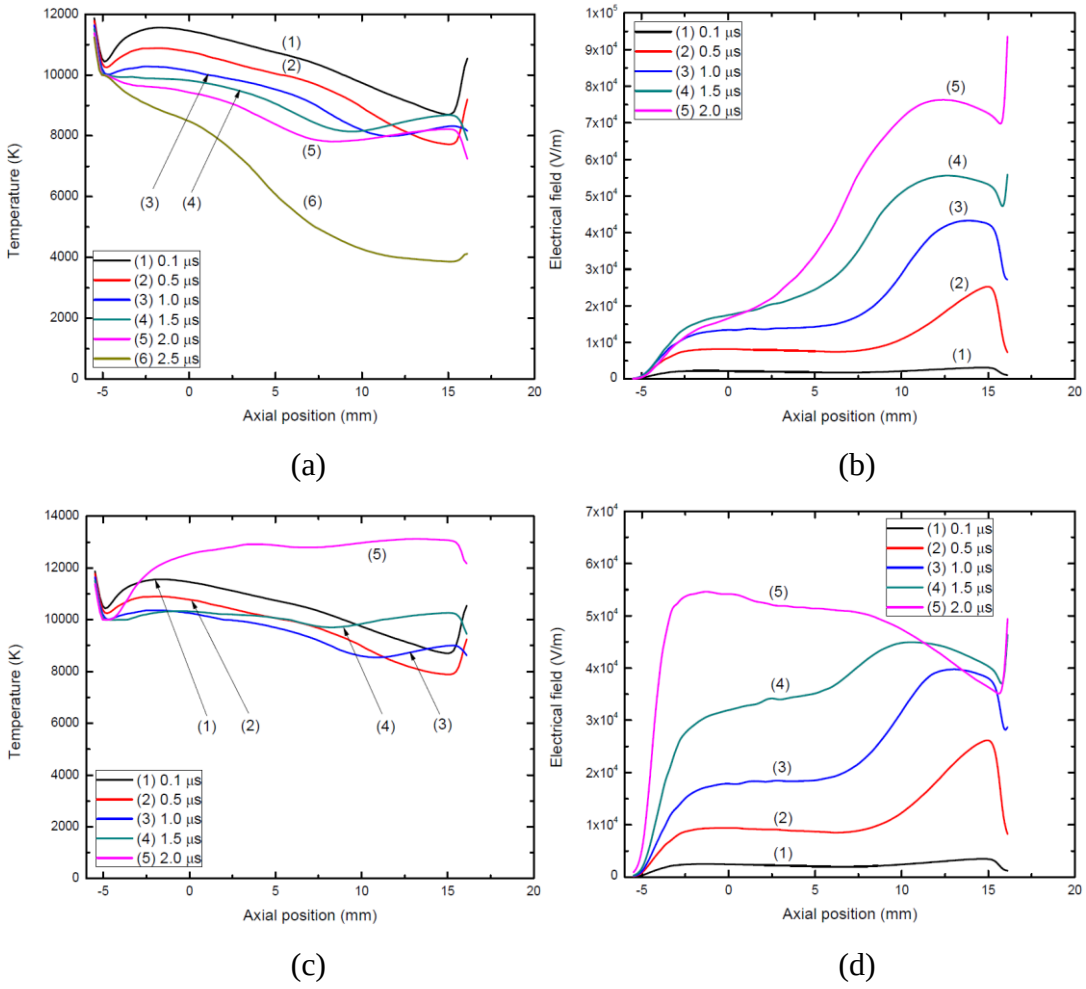

Figure 5.21. Variations of axis temperature and electrical field with axial position at various instants after current zero obtained by Chen-Kim k-epsilon model. (a) Axis temperature distribution and (b) electrical field distribution for dV/dt = 0.45 $kV\mu s^{-1}$ (thermal clearance); (c) Axis temperature distribution and (d) electrical field distribution for dV/dt = 0.5 $kV\mu s^{-1}$ (thermal reignition).

The laminar flow model predicts that the axis temperature for the whole arc decays during thermal recovery but the rate of temperature decay is the slowest in comparison with those predicted by the other turbulence models (Figure 5.22(a)). The electrical field increases with time due to temperature decay and the contraction of arc size as a result of radial inflow (Figure 5.22(b)). The peak of the electrical field moves from the upstream region to the downstream region of the nozzle throat (Figure 5.22(b)), which is due to strong axial convection downstream of the nozzle throat that effectively cools the arc. For the reignited case, the axis temperature for the whole arc is increased substantially in 5 μs (Figure 5.22(c)). The electrical field

increases monotonically with time (caused by arc contraction) after current zero. The maximum electrical field occurs at the nozzle throat (Z = 0) within 2 μs after current zero (figure 5.22(d)), which is expected to move to the upstream region of the nozzle throat at later times (e.g. 10 μs).

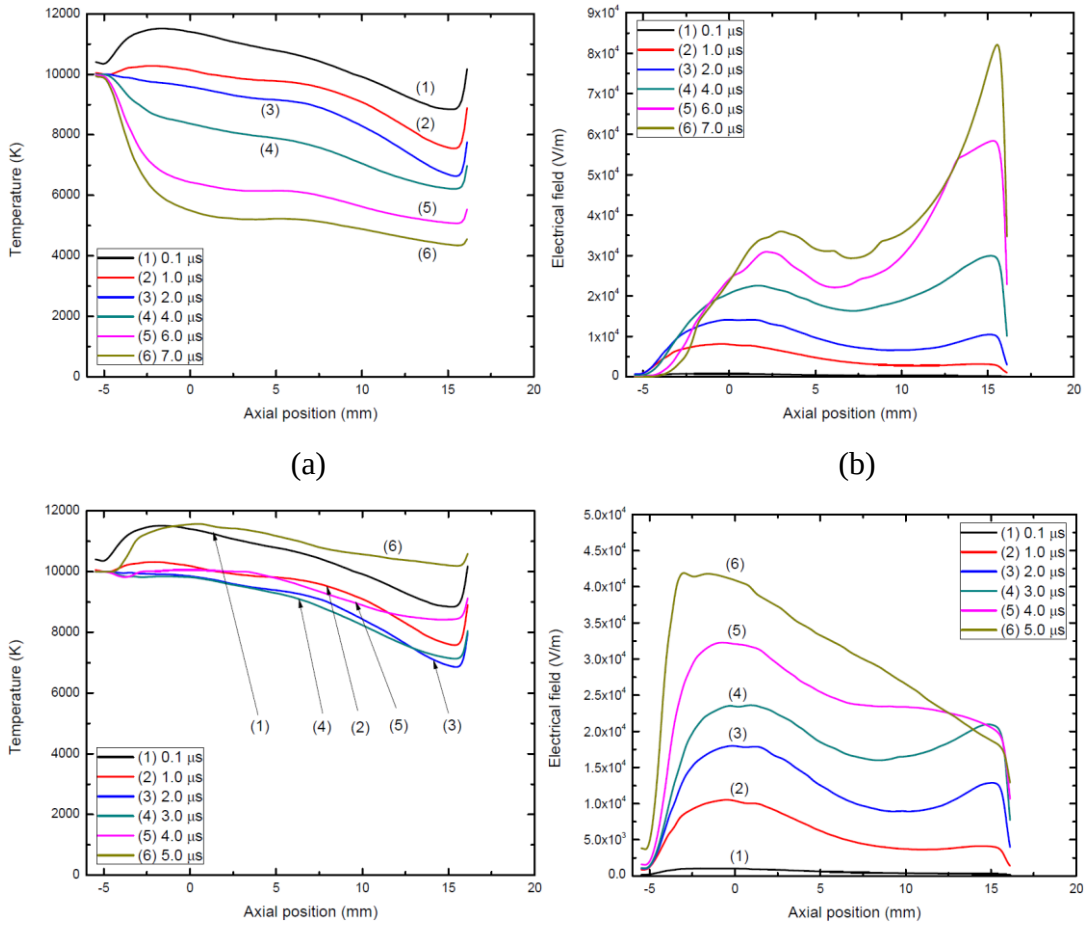

Figure 5.22. Variations of axis temperature and electrical field with axial position at various instants after current zero obtained by the laminar flow model. (a) Axis temperature distribution and (b) electrical field distribution for dV/dt = 0.1 $kV\mu s^{-1}$ (thermal clearance); (c) Axis temperature distribution and (d) electrical field distribution for dV/dt = 0.13 $kV\mu s^{-1}$ (thermal reignition).

5.3 Comparison with Experiments

The computed RRRV as a function of P_0 at di/dt=13 and 25 $A\mu s^{-1}$ are plotted in Figure 5.23 together with the experimental results given in [5.1] for comparison. The dependence of RRRV on P_0 at a given di/dt computed by the five flow models are

listed in Table 5.8.

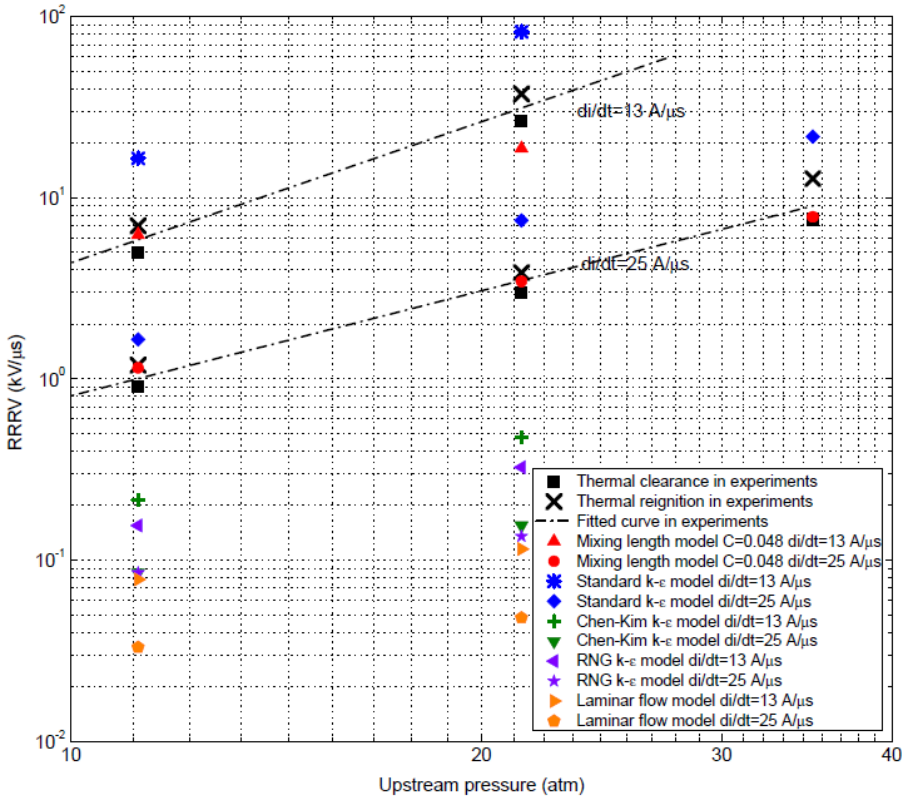

Figure 5.23. Comparison of measured RRRV and predicted RRRV computed by five flow models.

Table 5.8. The dependence of RRRV on P_0 at a given di/dt computed by five flow models.

	di/dt=13 A/μs		di/dt=25 A/μs	
	Predictions	Experiments	Predictions	Experiments
Laminar flow model	$RRRV \propto P_0^{0.6}$	$RRRV \propto P_0^{2.6}$	$RRRV \propto P_0^{0.58}$	$RRRV \propto P_0^{1.93}$
Prandtl mixing length model	$RRRV \propto P_0^{1.73}$		$RRRV \propto P_0^{1.69}$	
Standard k-epsilon model	$RRRV \propto P_0^{2.5}$		$RRRV \propto P_0^{2.26}$	
Chen-Kim k-epsilon model	$RRRV \propto P_0^{1.2}$		$RRRV \propto P_0^{0.93}$	
RNG k-epsilon model	$RRRV \propto P_0^{1.15}$		$RRRV \propto P_0^{0.66}$	

The RRRV predicted by the Prandtl mixing length model with optimised value of turbulence parameter shows excellent agreement with experiments at di/dt=25 $A\mu s^{-1}$. The model gives similar dependence of RRRV on P_0 at di/dt=13 $A\mu s^{-1}$ to that for di/dt= 25 $A\mu s^{-1}$ while experimental results indicate a much stronger pressure dependence at lower di/dt (Table 5.8). In theory, the dependence of RRRV on P_0 should not be sensitive to di/dt. If the dependence of RRRV on stagnation pressure is related to di/dt, this will result in the intersection of lines in Figure 5.23. Such intersection implies that at certain pressure range RRRV for a lower di/dt will be smaller than that for a higher di/dt. This is not physical. It is well-known that the value of RRRV has a large short to short variation. The scatter of the experimental results is not mentioned in [5.1]. Taking into account of experimental uncertainties, we feel that the predicted RRRV by the Prandtl mixing length model at 13 $A\mu s^{-1}$ and 21.4 atm is acceptable.

The standard k-epsilon model grossly over-predicts the values of RRRV, which also show much stronger dependence on P_0 at both values of di/dt (13 and 25 $A\mu s^{-1}$) in comparison with the dependence predicted by the Prandtl mixing length model.

The laminar flow model gives the lowest values of computed RRRV among all the five flow models, which is also significantly lower than corresponding measurements for the range of P_0 and di/dt considered in the present investigation. For both values of di/dt (13 and 25 $A\mu s^{-1}$), the computed RRRV is approximately proportional to square root of P_0, which is consistent with the investigation of [5.4].

The Chen-Kim model and the RNG model give similar predictions of RRRV, both of which grossly under-estimate RRRV for all cases under investigation. Compared with experiments, the RRRV computed by the Chen-Kim model and the RNG model also shows much weaker dependence on P_0 at di/dt =13 and 25 $A\mu s^{-1}$, which is only slightly stronger than the dependence predicted by the theory based on laminar flow as indicated in the present investigation and in [5.4].

It is noted that the experimentally measured RRRV, together with the computed RRRV obtained by the Prandtl mixing length model which gives the best prediction of measured values, shows that the RRRV is proportional to the square of stagnation

pressure. This is much stronger than the pressure dependence of arc voltage for the DC arcs investigated in Chapter 4, and the arcs under quasi-steady sate discussed earlier in this chapter, which is proportional to the square root of stagnation pressure. Up to now, there appears to be no satisfactory explanation for such pressure dependence of the RRRV. It is therefore necessary to further investigate factors affecting the dependence of the RRRV on stagnation pressure. Such investigation is, however, beyond the scope of this chapter, since the main objective of this chapter is to test the selected turbulence models in order to find a suitable turbulence model in predicting the thermal interruption capability of turbulent SF_6 switching arcs. Therefore, we present the work done for this investigation and the main findings in Appendix B for reference.

5.4 Relative Merits of Turbulence Models

Of the four turbulence models investigated, the Prandtl mixing length model is the simplest but the turbulence parameter needs to be tuned to give the best fit for a single set of experimental results (e.g. the value of RRRV for a given stagnation pressure, P_0, and and the rate of current decay, di/dt). If nozzle geometry is changed, this process needs to be repeated.

As regards the predicted RRRV, the Prandtl mixing length model can generally give reasonable predictions for a range of P_0 and di/dt with optimized value of turbulence parameter for a given nozzle geometry. It is obvious that the standard k-epsilon model overestimates RRRV of the nozzle arc for the nozzle investigated in this chapter, while its two variants (the Chen-Kim model and the RNG model) underestimate.

Since the recommended values of the turbulence parameters in the standard k-epsilon model and its two variants (the Chen-Kim model and the RNG model) need to be adjusted to achieve agreement with test results, the Prandtl mixing length model is, therefore, preferred as the tuning of the value of its turbulence parameter is much easier and quicker. It is also much easier to implement and the computational

cost is the lowest.

5.5 Concluding Remarks

The current zero behaviour of the SF_6 nozzle arc has been numerically investigated for Nozzle 2 using the five flow models employed in Chapter 4, i.e. the laminar flow model, the Prandtl mixing length model, the standard k-epsilon model, the Chen-Kim model and the RNG model.

A comparative study of different flow models has been conducted for P_0=21.4 atm and di/dt=13 $A\mu s^{-1}$. A detailed analysis of the physical mechanisms encompassed in each flow model is given to show the adequacy of a particular model in describing the rapidly varying arc during current zero period.

The RRRV has been calculated for two rates of current decay (di/dt=13 and 25 $A\mu s^{-1}$) and three stagnation pressures (P_0=11.2 atm, 21.4 atm and 35 atm) by applying the five flow models, which are compared with test results of Benenson et al. [5.1]. It has been shown that the Prandtl mixing length model can generally give satisfactory predictions of the RRRV with turbulence parameter adjusted to fit one test result of RRRV. The standard k-epsilon model grossly over-estimates RRRV which is much higher than measurements for all the discharge conditions investigated. The performances of the Chen-Kim model and the RNG model are similar, both of which grossly under-estimates the effect of turbulence, and the predicted RRRV is of the same order of magnitude of that predicted by the laminar flow model, which is much lower than measured RRRV. Based on the comparison between predicted RRRV, the relative merits of the turbulence models are discussed.

References

[5.1] Benenson D M, Frind G, Kinsinger R E, Nagamatsu H T, Noeske H O and Sheer, Jr R E 1980 Fundamental investigation of arc interruption in gas flows EPRI EL-1455 (Project 246-2)

[5.2] Cassie A M 1939 Arc rupture and circuit severity: a new theory (CIGRE, Rep. 102) pp 1-14

[5.3] Mayr O 1943 Contribution to the theory of static and dynamic arcs *Arch. Elect.* **37** 588-608

[5.4] Fang M T C and Zhuang Q 1992 Current-zero behaviour of an SF_6 gas-blast arc. Part I: laminar flow *J. Phys. D: Appl. Phys.* **25** 1197-204

Chapter 6
Effects of Nozzle Geometry on SF_6 Arc Thermal Interruption

6.1 Introduction

Supersonic nozzle interrupters are commonly used in modern gas blast circuit breakers for the control of arc discharge conditions [6.1]. It is well-known that turbulent energy transport plays a critical role in thermal extinction of an SF_6 nozzle arc [6.2]. Nozzle geometry determines the flow conditions, hence the turbulence level in the current zero period. Optimization of the nozzle interrupter is, therefore, an important part in the design process of a circuit breaker.

The investigation presented in this chapter forms the third part of the systematic investigation into the behaviour of a SF_6 nozzle arc (hereafter referred to as Part III). Part III studies the effects of the nozzle geometry on the turbulence level during the current zero period which affects the arc characteristics and the RRRV. Of the commonly used turbulence models, the Prandtl mixing length model gives overall better prediction of SF_6 arc behaviour during the current zero period as shown in Part II of the systematic investigation (Chapter 5) for Nozzle 2 of Benenson et al. [6.3], which will, therefore, be used in the present investigation to model the turbulent SF_6 nozzle arc. However, the application of the Prandtl mixing length model relies upon limited experimental data to fix the value of one turbulence parameter by matching the computed results with experiments for a given nozzle geometry, thus for a different nozzle geometry this turbulence parameter needs to be readjusted. The standard k-epsilon model, on the other hand, can also give satisfactory predictions for the certain nozzle geometries (e.g. Nozzle 1 in Figure 3.3, used in the experiments of Frind et al. [6.4]) under certain discharge conditions (e.g. P_0=21.4 and 35 atm, di/dt=13 $A\mu s^{-1}$) [6.5]. It is, therefore, believed that the standard k-epsilon

model can, at least qualitatively, give reasonable prediction on how the nozzle geometry will affect the turbulence level, although this model has not given satisfactory prediction on the thermal interruption capability of SF_6 nozzle arcs for Nozzle 2 as shown in Chapter 5. Thus, the standard k-epsilon model will also be applied in the present investigation.

Three nozzle designs, i.e. those of Frind et al. [6.4], Benenson et al. [6.3] and Frind of Rich [6.1] (given in Figure 3.3, hereafter referred to as Nozzle 1, Nozzle 2 and Nozzle 3, respectively), are considered in the present investigation. The measured RRRV for these three nozzles together with the computational results will be used to evaluate the turbulence level and the influence of the geometrical factors of a nozzle on thermal interruption.

6.2 Nozzle Geometry and Relevant Experimental Results

The test results in the form of the RRRV obtained from extensive GE experiments [6.1, 6.3, 6.4], which are described in detail in Section 3.6 of Chapter 3, are used for direct comparison with computational results as well as to evaluate the level of turbulence for different nozzle geometries. The three nozzle designs used in the present investigation are shown in Figure 3.3. The features of these nozzles and their key dimensional parameters are described in Section 3.6 of Chapter 3, which are not repeated here.

It should be noted that experiments on the three nozzles were not designed to study specifically the effects of nozzle geometry as the shapes and dimensions of the upstream electrodes and the locations of the electrode tip are different (Figure 3.3). These three nozzles, therefore, have no geometrical similarities. Because of these differences, the arc lengths before the nozzle throat are different for the three nozzles. In addition, flow before the nozzle throat can be affected by the upstream electrode, since the shape and dimension of the upstream electrode affect the effective nozzle area upstream of the nozzle throat. Nevertheless, it should be noted that, in general, the critical arc section for arc interruption is downstream the nozzle throat, and thus

differences in upstream electrode configurations are not expected to substantially affect RRRV. Apart from the effects of the upstream electrode, the shape and dimension of the downstream electrode also affect the flow behaviour in front of this electrode, which has been discussed in detail in Chapters 4 and 5 and also in [6.5]. Despite such effects, it has been found that the arc section influenced by the presence of the downstream electrode only account for less than 5% of the total arc voltage [6.5], and thus it cannot substantially affect RRRV, neither. We, therefore, consider that the differences in RRRV for the three nozzles are attributed to the influence of nozzle geometry and the influences of electrodes (e.g. shape, position and dimensions of the electrodes) on RRRV are negligible. The electrode distances (i.e. arc lengths) for Nozzles 1 and 2 are almost the same, approximately 20 mm. For Nozzle 3, the electrode distance is approximately 50 mm.

The computational results, unless otherwise specified, are obtained under discharge conditions identical with the experiments of [6.1, 6.3, 6.4]. These experimental results will be used to assess the performance of the two turbulence models (i.e. the Prandtl mixing length model and the standard k-epsilon model) in predicting the dependence of turbulence level on the nozzle geometry as well as to evaluate the influence of the geometrical factors of a nozzle on turbulence level and thermal interruption.

6.3 Results and Discussion

Computations were carried out using a current ramp with a plateau of 1 kA and a rate of current decay (di/dt) before current zero and a voltage ramp (dV/dt) after current zero to determine RRRV. The Prandtl mixing length model and the standard k-epsilon model are used to model the effects of turbulence. For Nozzles 1 and 2, the stagnation pressures (P_0) ranging from 11.2 atm to 35 atm and two values of di/dt (13 and 25 $A\mu s^{-1}$) are investigated with the static pressure at the nozzle exit (P_e) set to a very low value to ensure shock free in the nozzle. For Nozzle 3, the values of P_0 ranging from 7.8 atm to 37.5 atm and two values of di/dt (13.5 and 27 $A\mu s^{-1}$) have

been applied with $P_e=P_0/4$ which is consistent with the experimental conditions in [6.4].

For the Prandtl mixing length model, the turbulence parameter, *c*, was adjusted to give the closet agreement between the computed and measured RRRV for a given nozzle geometry. The values of *c* for the three nozzles are respectively 0.054 for Nozzle 1, 0.057 for Nozzle 2 and 0.045 for Nozzle 3.

Computational results show that the qualitative features of the arc behaviour for a given nozzle geometry are similar for different values of P_0 and di/dt. Unless otherwise specified, the predicted results at P_0=21.4 atm and di/dt=25 $A\mu s^{-1}$ (di/dt=27 $A\mu s^{-1}$ for Nozzle 3) will be used to illustrate the typical arc behaviour and the differences between nozzles. Based on these computational results, we can predict the behaviour of the switching arc inside different nozzle geometries and identify the main physical process taking place during current zero period. A detailed interpretation of the results and their indications are given below.

6.3.1 The Behaviour of the 1 kA DC Arc

Axial variations of axis pressure, axis velocity, axis temperature, arc radius and electrical field for the three nozzles computed by the two turbulence models are shown in Figures 6.1, 6.2, 6.3, 6.4 and 6.5, respectively. These results show that the qualitative features of the nozzle arc at 1 kA DC predicted by the two turbulence models are similar.

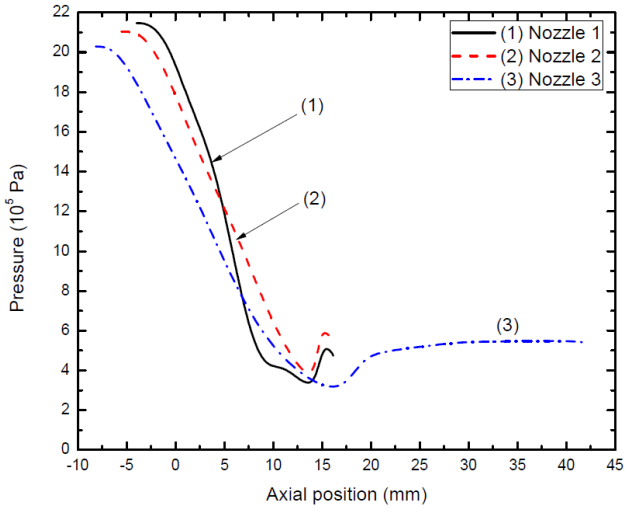

(a)

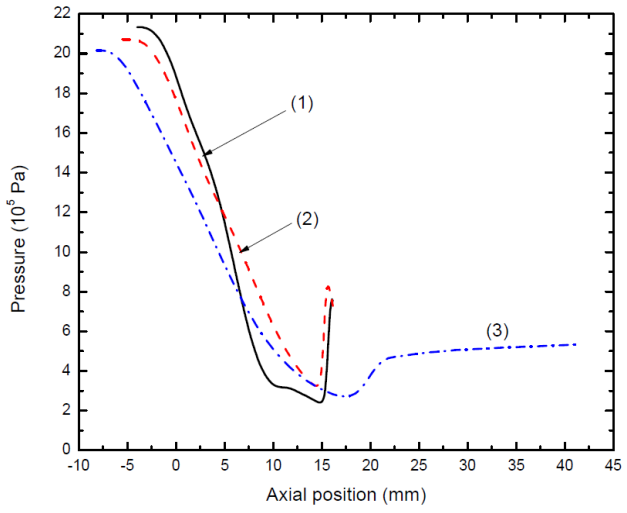

(b)

Figure 6.1. Variations of pressure along the nozzle axis at 1 kA DC computed by the two turbulence models. (a) Prandtl mixing length model and (b) standard k-epsilon model.

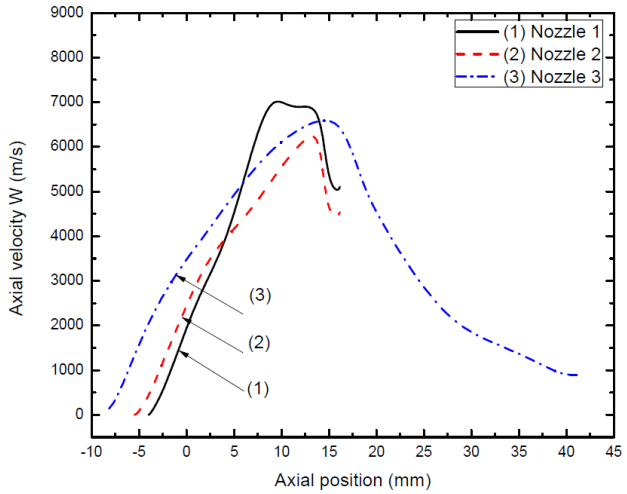

(a)

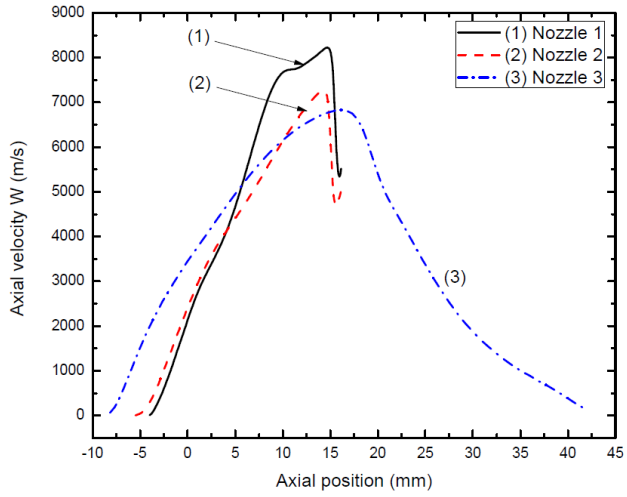

(b)

Figure 6.2. Variations of axial velocity along the nozzle axis at 1 kA DC computed by the two turbulence models. (a) Prandtl mixing length model and (b) standard k-epsilon model.

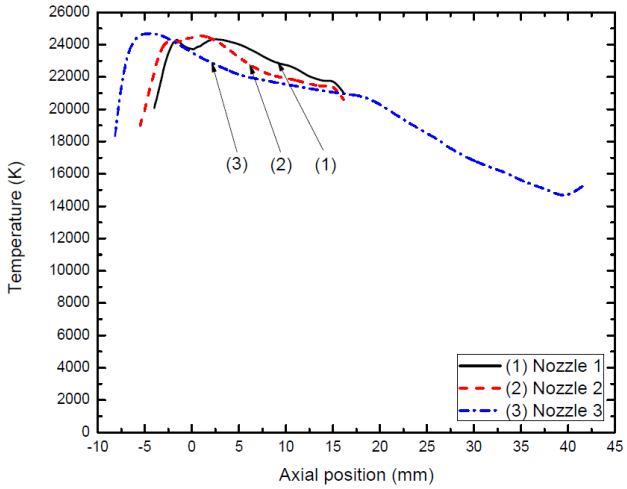

(a)

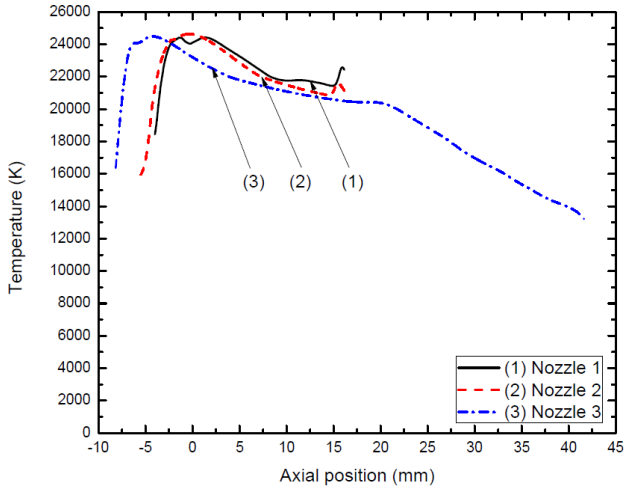

(b)

Figure 6.3. Variations of axis temperature along the nozzle axis at 1 kA DC computed by the two turbulence models. (a) Prandtl mixing length model and (b) standard k-epsilon model.

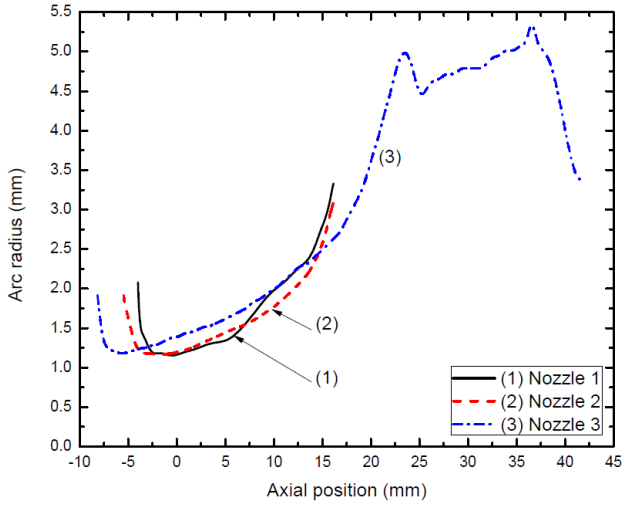

(a)

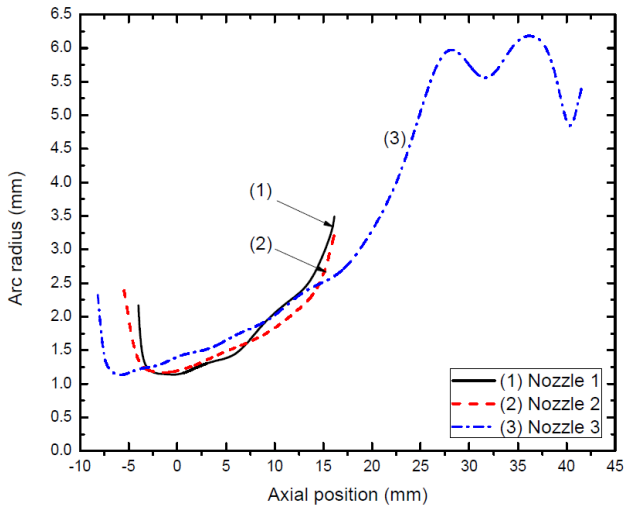

(b)

Figure 6.4. Variations of arc radius with axial position at 1 kA DC computed by the two turbulence models. (a) Prandtl mixing length model and (b) standard k-epsilon model.

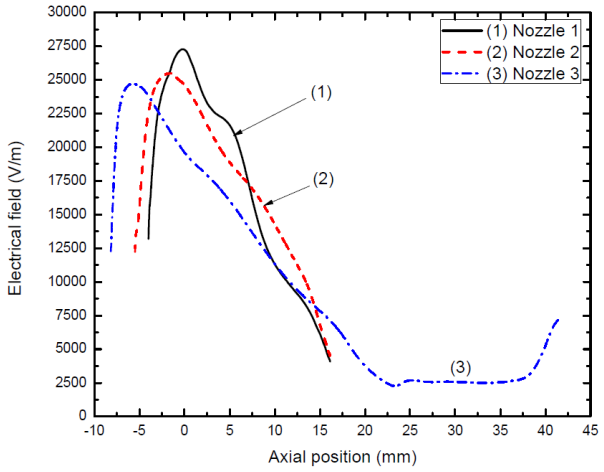

(a)

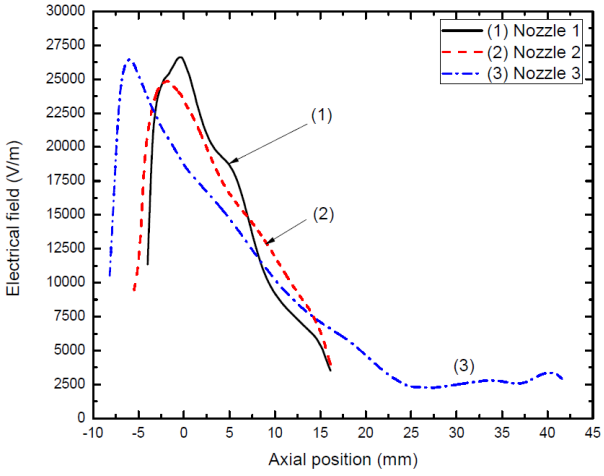

(b)

Figure 6.5. Variations of electrical field with axial position at 1 kA DC computed by the two turbulence models. (a) Prandtl mixing length model and (b) standard k-epsilon model.

For Nozzle 3, a shock is generated downstream of the nozzle throat which is due to the exit pressure not sufficiently low to ensure shock free inside the nozzle. The location of this shock almost coincides with the position of the downstream electrode tip in Nozzles 1 and 2 as shown in Figure 6.1 (Curve 3 which shows the pressure rise in the region between Z=15 mm and Z=20 mm). The adverse pressure gradient after the shock results in deceleration of the oncoming gas flow (Figure 6.2), which subsequently causes flow separation and formation of vortices after the shock [6.6, 6.7]. The vortices can deform the arc boundary, thus increasing the arc cross-section behind the shock as indicated by the arc radius [6.6, 6.7]. More information will be

given in Section 6.3.2 to show that the flow separation due to the presence of the shock results in slow thermal recovery of the arc section after the shock, thus reducing the effective arc length and subsequently the thermal interruption capability of a nozzle (characterized by RRRV of a nozzle arc). In the rest of this section, for Nozzle 3, attention will be paid to the arc section before the shock, since it is this part of the arc length (instead of the part behind the shock) that plays a crucial role in determining the thermal interruption capability of this nozzle.

For a given stagnation pressure and in the absence of a sizeable upstream electrode, the axial variation of nozzle area ratio (Nozzle cross-sectional area at a given axial position/Nozzle throat area=A/A_t) approximately determines the pressure distribution within the nozzle. The axial pressure gradient controls the axial growth of the arc radius through enthalpy transport while the absolute value of pressure determines the radiation loss. Therefore, optimization of nozzle geometry can achieve the best interruption performance by controlling arc temperature and radius.

With the same stagnation pressure, the mass flow rate of Nozzle 2 is approximately 4 times that of Nozzle 1. Compared with Nozzle 1, Nozzle 2 has a gentler area variation, which results in a slower rate of pressure decrease than Nozzle 1 (Figure 6.1). Thus, gas acceleration in Nozzle 1 is stronger than Nozzle 2 (Figure 6.2). The arc radius of Nozzle 1 is smaller in the region where Z<7.5mm than that of Nozzle 2 but the reduction in absolute pressure after Z=7.5mm makes the arc radius larger than that of Nozzle 2 (Figure 6.4). Thus, the electrical field distribution for Nozzle 1 is higher than that of Nozzle 2 in the region where Z<7.5 mm but is lower than that of Nozzle 2 after Z=7.5 mm (Figure 6.5).

Nozzles 2 and 3 have the same throat area with slightly different stagnation pressures, thus nearly the same mass flow rate. Nozzle 3 gives the smallest axial pressure gradient (dp/dz) as well as the lowest absolute pressure in comparison with the other two nozzles (Figure 6.1) for the major part of its length. The arc radius for Nozzle 3 is, therefore, the largest (Figure 6.4) and the electrical field the lowest (Figure 6.5). Thus, of the three nozzles, for the arc radius and electrical field averaged over the whole arc length Nozzle 2 has the smallest arc radius (Figure 6.4)

and highest electrical field (Figure 6.5).

It has been found that for the 1 kA DC arc, around 80% of the current is carried by the high temperature core, the boundary of which is defined as the radial position corresponding to a temperature of 83.3% of the axis temperature. Electrical field is mainly determined by the energy balance of this high temperature core. Energy balance calculations for the three nozzles show that Ohmic input into this core is largely taken out by radiation (consistent with investigations in Chapters 4 and 5). For such radiation transport dominated arc core, the axis temperature is not sensitive to nozzle geometry (Figure 6.3). The fact that radiation transport is the dominant energy transport mechanism for the arc at 1 kA DC explains the similar qualitative features of the arc computed by the two turbulence models for a given nozzle geometry, because at this current turbulence enhanced thermal conduction is not important in the determination of the aerodynamic and electrical behaviour of the arc. However, for the arc shortly before current zero the qualitative features and the electrical behaviour of the arc will be dependent on turbulence models for a given nozzle geometry, which will be discussed in Section 6.3.2.

6.3.2 The Behaviour of the Transient Arc before Current Zero

For the transient arc with the current ramping from 1 kA DC towards zero, the arc temperature decreases and the arc shrinks due to reduction of Ohmic heating, which result in the absolute value of pressure inside the arc to decrease with current decay. The axis pressure at current zero is, therefore, lower than that of 1 kA DC (Figure 6.6). Nevertheless, the qualitative features of the axial variations of axis pressure are always similar to those at 1 k A DC as shown in Figure 6.1. The location of the shock is not sensitive to current as indicated by Figures 6.1 and 6.6.

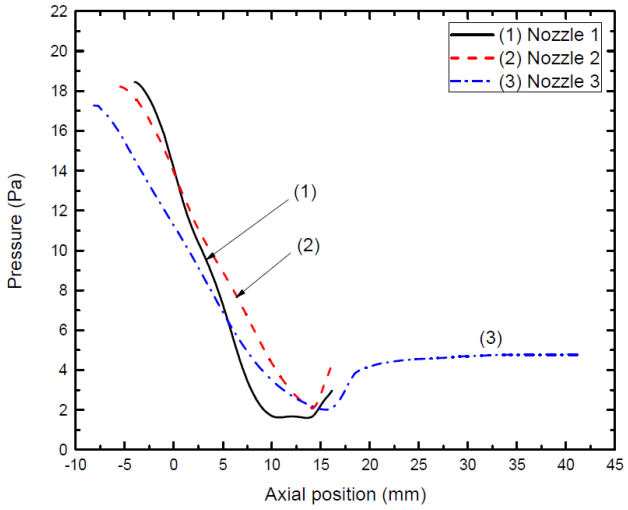

(a)

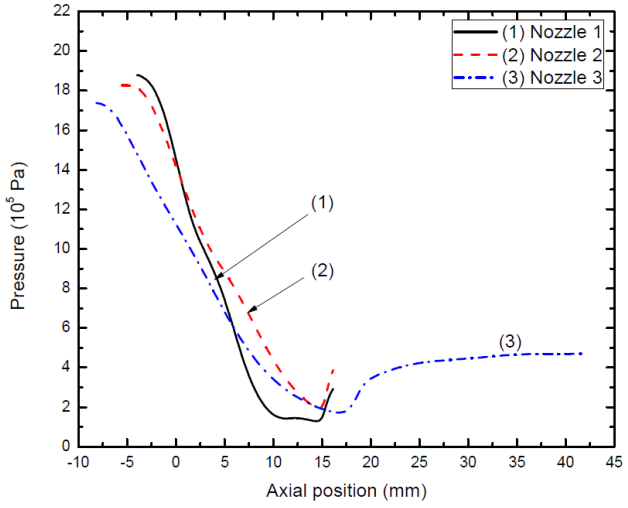

(b)

Figure 6.6. Variations of pressure along the nozzle axis at current zero computed by the two turbulence models. (a) Prandtl mixing length model and (b) standard k-epsilon model.

The time variations of axis temperature and arc radius for the three nozzles obtained by the Prandtl mixing length model and the standard k-epsilon model are given in Figures 6.7, 6.8 and 6.9. It is noted that for the arc section behind the shock, the rates of decrease of the axis temperature and the arc radius are significantly slower than those upstream of the shock. This means the presence of the shock results in slower recovery speed of the arc section behind the shock. As a result, the arc voltage taken by the section behind the shock accounts for less than 20% of the total arc voltage before current zero when the current is ramping down, which is even

negligible a few microseconds before current zero. This renders the effective arc length of Nozzle 3 for arc interruption almost the same as those of Nozzles 1 and 2. Therefore, the use of RRRV for the three nozzles as a means to assess the turbulence effects is meaningful. The effects of the shock on the behaviour of an SF_6 nozzle arc is beyond the scope of this chapter, thus no further discussion will be made in this chapter. Detailed investigation on this topic will be presented in Chapter 7. In the rest of this chapter, for Nozzle 3, attention will only be paid to the arc section before the shock when discussing the computational results unless otherwise specified.

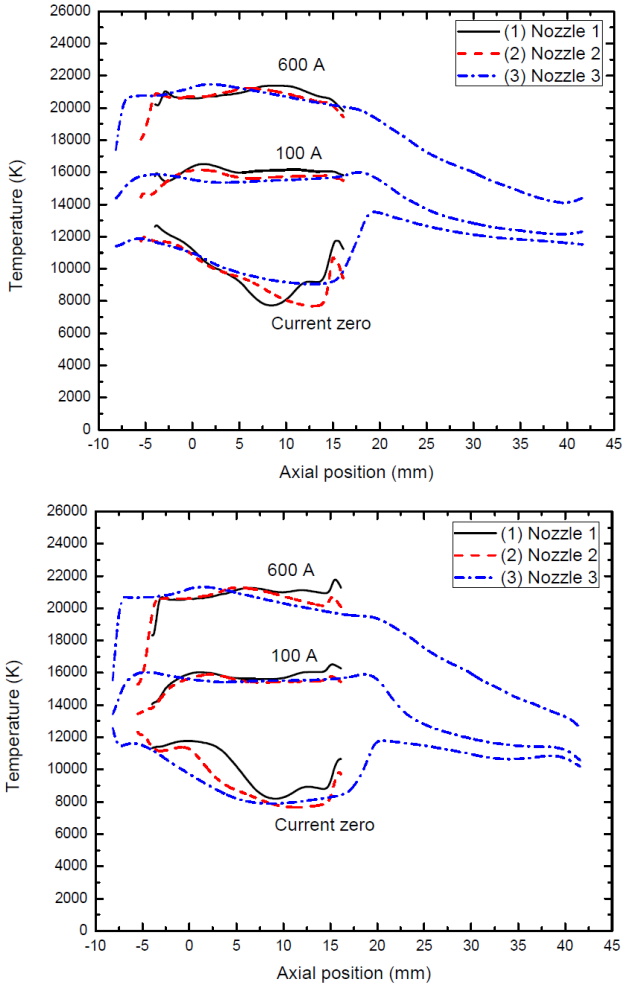

Figure 6.7. Variations of axis temperature with axial position at different current levels before current zero computed by the two turbulence models. P_0=21.4 atm and di/dt=25 Aμs^{-1}. (a) Prandtl mixing length model and (b) standard k-epsilon model.

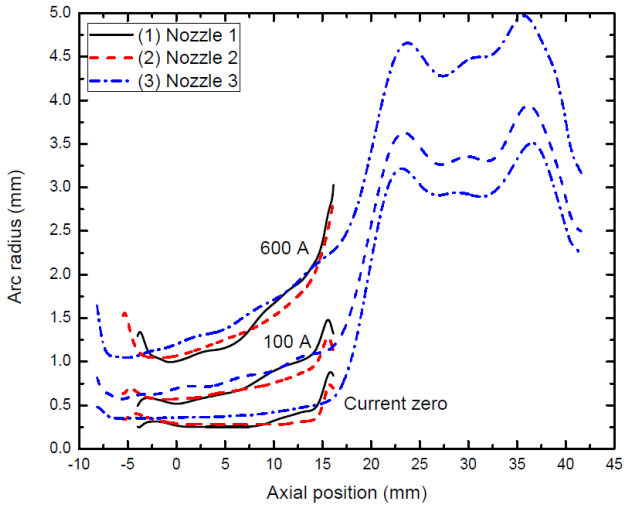

(a)

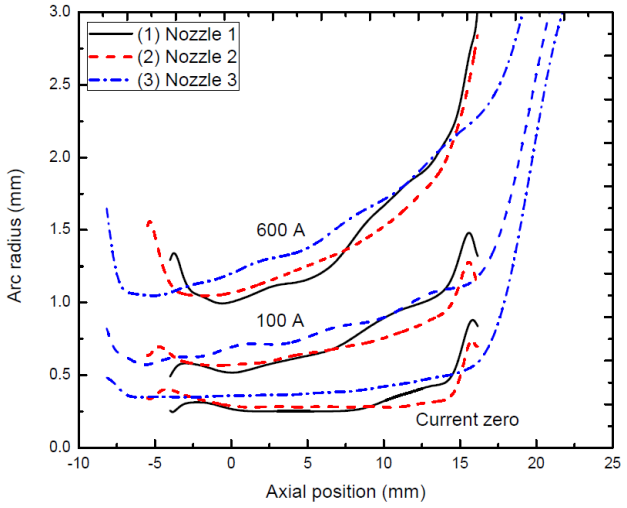

(b)

Figure 6.8. Variations of arc radius with axial position at different current levels before current zero computed by the Prandtl mixing length model. P_0=21.4 atm and di/dt=25 Aμs^{-1}. (a) Variation of arc radius between the contact gap and (b) enlarged diagram of (a) between Z=-10 mm and Z=25 mm.

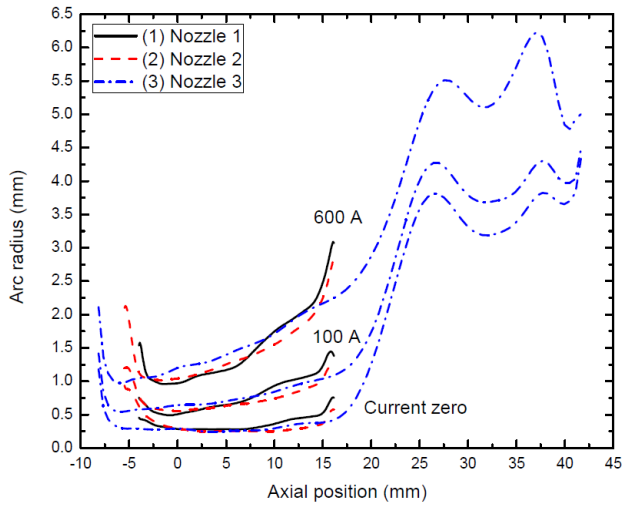

(a)

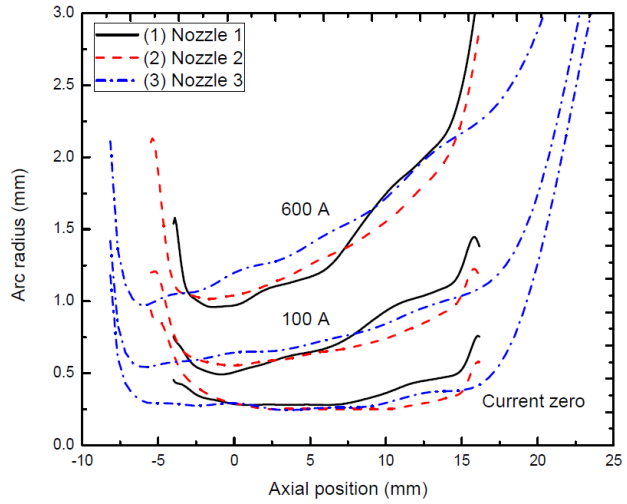

(b)

Figure 6.9. Variations of arc radius with axial position at different current levels before current zero computed by the standard k-epsilon model. P_0=21.4 atm and di/dt=25 $A\mu s^{-1}$. (a) Variation of arc radius between the contact gap and (b) enlarged diagram of (a) between Z=-10 mm and Z=25 mm.

For currents of 600 A and above, the qualitative features of the arc indicated by the axis temperature (Figure 6.7) and arc radius (Figures 6,8 and 6.9) are similar to those of the 1 kA DC arc for a given nozzle geometry. The results are not sensitive to different turbulence models, neither. This is because, for currents of 600 A and above, the arc is known to be in quasi-steady state stage. In this stage, the arc also has a radiation dominated arc core which takes approximately 80% of the current: similar to the arc at 1 kA DC. For such radiation transport dominated arc core, the axis temperature is not sensitive to nozzle geometry (Figure 6.7), and the arc voltage for a

given nozzle is almost independent of current for current greater than 600 A (Figure 6.10).

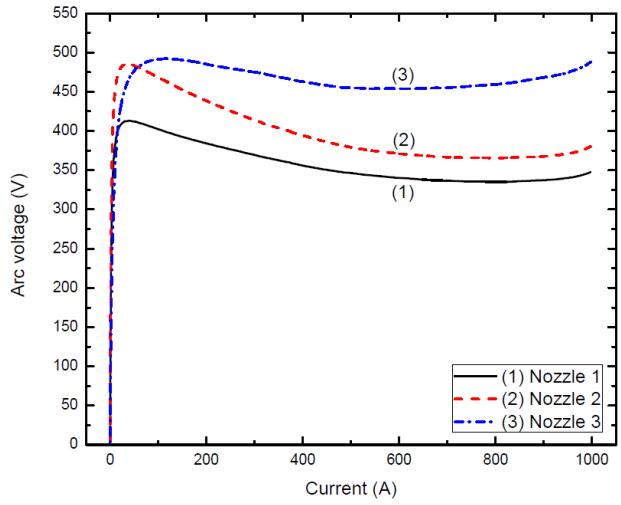

(a)

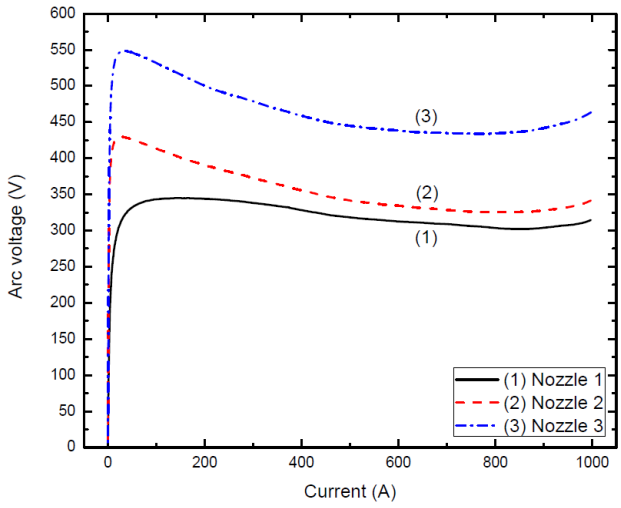

(b)

Figure 6.10. Voltage-current characteristics for the arcs in the three nozzles computed by the two turbulence models. P_0=21.4 atm and di/dt=25 Aμs^{-1}. (a) Prandtl mixing length model and (b) standard k-epsilon model.

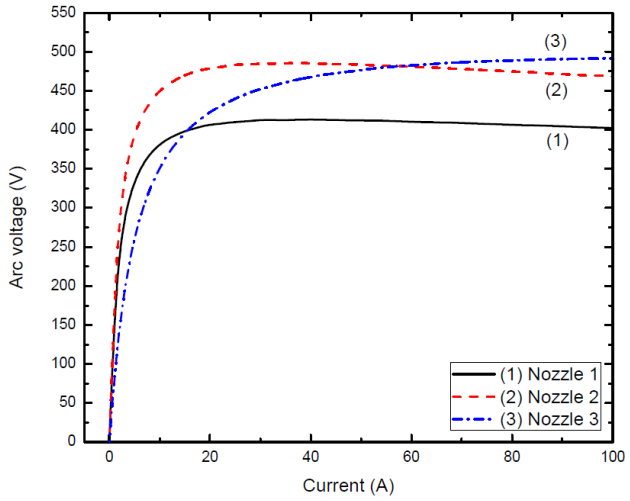

(a)

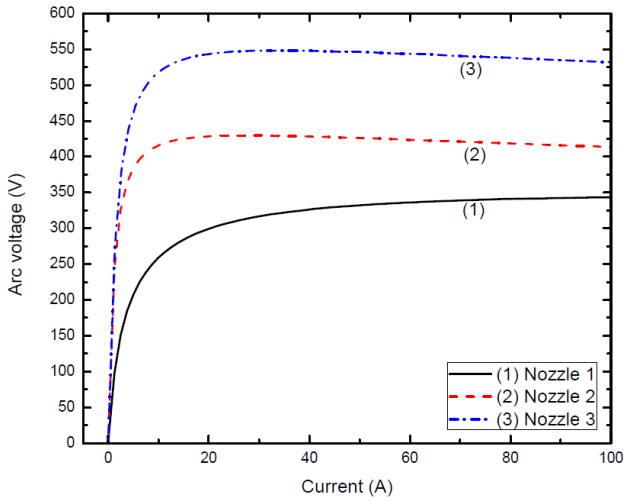

(b)

Figure 6.11. Enlarged voltage-current characteristics in the last 4 μs before current zero. P_0=21.4 atm and di/dt=25 $A\mu s^{-1}$. (a) Prandtl mixing length model and (b) standard k-epsilon model.

When the current further decays towards its zero point, the arc deviates from quasi-steady state. From the instant when the arc deviates from quasi-steady state to the instant of current zero, the arc is known to be in current zero period. During current zero period, the axis temperature further decreases and the arc column contracts which favours radial turbulent thermal conduction. At 100 A, the axis temperature is reduced to 17,000 K (Figure 6.7). As previously mentioned in Chapter 4, the radial turbulent thermal conduction is expected to become important due to, firstly, the relative importance of thermal conduction to radiation loss is inversely

proportional to the arc radius, and, secondly, net radiation loss decreases rapidly with temperature for temperatures below 18,000 K. As a result, turbulence thermal conduction gradually becomes the dominant energy loss mechanism and the arc voltage starts to rise (the reason for this has been explained in Chapter 4) as indicated by Figure 6.10. Thus, the accumulated turbulence effects determines the axis temperature and arc radius during the whole current zero period and those at current zero. Computational results are, therefore, dependent on the application of different turbulence models.

By applying the Prandtl mixing length model, the axis temperature (Figure 6.7 (a)) and arc radius (Figures 6.8 (a) and 6.8(b)) at 100 A and at current zero, as well as the electrical field distributions (Figure 6.12), indicate that Nozzle 2 tends to have the best thermal interruption capability while the thermal interruption capability of Nozzle 3 will be the worst. In addition to the axis temperature, arc radius and the electrical field distributions, arc voltage before the current zero point is the most sensitive indicator regarding the accumulated effects of turbulence cooling. As shown in Figure 6.10(a), when the current is high (i > 100 A), Nozzle 3 gives the highest arc voltage due to its arc length being 2.5 times larger than those of Nozzles 1 and 2. However, when current zero is approached, the effective arc length of Nozzle 3 becomes almost the same as those of the other two nozzles. The arc voltage for Nozzle 3 then becomes the lowest towards current zero (Figure 6.11(a)). Since during current zero period turbulence cooling is the most important energy transport mechanism, the highest extinction peak of Nozzle 2 (Figures 6.10(a) and 6.11(a)) indicates that the highest turbulence level is attained within Nozzle 2, whereas the lowest arc voltage of Nozzle 3 shortly before current zero (Figure 6.11(a)) indicates that the turbulence level within Nozzle 3 is the lowest among the three nozzles.

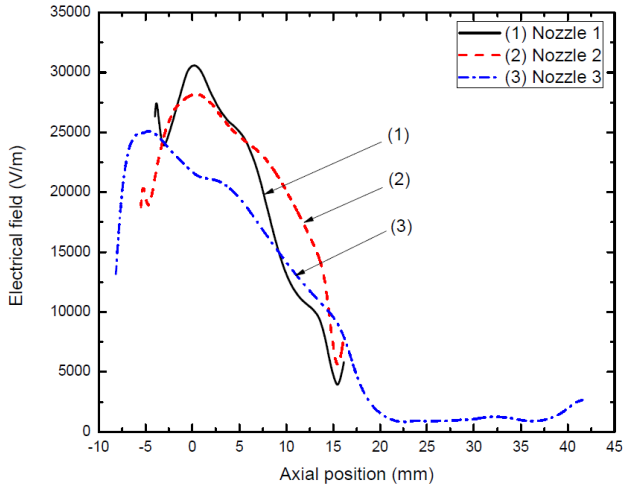

(a)

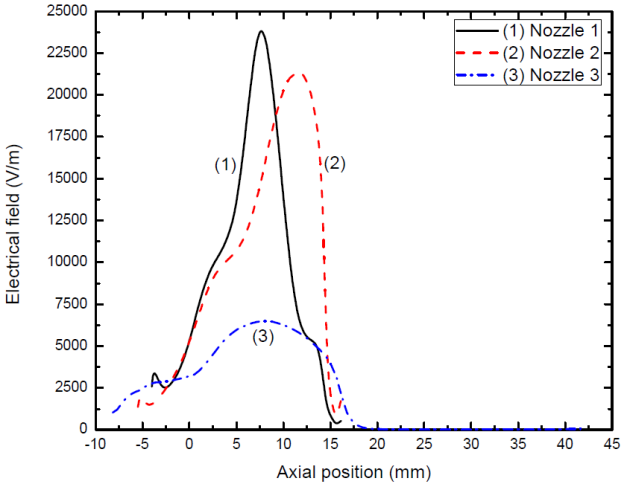

(b)

Figure 6.12. Variations of electrical field at two current levels before current zero computed by the Prandtl mixing length model. P_0=21.4 atm and di/dt=25 Aμs^{-1}. (a) 100 A and (b) 1.25 A (0.05 μs before current zero).

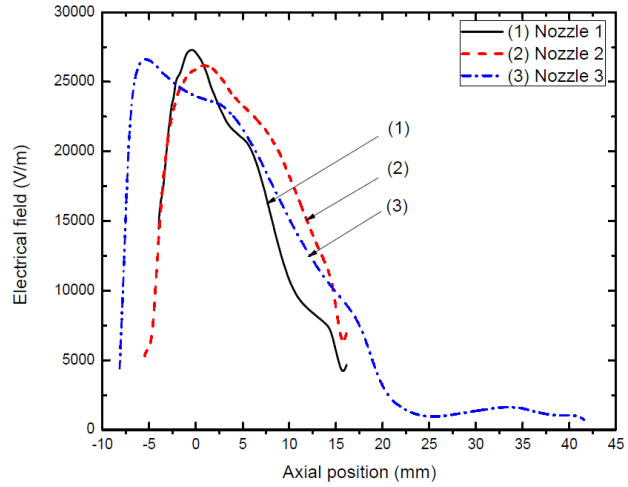

(a)

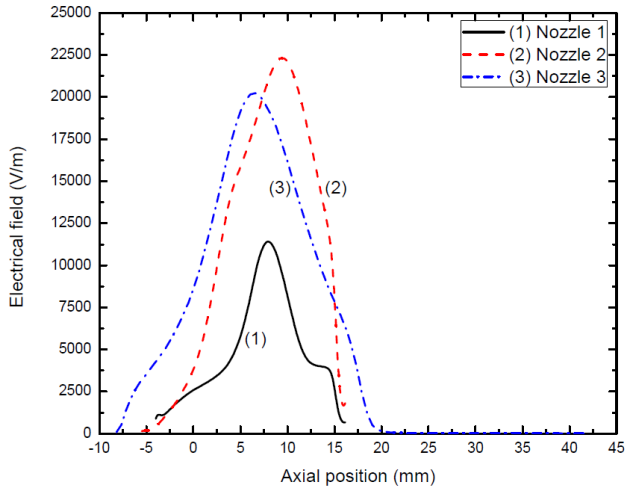

(b)

Figure 6.13. Variations of electrical field at two current levels before current zero computed by the Prandtl mixing length model. P_0=21.4 atm and di/dt=25 Aμs^{-1}. (a) 100 A and (b) 1.25 A (0.05 μs before current zero).

By applying the standard k-epsilon model, the axis temperature (Figure 6.9(b)), arc radius (Figures 6.9(a) and 6.9(b)) at current zero and electrical field distributions (Figure 6.13) all indicate that Nozzle 3 will have better thermal interruption capability than Nozzle 1. The thermal interruption capability of Nozzle 1 will be the worst as indicated by the axis temperature, arc radius and electrical field distributions. The electrical field distributions immediately before current zero (Figure 6.13(b)) show that the electrical field at a given axial position along the arc for Nozzle 3 is almost comparable to that of Nozzle 2. In addition, the effective arc length of Nozzle 3 is slightly longer than that of Nozzle 2 as indicated by the electrical field distributions (Figure 6.13(b)). This explains the highest arc voltage of Nozzle 3

shortly before current zero (Figure 6.11(b)), which means the highest turbulence level is attained within Nozzle 3. The lowest electrical field along the arc for Nozzle 1 (Figure 6.13), and thus the lowest arc voltage of Nozzle 1 (Figures 6.10(b) and 6.11(b)), indicates that the turbulence level within Nozzle 1 is the lowest among the three nozzles. Apparently, the results obtained by the standard k-epsilon model and their indications with regard to the influences of nozzle geometry on turbulence level are different from those obtained by the Prandtl mixing length model.

6.3.3 Computed RRRV and Comparison with Experiments

The RRRV of the nozzle arc has been determined by applying a linearly increasing voltage at a given rate of rise (dV/dt) after current zero. The computed RRRV as a function of P_0 (with P_0 ranging from 7.8 atm to 37.5 atm) at di/dt=13 and 25 $A\mu s^{-1}$ (di/dt=13.5 and 27 $A\mu s^{-1}$ for Nozzle 3) for the three nozzles, together with experimental results for comparison, are plotted in Figures 6.14 and 6.15 for those obtained by the Prandtl mixing length model and the standard k-epsilon model, respectively.

By applying the Prandtl mixing length model, the computed RRRV generally agrees well with the measured RRRV for the three nozzles (Figure 6.14). The model gives similar dependence of RRRV on P_0 for di/dt=13 $A\mu s^{-1}$ to that for di/dt= 25 $A\mu s^{-1}$ while the experimental results for Nozzles 1 and 2 indicate a much stronger pressure dependence at lower di/dt (Figure 6.16). In theory, the dependence of RRRV on P_0 should not be sensitive to di/dt. If the dependence of RRRV on stagnation pressure is related to di/dt, this will result in the intersection of lines in Figure 6.16. Such intersection implies that at certain range of stagnation pressure RRRV for a lower di/dt will be smaller than that for a higher di/dt. This is not physical. The experimental results for Nozzles 1 and 2 at di/dt=13 μs^{-1} are, therefore, not very reliable. It is well-known that the value of RRRV has a large short to short variation. Error bars of the experimental results of [6.1, 6.3, 6.4] are not given. Taking into account the experimental uncertainties, we feel that the predicted RRRV by the Prandtl mixing length model at 13 $A\mu s^{-1}$ for Nozzles 1 and 2 is acceptable. As

expected, the computed RRRV for Nozzle 2 is higher than those of the other two nozzles for the range of P_0 studied and at both two values of di/dt, which indicate that the highest turbulence level can be attained within Nozzle 2. However, it is noted that the RRRV of Nozzles 1 and 2 at different discharge conditions are close to each other. This means that the levels of turbulence for both two nozzles are similar, with that for Nozzle 2 slightly higher. Nozzle 3 has the lowest RRRV for all the discharged conditions (with different values of P_0 and di/dt), which means the turbulence level within Nozzle 3 is the lowest.

By applying the standard k-epsilon model, for Nozzles 2 and 3, computations grossly over-predicts the values of RRRV (Figure 6.15), which also show much stronger dependence on P_0 at both values of di/dt (13 and 25 $A\mu s^{-1}$) in comparison with the dependence predicted by the Prandtl mixing length model (comparing results shown in Figures 6.14 and 6.15). However, for Nozzle 1, the model can give reasonable predictions under certain discharge conditions (e.g. P_0=18 atm and 21.4 atm, di/dt=13 $A\mu s^{-1}$, as shown in Figure 6.15(a)). Therefore, the performance of the standard k-epsilon model is dependent on the nozzle geometry, and thus one cannot draw a general conclusion that the standard k-epsilon model always over predicts RRRV. The computational results indicate that Nozzles 2 and 3 have similar RRRV for all the discharge conditions investigated, with the RRRV of Nozzle 3 slightly higher (Figure 6.15). This means the highest turbulence level can be attained within Nozzle 3, but Nozzle 2 can produce similar turbulence level as compared with that of Nozzle 3. Nozzle 1 has the lowest computed RRRV for all the discharged conditions (with different values of P_0 and di/dt), which means the turbulence level within Nozzle 1 is the lowest.

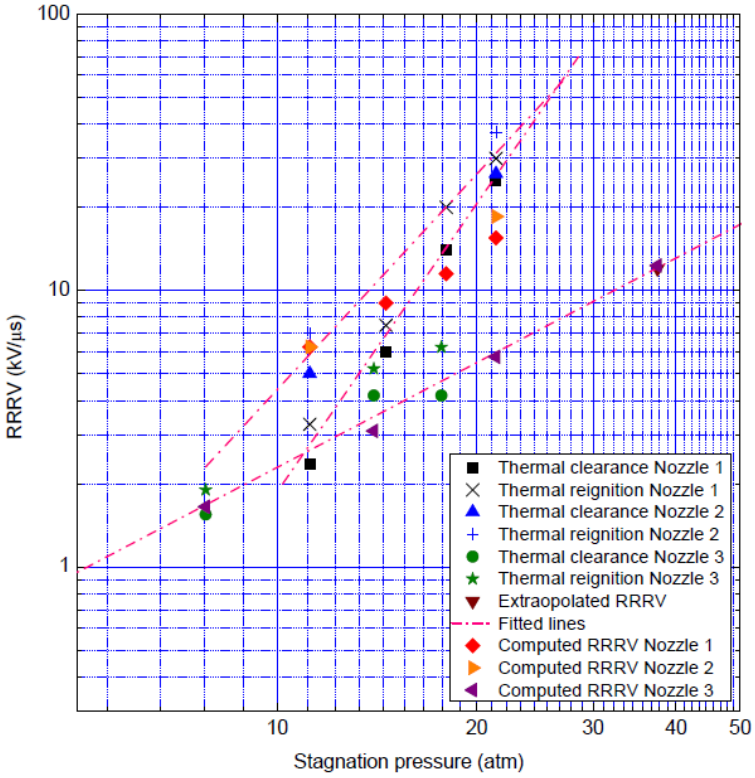

(a)

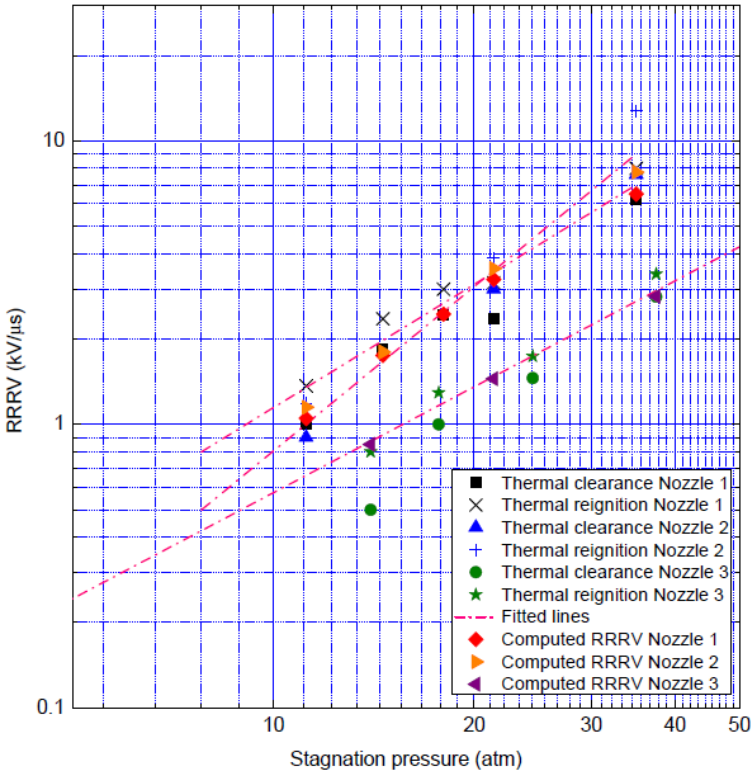

(b)

Figure 6.14. Comparison of measured RRRV and predicted RRRV computed by the Prandtl mixing length model. (a) di/dt=13 Aμs^{-1} (di/dt=13.5 Aμs^{-1} for Nozzle 3) and (b) di/dt=25 Aμs^{-1} (di/dt=27 Aμs^{-1} for Nozzle 3).

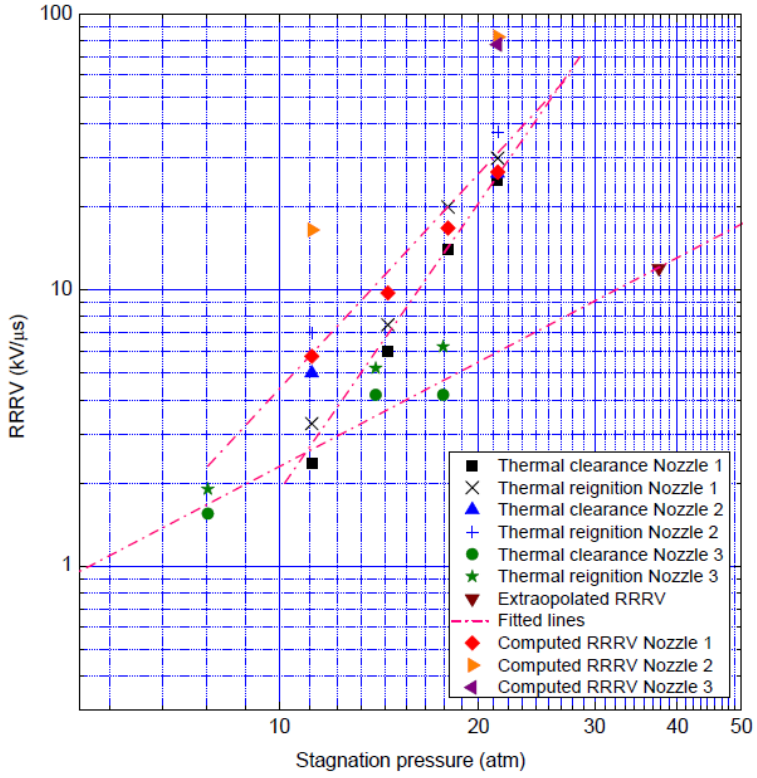

(a)

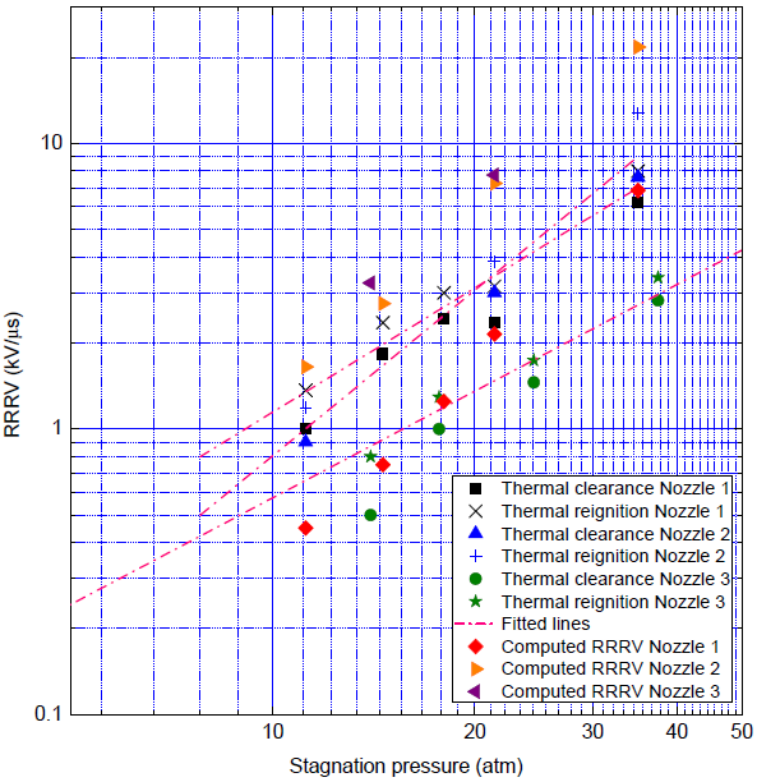

(b)

Figure 6.15. Comparison of measured RRRV and predicted RRRV computed by the standard k-epsilon model. (a) di/dt=13 $A\mu s^{-1}$ (di/dt=13.5 $A\mu s^{-1}$ for Nozzle 3) and (b) di/dt=25 $A\mu s^{-1}$ (di/dt=27 $A\mu s^{-1}$ for Nozzle 3).

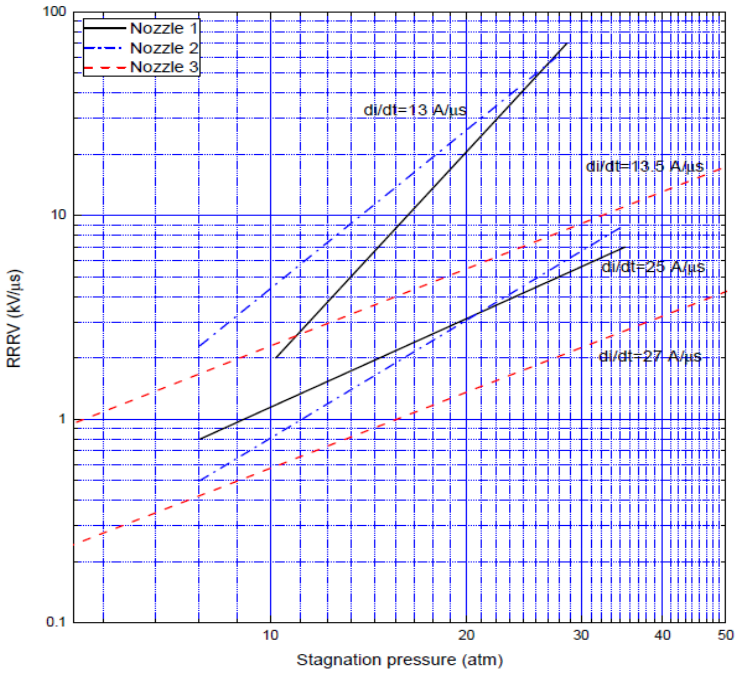

Figure 6.16. Measured RRRV for the three nozzles of Figure 3.3. These results are given in fitted lines only, and the measured points are not plotted.

The application of two turbulence models results in different indications with regard to the effects of nozzle geometry on the turbulence level and the thermal interruption capability of a given nozzle. However, as readily shown by the results presented in this section, the agreement between measured and computed RRRV obtained by the Prandtl mixing length model is still the best, although changes in nozzle and electrode configuration necessitates the readjustments of turbulence parameter for this model. Therefore, we believe that the computational results obtained by the Prandtl mixing length model have given correct prediction on the effects of nozzle geometry on turbulence level, i.e. the highest turbulence level can be attained by Nozzle 2, while Nozzle 3 gives the lowest turbulence level. In this sense, the geometry of Nozzle 2 is preferred in comparison with the other two nozzles in the design of circuit breakers.

As discussed in Section 6.2, there is no geometrical similarity of these three nozzles and their electrode configurations. However, the nozzle shape and the electrode effects can all affect the flow in the nozzle and the behaviour of the arc. For

such non-correlated nozzle geometries and their electrode configurations, it is not possible to separate the effects of nozzle geometry on turbulence from those of the electrodes. It is, therefore, difficult to quantify effects of nozzle geometry on turbulence and the effects of the turbulence on the arc for the nozzle geometries used in the present investigation. Since the experimental results suitable for this investigation is very limited, we have no other choice except the experimental results reported in [6.1, 6.3, 6.4], although the nozzle-electrode configurations used in their experiments do not have geometrical similarities. If attempts will have to be made to further investigate and quantify the effects of nozzle geometry on turbulence level and thermal interruption, more experimental results are required. Relevant experiments should be conducted using nozzle-electrode configurations which have geometrical similarities, i.e. the nozzle radius, the lengths of the different nozzle sections (upstream, throat and downstream sections) and the dimensions of electrodes (electrode length and radius) should be affinely related (suggestions for this will be given in the section for future work in Chapter 8).

6.4 Concluding Remarks

The effects of nozzle geometry on SF_6 arc thermal interruption are investigated using the Prandtl mixing length model and the standard k-epsilon model. The measured and computed RRRV for three nozzle-electrode configurations are used to evaluate the influence of nozzle geometry on turbulence level.

The application of different turbulence models results in different indications with regard to the influence of nozzle geometry on turbulence level. Since the RRRV predicted by the Prandtl mixing length model generally shows best agreement with corresponding measured RRRV, we believe that the Prandtl mixing length model can give the most consistent results once the value of the turbulence parameter for a given nozzle is fixed according to relevant experimental results. The results obtained by the Prandtl mixing length model show that Nozzle 2 gives the highest RRRV among the three nozzles investigated for a given set of discharge conditions (with

fixed P_0 and di/dt). This means the highest turbulence level can be attained by Nozzle 2. In this sense, the geometry of Nozzle 2 is preferred in comparison with the other two nozzles in the design of circuit breakers.

For Nozzle 3, computational results show that a shock is generated downstream of the nozzle throat which is due to the exit pressure not sufficiently low to ensure shock free inside the nozzle. This results in slow thermal recovery of the arc section after the shock, thus reducing the effective arc length and subsequently the thermal interruption capability of a nozzle. The effects of the shock on the behaviour of the SF_6 switching arc forms the subject matter of Chapter 7.

References

[6.1] Frind G and Rich J A 1974 Recovery speed of axial flow gas blast interrupter: dependence on pressure and di/dt for air and SF_6 *IEEE Trans. Power Appar. Syst.* **93** 1675-84

[6.2] Fang M T C, Zhuang Q and Guo X J 1994 Current zero behaviour of an SF_6 gas-blast arc Part II: turbulent flow *J. Phys. D: Appl. Phys.* **27** 74-83

[6.3] Benenson D M, Frind G, Kinsinger R E, Nagamatsu H T, Noeske H O and Sheer, Jr R E 1980 Fundamental investigation of arc interruption in gas flows EPRI EL-1455 (Project 246-2)

[6.4] Frind G, Kinsinger R E, Miller R D, Nagamatsu H T and Noeske H O 1977 Fundamental investigation of arc interruption in gas flows EPRI EL-284 (Project 246-1)

[6.5] Zhang Q, Liu J and Yan J D 2014 Flow structure near downstream electrode of a gas-blast circuit breaker *IEEE Trans. Plasma. Sci.* **42** 2726-7

[6.6] Fang M T C, Kwan S and Hall W 1996 Arc-shock interaction inside a supersonic nozzle *IEEE Trans. Plasma Sci.* **24** 85-6

[6.7] Yan J D, Fang M T C and Jones C 1997 Electrical and aerodynamic behaviour of arcs under shock conditions *IEEE Trans. Plasma Sci.* **25** 840-5

Chapter 7
Current Zero Behaviour of an SF_6 Nozzle Arc under Shock Conditions

7.1 Introduction

Supersonic nozzles are commonly used in modern gas blast circuit breakers as well as in other arc devices for the control of arc discharge conditions [7.1]. During the operation of such breakers (e.g. puffer circuit breakers), the presence of a shock in the nozzle interrupter cannot in general be avoided because the inlet and exit pressures of the nozzle may change greatly due to the limited gas supply from the puffer chamber, nozzle ablation and the confined exhausting space downstream of the nozzle exit.

It is well-known that in the absence of an arc, a shock can occur in the diverging section of a supersonic nozzle if the ratio of the back pressure at the nozzle exit plane to the upstream stagnation pressure (hereafter referred to as the pressure ratio) falls in between the pressure ratios corresponding to the subcritical and critical solutions predicted by one-dimensional isentropic flow theory [7.2]. For the nozzle of Frind and Rich [7.1] (Nozzle 3 as shown in Figure 3.3(c) in Chapter 3), the pressure ratio determined by the ratio of the exit nozzle area to that of the throat for supercritical solution is approximately 0.02 for SF_6. If an arc is drawn in a supersonic nozzle with the pressure ratio within this range it is expected that the shock in the cold flow will be modified by the presence of the arc and the arc itself by the shock. Arc-shock interaction in a supersonic nozzle for direct current arcs has been investigated by Fang et al. [7.3] and Yan et al. [7.4]. It has been shown that, in contrast with the shock without the arc, the shock in the presence of the arc has been considerably broadened with the shock centre shifted upstream which is accompanied by the formation of vortices due to flow separation. As a result, the arc is broadened after

the shock, thus slightly reducing the arc voltage [7.4].

It is now well recognized that an SF_6 arc in a nozzle interrupter of a high voltage circuit breaker is turbulent. Modelling of turbulent arc is still at its infancy as the mechanisms for generating arc instability and maintaining turbulence in the arc context are little understood. However, an arc in a supersonic nozzle has similarity to a shear boundary layer in that the axially dominant flow inside the arc attains a much higher speed than that of its surrounding cold flow and the axial momentum and energy diffusion can be neglected in comparison with their radial counterparts (as discussed in Chapter 2). Thus, there is a direct resemblance between a round free jet in a stagnant external flow and an arc surrounded by a cold and low speed flow in a nozzle (as discussed in Chapter 2). Turbulent arc modelling to date is exclusively based on the Prandtl mixing length model or the k-epsilon model and its variants (as discussed in Chapter 3). These turbulence models are originally devised for incompressible turbulent shear layer flow. The application of the Prandtl mixing length model relies upon limited experimental data to fix the value of one turbulence parameter (c) by matching the computed results with experiments for a particular nozzle geometry (as shown in Chapters 5 and 6). There are altogether 5 turbulence parameters in the k-epsilon model and even more in its variants (Section 3.5 of Chapter 3). The recommended default values for these parameters cannot give the correct prediction of temperature measurements [7.5, 7.6] and RRRV after current zero (as shown in Chapters 5 and 6). The necessity to adjust the values of turbulence parameters of the k-epsilon model and its variants and the high computing cost (in comparison with the Prandtl mixing length model) favour the adoption of the Prandtl mixing length model for the simulation of turbulent arc. Thus, the Prandtl mixing length model will be used for the present investigation.

The objective of the present work is to investigate arc-shock interaction under a rapidly varying current usually encountered by a gas blast breaker before current zero and to assess the effects of the shock on arc's thermal recovery capability after current zero. Since the value of a turbulence parameter in the Prandtl mixing length model needs to be found by matching the computed RRRV with that measured,

reproducible experimental results under well defined test conditions are essential. In addition, the elucidation of the physical processes occurring inside a nozzle in the presence of a shock requires the elimination of pressure waves often encountered in a circuit breaker operation due to the interaction between the nozzle arc interrupter and other parts of the breaker connected to the interrupter. Thus, the two-pressure system of Frind and Rich [7.1] is used for the current investigation. Computer simulation results for the nozzle arc experimentally investigated by Frind and Rich [7.1] have been reported in [7.7, 7.8, 7.9]. In [7.7], the presence of a shock is avoided by the use of a sufficiently low exhaust pressure at the nozzle exit. However, the exhaust pressure for all experiments reported in [7.1] is set at 25% of the upstream stagnation pressure, which will inevitably generate a shock inside the nozzle [7.2]. In [7.8, 7.9], the exhaust pressure is fixed at 0.3 MPa while the upstream stagnation pressure varies from 0.6 to 4.1 MPa. Thus, the resultant pressure ratios will generate a shock inside the nozzle in the absence of the arc according to one-dimensional isentropic flow theory [7.2]. The likely presence of the shock and its effects on the arc are not discussed in [7.8, 7.9]. It should also be noted that the pressure ratio is fixed for the experiments of Frind and Rich [7.1] while the exit pressure varies with the upstream pressure. The prescribed exhaust pressure in [7.8, 7.9] is, therefore, not consistent with the experimental conditions of [7.1].

In the presence of the shock, flow outside the nozzle is often sucked into the computation domain [7.4, 7.10]. The thermodynamic state of this sucked-in flow is usually not known. Attention will, therefore, be paid to the correct prescription of the boundary conditions at the flow exit when the gas is sucked in.

This chapter is organized as follows. Section 7.2 gives the information on the computational domain and grid system used in the investigation of this chapter. Discussion of the computational results and comparison with experiments are presented in Section 7.3. In Section 7.4, a comparison between a shock free arc and an arc under shock conditions is given. The influence of different specifications of boundary conditions at the nozzle exit plane on the arc behavior and thermal interruption performance is discussed in Section 7.5. Finally, appropriate conclusions

are drawn.

7.2 Computational Domain

Computation has been performed on the nozzle used by Frind and Rich [1]. The calculation domain is shown in Figure 7.1, which includes a convergent-divergent nozzle and two electrodes. The nozzle has an expansion half angle of 15° and the nozzle length is 94 mm. The diameter of the nozzle inlet is 25 mm and that of the outlet 38.4 mm. The nozzle throat is 31.3 mm away from the inlet plane and its diameter is 12.5 mm. The upstream electrode has a round tip and the downstream electrode is hollow, both of which have an outer diameter identical with the diameter of the nozzle throat. The inner diameter of the hollow contact is 4 mm.

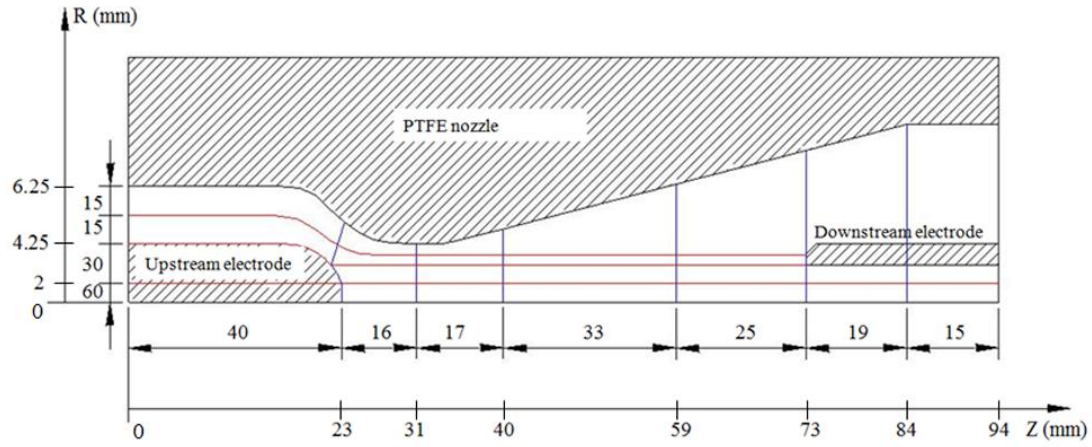

Figure 7.1. Nozzle geometry and grid system used in the computation. Body-fitted grid (BFC) system is used for the computation of gas flow. The domain is divided into 7 and 4 intervals in the axial and radial directions, respectively. The axial and radial coordinates defining the intervals as well as the number of cells over each interval are given. The axial position of the nozzle throat is 31.3 mm downstream of the nozzle inlet plane.

A grid system based on BFC is adopted in the computation to accommodate the nozzle and electrode geometries. The grid distribution is indicated in Figure 7.1, with fine radial grids being employed in the arc region and an average axial grid density of approximately 0.55 mm. Altogether 120×165 grids are used to obtain results.

7.3 Results and Discussion

Computations have been carried out for three upstream stagnation pressures P_0 (7.8 atm, 14 atm and 37.5 atm) and three corresponding downstream pressures P_e fixed at $0.25P_0$. The current is linearly ramped down to zero with a fixed rate of decay, di/dt, from a plateau of 1 kA DC. Two rates of current decay, 27 $A\mu s^{-1}$ and 13.5 $A\mu s^{-1}$, have been investigated. After current zero, a linearly increasing voltage ramp, dV/dt, is applied to investigate the thermal interruption capability of the nozzle in Figure 7.1. The turbulence parameter *c* is found to be 0.045 by matching the calculated RRRV with that measured at P_0 = 37.5 atm and di/dt = 27 $A\mu s^{-1}$. This value of *c* is used for the other cases.

Unless otherwise specified, computational results reported in this chapter are for an upstream pressure of 37.5 atm, an exit pressure of 9.2 atm, and di/dt = 27 $A\mu s^{-1}$. The qualitative features of results obtained with different stagnation pressures and di/dt but with the same exit pressure to inlet stagnation pressure ratio are very similar. Based on these computational results, we can predict the behaviour of the nozzle arc under shock conditions and identify the main physical process taking place during current zero period. A detailed interpretation of the results and their indications are given below.

7.3.1 The Behaviour of the 1 kA DC Arc

The temperature contours together with the pressure isobars for an arc at 1 kA DC in the nozzle of Figure 7.1 are given in Figures 7.2(a) and 7.2(b) which respectively correspond to stagnation pressures of 37.5 atm and 14 atm. The qualitative features of the arc and the surrounding flow field do not appear to be sensitive to the stagnation pressure, as long as the same pressure ratio (0.25) is maintained. However, the arc size for 14 atm is larger than that of 37.5 atm as it is known that the arc size for DC arcs is inversely proportional to the square root of the stagnation pressure [7.11].

For the discussion of arc-shock interaction, it is convenient to separate the

nozzle arc system into three regions: a high temperature core which carries the arc current with a boundary temperature of approximately 10,000 K (this is different from the arc core defined for radiation transport in Section 3.5 of Chapter 3), a thin layer (commonly known as the thermal layer) surrounding the arc core in which the temperature rapidly decays to that of the surrounding cold flow, and the cold flow region (see Figure 7.2 the arc section upstream of the shock). A shock generated in the cold flow due to the high ratio of exit pressure to the inlet stagnation pressure interacts with the arc core and thermal boundary layer. The adverse pressure gradient of the shock is felt by both the core and the thermal layer. The axial velocity in the core is reduced but not reversed. However, the flow in the thermal layer is reversed by the adverse pressure gradient, thus causing flow separation, which is similar to flow separation in a boundary layer attached to a solid wall [7.12]. The flow separation distorts the arc boundary. The cold flow from upstream cannot penetrate the distorted arc boundary due to its high temperature, hence low density (Figure 7.3(a)). Such a flow situation is similar to a supersonic flow passing a compression corner [7.13]. The equivalent angle of inclination α of compression corner in the presence of the arc is given in Figure 7.3(a). The equivalent compression corner deflects the cold flow from upstream and generates compression waves as indicated by the distribution of the isobars in Figure 7.3(b). Direct analogy with the compression corner in fluid dynamics is very limited as the nozzle arc system is far more complex because of highly non-uniform temperature distribution caused by Ohmic heating and the density gradients. In a large region inside the nozzle, the pressure is lower than the nozzle exit pressure (Figure 7.3(b)). The gas is, therefore, sucked into the nozzle. This relatively cold inflow gas stream forms the reverse flow in the flow separation region and is returned to the nozzle exit. In between the two counter streams, the inflow gas stream and the high velocity jet in the arc core, a vortex is formed in between (Figure 7.3(a)). Due to the close coupling of temperature and flow fields a complex flow pattern is formed within the nozzle. Gas flow originated upstream of the shock is exhausted through the cold flow region close to the nozzle wall and the hollow electrode. The sucked-in gas flow is returned to

nozzle exit through circulation, thus making no contribution to the mass flow rate through the nozzle.

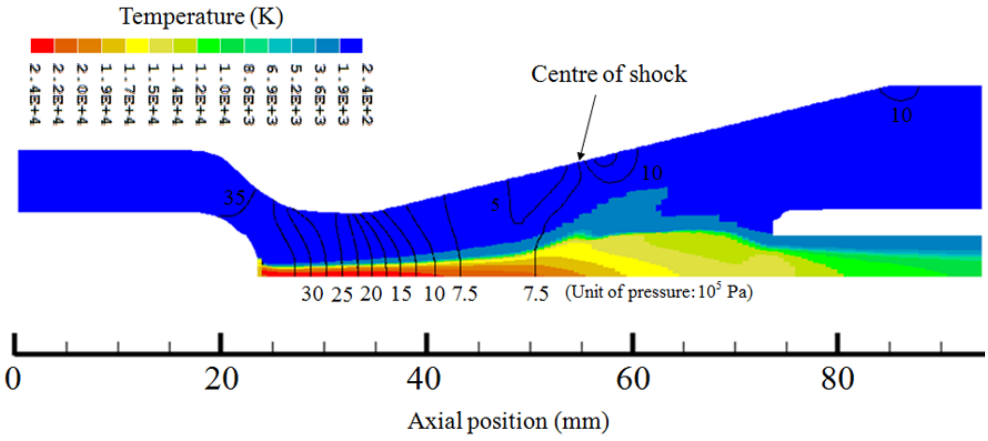

(a)

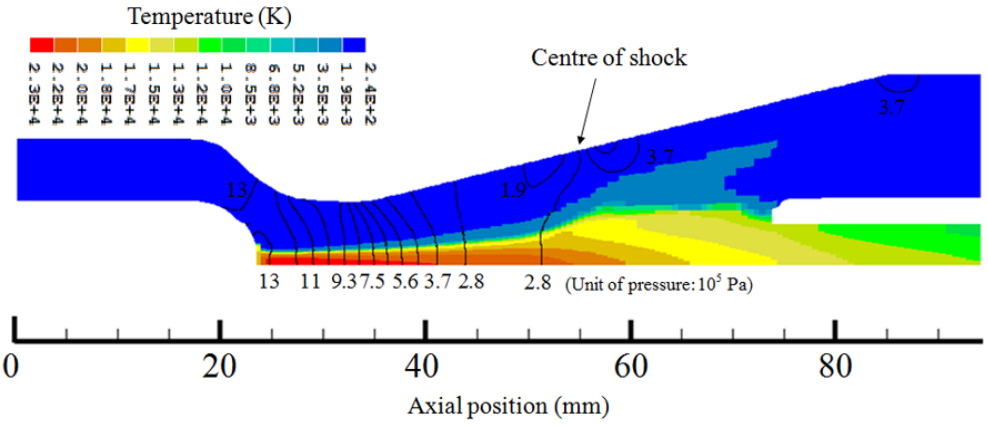

(b)

Figure 7.2. Temperature contour together with pressure distribution in the nozzle at 1 kA DC corresponding to different upstream stagnation pressures. The axial position is consistent with that of Figure 7.1. (a) P_0=37.5 atm and (b) P_0=14 atm.

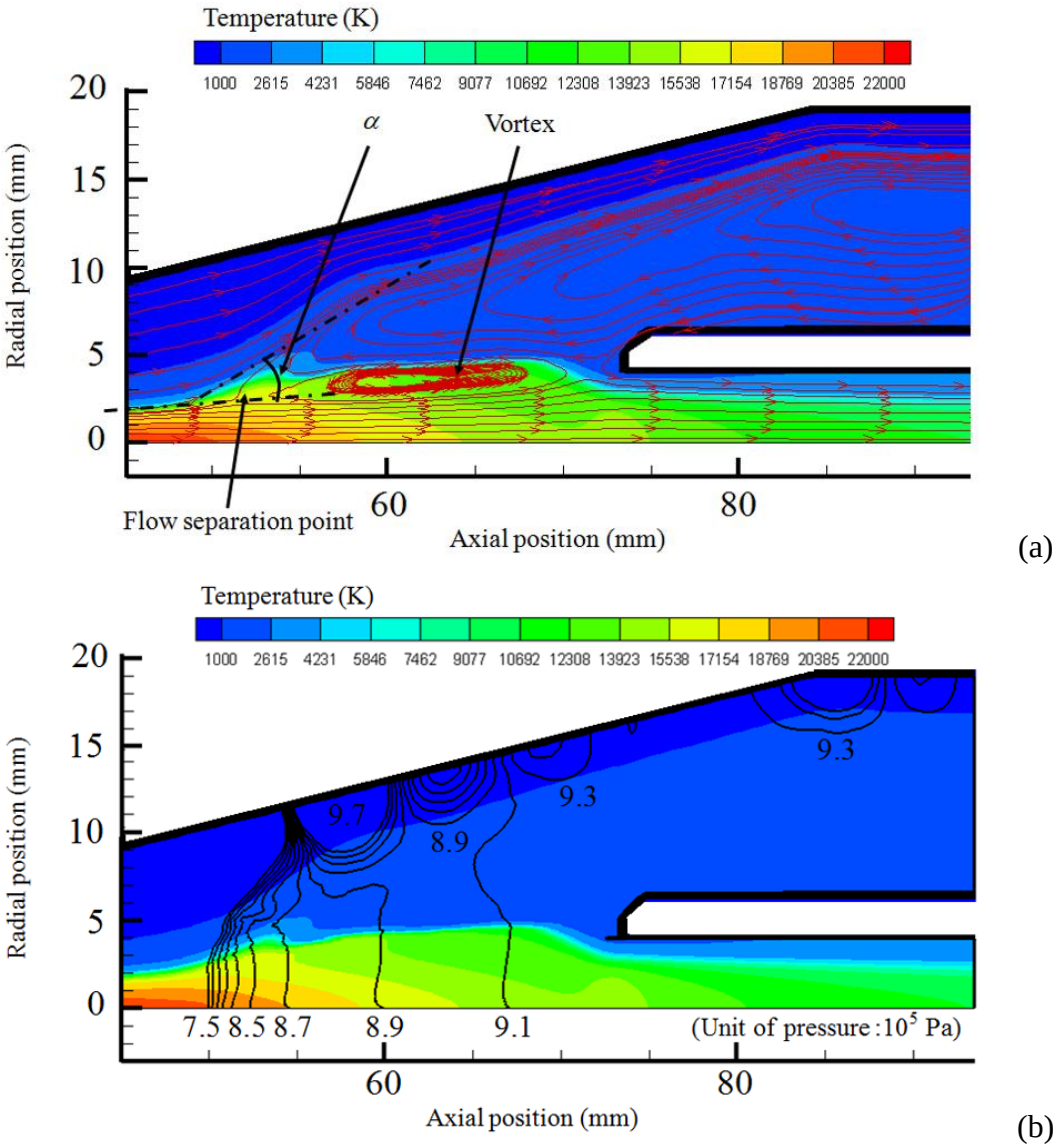

Figure 7.3. The streamline pattern, pressure and temperature contours in the arc-shock interaction region at 1 kA DC, P_0=37.5 atm. The axial position is consistent with that of Figure 7.1. (a) Streamline pattern and (b) Pressure and temperature contours.

Compared with the flow behaviour in the absence of the arc, the shock centre moves upstream and the shock is broadened which cannot be regarded as a normal shock (Figures 7.3, 7.4 and 7.5). The pressure and Mach number on the arc axis and those along the nozzle wall are respectively shown in Figure 7.4 and Figure 7.5. The Mach number behind the shock (Figures 7.4(b) and 7.5(b)) can still be above unity which corresponds to the weak shock, similar to that observed in a compression corner [7.13]. The arc cross-section is considerably broadened, thus reducing the voltage in the arc-shock interaction region.

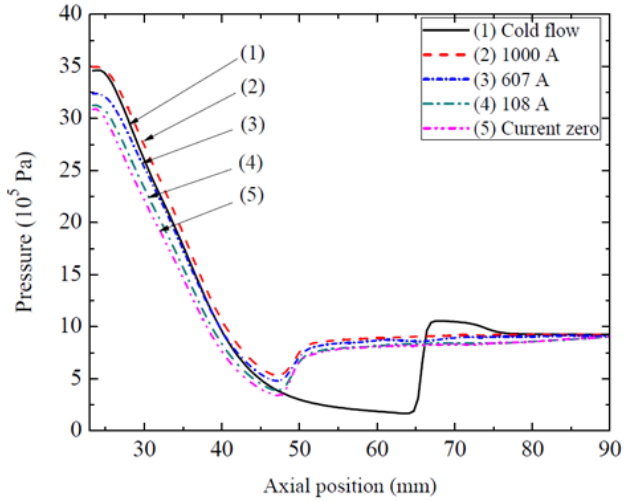

(a)

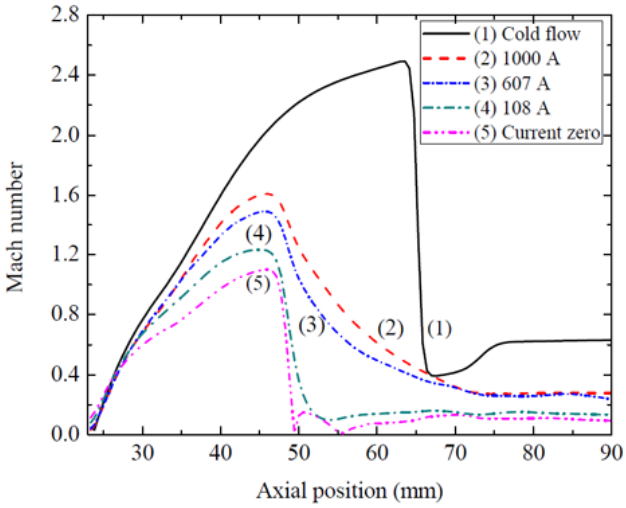

(b)

Figure 7.4. Variations of pressure and Mach number distributions on the axis with axial position for the cold flow and at different current levels during current zero period. P_0=37.5 atm and di/dt=27 Aμs^{-1}. The axial position is consistent with that of Figure 7.1. (a) Pressure distributions and (b) Mach number distributions.

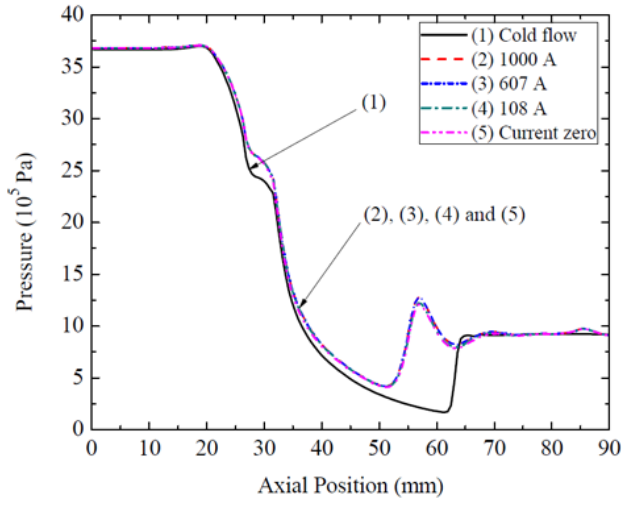

(a)

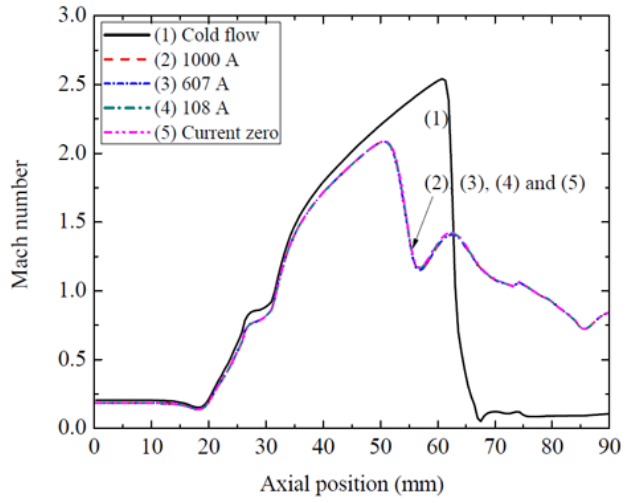

(b)

Figure 7.5. Variations of pressure and Mach number near the nozzle wall with axial position for the cold flow and at different current levels during current zero period. P_0=37.5 atm and di/dt=27 Aμs^{-1}. The axial position is consistent with that of Figure 7.1. (a) Pressure distributions and (b) Mach number distributions.

7.3.2 The Behaviour of the Transient Arc before Current Zero

7.3.2.1 Overall Features

As the current ramps down linearly towards zero, the arc shrinks due to the reduction of Ohmic heating. Variations of axis pressure and Mach number with axial position at different current levels before current zero are shown in Figure 7.4 and those of axis temperature, axis velocity, electrical field and arc radius defined as the position of 3000 K isotherm are given in Figure 7.6. The qualitative behavior of the arc

section before the shock is similar to those reported for a transient nozzle arc under shock free conditions [7.7]. The temperature decays and arc size shrinks the fastest downstream of the throat. However, the electrical field distribution only changes significantly when current zero is approached. This results in a small voltage extinction peak as shown in Figure 7.7 where the arc voltage for the shock free case (Section 7.4) is also plotted. The differences between an arc with and without shock under the same discharge conditions except the exit pressure are caused entirely by the arc section after the shock as indicated by curves (3) and (3a) in Figure 7.6. It is, therefore, important to discuss arc-shock interaction when current reduces towards zero and its influence on arc interruption.

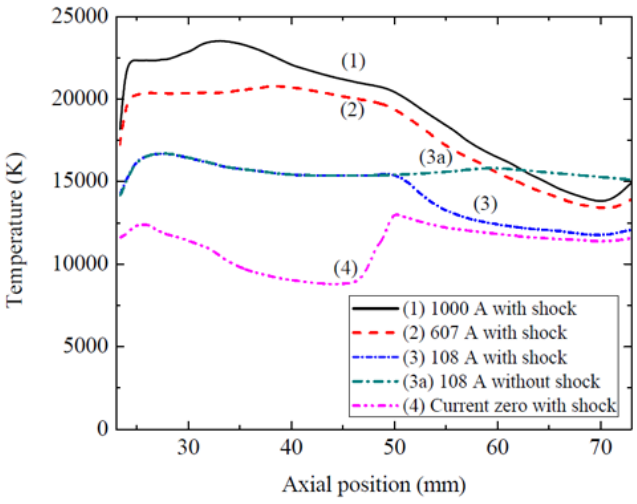

(a) of Figure 7.6

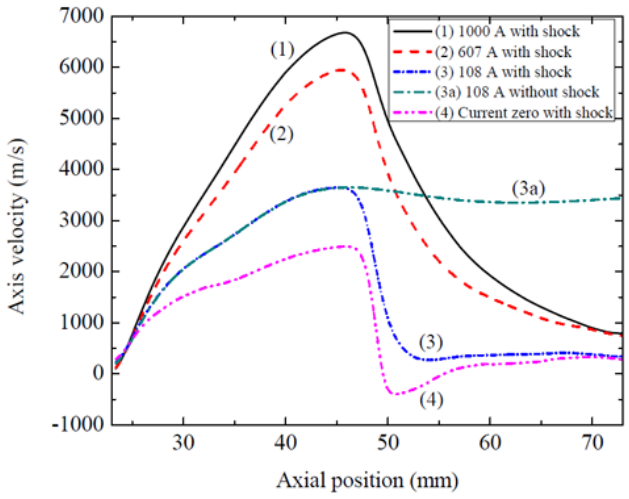

(b) of Figure 7.6

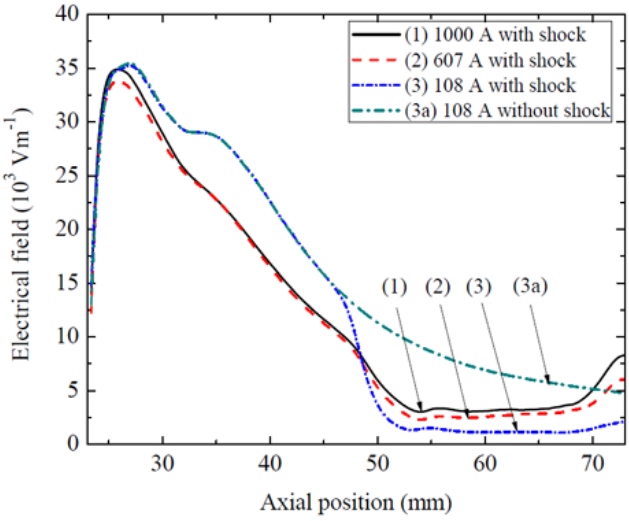

(c) of Figure 7.6

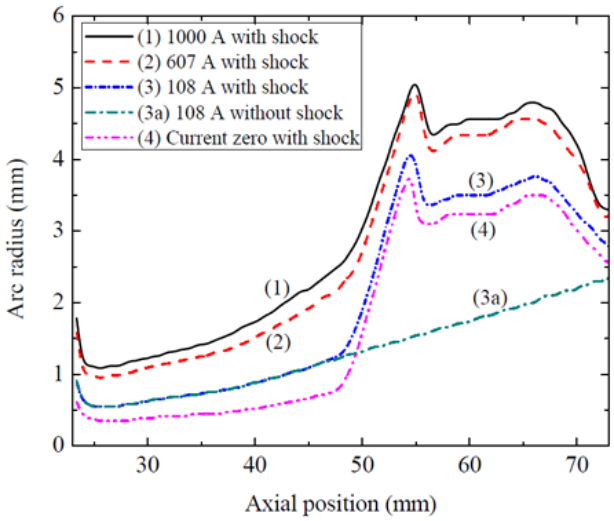

(d) of Figure 7.6

Figure 7.6. Variations of axis temperature, axis velocity, electrical field and arc radius with axial position at different current levels before current zero for P_0=37.5 atm and di/dt= 27 Aμs^{-1}. The axial position is consistent with that of Figure 7.1. Curve (3a) is shock free case. (a) axis temperature distribution, (b) axis velocity distribution, (c) electrical field distribution and (d) arc radius.

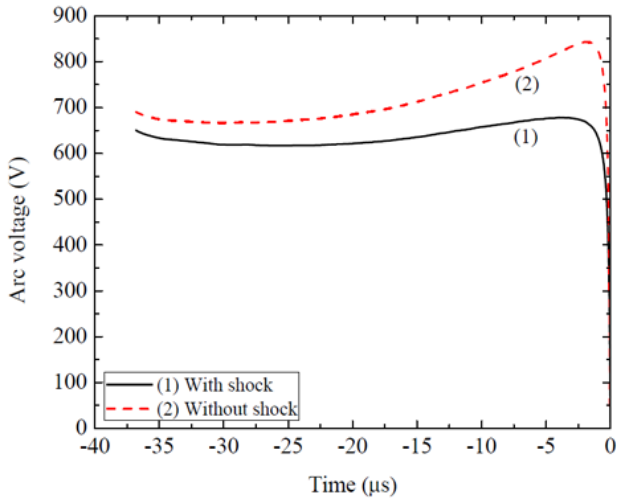

Figure 7.7. Comparison of the arc voltage variations computed with and without shock for P_0=37.5 atm and di/dt= 27 Aμs^{-1}.

In the cold flow region, the pressure (Figure 7.5(a)) and streamlines (Figure 7.8) hardly change as they cannot respond quickly to the current decay because of large momentum and thermal inertia. However, much change has occurred in the flow pattern in the arc-shock interaction region. As the rate of decay of temperature in the arc core is the fastest compared with other parts of the arc-shock interaction zone due to its small thermal inertia, the pressure is, therefore, immediately reduced by the decreasing temperature. This generates a radial mass inflow, thus increasing the density in the region where temperature has dropped. The instant streamlines at a current of 607 A show that, in the neighborhood of the flow separation point, gas is supplied to the arc region by reducing the size of the vortex (Figure 7.8(a)). At 4 μs before current zero (108 A), the flow in the arc region after the shock is almost entirely supplied from the surrounding region. Almost all flow from upstream is deflected by the "compression" corner. The flow separation point moves towards the axis when the current decreases and, at current zero, it is on the axis as shown by curve (4) in Figure 7.6(b) which indicates a flow stagnation point on the axis. Once the surrounding flow penetrates into the arc core, the flow becomes extremely stagnant near current zero (Figure 7.6(b)). The extremely stagnant flow is responsible for the slow decay of temperature (Figure 7.6(a)) and arc radius (Figure 7.6(d)) in this region.

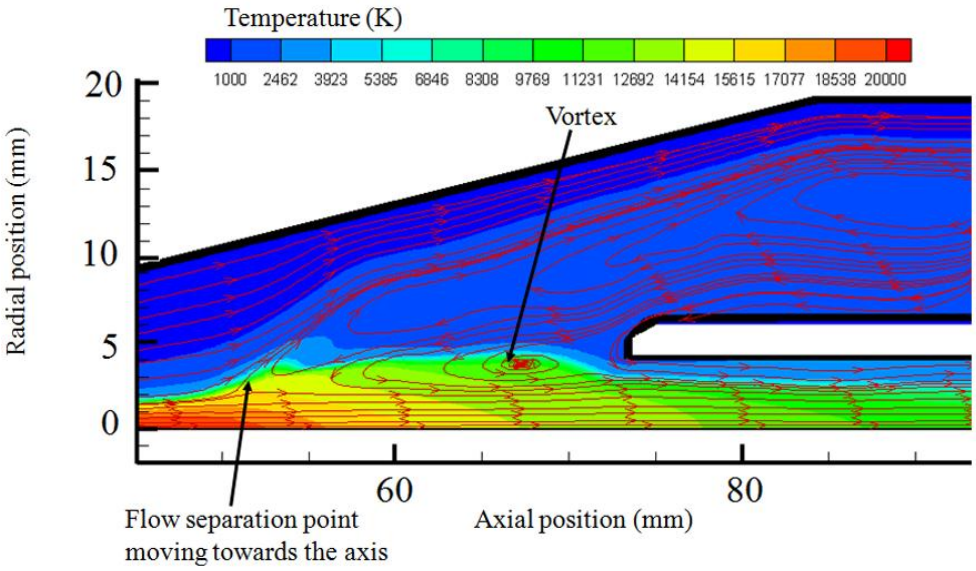

(a)

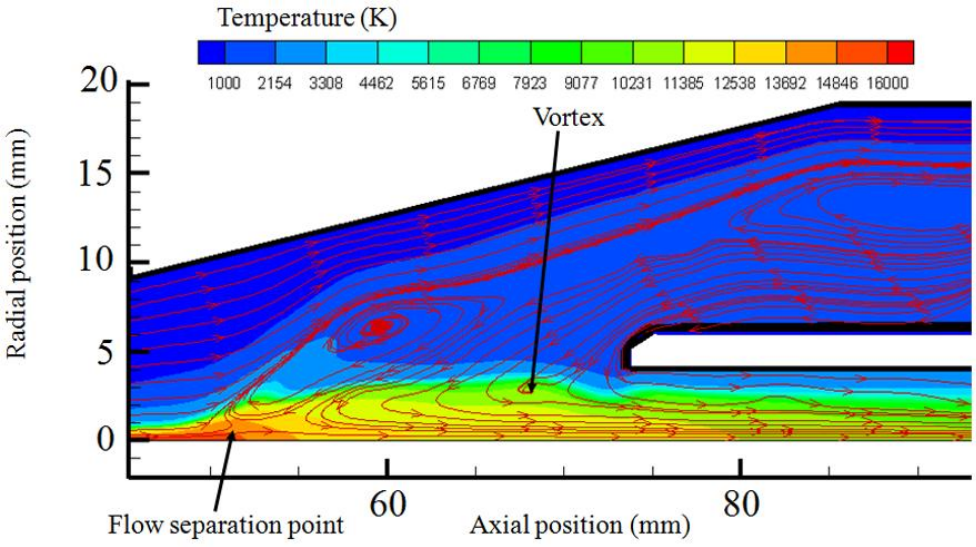

(b)

Figure 7.8. Streamline pattern of the gas flow in the nozzle during current zero period at P_0=37.5 atm and di/dt=27 Aμs^{-1}, with an instantaneous current of (a) 607 A and (b) 108 A. The axial position is consistent with that of Figure 7.1.

7.3.2.2 Energy Balance and the Dominant Process for Energy Transport

In order to identify the dominant energy transport processes, especially those in the arc-shock interaction region, the plots of radial integrated energy balance are given in Figures 7.9 and 7.10 at different instants for two typical cross-sections, one of which is the nozzle throat and the other at Z = 61 mm in the arc-shock interaction region.

At the nozzle throat, inside the electrically conducting core, the arc is still in

quasi-steady state at an instantaneous current of 607 A (22.5 μs before current zero) and radiation is the dominant energy loss mechanism (Figure 7.9(a)) in the region from the axis to the start of the radiation reabsorption region (corresponding to the maximum of curve (5)). In this region, axial enthalpy transport and radial turbulent thermal conduction are of equal importance. Turbulence is very strong in the radiation reabsorption region where both temperature and axial velocity decrease rapidly, thus resulting in the rapid increase of turbulent viscosity (Equation (3.25) given in Section 3.6.1 of Chapter 3). Therefore, in the radiation reabsorption region, power loss due to radial turbulent thermal conduction gradually becomes more important than other energy loss mechanisms. At the electrically conducting boundary (the starting point of the flat region of curve (4) in Figure 7.9), energy loss by turbulence becomes the most important. Because of axial acceleration and the decrease in temperature, a radial inflow is required for the mass balance which gives rise to equivalent power input (curve (2)) as the radial convection term is written in the conservation form (Equation (3.19) given in Section 3.5 of Chapter 3). This term includes the conventional radial convection term, $-\rho u \frac{\partial h}{\partial r}$, which represent power loss for a radial inflow. Qualitative features of radial energy balance at an instant current of 108 A (4μs before current zero, Figure 7.9(b)) are similar to those at 607 A except that axial enthalpy convection is negligible due to nearly constant axis temperature and the greatly reduced axial acceleration due to density increase accompanying the reduction in temperature (curve (3) in Figures 7.6(a) and 7.6(b)). At current zero, radiation is negligible at the nozzle throat because the temperature is below 12,000 K [7.14]. Turbulent energy transport becomes dominant (Figure 7.9(c)).

The energy balance at Z = 61 mm, which is in the arc-shock interaction region, shows an entirely different picture with regard to various energy transport processes in comparison with those at the nozzle throat. Because of the arc-shock interaction the arc cross section is much larger than that of the arc region before the shock (Figure 7.6(d)) and the flow in this region especially near current zero is extremely

stagnant (Figure 7.6(b)). At an instantaneous current of 607 A, arc radiation loss greatly exceeds Ohmic input which is balanced by the power input due to axial enthalpy convection in the arc core region. In the radiation reabsorption region, net radiation loss reduces (Figure 7.10(a)) and enthalpy convection associated with radial inflow due to flow separation (Figure 7.8(a)) has replaced axial convection as the main power input mechanism. Radial convection together with Ohmic input supply the energy taken away by turbulent radial thermal conduction and axial convection. When the current decreases to 108 A, Ohmic input is negligible in comparison with the power input due to radial convection (Figure 7.10(b)) in the arc core. Radial convection is mainly balanced by radiation loss, axial convection and the rate of change of energy storage. In the radiation reabsorption region and beyond, radial convection is balanced by turbulent thermal conduction and the rate of change of energy storage. The energy balance at current zero (Figure 7.10(c)) is similar to that at 108 A. In contrast with the energy balance near current zero in the arc section before the shock, energy transport associated with inward radial flow is very prominent and turbulent transport of energy in the electrically conducting core is not important. This is of course the consequence of weak turbulence intensity associated with the very stagnant flow (Figure 7.6(b)).

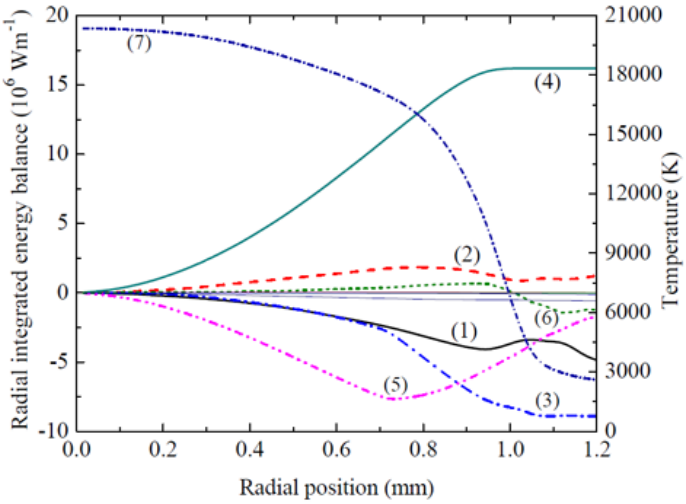

(a) of Figure 7.9

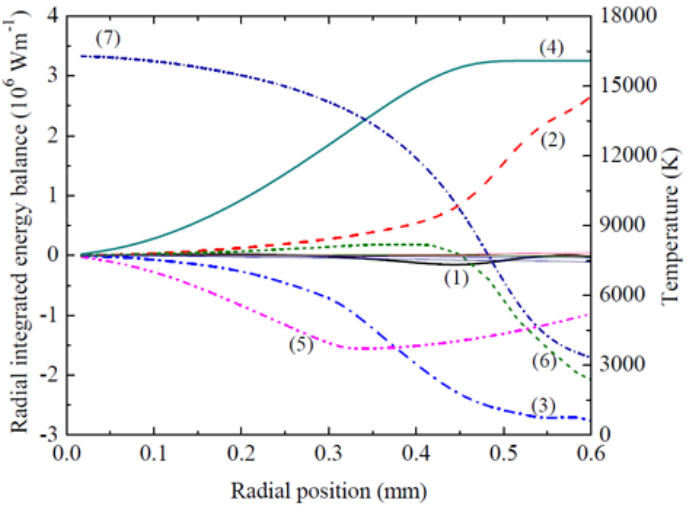

(b) of Figure 7.9

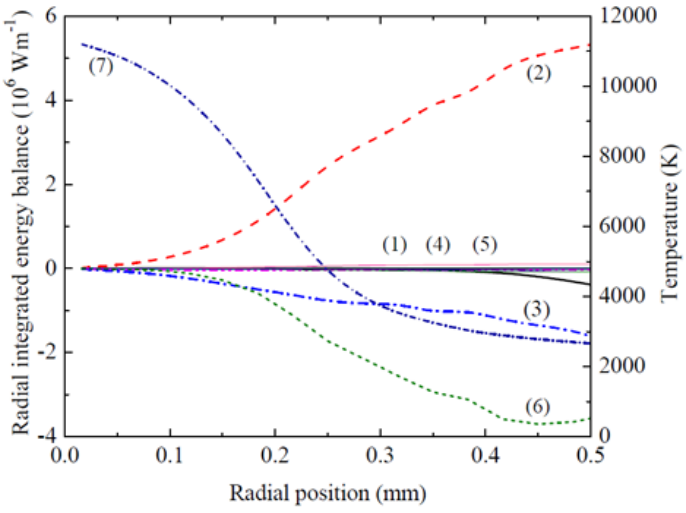

(c) of Figure 7.9

Figure 7.9. Radial integrated energy balance at different instants before current zero at the nozzle throat. P_0= 37.5 atm and di/dt= 27 Aμs^{-1}, with an instantaneous current of (a) 607 A, (b) 108 A and (c) current zero. Key of the curves is indicated as follows:

(1) Axial convection: $-\int \frac{\partial}{\partial z}(\rho w h) 2\pi r dr$,

(2) Radial convection: $-\int \frac{1}{r}\frac{\partial}{\partial r}(r\rho v h) 2\pi r dr$,

(3) Radial thermal and turbulent conduction: $-\int \frac{1}{r}\frac{\partial}{\partial r}\left(-r\frac{k}{c_p}\frac{\partial h}{\partial r}\right) 2\pi r dr$,

(4) Ohmic heating: $\int \sigma E^2 2\pi r dr$, (5) Radiation loss: $-\int q 2\pi r dr$,

(6) Rate of change of energy storage: $-\int \frac{\partial(\rho h)}{\partial t} 2\pi r dr$, and,

(7) Radial temperature profile.

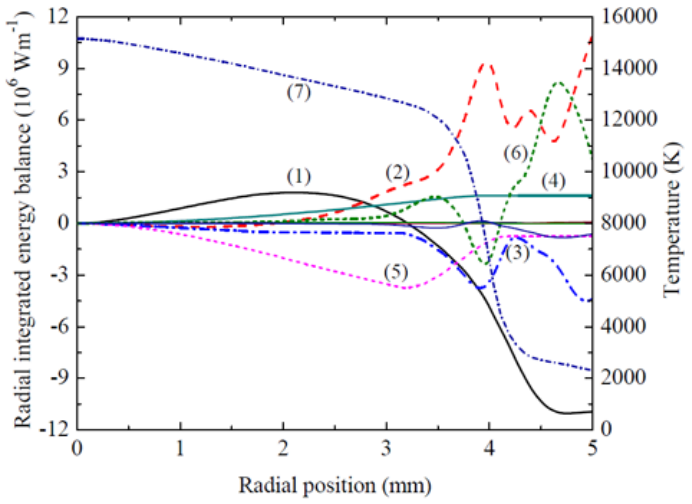

(a)

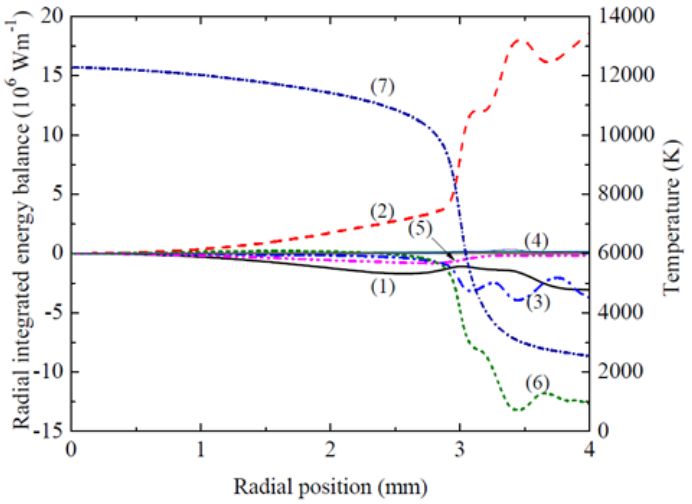

(b)

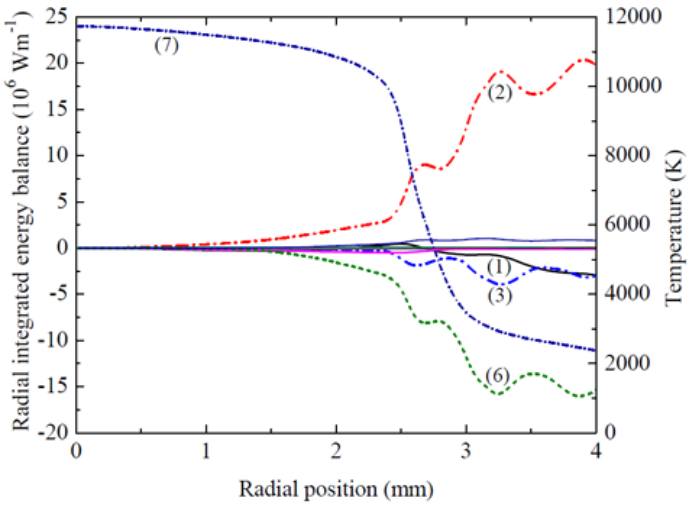

(c)

Figure 7.10. Radial integrated energy balance at different instants before current zero at Z= 61 mm downstream of the nozzle inlet plane. P_0= 37.5 atm and di/dt= 27 Aμs^{-1}, with an instantaneous current of (a) 607 A, (b) 108 A and (c) current zero. Key of the curves is the same as that indicated in Figure 7.9.

As a consequence of arc-shock interaction, the arc cross section is enlarged. Because of the stagnant flow leading to weak turbulence, temperature decay in this region is very slow (Figure 7.6(a)). The electrical field in this region is very low (Figure 7.6(c)). The voltage taken up by this section of the arc is only 16% of the total arc voltage at 1 kA, and it reduces to 3% at 0.5 μs before current zero. The presence of the shock, therefore, reduces the effective arc length for thermal interruption.

7.3.3 The behavior of the Transient Arc after Current Zero and RRRV

A linearly increasing voltage at a given rate of rise (dV/dt) is used after current zero to investigate the thermal interruption capability of the nozzle configuration. The value of the rate of rise of recovery voltage (dV/dt), at which the arc will just be extinguished, is commonly known as the critical rate of rise of recovery voltage (RRRV). This will be found computationally and the computed RRRV will be compared with the results given by [7.1].

Typical results of post-arc current at different values of dV/dt are shown in Figure 7.11 for P_0=37.5 atm and di/dt=27 $A\mu s^{-1}$. The axis temperature and electrical field distributions at different instants after current zero are given in Figures 7.12 and 7.13 respectively for dV/dt of 2.7 $kV\mu s^{-1}$ (thermal clearance) and 2.85 $kV\mu s^{-1}$ (thermal reignition). When the arc is thermally extinguished (e.g. dV/dt=2.7 $kV\mu s^{-1}$), the arc temperature decays rapidly in 1 μs before current zero in the region of approximately 15 mm long downstream of the nozzle throat but before the shock (referred hereafter to as the critical section for interruption) (Figure 7.12(a)). It is this critical section of the arc that takes up most of the recovery voltage (more than 95%). In this region, turbulent thermal conduction is responsible for the rapid cooling of the arc. The temperature downstream of the critical section hardly changes while the critical section recovers thermally. If dV/dt exceeds RRRV, temperature in the critical region still reduces immediately after current zero (Figure 7.13(a)) but this temperature decay is soon arrested as Ohmic input is pumped into a very thin core of the critical section. Temperature outside of this core still reduces as shown in Figure

7.13(b) where the radial temperature profiles at Z = 42 mm at different instants are plotted. The applied voltage is again mainly taken up by this section (Figure 7.13(c)). Thus, the critical section is also responsible for thermal reignition in the time duration of 1 μs after current zero if dV/dt is too high.

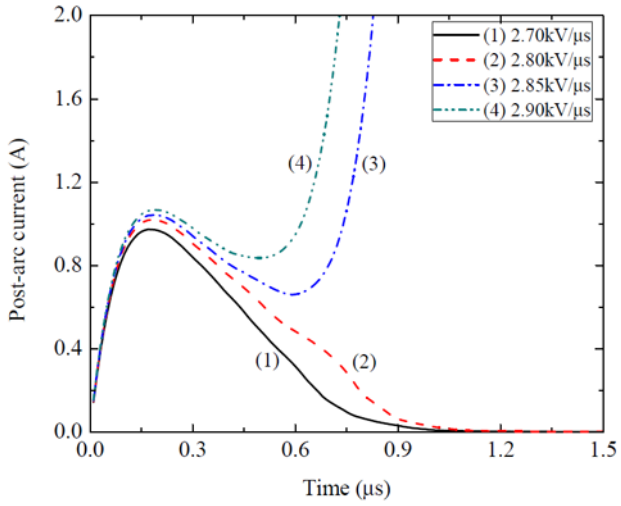

Figure 7.11. Post-arc current for different values of dV/dt. P_0= 37.5 atm and di/dt=27 $A\mu s^{-1}$. The RRRV is 2.83 $kV\mu s^{-1}$.

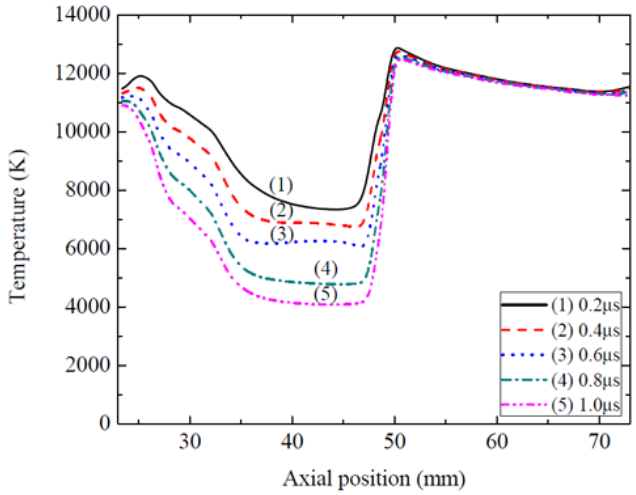

(a)

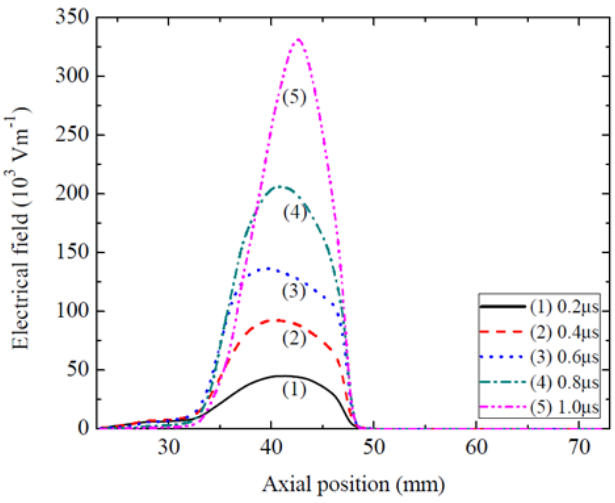

(b)

Figure 7.12. Axis temperature and electrical field distributions at various instants after current zero for dV/dt = 2.7 kVμs^{-1} (thermal clearance). The axial position is consistent with that of Figure 7.1. (a) Axis temperature distribution and (b) Electrical field distribution.

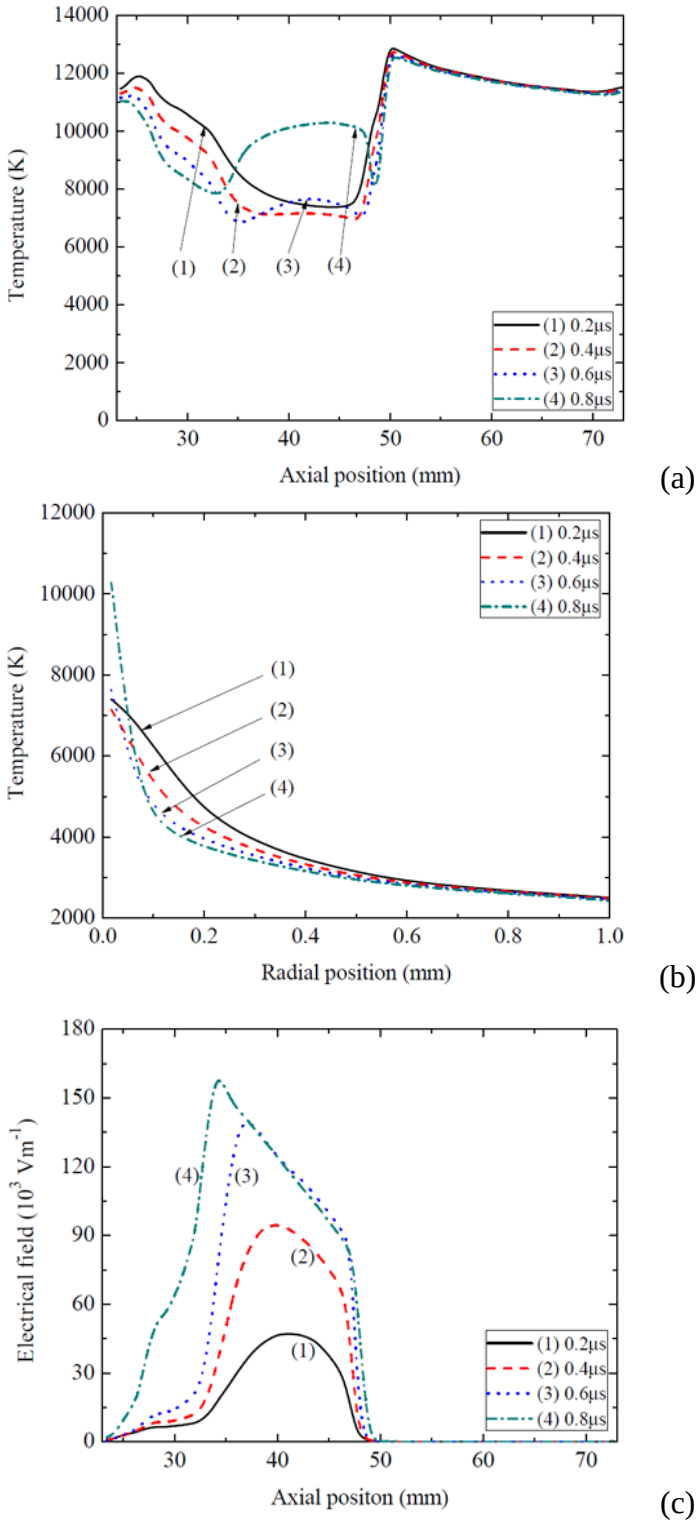

Figure 7.13. (a) Axis temperature distribution, (b) instantaneous radial temperature profiles at 4 instants at Z = 42 mm and (c) electrical field distributions at various instants after current zero for dV/dt= 2.85 kVμs^{-1} (thermal reignition). The axial position is consistent with that of Figure 7.1.

The qualitative features of the arc behaviour at other stagnation pressures, di/dt and dV/dt are similar to those reported here. The computed values of RRRV at 37.5 atm, 14 atm and 7.8 atm for di/dt= 27 $A\mu s^{-1}$ and 13.5 $A\mu s^{-1}$ are plotted in Figure 7.14 together with the experimental results given in [7.1] for comparison. The experimental scatter for clearance and reignition is not known but it could be as large as the difference between clearance and reingition (Figure 7.14). Certain experimental points appear less reliable (e.g. at 14 atm). The only experimental information on the likely magnitude of the scatter is the measurement of arc conductance around current zero of a nitrogen arc by Hermann et al. [7.15]. The average relative scatter of arc conductance around its mean after current zero is no less than $\pm 30\%$ due to turbulence [7.15]. As the SF_6 nozzle arc is also turbulent, experimental scatter in the measured RRRV is expected to be substantial. In view of these uncertainties of the test results, the computed RRRV with the chosen value of the turbulence parameter, *c*, is considered to give satisfactory prediction.

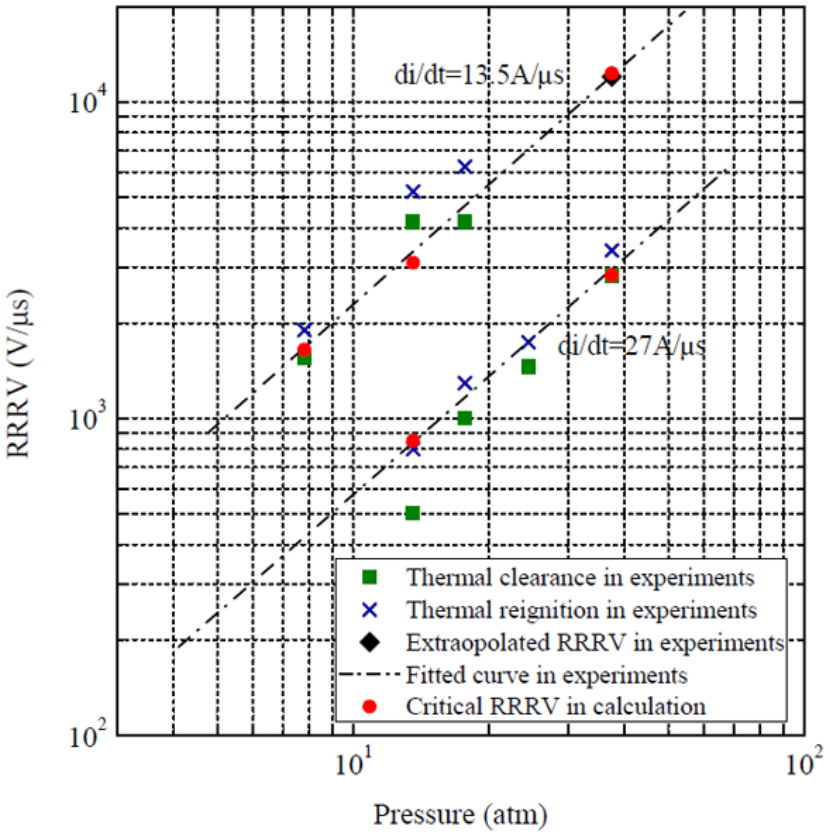

Figure 7.14. Comparison of computed and measured RRRV.

7.3.4 Dependence of RRRV on P_0 and di/dt

The computed dependence of RRRV on P_0 at a given di/dt appears to be weakly dependent on the value of di/dt. It has been found that

$$\text{RRRV} \propto P_0^{1.2} \quad \text{at di/dt} \quad = 27\ \text{A}\mu\text{s}^{-1}$$

$$\text{RRRV} \propto P_0^{1.3} \quad \text{at di/dt} \quad = 13.5\ \text{A}\mu\text{s}^{-1}$$

The average slope of the two straight lines (Figure 7.14) which are the best fits for the experimental results indicate $\text{RRRV} \propto P_0^{1.25}$ for both values of di/dt. The calculated dependence of RRRV on stagnation pressure at a given di/dt is, therefore, acceptable in view of the experimental uncertainties mentioned above. The reason for such a pressure dependence of RRRV at a given di/dt is attributed to the pressure dependence of electrical conductivity, and the specific heat at a constant pressure in the temperature range below 10,000 K [7.7, 7.10].

The dependence of the calculated and the measured RRRV on di/dt at a fixed stagnation pressure are in agreement, given as

$$\text{RRRV} \propto \left(\frac{\mathrm{d}i}{\mathrm{d}t}\right)^{-2.0}$$

7.4 Comparison of Shock Free Nozzle Arc with that under the Influence of a Shock

It would be of interest to breaker designers to know the thermal interruption performance under shock free conditions. Computation for the nozzle in Figure 7.1 has been performed for P_0=37.5 atm and di/dt= 27 $\text{A}\mu\text{s}^{-1}$ under shock free conditions by lowering the exit pressure. It has been found that arc temperature, velocity, electrical field and arc radius of the arc section upstream of the shock are identical with those of the shock free arc (curves 3 and 3(a) in Figure 7.6). This is not surprising as the arc section before the shock has no knowledge of the arc-shock interaction region due to supersonic flow ahead of the shock. The mass flow rate

passing the nozzle is the same for the cases with and without the presence of a shock provided that the upstream stagnation pressure and temperature are the same. The difference between the two is that the effective length of the arc for the shock free case is longer than that of the arc with shock. As a result, the voltage of a shock free arc is slightly higher (Figure 7.7). RRRV for the shock free case is increased from 2.83 $kV\mu s^{-1}$ with shock to 3.77 $kV\mu s^{-1}$, i.e. RRRV of a nozzle arc with shock is 25% lower than that of a corresponding shock free nozzle arc. In addition to the improved thermal interruption capability, the speed of dielectric recovery for the shock free case is expected to be much faster than that of the shock case, as the shock free arc does not have a region where flow is very stagnant.

7.5 Effects of the Exit Flow Conditions on the Arc in the Nozzle

Results reported in the previous sections show that, at the nozzle exit, gas is sucked into the nozzle which travels through the flow separation region and returns to the nozzle exit (see the streamlines in Figure 7.3(a)). Such a flow is produced by the pressure within the nozzle which is lower than the prescribed exit pressure. The thermodynamic state of the sucked in gas cannot be calculated using the same method for the gas flowing into the nozzle at the nozzle entrance (Section 3.7 of Chapter 3). This is because the sucked in gas can form a closed streamline (i.e. part of a vortex) part of which is outside the nozzle. When such a situation arises, the calculation domain should be extended to include such circulating flow within the computation domain. Attempts have been made to extend the calculation domain. It has been found that even the calculation domain (i.e. move the exit plane of Figure 7.1 further downstream) is extended well into the downstream dumping tank of the experiments [7.1], gas is still suck into the nozzle. It is, therefore, decided to include the dumping tank as part of the solution domain.

With the fixed exit pressure, thermal conduction at the nozzle exit is assumed to be negligible in comparison with convection (Point (c) in Section 3.7.5 of Chapter 3). The temperature at the nozzle exit can be extrapolated from the nozzle side. The

thermodynamic state of the gas is thus determined with the prescribed pressure at the exit. For computational investigations of Nozzles 1 and 2, it is suitable to extrapolate temperature at the nozzle exit from the interior of the nozzle. This is because, for these two nozzles, the exit pressure is very low to ensure shock free inside the nozzle, and thus there is no flow sucked in. Under such circumstances, the thermodynamic state of the gas at the nozzle exit is always determined by the gas inside the nozzle the state of which is obtained during computation and is, therefore, known. Thus, we do not require information on flow conditions downstream of the nozzle exit, for which the downstream tank is not needed in the computations. The aforementioned boundary conditions are, therefore, always applied to simulations of nozzle arcs with the same flow conditions [7.5, 7.7, 7.16], which have also been applied to investigations of Nozzles 1 and 2 as presented in previous chapters. However, if there is flow sucked into the nozzle from outside the nozzle exit, as for Nozzle 3, the thermodynamic state of the gas sucked in is usually not known. Under such circumstances, using fixed pressure and extrapolation of temperature at the nozzle exit is reasonable in that the temperature is quite uniform in the computation domain which is influenced by the sucked in gas. Otherwise, the information on flow conditions downstream of the nozzle exit is required to correctly specify the exit flow conditions, which can be done by including the dumping tank. Therefore, the question is whether the prescribed exit pressure and the temperature thus calculated in the exit plane are close to those computed when the dumping tank is included. Simulation is, therefore, carried out by including the dumping tank to assess if the arc behavior can be reasonably simulated using a fixed pressure at the nozzle exit.

The cylindrical gas dumping tank is 250 mm long with a radius of 192 mm, which is initially filled with SF_6 gas at an absolute pressure of $0.25P_0$ at room temperature. The downstream of the tank is sealed and, therefore, no flow exit is available in the calculation. The size of the tank is determined such that the total mass of the gas flowing from the nozzle to the tank is negligible in comparison with the mass of the gas inside the tank during the whole arcing period under investigation. The variation of the average pressure caused by mass flow from the nozzle within the

downstream tank is thus negligible. Calculation is performed with a current plateau of 1000 A followed by a linear current ramp with di/dt=27 $A\mu s^{-1}$. The upstream stagnation pressure is 37.5 atm. Results obtained with this modified calculation domain are compared with those discussed in previous sections.

At 1 kA DC, the temperature distribution together with the pressure isobars are given in Figure 7.15, and the streamline pattern in the arc-shock interaction region is shown in Figure7.16. With the modified downstream condition, there is little change on the qualitative features of the arc and the surrounding gas flow between two electrodes in comparison with those illustrated in Figure 7.2. As shown in Figure 7.17, the hot gas away from the nozzle wall exhausts into the dumping tank through the nozzle exit as well as through the hollow contact. The temperature of the gas exhausted through the nozzle exit into the tank is above 1500 K and above 10,000 K from the hollow contact (Figure 7.17). The gas jet exhausted from nozzle exit is divided into two streams: a part is returned to the nozzle via a region close to the axis and the other forms part of the circulating flow in the tank (Figure 7.17(b)), thus forming a stagnation point on the axis. The high temperature gas exhausted through the hollow electrode collides with the stream returning to the nozzle exit creating another flow stagnation point close to the hollow electrode exit. Almost all gas exhausted from the hollow electrode is returned to the nozzle (Figure 7.16). Several vortices near the nozzle exit are formed (Figure 7.17(b)).

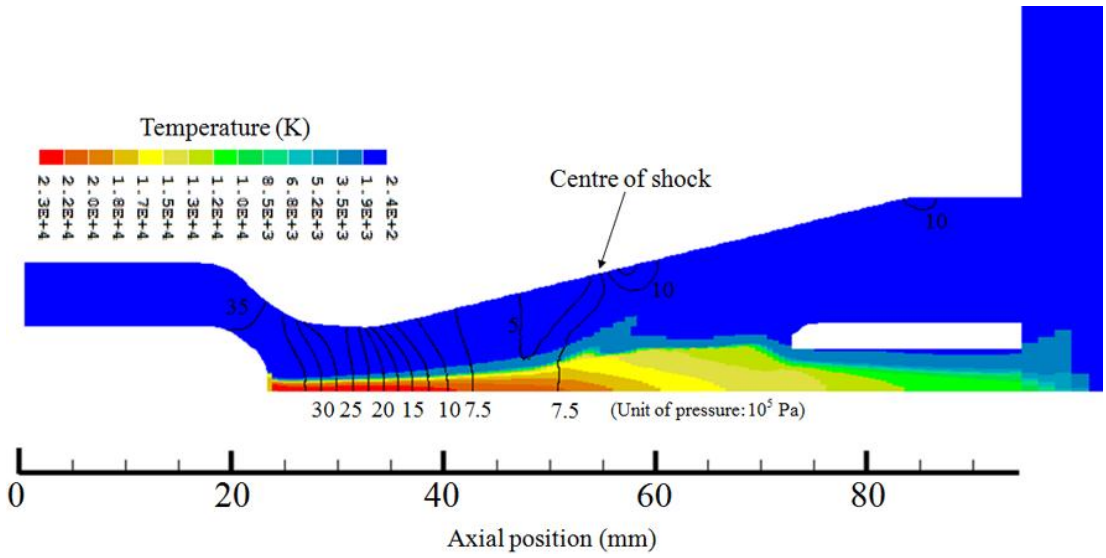

Figure 7.15. Temperature contour together with the pressure distribution in the nozzle at 1000 A DC, P_0=37.5 atm: obtained with the dumping tank. Only part of the dumping tank is shown.

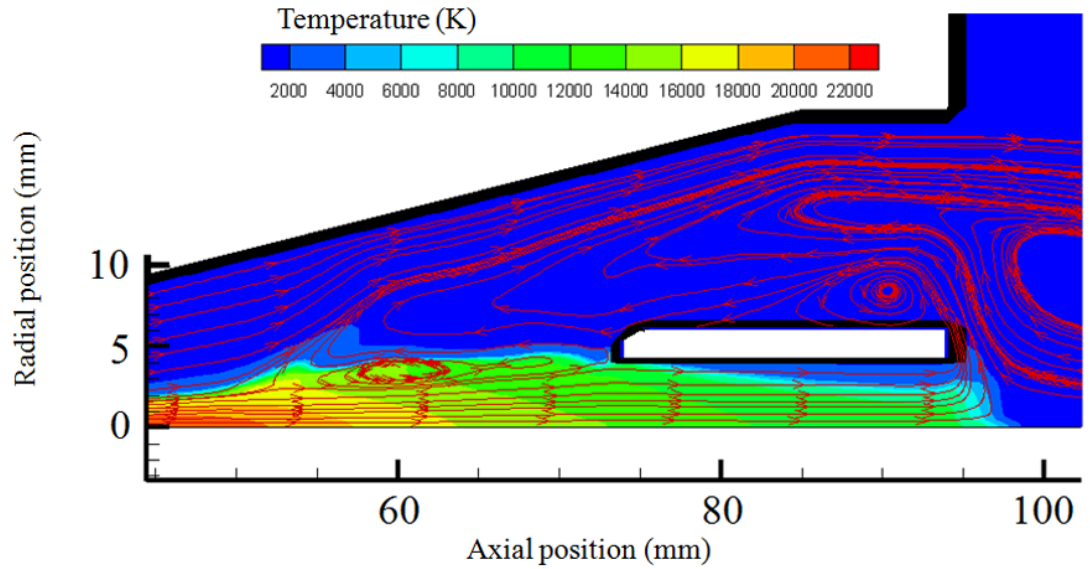

Figure 7.16. Streamline pattern in the arc-shock interaction region at 1000 A DC, P_0=37.5 atm: obtained with the dumping tank. Only part of the dumping tank is shown.

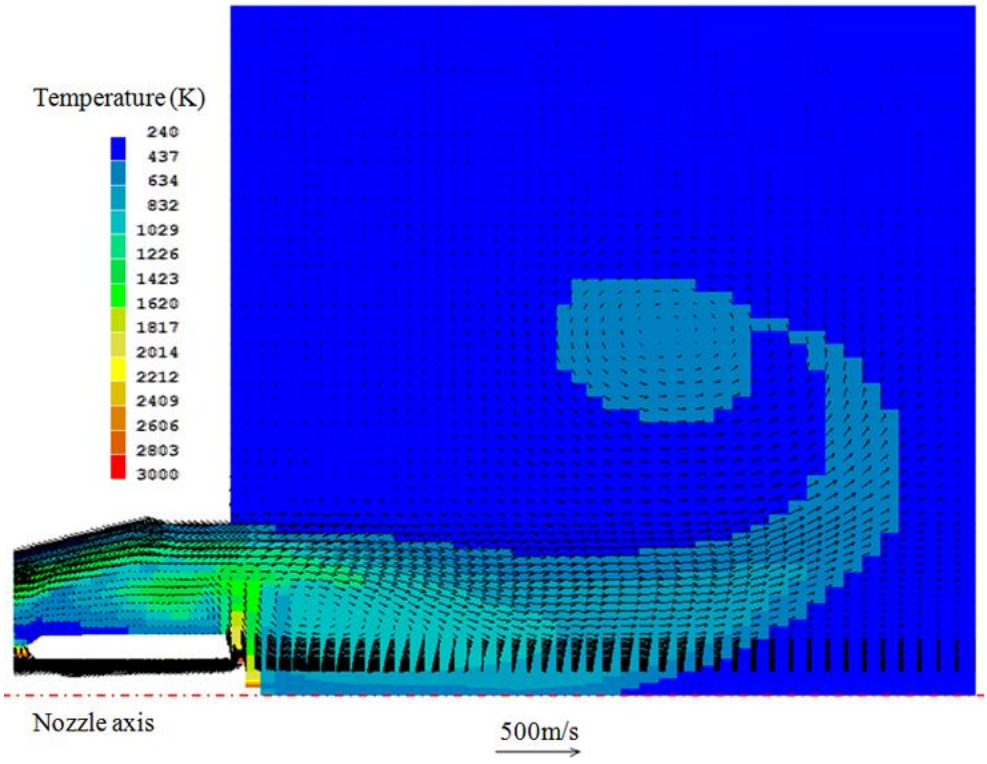

(a)

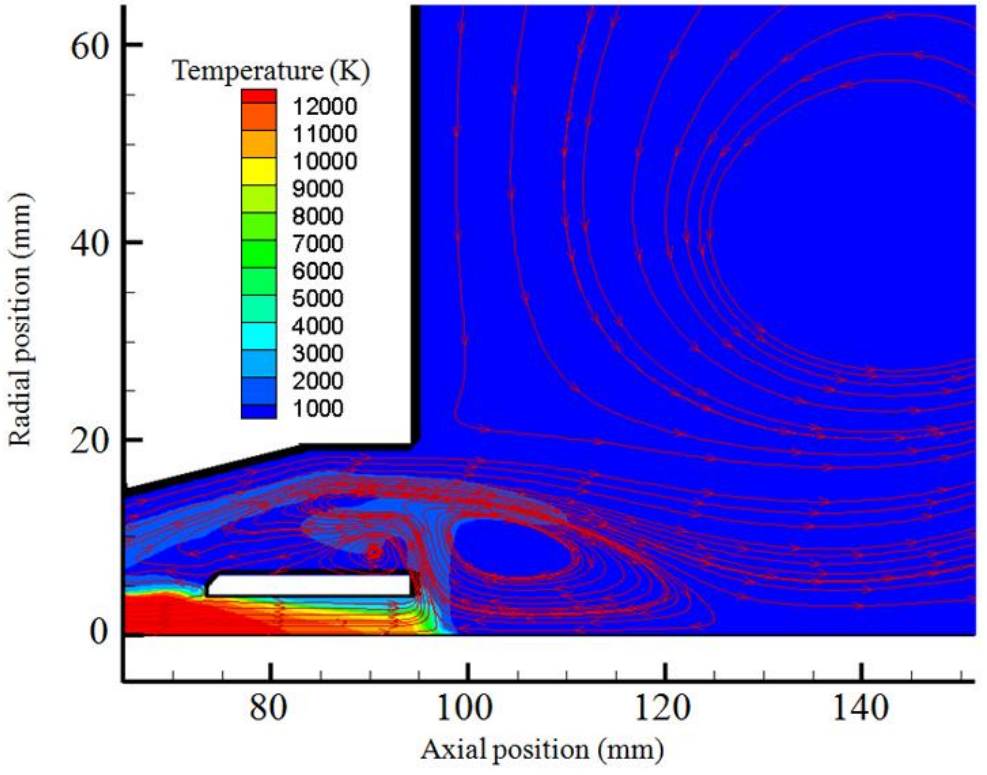

(b)

Figure 7.17. Flow behaviour downstream of the nozzle exit at 1000 A DC, P_0=37.5 atm: obtained with the dumping tank. (a) Temperature contour together with velocity vector and (b) Temperature contour together with streamline pattern. Only part of the dumping tank is shown.

The presence of three vortices near the nozzle exit makes the local flow pattern very different from that computed with exit pressure fixed (Figure 7.3(a)), which in turn affects the pressure, density and temperature at the nozzle exit plane. The nozzle exit pressure with a dumping tank is different from the prescribed exit pressure (Figure 7.18(a)). The computed density and temperature at the nozzle exit plane with a dumping tank are substantially different from those computed assuming constant exit pressure (Figure 7.18). In spite of these differences, the location of the shock centre is only shifted by 0.6 mm, which is negligible in comparison with the total arc length. Axis temperature and electric field distributions are given in Figure 7.19 inside the arc which indicates that the arc characteristics with and without the dumping tank are hardly affected by the conditions at the exit plane. The arc and its surrounding flow upstream of the shock cannot be affected by the nozzle exit conditions nor is the arc section in the arc-shock interaction region sensitive to these conditions.

The arc voltage before current zero and the post arc current after current zero are nearly identical with those shown in Figures 7.7 and 7.11. Thus, RRRV is the same as that of the nozzle arc with exit pressure fixed. The calculated thermal interruption capability of the nozzle arc is, therefore, not sensitive to the exit boundary conditions.

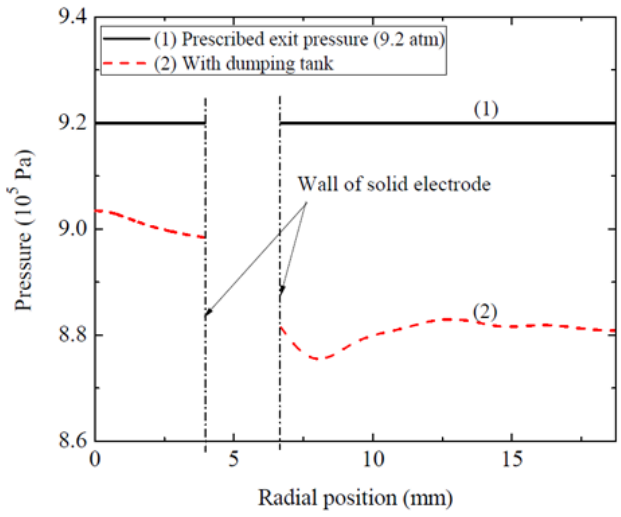

(a)

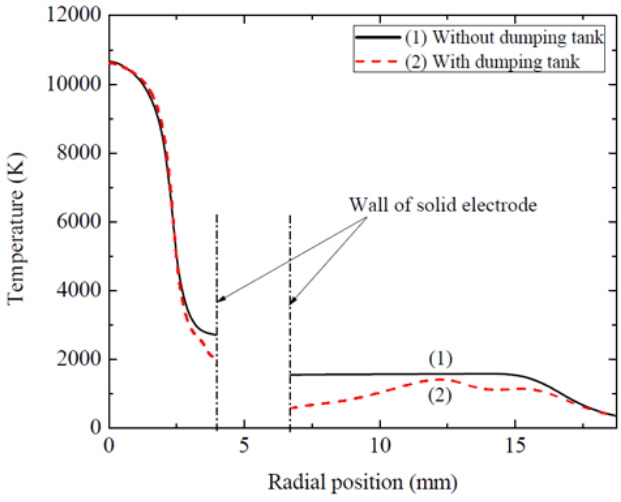

(b)

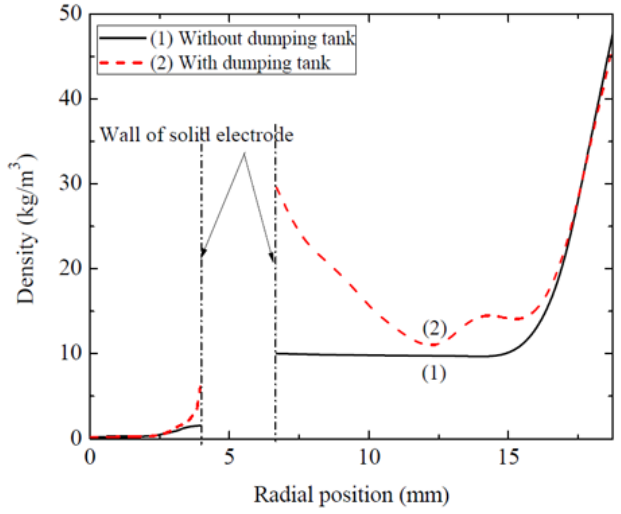

(c)

Figure 7.18. Radial distributions of pressure, temperature and density at the nozzle exit plane at 1000 A DC, P_0=37.5 atm. (a) radial pressure distribution with the dumping tank, (b) radial temperature distributions with and without the dumping tank and (c) radial density distributions with and without the dumping tank.

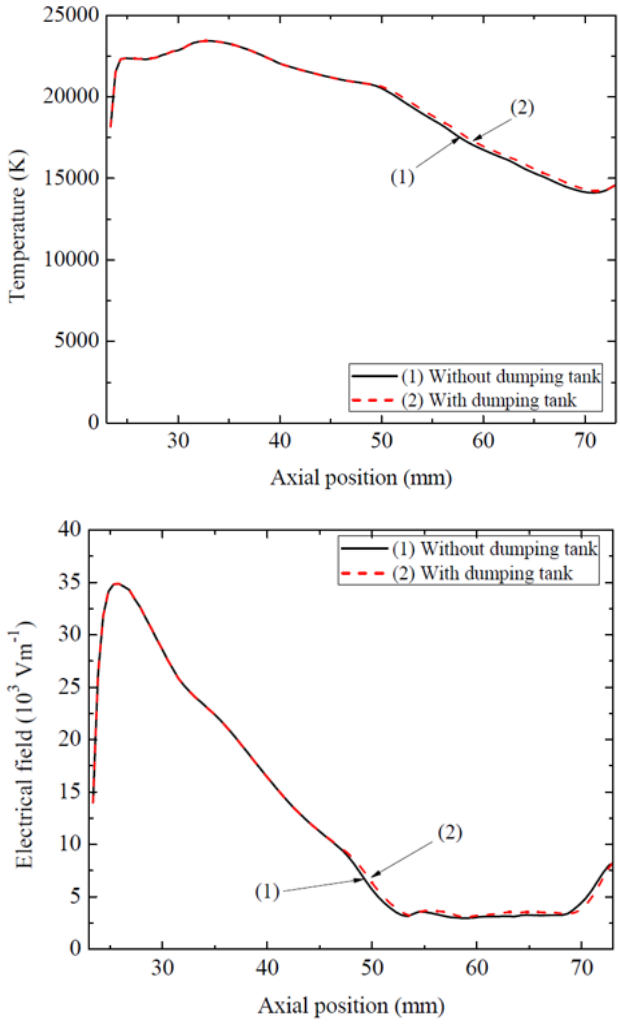

Figure 7.19. Axis temperature and electrical field distributions computed with and without the dumping tank at 1000 A DC, P_0=37.5 atm. (a) axis temperature distributions and (b) electrical field distributions.

7.6 Concluding Remarks

The effects of the arc-shock interaction on the behaviour of an SF_6 arc have been numerically investigated with a current ramp before current zero and a voltage ramp after current zero. Results show that the presence of the shock causes flow separation in the thermal boundary layer of the arc, which generates vortices and broadens the arc cross-section. When the current is ramped down to zero, the flow separation point moves to the axis thus creating a stagnation point on the axis, which results in very slow thermal recovery in the arc-shock interaction region. It has been found that the arc voltage is mainly taken up by the arc section before the shock. The effective arc

length is reduced and, thus, the RRRV of a nozzle arc under the influence of a shock is lower than that of a corresponding shock free nozzle arc by 25% for the pressure ratio investigated. The predicted values of RRRV with the chosen value of turbulence parameter are compared with test results of Frind and Rich [7.1] which shows good agreement between each other.

The effects of the boundary conditions at the nozzle exit on the arc behaviour are also investigated by including a gas dumping tank in the calculation domain. It has been found that the arc section before the shock and the current carrying part of the arc behind the shock are not affected by the conditions near the nozzle exit. The RRRV with or without a gas dumping tank is almost identical, which means that the prediction of thermal interruption capability for the nozzle arc is not affected by exit flow conditions.

References

[7.1] Frind G and Rich J A 1974 Recovery speed of axial flow gas blast interrupter: dependence on pressure and di/dt for air and SF_6 *IEEE Trans. Power Appar. Syst.* **93** 1675-84

[7.2] Anderson J D 1982 *Modern Compressible Flow* (New York: McGraw-Hill)

[7.3] Fang M T C, Kwan S and Hall W 1996 Arc-shock interaction inside a supersonic nozzle *IEEE Trans. Plasma Sci.* **24** 85-6

[7.4] Yan J D, Fang M T C and Jones C 1997 Electrical and aerodynamic behaviour of arcs under shock conditions *IEEE Trans. Plasma Sci.* **25** 840-5

[7.5] Yan J D, Nuttall K I and Fang M T C 1999 A comparative study of turbulence models for SF_6 arcs in a supersonic nozzle *J. Phys. D: Appl. Phys.* **32** 1401-6

[7.6] Zhang Q, Yan J D and M T C Fang 2012 Modelling of turbulent arc burning in a supersonic nozzle *Proc. Int. Conf. on 19th Gas Discharges and Their Applications (Beijing, China (2-7 Sept 2012)) (High Voltage Engineeing: Special Issue on Gas Discharges and Their Applications* vol 38*)* ed Z C Guan (Wuhan: High Voltage Engineering) pp 202-5

[7.7] Fang M T C, Zhuang Q and Guo X J 1994 Current zero behaviour of an SF_6 gas-blast arc Part II: turbulent flow *J. Phys. D: Appl. Phys.* **27** 74-83

[7.8] Song K D, Lee B Y and Park KY 2003 Analysis of thermal recovery for SF_6 gas blast arc within a Laval nozzle, *Japan. J. Appl. Phys.* **42** 7073-79

[7.9] Song K D, Lee B Y and Park K Y 2004 Calculation of the post-arc current in a supersonic nozzle by using the K-epsilon model *Journal of Korean Physical Society.* **45** 1537-43

[7.10] Zhang J L, Yan J D and Fang M T C 2000 Investigation of the effects of pressure ratios on arc behaviour in a supersonic nozzle *IEEE Trans. Plasma Sci.* **28** 1725-34

[7.11] Chan S K, Fang M T C and Cowley M D 1978 The DC arc in a supersonic nozzle *IEEE Trans. Plasma Sci.* **4** 394-405

[7.12] Schlichting H 1979 *Boundary Layer Theory* 7th Ed. (New York: McGraw Hill)

[7.13] Knight D, Yan H, Panaras A G and Zheltovodov A 2003 Advances in CFD prediction of shock wave turbulent boundary layer interaction *Progress in aerospace sciences.* **39** 121- 84

[7.14] Liebermann R W and Lowke J J 1976 Radiation emission coefficients for sulfur hexafluoride arc plasmas *J. Quant. Spectrosc. Radiat. Transf.* **17** 253-64

[7.15] Hermann W, Kogelschatz U, Niemyer L, Ragaller K and Schade E 1976 Investigation on the phenomena around current zero in HV gas blast circuit breakers *IEEE Trans. Power Appr. Syst.* **95** 1165-76

[7.16] Zhang X D, Trépanier J Y and Camarero R 1997 Numerical simulation of a 2 kA convection-stabilized nitrogen arc using CFD tools *J. Phys. D: Appl. Phys.* **30** 3240-52

Chapter 8
Conclusions and Future Work

8.1 Conclusions

This thesis is exclusively concerned with the mathematical modelling of turbulent switching arcs. Turbulent arc modeling is still in its infancy as the mechanisms for driving arc instability are not fully understood. However, there is a direct resemblance between a nozzle arc and a rounded free jet both of which are dominated by shear flow. Thus, the modelling of turbulent switching arcs follows the same approach as that for modelling of turbulent jets. We, therefore, derive the time averaged conservation equations for switching arcs using Reynolds's approach. We, then, borrow method for the closure of the time averaged conservation equations (commonly known as turbulence models) from the modelling of turbulent jet, which is based on the adoption of Boussinesq assumption to relate Reynolds stress to the time averaged velocity gradient through eddy viscosity. The turbulent heat flux is assumed to be related to Reynolds stress through a constant turbulent Prandtl number.

Additional equations are introduced to determine the turbulence length scale and velocity scale required by eddy viscosity. There are numerous turbulence models and the most fruitful approach for turbulent arc modelling is to examine the applicability of those turbulence models, which have a track record of success in fluid mechanics and aerodynamics, to turbulent SF_6 arcs. Careful comparison of the flow conditions of a turbulent nozzle arc with those of a turbulent free jet results in the selection of the standard k-epsilon model and its two variants (the Chen-Kim model and the RNG model) for the modeling of SF_6 turbulent switching arc. Since the application of the Prandtl mixing length model to SF_6 switching arc has met some success, this turbulence model is included in our present investigation. In order to

demonstrate the effects of turbulence, laminar flow model is also included. Therefore, altogether five flow models have been used to study the turbulent nozzle arc.

The applicability of the turbulence models are subject to verification by experimental results under a wide range of discharge conditions. To avoid these complications and to focus our attention on the modelling of turbulent effects we choose the experimental results obtained using a two-pressure system and a simple nozzle-electrode configuration (i.e. those reported by Benneson et al. [8.1], Frind et al. [8.2] and Frind and Rich [8.3]) for the verification of turbulence arc models.

Altogether, arcs in three nozzles (i.e. the nozzle of Frind et al. [8.2], the nozzle of Benneson et al. [8.1] and the nozzle of Frind and Rich [8.3], respectively referred to as Nozzle 1, Nozzle 2 and Nozzle 3 in Chapter 3) with different shapes and dimensions as well as electrode configurations at different stagnation pressures have been studied. Detailed computational results obtained by the five flow models are given for Nozzle 2 since the qualitative features of the computational results for the other two nozzles are the same.

The cold flow in Nozzle 2 has been computed by four flow models (Prandtl mixing length excluded). Results show that turbulence effects are negligible in the regions away from electrodes. All the four flow models predict a wake near the tip of the upstream electrode and a bow shock in front of the downstream electrode. However, the size of the wake and the strength and the structure of the shock differ widely between flow models. The implications of the wake and shock on dielectric breakdown have been discussed.

The characteristics of nozzle arc under direct currents are then investigated by the five flow models. The V-I characteristic of the nozzle arc is given and the reasons for the shape of the V-I characteristic are explained for the first time. At currents above 600 A, radiation is the dominant energy transport process, while the effects turbulence enhanced thermal conduction is not important. The computed arc voltage is, therefore, not sensitive to the flow models. Thus, arc voltage at high current is not an effective means for the verification of flow models. For arc currents below 600 A, turbulence enhanced thermal conduction and radiation become dominant which give

rise to the negative V-I characteristic. There is a large difference between voltages predicted by different flow models with those predicted by the Prandtl mixing length model the highest and that by the laminar flow model the lowest. It is found that the arc voltage for DC nozzle arcs is proportional to the square root of stagnation pressure for all the current range investigated.

The current zero behaviour of the SF_6 switching arc has been numerically investigated for Nozzle 2 using the five flow models. The computed RRRV is compared with that measured for Nozzle 2. Such a comparison shows that for Nozzle 2 the Prandtl mixing length model can generally give satisfactory predictions of the RRRV with turbulence parameter adjusted to fit one test result of RRRV. The standard k-epsilon model grossly over-estimates RRRV which is much higher than measurements for all the discharge conditions investigated. The performances of the Chen-Kim model and the RNG model are similar, both of which grossly under-estimates the effect of turbulence and the predicted RRRV is of the same order of magnitude of that predicted by the laminar flow model, which is much lower than measured RRRV.

The effects of the nozzle geometry on turbulence have been computationally investigated using the Prandtl mixing length model and the standard k-epsilon model. The computed RRRV obtained by the two turbulence models for the three nozzles are compared with corresponding measured RRRV [8.1, 8.2, 8.3]. The standard k-epsilon model under predicts RRRV for Nozzle 1 for most discharge conditions investigated, while good agreement between predictions and measurements can be achieved by using the Prandtl mixing length model. We therefore believe that the Prandtl mixing length model can give the most consistent results once the value of the turbulence parameter for a given nozzle is fixed according to relevant experimental results. The results obtained by the Prandtl mixing length model show that Nozzle 2 gives the highest RRRV among the three nozzles investigated for a given set of discharge conditions (with fixed P_0 and di/dt). This means the highest turbulence level can be attained by Nozzle 2.

Shock waves inevitably occur during the operation of a circuit breaker. The

effects of shock wave on thermal interruption are investigated using the Prandtl mixing length model for Nozzle 3 where the exit pressure is set at a quarter of the stagnation pressure ($P_0/4$) consistent with the experimental conditions of Frind and Rich [8.3]. Results show that the presence of the shock causes flow separation and generation of vortices in the arc-shock interaction region, which results in very slow thermal recovery in this region. It has been found that the arc voltage is mainly taken up by the arc section before the shock. The effective arc length is therefore reduced. Thus, RRRV of a nozzle arc under the influence of a shock is lower than that of a corresponding shock free nozzle arc by 25% for the pressure ratio investigated. The predicted RRRV with the chosen value of turbulence parameter are compared with test results of Frind and Rich [8.3], which shows good agreement between each other. The effects of the boundary conditions at the nozzle exit on the arc behaviour are also investigated by including a gas dumping tank in the computational domain, which shows that the arc between two electrodes and subsequently, RRRV, are not affected by the conditions near the nozzle exit.

In summary, altogether five flow models have been used to predict the behaviour of SF_6 switching arc under a wide range of discharge conditions. RRRV predicted by laminar flow model is a few orders of magnitude lower than that measured, which indicates that turbulence plays a decisive role in the determination of thermal interruption capability of a nozzle arc. Of the four turbulence models, the Prandtl mixing length model gives the best prediction of RRRV when compared with experimental results. The drawback is that the value of the turbulence parameter of the Prandtl mixing length model needs to be derived from one test result for a given geometry. With our current understanding of the physics of turbulent arc, the Prandtl mixing length model is the only turbulence model which can be used to predict the thermal interruption capability of a nozzle arc arrangement.

8.2 Future Work

The key to the achievement of predictive design of high voltage circuit breakers lies with the accurate prediction of turbulent arc behaviour especially during current zero period. Although it is commonly recognized that the physics of turbulence is contained within the conservation equations for arcs, direct numerical solution of arc conservation equations with the grid size and time step required for a complete description of turbulence is not possible at present even with the most advanced computer. Such approach is neither practical in terms of the computational cost nor is necessary as the majority of engineering designs only require the statistical information about a system. This means that, in the foreseeable future, theoretical investigation of turbulent arcs will be based on the derivation of the statistical behaviour of arcs from arc conservation equations. The application of statistical treatment (e.g. Reynolds time average) to conservation equations results in the so-called closure problem: that is the number of equations is always greater than the number of unknowns. The closure of the equations involves ad hoc assumptions, which introduce unknown constants. The values of these constants will have to be optimized according to experimental results.

Successful modeling of turbulent arc critically depends on reproducible experimental results under well defined conditions for fixing the values of constants and for verification. Up to now, no experiments have been performed to characterize the turbulent nozzle arc. As indicated in the thesis, turbulent arc modeling is at its infancy. What has been done so far in turbulent arc modeling is to apply turbulence models designed for incompressible turbulent free jet to turbulent nozzle arc. It is in a way surprising that the Prandtl mixing length model and the standard k-epsilon model can predict arc features a few microseconds before current zero. The Prandtl mixing length model is able to predict the thermal interruption capability under a wide range of discharge conditions provided that its turbulence parameter is derived from a single test result of the nozzle concerned. Thus, its range of application is limited.

The work proposed below is for immediate future. The list is, therefore, not exhaustive. It rather reflects the author's view on the most fruitful line which should be followed in order to make progress in turbulent arc modelling.

8.2.1 Experimental Work

8.2.1.1 Investigation of Scaling Laws for DC arcs Burning in Affinely Related Nozzles in a Two-Pressure System

Although the highly non-linear nature of arc conservation equations prevents the derivation of scaling laws, the approximately method for arc analysis, the integral method, does indicate the existence of scaling laws [8.4]. Arc experiments should be performed in a set of affinely related nozzles defined by $A/A_t = f(z/z_t)$, where A_t and Z_t are respectively the throat area and the distance between the nozzle entrance and the throat. In order to avoid the influence of electrodes on the flow within the nozzle, the two electrodes need to be located outside the nozzle. Measurements of arc voltage and pressure within the nozzle would be sufficient to see if experimental arcs can be scaled according to the work of Fang et al. [8.4]. Experimental proof of scaling laws would greatly facilitate high voltage breaker development based on existing products with lower current and voltage ratings.

8.2.1.2 Experimental Investigation of DC Nozzle Arcs Burning in Different Gases

The superior arc quenching capability of SF_6 is due to turbulence cooling of the arc. However, the green house effects of SF_6 make its replacement by environmentally friendly gases highly desirable. If turbulence also plays a decisive role for arc extinction in gases other than SF_6, experiments should be performed on DC arcs in different gases to determine the onset of arc instability and the material properties of the gas which influence the onset. In addition to the measurements of current, voltage and pressure, temperature measurement using emission spectroscopy would be

necessary to characterize the arc along the arc length. In addition to SF_6, gases to be investigated include air, CO_2 and mixtures of SF_6.

8.2.1.3 Experimental Investigation of DC Nozzle Arcs under Shock Conditions

No experimental results can be found in the literature for DC nozzle arcs under shock conditions. With a two-pressure system standing shock can be produced by choosing proper exit pressure. Quantities to be measured are the same as those in Section 8.2.1.2.

8.2.1.4 Experimental Investigation of Current Zero Period and the Measurement of RRRV under Shock Free and Shock Conditions

The current zero period will be investigated using a current ramp before current zero and a voltage ramp after current zero, the same as in Benenson et al. [8.1]. Measurements close to current zero require high time resolution of no bigger than 0.2 μs. Accurate measurement of post arc current is essential for the verification of turbulence models. Emission spectroscopy of temperature measurement close to current zero is unlikely to be feasible as the arc temperature will be below 10,000K.

8.2.1.5 Investigation of Electrode Effects on RRRV

The above experiments will be repeated after the insertion of electrodes into the nozzle to investigate the effects of wake and bow shock on RRRV.

8.2.2 Theoretical Work

Once the experimental information associated with the proposed future experimental work is available, one could seriously contemplate improving the modeling of turbulent arc. Turbulence modeling in fluid and aerodynamics has been an active research field since the introduction of time averaged conservation equations by Reynolds over 100 years ago [8.5]. Much valuable experience has been accumulated [8.6] especially in the area of turbulent combustion [8.7].

Prandtl mixing length model, the standard k-epsilon model and its variants are devised for turbulent fluids with constant density and fluid property. Such assumptions are apparently not valid for arcs. Density variation inside a nozzle arc will be very large as temperature varies from ambient to around 28,000K and pressure drop of 10 bar or more from nozzle entrance to exit. The gas is, therefore, highly compressible and the effects of density fluctuation due to turbulence cannot usually be neglected. In addition, computational results given in this thesis show that the characteristic time for temperature variation is much shorter than that for velocity. The use of unity turbulent Prandtl number assumes that temperature and velocity vary with the same characteristic time. More accurate prediction of the temperature variation during the current zero period is crucial for the correct prediction of RRRV, as temperature determines electrical conductivity.

A good turbulence model should achieve universality at a reasonable computation cost. The approach adopted for the modelling of turbulent combustion problems appears to be a realistic path to follow for turbulent arc modelling [8.8]. It is proposed to use Favre average to derive the mass averaged conservation equations, thus taking care of density fluctuation and compressible effects. Mass averaged conservation equations retain the same form as those time averaged conservation equations for constant density fluid. The introduction of a time scale for turbulent temperature variation requires two additional equations, the temperature (or enthalpy) variance equation and the dissipation rate of temperature variance. The turbulent kinetic energy equation and its dissipation rate equation of the k-epsilon model are included, which enable eddy viscosity to be calculated. Gradient transport will be used to link the corresponding unknown turbulent fluxes involving the correlation of the time or mass averaged product of two fluctuating quantities [8.9].

The comparison of the predicted temperature with experimental results requires the conversion of mass averaged temperature to time averaged temperature. It is recommended to adopt the method of Lee [8.10] for such a conversion, which uses a probability density distribution function.

References

[8.1] Benenson D M, Frind G, Kinsinger R E, Nagamatsu H T, Noeske H O and Sheer, Jr R E 1980 Fundamental investigation of arc interruption in gas flows EPRI EL-1455 (Project 246-2)

[8.2] Frind G, Kinsinger R E, Miller R D, Nagamatsu H T and Noeske H O 1977 Fundamental investigation of arc interruption in gas flows EPRI EL-284 (Project 246-1)

[8.3] Frind G and Rich J A 1974 Recovery speed of axial flow gas blast interrupter: dependence on pressure and di/dt for air and SF_6 *IEEE Trans. Power Appar. Syst.* **93** 1675-84

[8.4] Fang M T C, Ramakrishnan S and Messerle H K 1980 Scaling laws for gas-blast circuit-breaker arcs during the high current phase *IEEE Trans. Plasma Sci*. **PS-8** 357-62

[8.5] Schlichting H 1979 *Boundary Layer Theory* 7th edn (New York: McGraw Hill)

[8.6] Wilcox D C 2006 *Turbulence Modeling for CFD* (La Cañada, CA: DCW Industries)

[8.7] Poinsot T and Veynante D 2005 *Theoretical and Numerical Combustion* 2nd edn (Philadelphia: Edwards)

[8.8] Libby P A and Williams F A 1980 *Turbulent Reacting Flow* (Berlin: Spring-Verlag)

[8.9] Sarkar S and Balakrishnan L 1990 Application of a Reynolds Stress Turbulence Model to the Compressible Shear Layer ICASE Report (No. 90-18)

[8.10] Lee Y C 1984 *Modelling Work in Thermal Plasma Processing* (PhD thesis: University of Minnesota)

Appendix A
Properties of High Pressure Arc in Local Thermodynamic Equilibrium (LTE)

A.1 Introduction

The gas pressure encountered in circuit breakers is at atmospheric and above. At such pressure, collisions between particles in the arc column are very frequent. For such collision dominated arc and for the discharge conditions normally met in circuit breakers the arc can be regarded as in the state of local thermodynamic equilibrium (LTE). The properties of LTE plasmas and the conditions to ensure LTE in the context of circuit breaker plasmas are given in this Appendix.

A.2 Properties of LTE Plasmas and Conditions for the Attainment of LTE in Circuit Breaker Arcs

The properties of an LTE plasmas are characterized by [A.1, A.2]:

(a) All species attain a single temperature, T, and the velocity distribution of each species obeys Maxwellian distribution: for species *r*, the number density of particles with speed in v_r and v_r+dv_r is given by

$$dn_r = n_r f(v_r) dv_r \tag{A.1a}$$

where

$$f(v_r) = \frac{4v_r^2}{\sqrt{\pi(2kT/m_r)^3}} \exp\left(-\frac{m_r v_r^2}{2kT}\right) \tag{A.1b}$$

where v_r is the magnitude of the velocity vector, n_r the number density and m_r the mass per particle of species *r*. *T* is the common temperature for all particle species and *k* is the Boltzmann constant.

To attain a single temperature within a circuit breaker arc requires the largest temperature relaxation time to be much smaller than the characteristic times for the variation of discharge conditions (e.g. current variation) and the transient time of a plasma element travelling form upstream electrode to the downstream electrode.

(b) The population density of excited stages for each particle species at every energy level (the distribution of internal energy) obeys the Boltzmann distribution:

$$n_{r,k} = n_r \frac{g_{r,k}}{Q_r} \exp\left(-\frac{E_{r,k}}{kT}\right) \tag{A.2}$$

where n_r is the total number density of ions of species r, Q_r is the partition function the detail of which is given in [A.1], $E_{r,k}$ is the energy of the kth quantum state, and $g_{r,k}$ is the statistical weight of this state, the detail of which is given in [A.1].

To attain Boltzmann distribution in plasma of finite dimension, we require that the effects of photo excitation and radiation decay are not important in comparison with electron impact excitation and collision of second kind. Thus, the electron number density must be sufficiently high to maintain the Boltzmann distribution at lower energy level E_i and at a higher energy level E_k . Such electron number density (N_e) is related to the energy difference between the two energy levels concerned and the temperature (T) of the plasma: for Hydrogen for example, we require [A.2]

$$N_e \geq 10^{12} T^{1/2} \left(E_k - E_i\right) \tag{A.3}$$

where N_e in cm^{-3}, T in K and E_i and E_k in eV.

(c) The number densities of charged particle species (electrons, positive and negative ions) are related by Saha-Eggert equation:

$$\frac{n_{r+1} n_e}{n_r} = \frac{2Q_{r+1}}{Q_r} \frac{\left(2\pi m_e kT\right)^{3/2}}{h^3} \exp\left(-\frac{E_{r+1}}{kT}\right) \tag{A.4}$$

where n_r and n_{r+1} are respectively the number density of ion species in the rth and (r+1)th ionization state. n_e is the electron number density, E_{r+1} is the ionization energy which is required to produce an ion in the (r+1)th state from the rth state, m_e

the electron mass and *h* the Planck constant.

When Equation (A.4) is applied to ionization, the relation is known as Saha's equation. For the electron number density in a plasma to attain the value given by Equation A.4, the electron number density must exceed the value given below [A.2]:

$$N_e > 5\times10^{15}\ \mathrm{cm}^{-3} \tag{A.5}$$

Chemical equilibrium is assumed when Equation (A.4) is applied. This requires that the life time of a plasma element between two contacts and the characteristic times of time variation of discharge conditions (e.g. characteristic time for current variation, $\tau_i = i/|di/dt|$) should be much greater than that of the slowest reaction of all chemical reactions involved.

Because of the above properties, the composition of LTE plasmas and thermodynamic properties can be calculated using the same method as that for plasmas in thermodynamic equilibrium.

A.3 Conservation Equations of LTE Flowing Plasmas

The arc plasma under LTE state can be treated as a single conductive fluid. The conservation equations for arc plasma are, therefore, similar to Navier-Stokes equations [A.3] but modified to take into account the effects of radiation transport and the effects of electromagnetic fields. These conservation equations can be written as:

(a) Continuity equation (Conservation of mass)

$$\frac{\partial\rho}{\partial t} + \nabla\cdot(\rho\mathbf{V}) = 0 \tag{A.6}$$

where *t* is the time, ρ the gas density and **V** the velocity vector.

(b) Momentum equation (Newton's second law of motion)

$$\frac{\partial}{\partial t}(\rho\mathbf{V}) + \nabla\cdot(\rho\mathbf{V}\mathbf{V}) = \nabla\cdot\prod_{ij} + \mathbf{J}\times\mathbf{B} \tag{A.7}$$

where **J** is the current density, **B** the magnetic flux density, and $\prod_{ij}$ the stress tensor. For a Newtonian fluid obeying Stokes' relation, the stress tensor is

$$\prod_{ij} = -p\delta_{ij} + \mu\left(\frac{\partial u_i}{\partial x_j} + \frac{\partial u_j}{\partial x_i}\right) + \delta_{ij}\mu'\frac{\partial u_k}{\partial x_k} \qquad (i, j, k = 1, 2, 3) \qquad \text{(A.8)}$$

where p is the pressure, δ_{ij} is the Kronecker delta function ($\delta_{ij} = 1$ if $i = j$ and $\delta_{ij} = 0$ if $i \neq j$). u_1, u_2, u_3 are the three components of the velocity vector **V** and x_1, x_2, x_3 the three components of the position vector, μ is the coefficient of viscosity and μ' the second coefficient of viscosity, both of which are related to the coefficient of bulk viscosity (κ) by the expression [A.3, A.4]:

$$\kappa = \frac{2}{3}\mu + \mu' \qquad \text{(A.9)}$$

If not for study of the structure of shock waves and in the absorption and attenuation of acoustic waves, the coefficient of bulk viscosity can be neglected according to Stokes' hypothesis. The stress tensor can then be written as [A.4]:

$$\vec{\prod}_{ij} = -p\delta_{ij} + \boldsymbol{\tau}_{ij} \qquad (i, j, k = 1, 2, 3) \qquad \text{(A.10)}$$

where $\boldsymbol{\tau}_{ij}$ is the viscous stress tensor given by

$$\boldsymbol{\tau}_{ij} = \mu\left[\left(\frac{\partial u_i}{\partial x_j} + \frac{\partial u_j}{\partial x_i}\right) - \frac{2}{3}\delta_{ij}\frac{\partial u_k}{\partial x_k}\right] \qquad (i, j, k = 1, 2, 3) \qquad \text{(A.11)}$$

(c) Energy equation (Thermodynamics first law)

$$\frac{\partial}{\partial t}\left[\rho\left(e + \frac{\mathbf{V}^2}{2}\right)\right] + \nabla\cdot\left[\rho\left(e + \frac{\mathbf{V}^2}{2}\right)\mathbf{V}\right] = -\nabla\cdot(p\mathbf{V}) + \nabla\cdot(k\nabla T) + \mathbf{J}\cdot\mathbf{E} - q + \Phi \qquad \text{(A.12)}$$

where e is the internal energy, T the temperature, p the pressure, k the thermal conductivity, **J** the current density, **E** the electrical field intensity, and q the net radiation loss per unit volume and time. Φ is the viscous dissipation function which is given by [A.4]

$$\Phi = \tau_{ij}\frac{\partial u_i}{\partial x_j} \qquad (i, j, k = 1, 2, 3) \qquad \text{(A.13)}$$

For computer simulation of circuit breaker arcs, the conservation equation is often written in terms of enthalpy:

$$\frac{\partial}{\partial t}(\rho h)+\nabla\cdot\left(\rho\vec{V}h\right)=\frac{dp}{dt}+\nabla\cdot\left(\frac{k}{c_p}\nabla h\right)+\mathbf{J}\cdot\mathbf{E}-q+\Phi \tag{A.14}$$

where c_p is the specific heat at constant pressure, and h is the enthalpy given by

$$h=e+\frac{p}{\rho} \tag{A.15}$$

(d) For low frequency (i.e. at industrial frequency of 50 Hz or 60 Hz), the equations describe electromagnetic fields are simplified to

Ohm's law: $$\vec{J}=\sigma\left(\vec{E}\right) \tag{A.16}$$

Ampere's law: $$\nabla\times\vec{B}=\mu_0\left(\vec{J}\right) \tag{A.17}$$

Current continuity equation: $$\nabla\cdot\left(\vec{J}\right)=\nabla\cdot(\sigma\vec{E})=0 \tag{A.18}$$

Introducing electrical potential, ϕ, the above equation can be written as

$$\nabla\cdot(\sigma\nabla\phi)=0 \tag{A.19}$$

which is commonly used for the computation of electrical potential distribution inside the arc interrupter of a circuit breaker.

A.4 Thermodynamic Properties (Equation of State) and Transport Properties of LTE SF_6 Arc Plasma

The present thesis is solely concerned with SF_6 due to its excellent dielectric and arc quenching properties and, therefore, its exclusive use at transmission voltage level. The solution of conservation equations requires knowledge of the equation of state and transport properties. For SF_6 arc plasma in LTE, the thermodynamic state and the transport properties are determined by two thermodynamic quantities (commonly pressure, p, and temperature, T). The equation of state is then relating the density to p and T. Since the temperature in a circuit breaker can reach 30,000K, the composition of SF_6 plasma is very complex due to chemical and ionization reactions (Figure A.1 [A.5]). The equation of state, thermodynamic properties and the transport properties are, therefore, given in tabulated or graphic form [A.6].

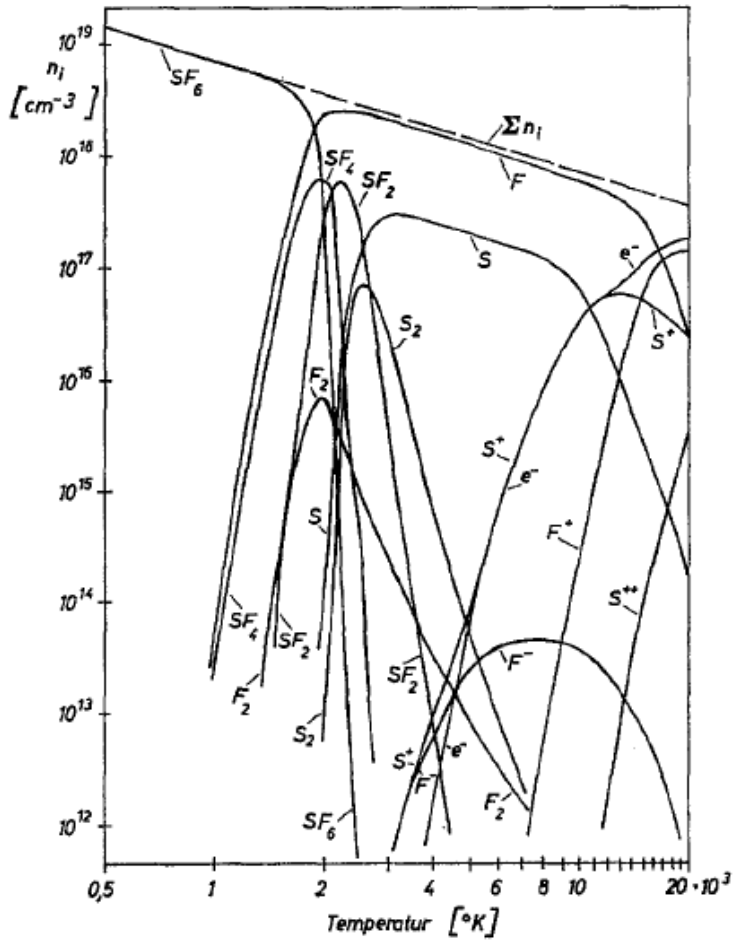

Figure A. 1. Variation of particle density with temperature for SF_6 arc plasma for pressure of 1 atm, reproduced from [A.5].

A.4.1 Thermodynamic Properties

For completeness, those frequently used thermodynamic properties of SF_6 for switching arc applications are given as a function of pressure and temperature taken from Frost and Liebermann [A.6]. Figures A.2 to A.5 give respectively the density, the enthalpy, the specific heat at constant pressure, and the sound speed.

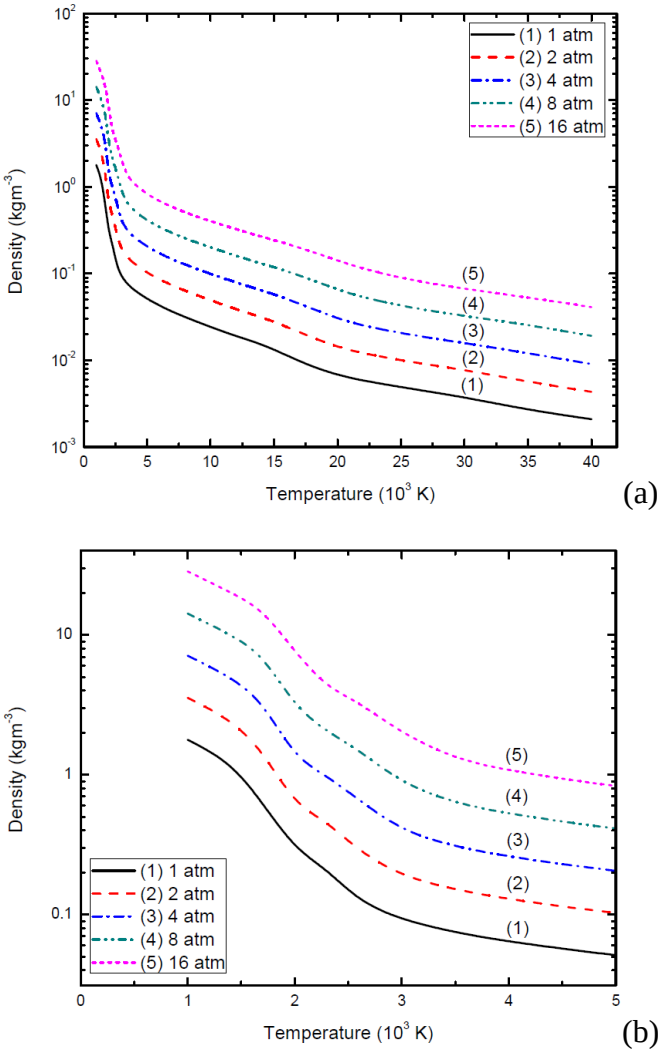

Figure A. 2. Density (ρ) of SF_6 arc plasma as a function of temperature for pressure of 1, 2, 4, 8 and 16 atm, reproduced from [A.6]. (a) Density and (b) enlarged diagram of (a) in the temperature range of 0 to 5,000 K.

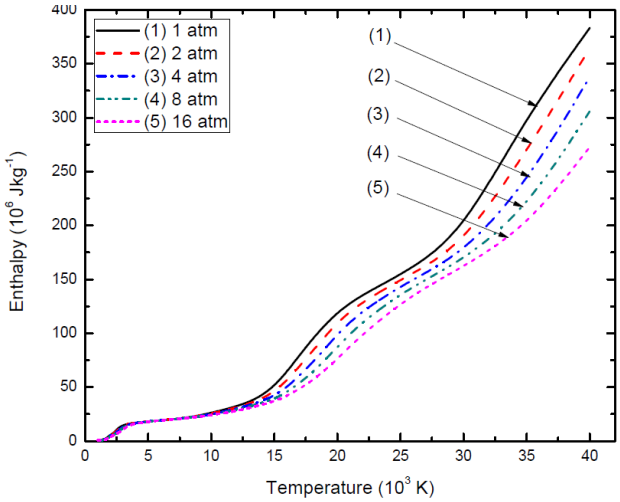

Figure A. 3. Enthalpy (h) of SF_6 arc plasma as a function of temperature for pressure of 1, 2, 4, 8 and 16 atm, reproduced from [A.6].

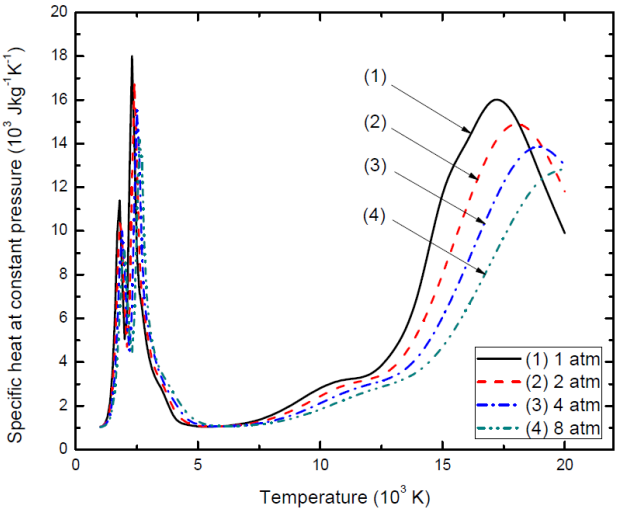

(a)

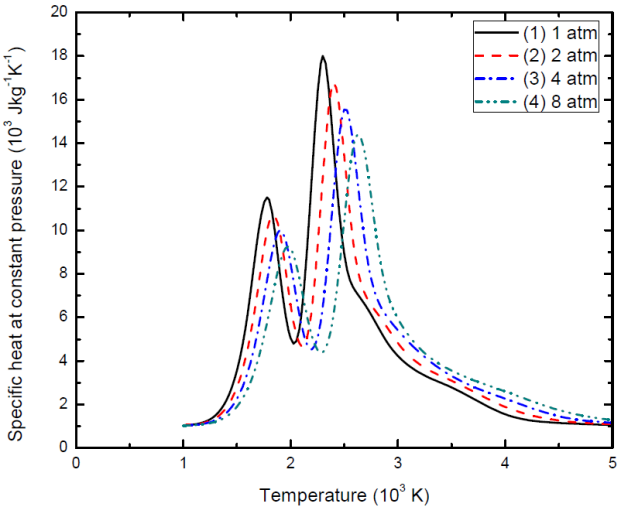

(b)

Figure A. 4. Specific heat at constant pressure (c_p) of SF_6 arc plasma as a function of temperature for pressure of 1, 2, 4 and 8 atm, reproduced from [A.6]. (a) Specific heat and (b) enlarged diagram of (a) in the temperature range of 0 to 5,000 K.

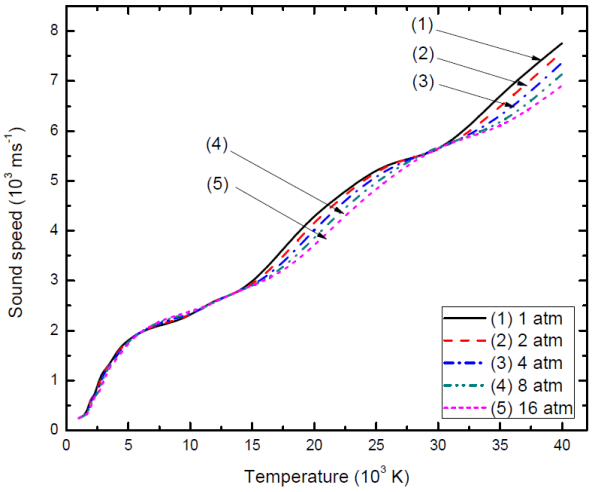

Figure A. 5. Sound speed (c) of SF_6 arc plasma as a function of temperature for pressure of 1, 2, 4, 8 and 16 atm, reproduced from [A.6].

A.4.2 Transport Properties

The transport properties characterize momentum transport (viscocity), energy transport (thermal conductivity) and charge transport (electrical conductivity). For LTE plasma, these transport properties are uniquely determined by two thermodynamic quantities (p and T). For SF_6, these transport properties are also tabulated by Frost and Liebermann [A.6] as a function of p and T. In graphic form, they are given in Figure A.6 for electrical conductivity, Figure A.7 for the viscosity and Figure A.8 for the thermal conductivity.

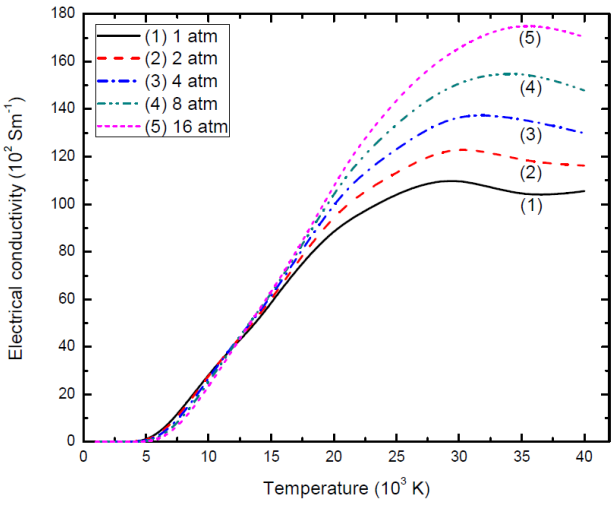

Figure A. 6. Electrical conductivity (σ) of SF_6 arc plasma as a function of temperature for pressure of 1, 2, 4, 8 and 16 atm, reproduced from [A.6]. (a) Electrical conductivity and (b) enlarged diagram of (a) in the temperature range of 0 to 20,000 K.

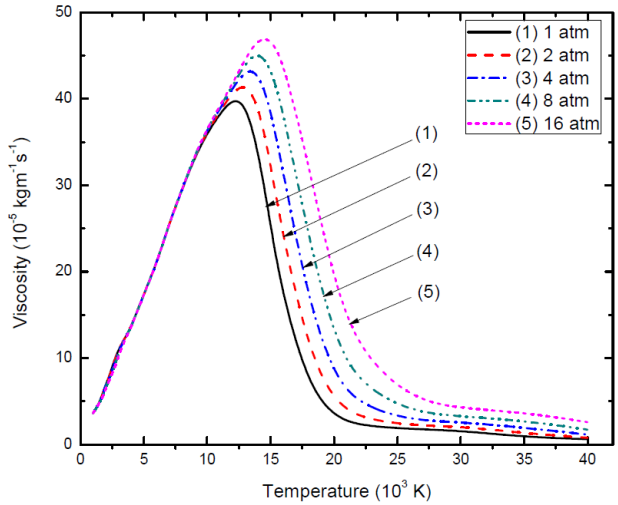

Figure A. 7. Molecular viscosity (μ) of SF_6 arc plasma as a function of temperature for pressure of 1, 2, 4, 8 and 16 atm, reproduced from [A.6].

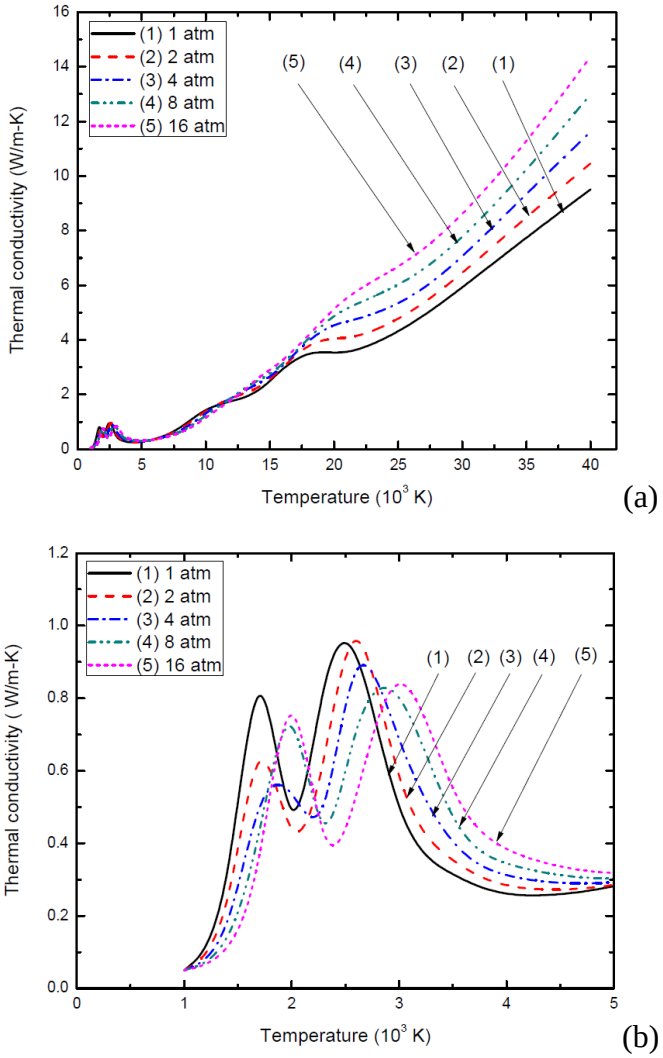

Figure A. 8. Thermal conductivity (k) of SF_6 arc plasma as a function of temperature for pressure of 1, 2, 4, 8 and 16 atm, reproduced from [A.6]. (a) Thermal conductivity and (b) enlarged diagram of (a) in the temperature range of 0 to 1,000 K.

A.5 Radiation Transfer

It has been confirmed by experimental observations that radiation is an important transport mechanism for high pressure and high temperature arcs [A.7, A.8]. However, radiation transfer in arc plasma is an extremely complex phenomenon.

The effects of radiation transport inside the arc plasma is represented by the net radiation loss (emission minus absorption) in the energy conservation equation (Equation (A.14)) which is related to the radiation flux vector (**F**) by [A.2]

$$q = \nabla \cdot \mathbf{F} \tag{A.20}$$

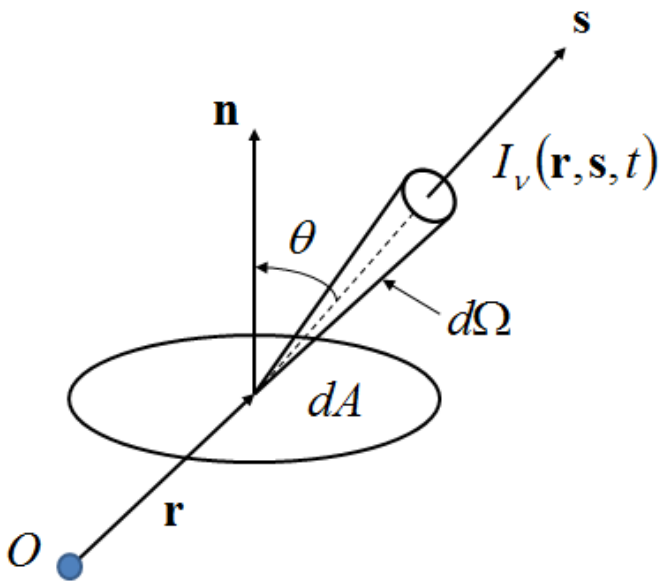

Figure A. 9. Definition of the monochromatic radiation intensity of the radiation field.

The radiation flux (**F**) at a position vector **r** can be calculated through the integration of monochromatic radiation intensity $I_\nu(\mathbf{r},\mathbf{s},t)$ (Figure A.9) over the emission spectra of of the arc and over the solid angle (Ω), which is given by

$$\mathbf{F} = \int_0^\infty \left[\int_0^{4\pi} I_\nu(\mathbf{r},\mathbf{s},t)\mathbf{s}\, d\Omega \right] d\nu \tag{A.21}$$

where **s** is the unit vector and ν the frequency of radiation. The monochromatic radiation intensity, $I_\nu(\mathbf{r},\mathbf{s},t)$, at a given frequency ν can be derived from the radiation transport equation given by

$$\mathbf{s}\cdot\nabla I_\nu(\mathbf{r},\mathbf{s},t) = \varepsilon_\nu - K'_\nu I_\nu(\mathbf{r},\mathbf{s},t) \tag{A.22}$$

where ε_ν is the volumetric emission coefficient and K'_ν the total spectral absorption coefficient at frequency ν taking into account of stimulated emission. For collision-dominated plasmas in LTE, K'_ν, can be expressed as

$$K'_\nu = K(\nu,T,P)\left[1-\exp\left(-\frac{h\nu}{kT}\right)\right] \tag{A.23}$$

where $K(\nu,T,P)$ is the true spectral absorption coefficient as a function of frequency, temperature and pressure [A.9]. For high pressure plasmas at LTE

emission can be calculated using

$$\varepsilon_\nu = K'_\nu B_\nu \tag{A.24}$$

where B_ν is the radiation intensity of black body which is given by

$$B_\nu(T) = \frac{2h\nu^3}{c^2}\frac{1}{\exp(h\nu/kT)-1} \tag{A.25}$$

Thus, in addition to the boundary condition, the solution of radiation transport equation (Equation (A.22)) needs the knowledge of K'_ν. For the plasma as a whole, the calculation of q requires the solution of radiation transport equation in three-dimension (3D) for the whole radiation spectrum and in the volume occupied by the arc. However, radiation transfer in an arc plasma is extremely complex which renders the above method of calculation net radiation loss impractical in terms of computational cost and the required time. This is because for SF_6 arc plasma we encounter the following difficulties:

(a) The radiation spectra of SF_6 span from infrared to vacuum ultra violet. The computation of the absorption coefficient at a given point in the arc and at a given frequency requires the computation of SF_6 composition at the local temperature and pressure. Such computation is very costly. The computation of the spectra absorption coefficient requires the photo absorption cross section over hundreds of lines, the basic spectra data of which is not complete. In addition, the variation of absorption coefficient in the vicinity of a line can change by 5 to 6 orders of magnitude. Thus, the accurate integration over frequency (Equation (A.21)) requires a very small frequency interval, which increases the computation cost enormously.

(b) Radiation transport within an SF_6 arc is dominated by hundreds of lines which are neither optically thick nor optically thin. Thus, radiation absorption is important within an SF_6 arc. The calculation of absorption is three dimensional.

Thus, an approximate method for radiation transport calculation must be found. Zhang et al. [A.10] have found that the use of the net emission coefficients derived at the arc axis by Liebermann and Lowke [A.9] for an infinitely long cylindrical wall

stabilized arc can be used to predict correctly the temperature of nozzle arcs. For such a wall stabilized arc, the 3D computation can be reduced to a 2D computation within a plane perpendicular to arc axis. The net emission coefficient on the axis for a wall stabilized arc with a top hat radial temperature profile can easily be calculated using

$$\varepsilon_N = \int_0^\infty B_\nu K'_\nu \exp(-K'_\nu R) d\nu \qquad \text{(A.26)}$$

where R is the tube radius. ε_N is a function of temperature (T), pressure (p) and tube radius (R), the typical results of which are given in Figure A.10(a).

This method is commonly known as the net emission coefficient (NEC) method. The NEC has also been calculated for air [A.11], nitrogen [A.12] and SF_6 arcs [A.9], etc. This method has been modified by Zhang et al [A.10] considering re-absorption of the radiative energy escaping from the high temperature arc core, which has achieved considerable success in predicting the behaviour of nitrogen [A.10] and SF_6 arcs [A.13, A.14].

With the rapid increase in computing power, more advanced methods for the radiaton modelling, for example the five band P1 model [A.15] and the method of partial characteristics [A.16], has become attractive. However, a comparative study of the aforementioned three radiation models for the prediction of SF_6 nozzle arc behaviour recently performed by Dixon et al. [A.17] shows that the method of Zhang et al. [A.10] generally gives the best performance. The modified method of Zhang et al. [A.10], which is virtually a one dimensional model, will therefore be applied to account for radiation transport in all the computations presented in this thesis. The procedure for the calculation of net radiation loss (q) with this one dimensional model is given below:

(a) Search the maximum temperature T_{max} (Figure A.10(b)), which is normally on the arc axis. Radiation will not be calculated if T_{max} is lower than 10,000 K.

(b) Search in the negative r-direction (from the cold gas surrounding the arc towards the arc axis) for the radial position where the temperature is 4000 K. The radius of this position corresponds to the edge of the arc column, which is therefore

known as the arc radius and is designated as *R*4*K* (Figure A.10(b)).

(c) Search in the negative r-direction for the radial position where the temperature is 83.3% of T_{max}. The region from the arc axis to this position (i.e. $0 \le r \le R833$) is defined as the arc core (Figure A.10(b)), and *R*833 therefore corresponds to the radius of the arc core edge. The region between the arc core edge and the edge of the arc column (i.e. $R833 \le r \le R4K$) is defined as the radiation re-absorption layer (Figure A.10(b)).

(d) The radiation radius (*R*) of the arc is defined as *R*=0.5(*R*833+*R*4*K*).

(e) The net radiation loss (q) at any point inside the arc core (q_e) is calculated using the NEC (Figure A.10 (a)) for a given radiation radius *R* (defined in (d)) and according to the local temperature and pressure at that point. The total amount of radiation emitted from the arc core, Q_e, is then calculated by integrating q_e over all emitting volumes for a unit length:

$$Q_e = \int_0^{R833} q_e 2\pi r dr \tag{A.27}$$

(f) In the radiation re-absorption region, the radiation coefficient (q_a) is assumed to have a radial profile given by

$$\frac{q_a(r)}{q_0} = 1.1 - \left(\frac{R_{4K} + R_{833} - 2r}{R_{4K} - R_{833}} \right)^2 \tag{A.28}$$

where

$$q_0 = \frac{Q_e \times PCT}{A_{eq}} \tag{A.29}$$

where *PCT* means the percentage of the total radiation emission from the arc core edge (Q_e) which are re-absorbed into the re-absorption layer. For SF_6 nozzle arcs *PCT* is assumed to be 80%, which is determined to achieve agreement between computed and measured temperature profile [A.14]. A_{eq} represents the equivalent radiation area for re-absorption region which is defined as

$$A_{eq} = \int_{R833}^{R4K} \left[1.1 - \left(\frac{R_{4K} + R_{833} - 2r}{R_{4K} - R_{833}} \right)^2 \right] \cdot 2\pi r dr \tag{A.30}$$

(g) Set q_e to be positive indicating the radiation emission and q_a to be negative

indicating radiation re-absorption. The net radiation loss is then $q=q_e$ in the arc core and $q=q_a$ in the radiation re-absorption layer (Figure A.10(b)).

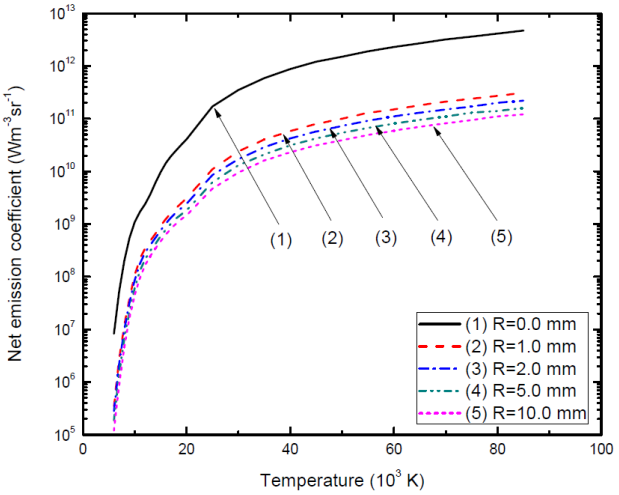

(a)

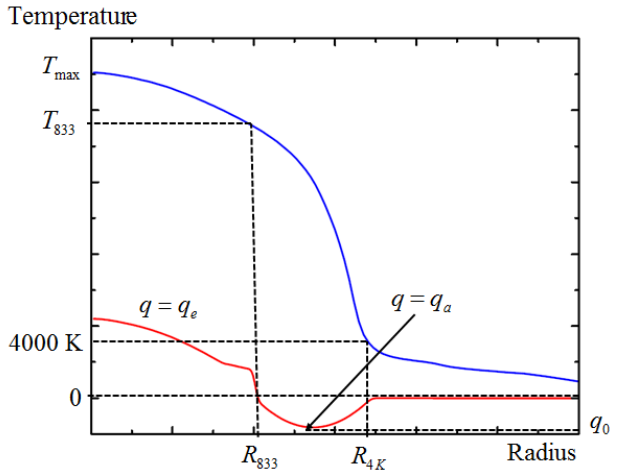

(b)

Figure A. 10. Calculation of net radiation. (a) NEC for SF_6 plasma of various radii at p=1 atm, reproduced from [30] and (b) Schematic diagram of the modified model of Zhang et al [A.10].

References

[A.1] Boulos M I, Fauchais P and Pfender E 1994 *Thermal Plasmas Fundamentals and Applications* (New York: Plenum Press)

[A.2] Fang M T C 2009 Xi'an Jiaotong Lecture Notes

[A.3] Schlichting H 1979 *Boundary Layer Theory* 7th edn. (New York: McGraw Hill)

[A.4] Anderson D A, Tannehill J C and Pletcher R H 1984 *Computational Fluid Mechanics and Heat Transfer* (New York: Hemisphere Publishing Corporation)

[A.5] Frie W 1967 Berechnung der Gaszusammensetzung und der Materialfunktionen *Z. Phys.* **201** 269-94

[A.6] Frost L S and Liebermann R W 1971 Composition and transport properties of SF_6 and their use in a simplified enthalpy flow arc model *Proc. IEEE.* **59** 474-85

[A.7] Ernst K A, Kopainsky J G and Maeher H H 1973 The energy transport, including emission and absorption, in N_2-arcs of different radii *IEEE Trans.* **PS-1**: 3

[A.8] Hermann W, Kogelschatz U, Ragaller K and Schade E 1974 Investigation of a cylindrical axially blown high-pressure arc *J. Phys. D: Appl. Phys.* **7** 1257

[A.9] Liebermann R W and Lowke J J 1976 Radiation emission coefficients for sulfur hexafluoride arc plasmas *J. Quant. Spectrosc. Radiat. Transf.* **17** 253-64

[A.10] Zhang J F, Fang M T C and Newland D B 1987 Theoretical investigation of a 2 kA arc in a supersonic nozzle *J. Phys. D: Appl. Phys.* **20** 368-79

[A.11] Lowke J J 1974 Prediction of arc temperature profiles using approximate emission coefficients for radiation losses *J. Quant. Spectrosc. Radiat. Transfer.* **14** 111-22

[A.12] Shayler P J and Fang M T C 1978 Radiation transport in wall stabilised nitrogen arcs *J. Phys. D: Appl. Phys.* **11** 1743

[A.13] Fang M T C, Zhuang Q and Guo X J 1994 Current zero behaviour of an SF_6 gas-blast arc Part II: turbulent flow *J. Phys. D: Appl. Phys.* **27** 74-83

[A.14] Yan J D, Nuttall K I and Fang M T C 1999 A comparative study of turbulence models for SF_6 arcs in a supersonic nozzle *J. Phys. D: Appl. Phys.* **32** 1401-6

[A.15] Eby S D, Trepanier J Y and Zhang X D 1998 Modelling radiative transfer in SF_6 circuit-breaker arcs with the P-1 approximation *J. Phys. D: Appl. Phys.* **31** 1578-88

[A.16] Aubrecht V and Lowke J J 1994 Calculations of radiation transfer in SF6 plasmas using method of partial characteristics *J. Phys. D: Appl. Phys.* **27** 2066-73

[A.17] Dixon C M, Yan J D and Fang M T C 2004 A comparison of three radiation models for the calculation of nozzle arcs *J. Phys. D: Appl. Phys.* **37** 3309-18

Appendix B
The Dependence of the RRRV on Stagnation Pressure

B.1 Introduction

It has been known that, for a given nozzle, the DC arc voltage is proportional to the square root of stagnation pressure (Section 4.3.2.2 of Chapter 4). However, the experimentally measured RRRV is approximately proportional to the square of stagnation pressure, which is much stronger than the pressure dependence of arc voltage. There appears, up to now, no satisfactory explanation for such pressure dependence of RRRV. Efforts have, therefore, been made to investigate further the factors which will affect the dependence of RRRV on pressure. Of the five flow models used in this thesis, the Prandtl mixing length model and the standard k-epsilon model give the best RRRV in comparison with the measured values. The results obtained by these two models will be used to investigate the effects of pressure on RRRV.

B.2 The Effects of Pressure Dependence of Electrical Conductivity

For DC nitrogen nozzle arc, the arc voltage computed with pressure dependent electrical conductivity is close to that computed with electrical conductivity fixed at 10 atm [B.1]. The computational results reported in this thesis are, therefore, obtained using SF_6 electrical conductivity at 8 atm. However, a careful examination of the dependence of electrical conductivity on pressure and temperature (Figures B.1(a) and B.1(b)) reveals two distinct regimes. That is, for temperature below approximately 12,000K, electrical conductivity reduces with increased pressure at a given temperature. This trend is reversed above 12,000K. In the low temperature

range, arc plasma is weakly ionized. Thus, electron collisions are dominated by electron-neutral collisions. The reduction in electrical conductivity at higher pressure is mainly due to the increase in neutral number density, which results in an increase of electron collision frequency. When the temperature is raised, the plasma density increases with gas pressure due to thermal ionization. However, when temperature is above 12,000K, electron collisions with neutrals gradually become less important than the collisions between electrons and ions. Electrical conductivity in this temperature range increases with plasma density (hence the gas pressure [B.2]).

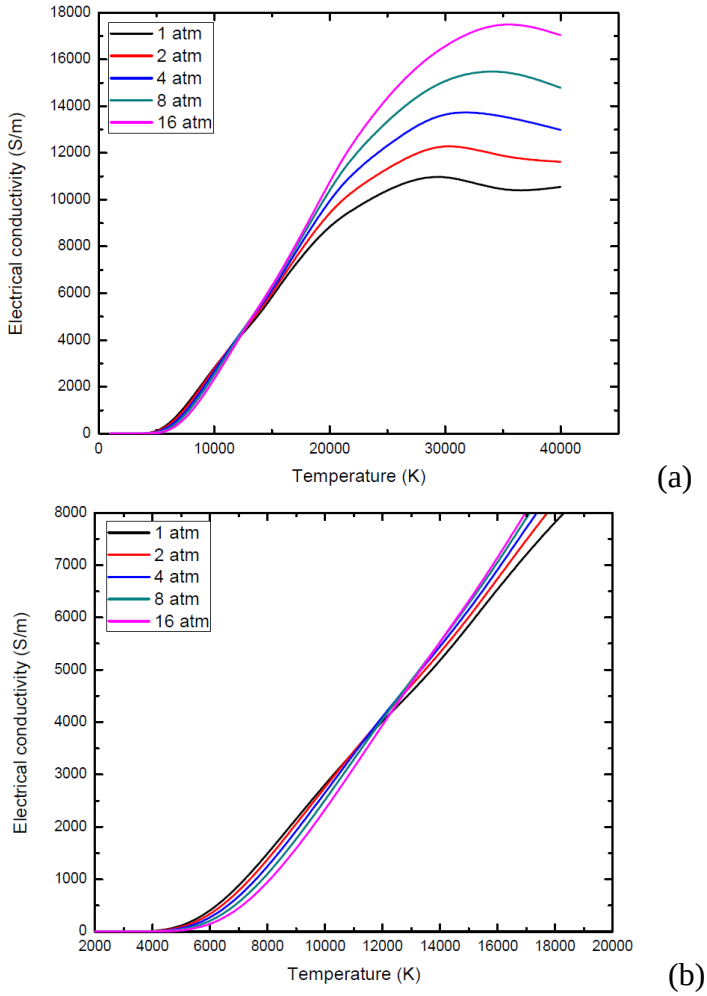

Figure B. 1. Electrical conductivity as a function of temperature at five pressures: 1, 2, 4, 8 and 16 atm. (a) Electrical conductivity and (b) enlarged diagram of Figure 5.27(a) within temperature range of 2,000K to 20,000 K.

Since the pressure effects on electrical conductivity are considerable, a computational study has been carried out using the Prandtl mixing length model and

the standard k-epsilon model with pressure dependent electrical conductivity. The qualitative features of the computational results are similar for the two turbulence models. We use the results obtained by the standard k-epsilon model to illustrate the influence of pressure dependent electrical conductivity on arc features and on the value of RRRV.

Figure B.2 shows a comparison of the computational results obtained by taking into account the pressure dependence of electrical conductivity (hereafter referred to as variable conductivity) and that by using the electrical conductivity fixed at 8 atm (referred to as the fixed conductivity for future reference) at the plateau of 1 kA DC for P_0 = 11.2 atm and di/dt= 25 $A\mu s^{-1}$. There are virtually no differences in axis temperature (Figure B.2(a), arc radius (Figure B.2(b)) and axis pressure (Figure B.2(c)). However, in comparison with fixed conductivity, electrical conductivity upstream of nozzle throat is higher while that downstream of throat is lower (Figure B.2(d)). This results in the axial electrical field distribution shown in Figure B.2(e). The difference in overall arc voltages is negligible as shown in Figure B.3, where the V-I characteristics for the variable conductivity and the fixed conductivity are plotted.

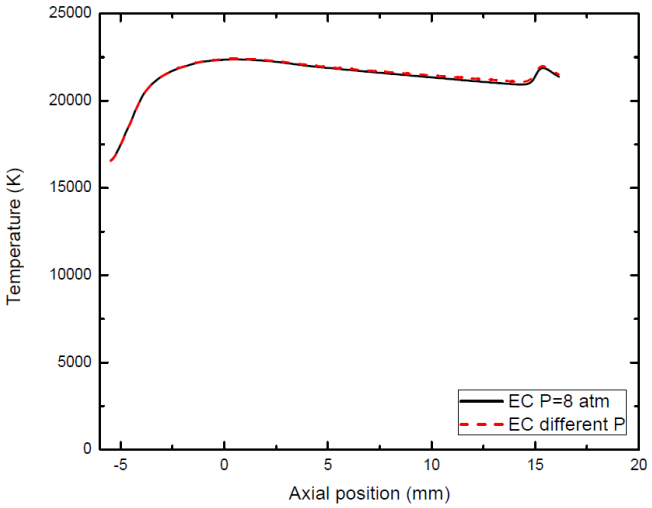

(a) of Figure B.2

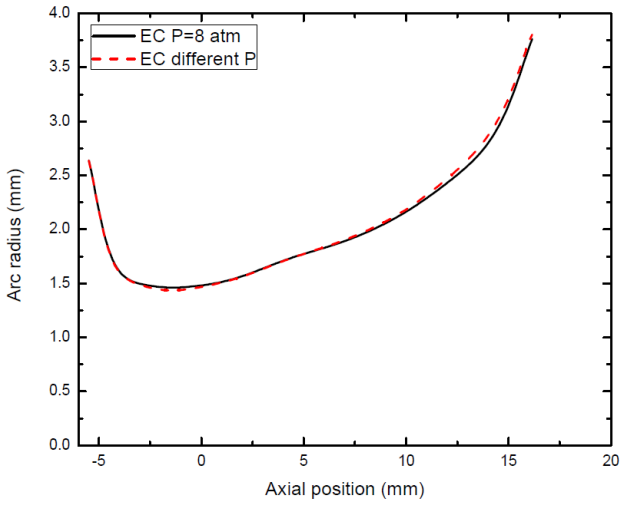

(b) of Figure B.2

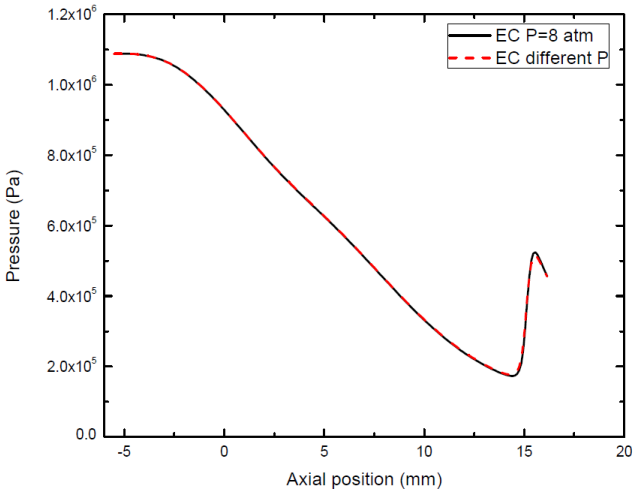

(c) of Figure B.2

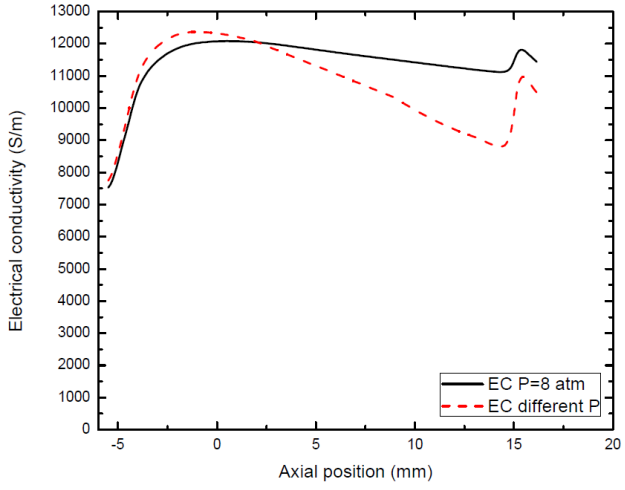

(d) of Figure B.2

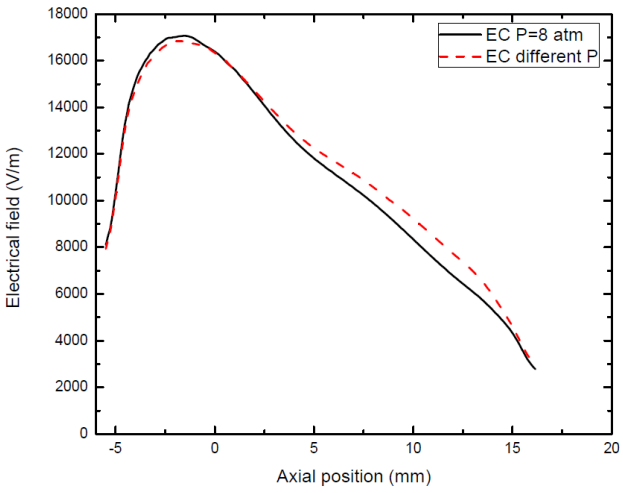

(e) of Figure B.2

Figure B. 2. Comparison of computational results on the arc axis obtained by taking into account variable conductivity (EC different P in the figure legend) and fixed conductivity (EC P=8 atm in the figure legend). The current is 1 kA DC and P_0=11.2 atm. The results are obtained by the standard k-epsilon model. (a) Axis temperature, (b) arc radius, (c) axis pressure, (d) axis electrical conductivity and (e) electrical field.

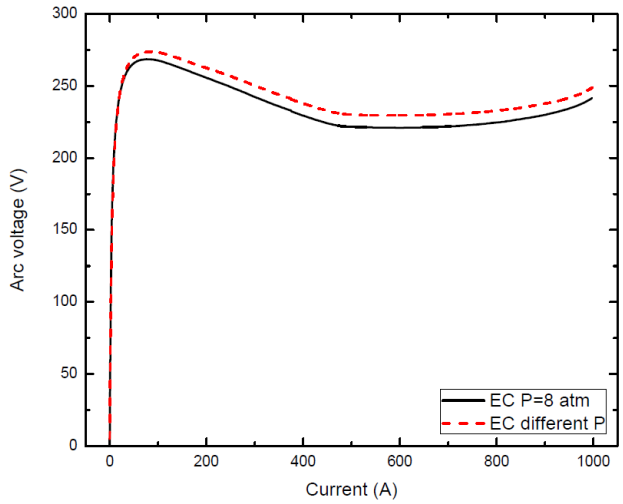

Figure B. 3. Comparison of V-I characteristics obtained by taking into account variable conductivity (EC different P in the figure legend) and fixed conductivity (EC P=8 atm in the figure legend). Results are obtained by the standard k-epsilon model. P_0=11.2 atm and di/dt=25 Aμs^{-1}.

When the current decays towards zero, the effects of variable conductivity on arc characteristics are accumulated. However, the axis temperature, arc radius and axis pressure for variable and fixed conductivities at 0.05 μs before current zero are remarkably close to each other (Figure B.4). In the low pressure region, electrical conductivity for the variable conductivity is higher than that of fixed conductivity

(Figure B.4(d)), which results in a lower electrical field in this region (Figure B.4(e)). The arc voltage for variable conductivity at this instant (67.1 V) is about 12% lower than that of fixed conductivity (76.3 V). RRRV for the variable conductivity (1.45 $kV\mu s^{-1}$) is lower than that of fixed conductivity (1.65 $kV\mu s^{-1}$) by a similar percentage.

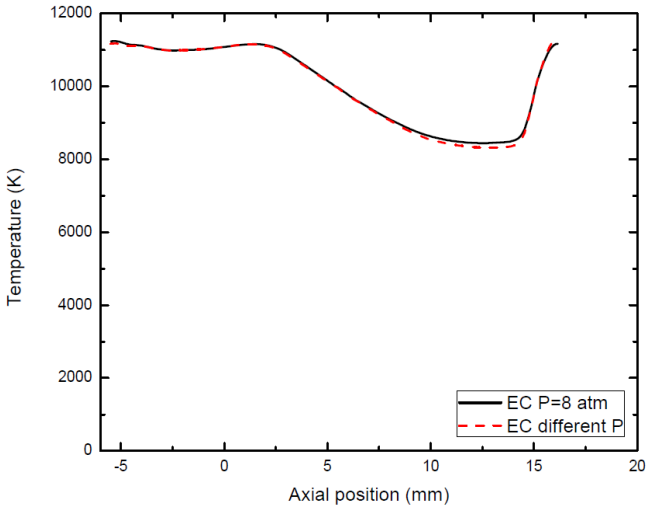

(a) of Figure B.4

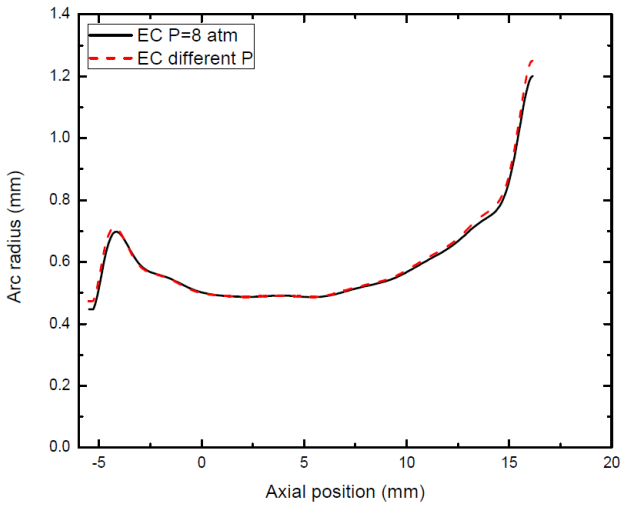

(b) of Figure B.4

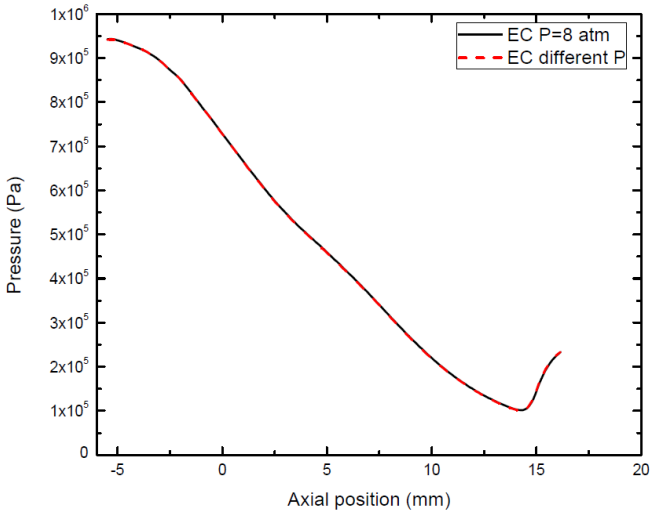

(c) of Figure B.4

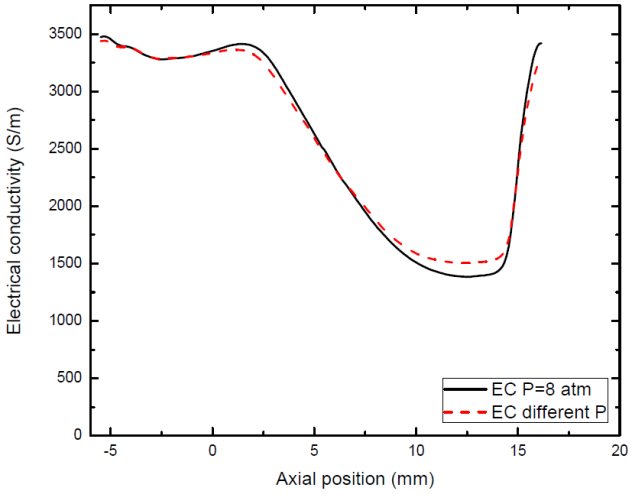

(d) of Figure B.4

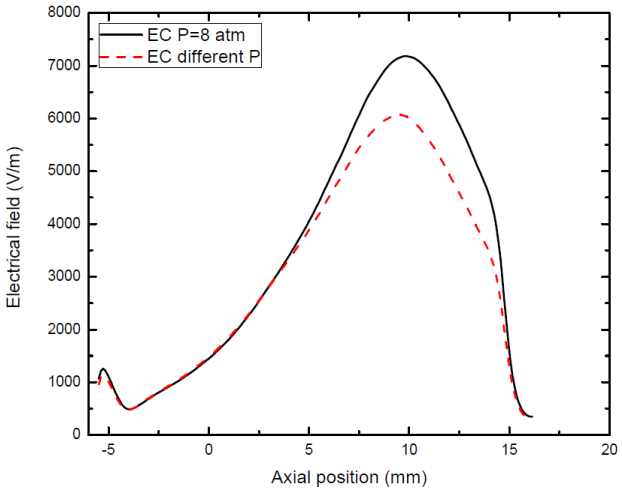

(e) of Figure B.4

Figure B. 4. Comparison of computational results on the arc axis obtained by taking into account variable conductivity (EC different P in the figure legend) and fixed conductivity (EC P=8 atm in the figure legend). The current is 1.25 A corresponding to the instant of 0.05μs before current zero. P_0=11.2 atm and di/dt=25 Aμs^{-1}. The results are obtained by the standard k-epsilon model. (a) Axis temperature, (b) arc radius, (c) axis pressure, (d) axis electrical conductivity and (e) electrical field.

Similar results to those of the standard k-epsilon model have been obtained for the Prandtl mixing length model with the results summarized in Figure B.5 (Similar to Figure B.3). The differences in RRRV predicted by the Prandtl mixing length model for variable and fixed conductivities is about 15% (RRRV considering fixed conductivity=1.15 kVμs^{-1} and RRRV considering variable conductivity=1.0 kVμs^{-1}).

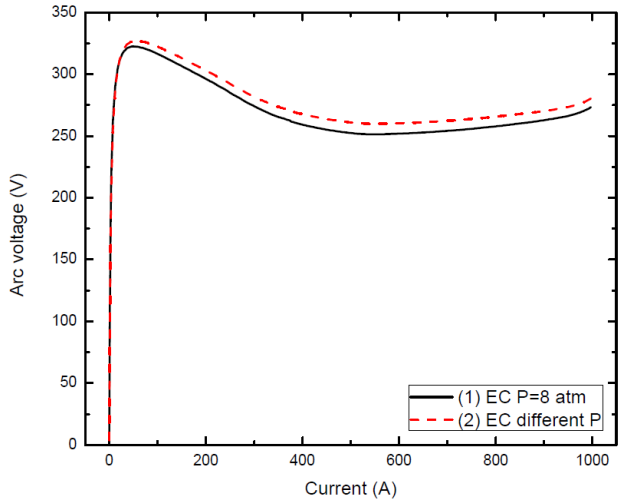

Figure B. 5. Comparison of V-I characteristics obtained by taking into account variable conductivity (EC different P in the figure legend) and fixed conductivity (EC P=8 atm in the figure legend). Results are obtained by the Prandtl mixing length model. P_0=11.2 atm and di/dt=25 Aμs^{-1}.

The differences in RRRV predicted by the two turbulence models for variable and fixed conductivities are well within the experimental scatter of the measured RRRV. Thus, variable electrical conductivity will not alter the pressure dependence of RRRV as predicted by the two turbulence models (Section 5.3).

B.3 The Effects of Nonlinear System Dynamics on the Pressure Dependence of RRRV

The governing equations which determine the dynamic behaviour of a turbulent arc during current zero period are highly nonlinear. The temperature and velocity fields, electrical field and turbulent effects are closely coupled through the nonlinear transport properties, radiation characteristics and eddy viscosity. Before current zero

the arc is highly transient. The state of the arc at current zero depends on the arcing history after the breakdown of quasi-steady state. It is, therefore, very difficult to identify a particular physical process to be associated with the influence of stagnation pressure. Nonetheless, attempts will be made to examine the computational results at P_0 =21.4 atm and 11.2 atm, and, at dt/dt= 13 $A\mu s^{-1}$, in the hope that certain arc features can be identified with a change in stagnation pressure, hence the causes of pressure dependence of RRRV.

For DC nozzle arcs, the arc cross section is inversely proportional to the square root of stagnation pressure (as indicated in Section 4.3.2.5 of Chapter 4). Since the arc is smaller at higher stagnation pressure (Chapter 4), it is expected that a nozzle arc at higher stagnation pressure will be able to maintain quasi-steady state longer than that of an arc at a lower stagnation pressure for the same di/dt. When a nozzle arc at a lower stagnation pressure departs from quasi-steady state, the arc at a higher stagnation pressure would still be able to maintain quasi-steady state for the same di/dt. Thus, the voltage ratio of the two arcs would be higher than the square root of the pressure ratio. This implies that the pressure dependence of RRRV for a given di/dt would be stronger than the square root of pressure. However, the results shown in Figure B.6 indicate that the voltage ratio from 1 kA to 5 A, defined as the arc voltage at 21.4 atm divided by that at 11.2 atm, is only about 10% higher than the square root of the pressure ratio. This cannot explain the pressure dependence of RRRV of the experimental results and those predicted by the two turbulence models (Table 5.8 in Section 5.3 of Chapter 5).

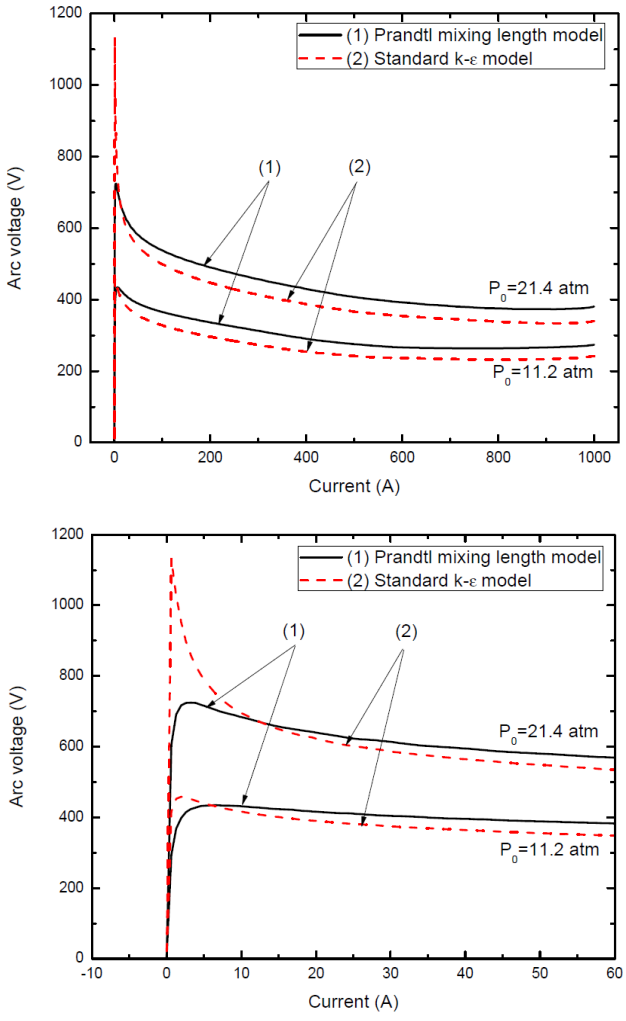

Figure B. 6. The voltage-current (V-I) characteristics for the nozzle arcs computed by the Prandtl mixing length model and the standard k-epsilon model corresponding to the current ramp. P_0= 11.2 atm and 21.4 atm, and, di/dt=13 Aμs^{-1}. (a) V-I characteristics and (b) enlarged V-I characteristics in the last 5 μs before current zero.

As noted in Section 4.3.2.1 of Chapter 4, the arc thermal influence region is less than 8% of the nozzle cross section area at 1 kA DC and at 11.2 atm, and this percentage is even lower for 21.4 atm. The pressure imposed on the arc outside the thermal influence region is the same as that in the absence of the arc. This pressure distribution will not be affected when the current decays from 1 kA DC to current zero. When current is reduced from 600 A to current zero, axis temperature drops on average over the arc length by 13,000K (Figure B.7) for the two turbulence models and at two stagnation pressures. Such a large drop in axis temperature only results in a decrease in axis pressure of less than 5% (Figure B.8). Such a small drop in

pressure is sufficient to generate a radial inward flow to supply the mass in the arc region required by the decreasing arc temperature.

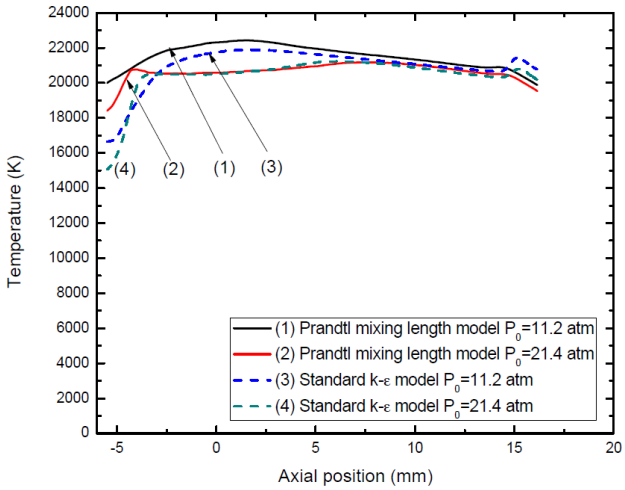

(a)

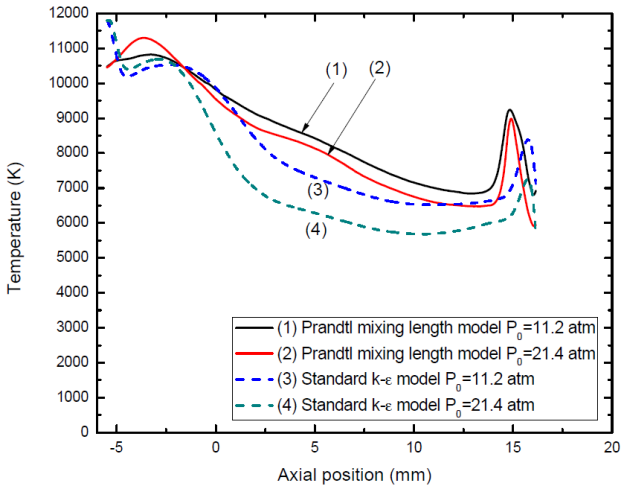

(b)

Figure B. 7. Variation of axis temperature at different instants (different currents) before current zero and at current zero. Results are obtained by the Prandtl mixing length model and the standard k-epsilon model. P_0= 11.2 atm and 21.4 atm, and, di/dt=13 Aμs^{-1}. (a) 600 A and (b) current zero.

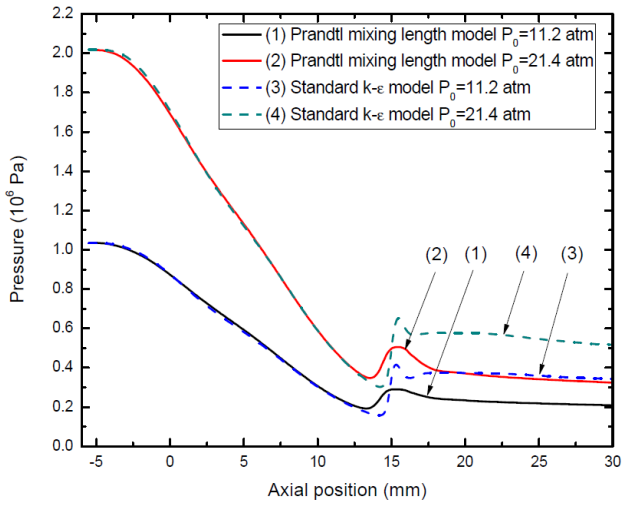

(a)

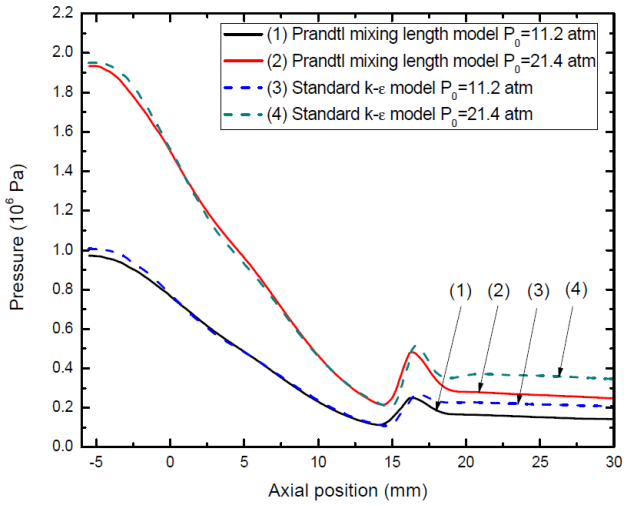

(b)

Figure B. 8. Variation of axis pressure at different instants (different currents) before current zero and at current zero. Results are obtained by the Prandtl mixing length model and the standard k-epsilon model. P_0= 11.2 atm and 21.4 atm, and, di/dt=13 $A\mu s^{-1}$. (a) 600 A and (b) current zero.

The qualitative features of the radial temperature profiles calculated by the two turbulence models when the current decays towards zero at Z=2.3 mm (Figure B.9) and 7.9 mm (Figure B.10) are similar to those of DC arc. However, the instant radial profiles of radial velocity *v* are the most complex. For example, at Z=7.9 mm there is an outward radial flow at an instant current of 600 A (Figure B.11(a)). The speed of this outflow reduces when current is decreased (Figure B.11(b) at 200A instant). In order to maintain instant mass balance the outward flow region around the axis of the arc shrinks when temperature in this region decreases with current. An inward flow is developed at the electrical boundary at 50A (Figure B.11(c)). Rapid temperature

decay in the last 1 μs before current zero within the electrically conducting core (Figures B.10(e) and B.10(f)) requires a radially inward flow to main mass balance as shown in Figures B.11(e) and B.11(f). Accompanied with this change of radial flow pattern, radial enthalpy convection assumes an increasingly important role as an energy removal mechanism especially at high stagnation pressure when current decays towards zero. This is clearly shown in the arc energy balance calculation in Tables B.1 (for P_0=21.4 atm) and B.2 (for P_0=11.2 atm).

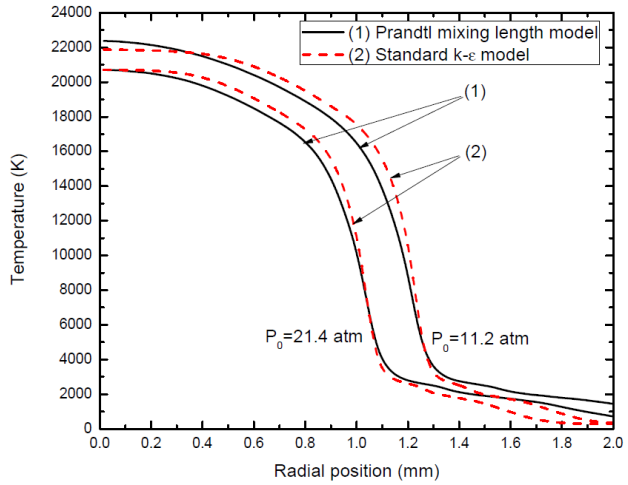

(a) of Figure B.9

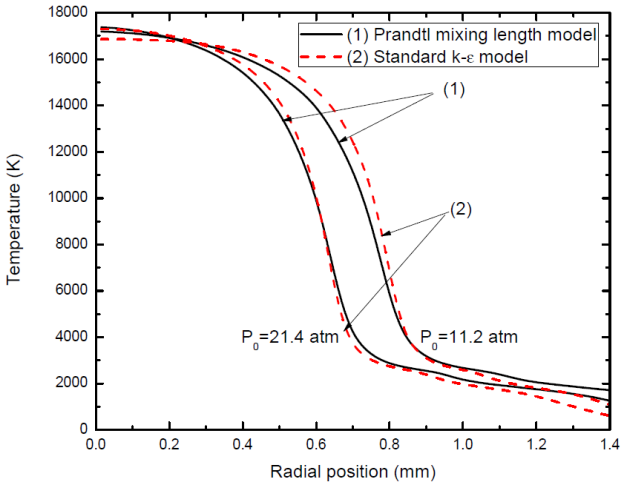

(b) of Figure B.9

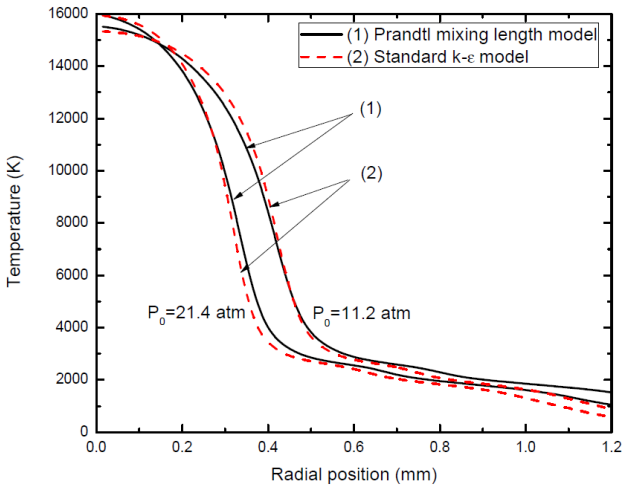

(c) of Figure B.9

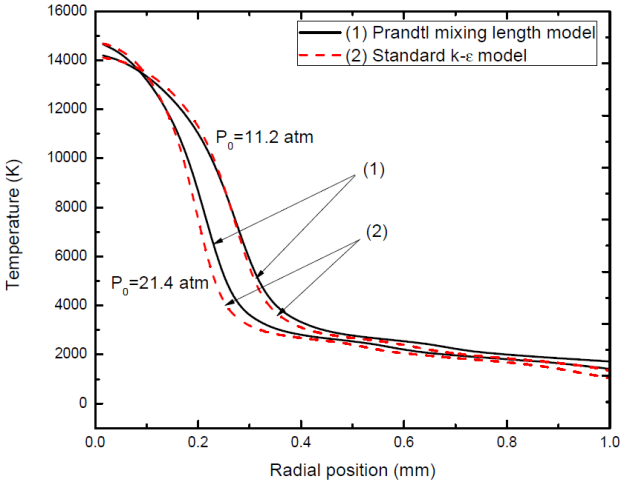

(d) of Figure B.9

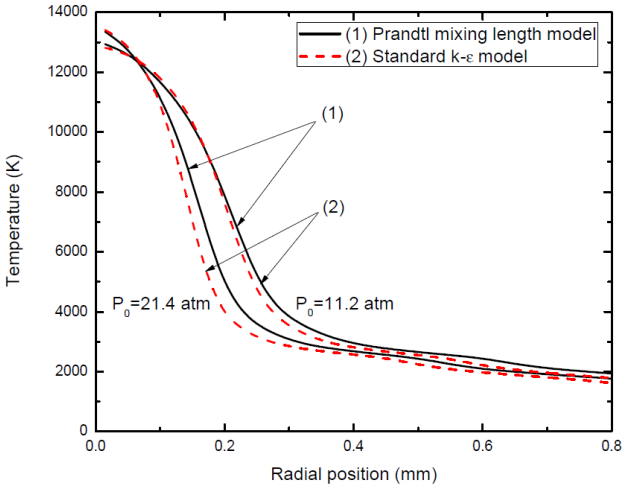

(e) of Figure B.9

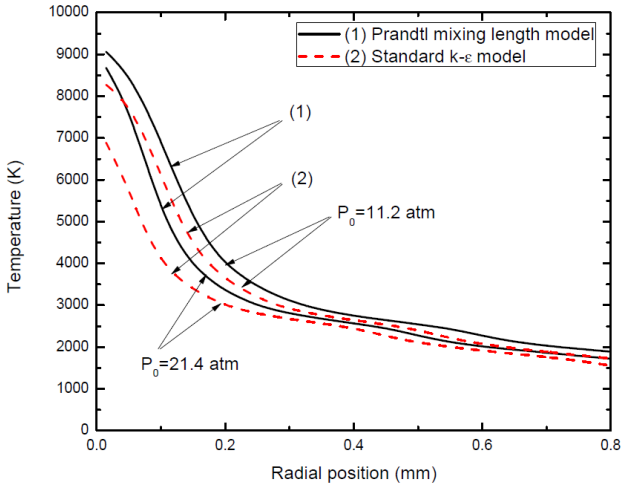

(f) of Figure B.9

Figure B. 9. Radial temperature profiles at different instants (different currents) before current zero and at current zero for Z=2.3 mm. Results obtained by the Prandtl mixing length model and the standard k-epsilon model. P_0= 11.2 atm and 21.4 atm, and, di/dt=13 Aμs^{-1}. (a) 600 A, (b) 200 A, (c) 50 A, (d) 20 A, (e) 10 A and (f) current zero.

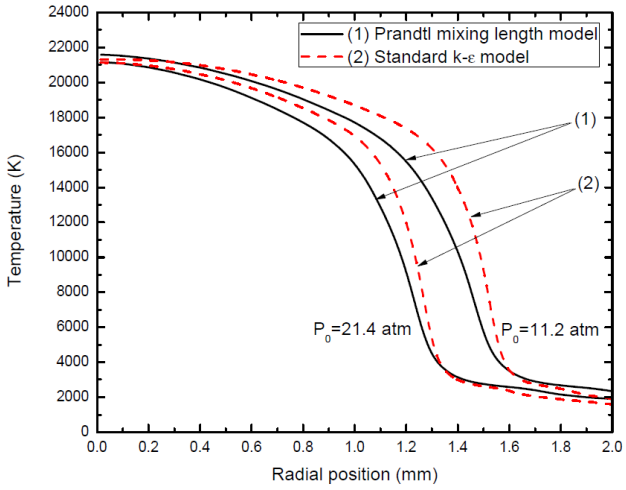

(a) of Figure B.10

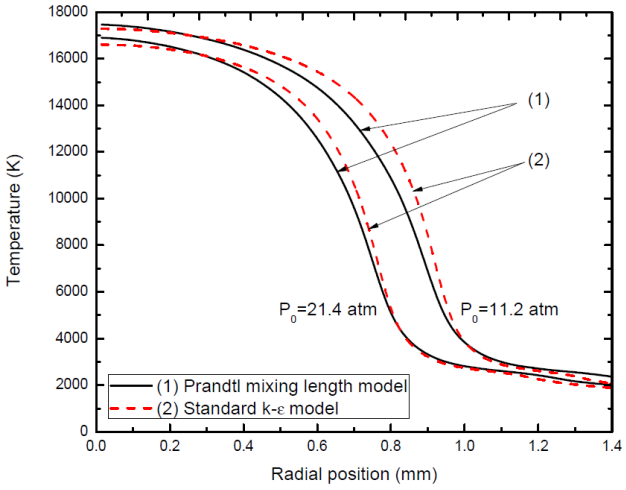

(b) of Figure B.10

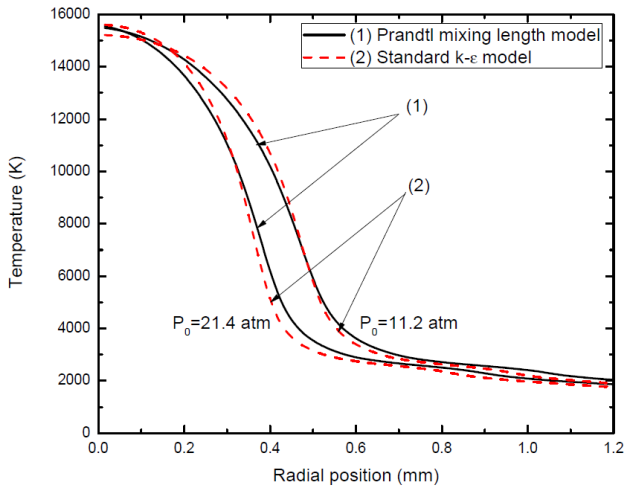

(c) of Figure B.10

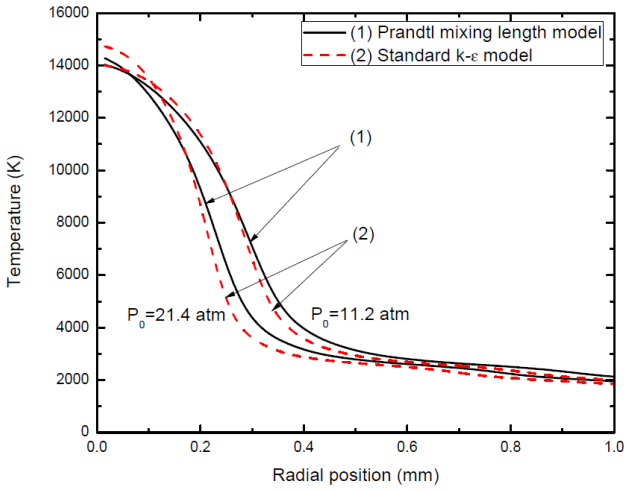

(d) of Figure B.10

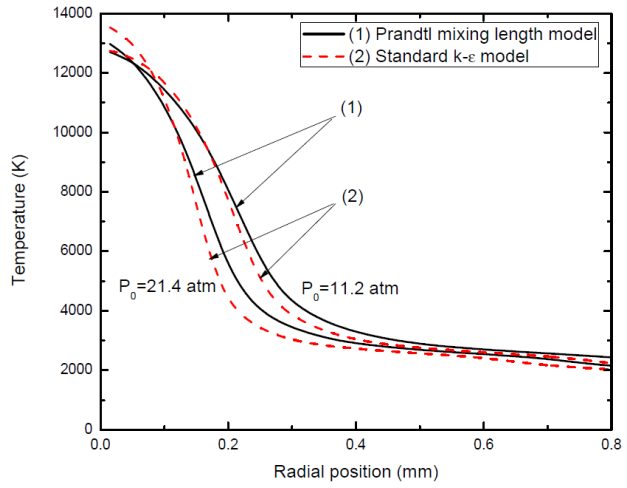

(e) of Figure B.10

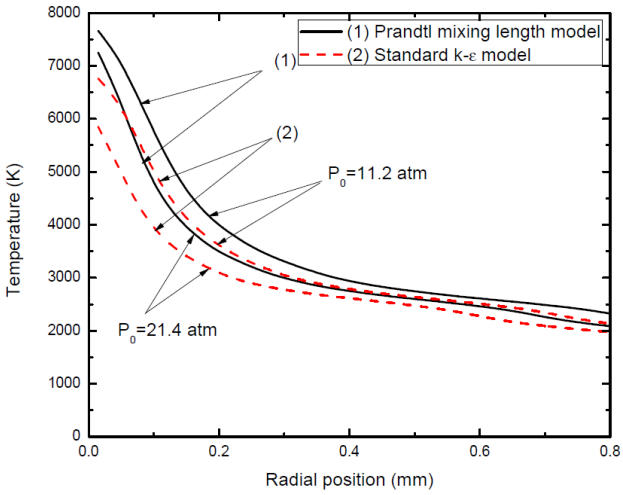

(f) of Figure B.10

Figure B. 10. Radial temperature profiles at different instants (different currents) before current zero and at current zero for Z=7.9 mm. Results obtained are by the Prandtl mixing length model and the standard k-epsilon model. P_0= 11.2 atm and 21.4 atm, and, di/dt=13 Aμs^{-1}. (a) 600 A, (b) 200 A, (c) 50 A, (d) 20 A, (e) 10 A and (f) current zero.

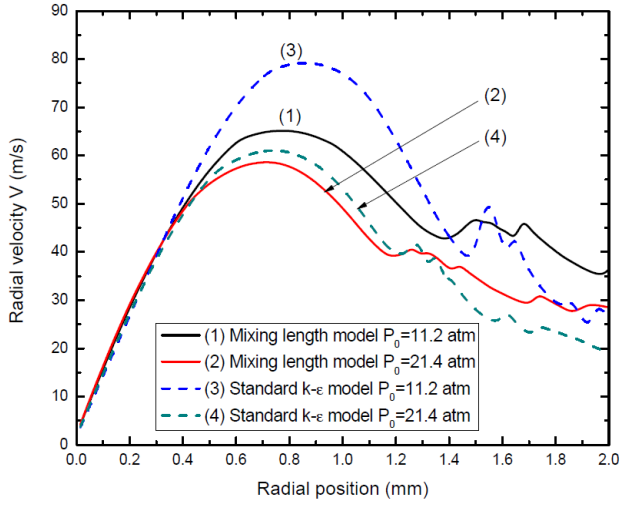

(a) of Figure B.11

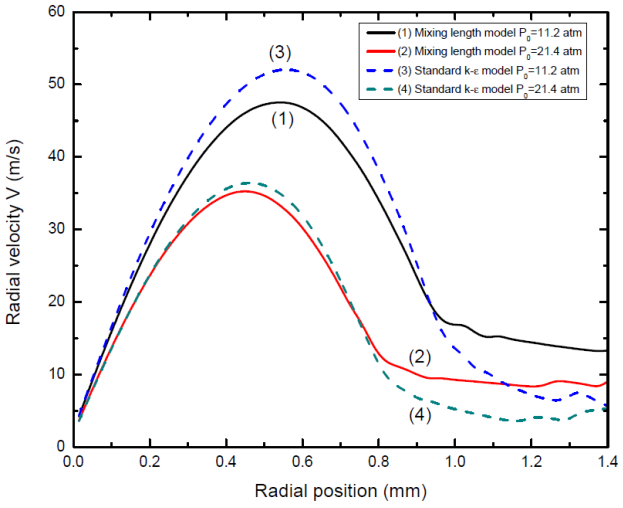

(b) of Figure B.11

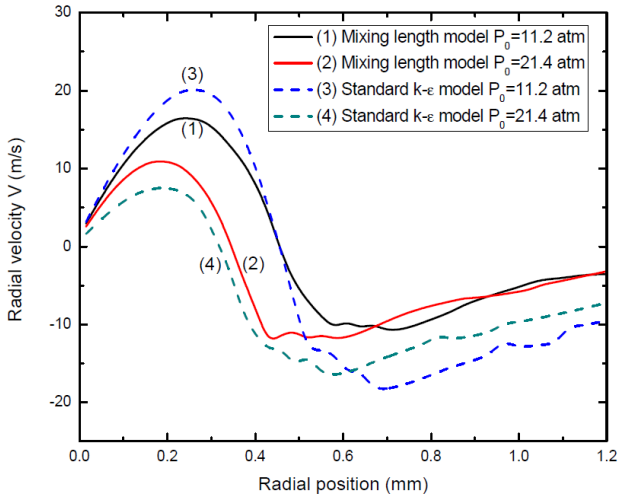

(c) of Figure B.11

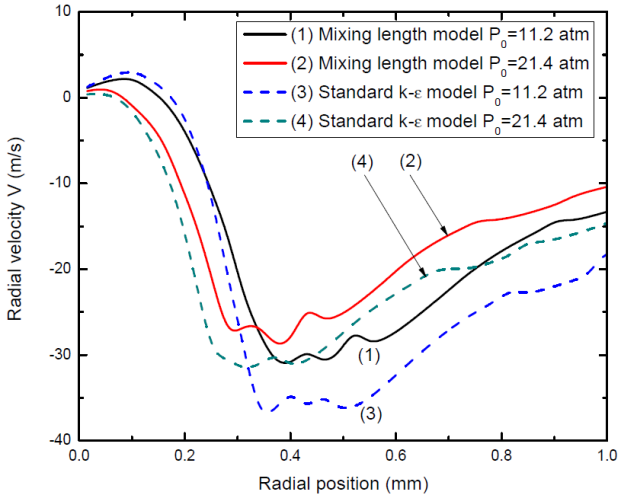

(d) of Figure B.11

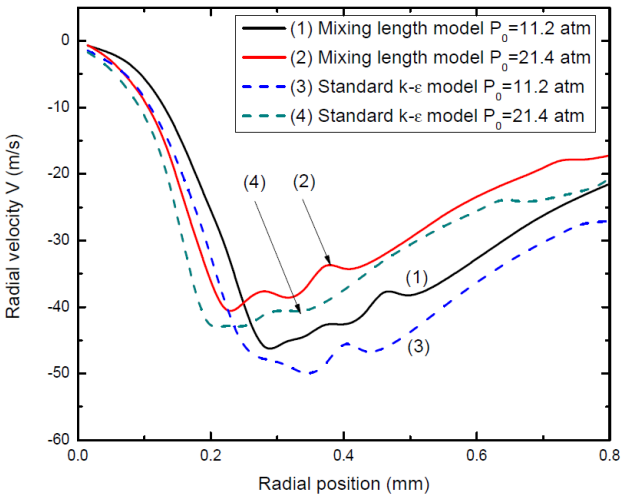

(e) of Figure B.11

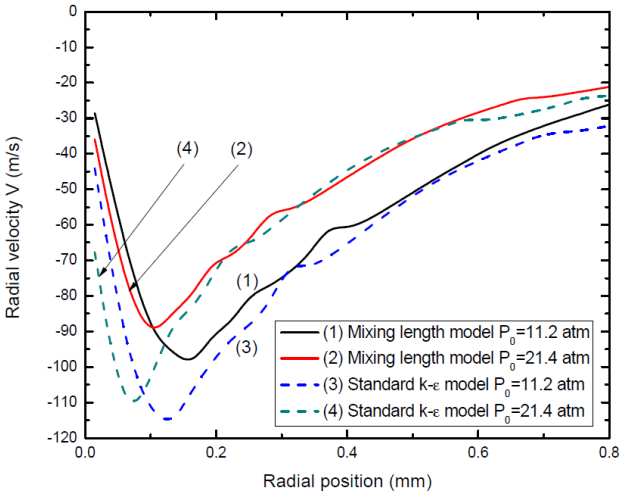

(f) of Figure B.11

Figure B. 11. Radial profiles of radial velocity *v* at different instants (different currents) before current zero and at current zero for Z=7.9 mm. Results are obtained by the Prandtl mixing length model and the standard k-epsilon model. P_0= 11.2 atm and 21.4 atm, and, di/dt=13 Aμs^{-1}. (a) 600 A, (b) 200 A, (c) 50 A, (d) 20 A, (e) 10 A and (f) current zero.

When current is reduced from 1 kA plateau to current zero, turbulence enhanced radial thermal conduction predicted by the Prandtl mixing length model is always stronger than that by the standard k-epsilon model (Tables B.1 and B.2). This explains why V-I characteristics for the Prandtl mixing length model is always above that for the standard k-epsilon model (Figure B.6(a)). However, such a trend is reversed in the interval starting approximately 1 μs before current zero (Figure B.6(b)) during which the temperature decay and the contraction of electrically conducting region for the standard k-epsilon model are much faster than those for the Prandtl mixing length model.

Table B. 1. Electrical power input together with various energy transport processes for the whole arc length at the electrical boundary (4000 K isotherm) at different instants (different currents) before current zero and at current zero. Results are obtained by the Prandtl mixing length model and the standard k-epsilon model. P_0=21.4 atm and di/dt=13 A/μs. Mathematical expressions for power input and power loss are the same as those in Table 5.1 of Chapter 5.

Model	Power input (W)	Radiation loss (W)	Radial thermal conduction (W)	Axial enthalpy convection (W)	Radial enthalpy convection (W)	Rate of change of energy storage (W)
600 A instant						
(1)	2.336×10^{5}	-3.504×10^{4}	-1.510×10^{5}	-8.327×10^{4}	2.467×10^{4}	-2.463×10^{4}
(2)	2.112×10^{5}	-4.894×10^{4}	-9.714×10^{4}	-1.107×10^{5}	3.240×10^{4}	-2.774×10^{4}
200 A instant						
(1)	9.816×10^{4}	-2.644×10^{4}	-6.852×10^{4}	-1.823×10^{4}	2.977×10^{3}	-1.769×10^{4}
(2)	8.971×10^{4}	-3.155×10^{4}	-5.366×10^{4}	-2.079×10^{4}	1.107×10^{3}	-2.090×10^{4}
50 A instant						
(1)	2.993×10^{4}	-7.128×10^{3}	-2.811×10^{4}	-4.799×10^{3}	-3.330×10^{3}	-1.503×10^{4}
(2)	2.829×10^{4}	-8.608×10^{3}	-2.509×10^{4}	-3.496×10^{3}	-5.801×10^{3}	-1.634×10^{4}
20 A instant						
(1)	1.244×10^{4}	-2.269×10^{3}	-1.624×10^{4}	-1.828×10^{3}	-4.482×10^{3}	-1.317×10^{4}
(2)	1.215×10^{4}	-2.758×10^{3}	-1.563×10^{4}	-1.180×10^{3}	-6.614×10^{3}	-1.485×10^{4}
10 A instant						
(1)	6.643×10^{3}	-9.574×10^{2}	-1.177×10^{4}	-1.213×10^{3}	-5.011×10^{3}	-1.285×10^{4}
(2)	6.778×10^{3}	-1.203×10^{3}	-1.176×10^{4}	-7.388×10^{2}	-6.587×10^{3}	-1.408×10^{4}
5 A instant						
(1)	3.692×10^{3}	-5.454×10^{2}	-9.259×10^{3}	-9.382×10^{2}	-4.912×10^{3}	-1.232×10^{4}
(2)	4.059×10^{3}	-7.046×10^{2}	-9.295×10^{3}	-5.204×10^{2}	-6.252×10^{3}	-1.314×10^{4}
Current zero						
(1)	0.0	-1.788×10^{2}	-5.663×10^{3}	-6.229×10^{2}	-4.105×10^{3}	-1.078×10^{4}
(2)	0.0	-3.523×10^{2}	-5.429×10^{3}	-4.298×10^{2}	-4.991×10^{3}	-1.157×10^{4}
Key of the models: (1) Prandtl mixing length model and (2) Standard k-epsilon model						

Table B. 2. Electrical power input together with various energy transport processes for the whole arc length at the electrical boundary (4000 K isotherm) at different instants (different currents) before current zero and at current zero. Results are obtained by the Prandtl mixing length model and the standard k-epsilon model. P_0=11.2 atm and di/dt=13 A/μs. Mathematical expressions for power input and power loss are the same as those in Table 5.1 of Chapter 5.

Model	Power input (W)	Radiation loss (W)	Radial thermal conduction (W)	Axial enthalpy convection (W)	Radial enthalpy convection (W)	Rate of change of energy storage (W)
600 A instant						
(1)	1.583×10^{5}	-1.656×10^{4}	-1.043×10^{5}	-6.954×10^{4}	2.309×10^{4}	-1.782×10^{4}
(2)	1.408×10^{5}	-2.603×10^{4}	-5.936×10^{4}	-9.654×10^{4}	3.009×10^{4}	-2.095×10^{4}
200 A instant						
(1)	6.716×10^{4}	-1.645×10^{4}	-4.736×10^{4}	-1.716×10^{4}	3.848×10^{3}	-1.354×10^{4}
(2)	5.931×10^{4}	-1.991×10^{4}	-3.331×10^{4}	-2.082×10^{4}	3.396×10^{3}	-1.572×10^{4}
50 A instant						
(1)	2.004×10^{4}	-4.802×10^{3}	-1.897×10^{4}	-3.842×10^{3}	-1.835×10^{3}	-1.069×10^{4}
(2)	1.836×10^{4}	-5.763×10^{3}	-1.628×10^{4}	-3.919×10^{3}	-3.540×10^{3}	-1.253×10^{4}
20 A instant						
(1)	8.083×10^{3}	-1.576×10^{3}	-1.090×10^{4}	-1.697×10^{3}	-3.012×10^{3}	-9.732×10^{3}
(2)	7.603×10^{3}	-1.892×10^{3}	-1.017×10^{4}	-1.362×10^{3}	-4.351×10^{3}	-1.082×10^{4}
10 A instant						
(1)	4.190×10^{3}	-8.679×10^{2}	-7.961×10^{3}	-1.083×10^{3}	-3.324×10^{3}	-9.408×10^{3}
(2)	4.060×10^{3}	-9.411×10^{2}	-7.686×10^{3}	-7.745×10^{2}	-4.285×10^{3}	-1.011×10^{4}
5 A instant						
(1)	2.241×10^{3}	-4.160×10^{2}	-6.343×10^{3}	-8.253×10^{2}	-3.232×10^{3}	-8.927×10^{3}
(2)	2.276×10^{3}	-5.449×10^{2}	-6.257×10^{3}	-5.724×10^{2}	-4.249×10^{3}	-9.725×10^{3}
Current zero						
(1)	0.0	-1.381×10^{2}	-4.161×10^{3}	-5.318×10^{2}	-2.807×10^{3}	-7.843×10^{3}
(2)	0.0	-2.513×10^{2}	-3.939×10^{3}	-3.965×10^{2}	-3.622×10^{3}	-8.462×10^{3}
Key of the models: (1) Prandtl mixing length model and (2) Standard k-epsilon model						

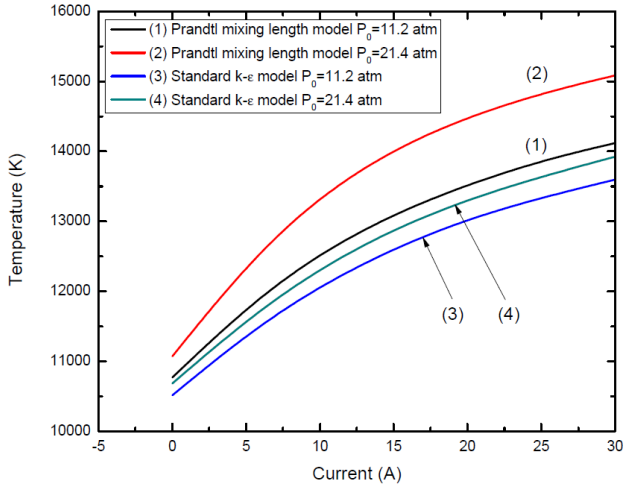

Figure B. 12. Variation of temperature on the arc axis as a function of current (instant) shortly before current zero for three axial positions. Results are obtained by the Prandtl mixing length model and the standard k-epsilon model. P_0= 11.2 atm and 21.4 atm, and, di/dt=13 $A\mu s^{-1}$. (a) Z=-2.6mm, upstream of nozzle throat, (b) Z=2,3mm, middle section of parallel nozzle throat region and (c) Z=7.9mm in downstream region of nozzle throat.

The rates of temperature decay in three typical regions of the nozzle arc (Figure B.12) start to increase rapidly towards current zero approximately 1 μs before current zero. The accelerated temperature decay is the result of the combined effects of turbulence enhanced thermal conduction and the cooling by the cold gas brought in by the radial inflow. Within the parallel throat region and the region downstream of the nozzle throat axis temperature is in the region of 9,000K to 6,000K for the two turbulence models and for the two stagnation pressures investigated (Figures B.7 and B.12). In this temperature range, electron density varies with temperature exponentially as given by Saha's equation for thermal ionization. Thus, associated with the rapid decay of temperature the arc resistance increases rapidly before current zero (Figure B.13). At di/dt= 13Aμs^{-1}, arc resistance ratio at current zero, which is defined as arc resistance at 21.4 atm divided by that at 11.2 atm (i.e. $R_{21.4atm} / R_{11.2atm}$), is approximately 1.95 for the Prandtl mixing length model and 2.71 for the standard k-epsilon model. These ratios are close to the pressure dependence of RRRV predicted by the two turbulence models (Table 5.8 in Section 5.3 of Chapter 5). Since arc resistance at current zero determines the post arc current, pressure scaling of RRRV according to resistance ratio at current zero appears reasonable.

The analysis of computational results shows that the pressure dependence of RRRV greater than the square root of stagnation pressure is the consequence of accelerated temperature decay rate approximately 1μs before current zero. Turbulence enhanced thermal conduction and radial cooling are the two dominant energy transport mechanisms. This is of course the accumulated effects of the non-linear interaction between turbulent fluctuation, temperature, velocity and electrical fields from the breakdown of quasi-steady state to current zero. It is not possible to derive analytically a simple expression for RRRV as all processes are strongly coupled. However, radial enthalpy transport associated with increasingly strong radial inflow just before current zero plays a critical role in determining the temperature decay rate and the speed of contraction of the arc conducting core. The rapid rise of arc resistance just before current zero makes RRRV approximately

proportional to the square of stagnation pressure.

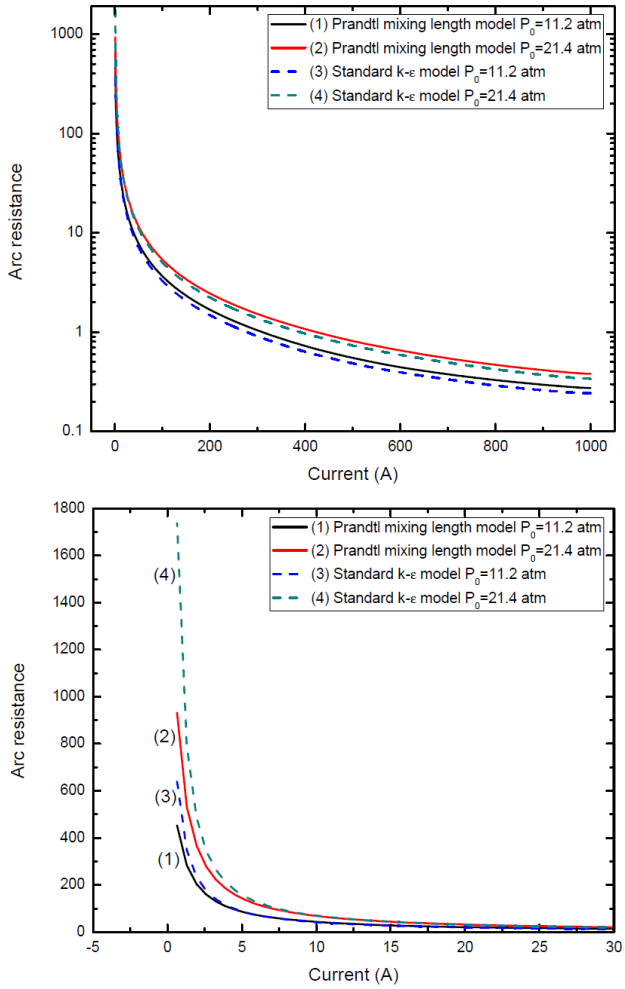

Figure B. 13. Variation of arc resistance as a function of current. Results are obtained by the Prandtl mixing length model and the standard k-epsilon model. P_0= 11.2 atm and 21.4 atm, and, di/dt=13 Aμs^{-1}. (a) Variation of arc resistance and (b) enlarged arc resistance variation shortly before current zero.

B.4 Concluding Remarks

The pressure dependence of the measured RRRV and that of those predicted by the Prandtl mixing length model and the standard k-epsilon model are close to the square of stagnation pressure rather than to the square root of the stagnation pressure for the DC arc. Such strong pressure dependence is due to the rapid decay of arc temperature and the shrinkage of the electrically conducting core 1 μs before current zero under the combined influence of turbulent enhanced thermal conduction and the

radial inflow of cold gas. It has been found that the arc resistance at current zero increases with the square of stagnation pressure. It has been suggested that RRRV is strongly correlated to the arc resistance at current zero, hence the pressure dependence of RRRV.

References

[B.1] Zhang J F, Fang M T C and Newland D B 1987 Theoretical investigation of a 2kA arc in a supersonic nozzle *J. Phys. D: Appl. Phys.* **20** 368-79

[B.2] Delcroix J K 1964 *Introduction to the Theory of Ionized Gases* (New York: Interscience Publishers)

Appendix C
List of Publications

2014

- Zhang Q, Yan J D and Fang M T C 2014 Effects of nozzle geometry on SF_6 arc thermal interruption *Proc. Int. Conf. on 20th Gas Discharges and Their Applications (Orleans, France (7-11 Jul 2014)) (Proceedings on Gas Discharges and Their Applications)* ed D P Hong pp 99-102

- Zhang Q, Yan J D and Fang M T C 2014 Modelling of SF_6 arc in a supersonic nozzle. Part I: Cold flow features and DC arc characteristics *J. Phys. D: Appl. Phys.* **47** 215201

- Zhang Q, Liu J and Yan J D 2014 Flow structure near downstream electrode of a gas-blast circuit breaker *IEEE Trans. Plasma. Sci.* **42** 2726-7

2013

- Zhang Q, Yan J D and Fang M T C 2013 Current zero behaviour of an SF_6 nozzle arc under shock conditions *J. Phys. D: Appl. Phys.* **46** 165203

2012

- Zhang Q, Yan J D and Fang M T C 2012 Computer aided design studies of auto-expansion circuit breakers *Proc. Int. Conf. on 19th Gas Discharges and Their Applications (Beijing, China (2-7 Sept 2012)) (High Voltage Engineeing: Special Issue on Gas Discharges and Their Applications* vol 38*)* ed Z C Guan (Wuhan: High Voltage Engineering) pp 202-5

- Zhang Q, Yan J D and Fang M T C 2012 Modelling of turbulent arc burning in a supersonic nozzle *Proc. Int. Conf. on 19th Gas Discharges and Their Applications (Beijing, China (2-7 Sept 2012)) (High Voltage Engineeing: Special Issue on Gas Discharges and Their Applications* vol 38*)* ed Z C Guan (Wuhan: High Voltage Engineering) pp 202-5